

# SUNFEST

([www.esse.upenn.edu/~sunfest](http://www.esse.upenn.edu/~sunfest))



## 2004

### *SUMMER UNDERGRADUATE FELLOWSHIPS IN SENSOR TECHNOLOGIES*



*TECHNICAL REPORT  
TR-CST01NOV04  
Center for Sensor Technologies  
University of Pennsylvania  
Philadelphia, PA 19104*

# *SUNFEST 2004*

## SUMMER UNDERGRADUATE FELLOWSHIP IN SENSOR TECHNOLOGIES

Sponsored by the National Science Foundation (EEC-0244055) and  
Microsoft Corporation

### PREFACE

*This report is the result of 11 undergraduate students' research efforts during the summer of 2004. From May 24 through July 31, 2004, students from Penn and other colleges participated in the SUNFEST program, which is organized by the Center for Sensor Technologies of the School of Engineering and Applied Science at the University of Pennsylvania. This unique "Summer Experience for Undergraduates in Sensor Technologies" program was initiated in 1986 and has grown considerably in size. It is now recognized as one of the most successful summer programs for undergraduates in the country. I would like to express my sincere gratitude to the National Science Foundation for their continued support for this REU Site, as well as Microsoft Corporation for sponsoring two of our students.*

*The purpose of the SUNFEST program is to provide bright, motivated undergraduate students with the opportunity to become involved in active research projects under the supervision of a faculty member and his graduate student(s). The general area of research concentrates on sensor technologies and includes projects such as materials and technology for sensors, microstructures, smart imagers, and neural networks for sensory processing and robotics. By providing the students with hands-on experience and integrating them with a larger research group where they can work together with other students, the program intends to guide them in their career choices. By exposing the students to the world of research, we hope they will be more inclined to go on for advanced degrees in science and engineering.*

*The students participated in a variety of hands-on workshops in order to give them the tools to do first-rate research or enhance their communication skills. These included "Giving Effective Presentations", "Ethics in Science and Engineering", "Use of Electronic Databases" and "Writing Technical Reports". Students also had plenty of opportunity for social interactions among themselves or with faculty and graduate student advisors.*

*The success of such a program is best measured in terms of the number of students who have gone on to graduate school. To date a total of 167 students have participated in the SUNFEST program. Of the students who have since graduated, about 70% have*

*gone on to graduate school or have received their masters and doctorate degrees. Several students also received awards based on their summer research.*

*This booklet contains reports from this year's projects, the quality of which testifies to the high level of research and commitment by these students and their supervisors. I would like to express my sincere thanks to the students for their enthusiastic participation; the help of the faculty members, graduate students and support staff is very much appreciated. I would also like to thank Ms. Delores Magobet, Shelley Brown, Denice Gorte, Sid Deliwala, Scott Slavin, Janet White and the rest of the ESE staff for their invaluable help in making this program run smoothly.*

Jan Van der Spiegel, Director  
Center for Sensor Technologies

**FINAL REPORT**  
**2004 SUMMER UNDERGRADUATE FELLOWSHIP**  
**IN SENSOR TECHNOLOGIES**  
**Sponsored by the National Science Foundation**  
**and Microsoft Corp.**

**TABLE OF CONTENTS**

<b>LIST OF STUDENT PARTICIPANTS</b>	<b>v-xi</b>
<b>THE IMPLEMENTATION OF THE SEGWAY ROBOTIC MOBILITY PLATFORM (RMP) FOR AUTONOMOUS NAVIGATION</b> <i>Benjamin Bau (Department of Electrical Engineering and Computer Science) – Massachusetts Institute of Technology</i> <i>Advisor: Dr. Vijay Kumar and James Keller</i>	<b>1-23</b>
<b>EXPERIMENTAL DEVELOPMENT OF THE MOBILE VESTIBULAR PLATFORM</b> <i>Alexander H. Chang (Comp. And Telecom. Engineering ) – University of Pennsylvania</i> <i>Advisor:Dr. Daniel Lee</i>	<b>24-75</b>
<b>VISUALIZATION OF REACHABILITY GRAPHS IN HYBRID SYSTEMS</b> <i>Seth Charlip-Blumlein (Electrical Engineering) – University of Pennsylvania</i> <i>Advisor: Dr. Vijay Kumar</i>	<b>76-82</b>
<b>CONQUERING TISSUE-SENSOR CONTACT</b> <i>Ling Dong (Biomedical Engineering) – University of Rochester</i> <i>Advisor: Dr. Britton Chance</i>	<b>83-96</b>
<b>INTERVERTEBRAL DISC IMAGING AND ANALYSIS PROTOCOL ENHANCEMENT</b> <i>David Jamison, IV (Engineering Mechanics) – The Johns Hopkins University</i> <i>Advisors: Dr. Dawn M .Elliott, PhD and Chandra S. Yerramalli, PhD.</i>	<b>97-112</b>
<b>DEVELOPMENT OF A NOVEL THERAPY FOR OCULAR NEOVASCULARIZATION</b> <i>Dominique Low (Mathematical and Computational Biology) – University of Pennsylvania</i> <i>Advisors: Elaine Wu and Dr. Tolentino</i>	<b>113-129</b>
<b>INTEGRATED ELECTROCHEMICAL GATING OF CARBON NANOTUBE FETs FOR BIOSENSING APPLICATIONS</b> <i>Emmanuel U. Onyegam (Electrical Engineering) – University of Texas @ Dallas</i> <i>Advisors: Dr. A.T. Charlie Johnson</i>	<b>130-140</b>
<b>THE HAND-HELD BREAST CANCER DETECTOR: A 2-D PHASED ARRAY SYSTEM</b> <i>J. Miguel Ortigosa (Electrical Engineering) – Florida Atlantic University</i> <i>Advisor: Dr. Britton Chance</i>	<b>141-158</b>

# TABLE OF CONTENTS

(Continued)

**MINIMIZATION OF DISTORTION AND INCREASING RESOLUTION IN WIDE-ANGLE VIEWING BY MEANS OF ACTUATED MICRO-MIRRORS**

*William Rivera (Electrical Engineering) – University of Puerto Rico, Mayaguez*

*Advisors: Dr. Suresh G.K. Ananthasuresh and Dr. Andrew Hicks*

**159-180**

**PORPHYRIN THIN FILM DIELECTRICS**

*Matthew Saucedo (Electrical Engineering) – Texas A&M University, Kingsville*

*Advisor: Dr. Jorge Santiago*

**181-198**

**DYNAMOMETER – THE NEW ACTIVITY MONITOR**

*Olivia Tsai (Electrical & Computer Engineering/Psychology) – Carnegie Mellon University*

*Advisor: Dr. Jay N. Zemel*

**199-221**

**LIST OF STUDENT PARTICIPANTS  
IN THE SUNFEST PROGRAM SINCE 1986**

**Summer, 2004**

Benjamin Bau	Massachusetts Institute of Technology
Alexander H. Chang	University of Pennsylvania
Seth Charlip-Blumlein	University of Pennsylvania
Ling Dong	University of Rochester
David Jamison	Johns Hopkins University
Dominique Low	University of Pennsylvania
Emmanuel U. Onyegam	University of Texas, Dallas
J. Miguel Ortigosa	Florida Atlantic University
William Rivera	University of Puerto Rico, Mayaguez
Matthew Saucedo	Texas A&M University, Kingsville
Olivia Tsai	Carnegie Mellon University

**Summer, 2003**

Emily Blem	Swarthmore College
Brian Corwin	University of Pennsylvania
Vinayak Deshpande	University of Virginia
Nicole DiLello	Princeton University
Jennifer Geinzer	University of Pittsburgh
Jonathan Goulet	University of Pennsylvania
Mpitulo Kala-Lufulwabo	University of Pittsburgh
Emery Ku	Swarthmore College
Greg Kuperman	University of Pennsylvania
Linda Lamptey	University of Pennsylvania
Prasheel Lillaney	University of Pennsylvania
Enrique Rojas	University of Pennsylvania

**Summer, 2002**

Christopher Bremer	Colorado School of Mines
Aslan Etehadien	Morgan State University
April Harper	Hampton University
Catherine Lachance	University of Pennsylvania
Adrian Lau	University of Pennsylvania
Cynthia Moreno	University of Miami
Yao Hua Ooi	University of Pennsylvania
Amber Sallerson	University of Maryland/Baltimore County
Jiong Shen	University of California-Berkeley
Kamela Watson	Cornell University
John Zelena	Wilkes University

**LIST OF STUDENT PARTICIPANTS  
IN THE SUNFEST PROGRAM SINCE 1986  
(continued)**

**Summer, 2001**

Gregory Barlow	North Carolina State University
Yale Chang	University of Pennsylvania
Luo Chen	University of Rochester
Karla Conn	University of Kentucky
Charisma Edwards	Clark Atlanta University
EunSik Kim	University of Pennsylvania
Mary Kutteruf	Bryn Mawr College
Vito Sabella	University of Pennsylvania
William Sacks	Williams College
Santiago Serrano	Drexel University
Kiran Thadani	University of Pennsylvania
Dorci Lee Torres	University of Puerto Rico (Humacao)

**Summer, 2000**

Lauren Berryman	University of Pennsylvania
Salme DeAnna Burns	University of Pennsylvania
Frederick Diaz	University of Pennsylvania (AMPS)
Hector Dimas	University of Pennsylvania (AMPS)
Xiomara Feliciano	University of Turabo (Puerto Rico)
Jason Gillman	University of Pennsylvania
Tamara Knutsen	Harvard University
Heather Marandola	Swarthmore College
Charlotte Martinez	University of Pennsylvania
Julie Neiling	University of Evansville, Indiana
Shiva Portonova	University of Pennsylvania

**Summer, 1999**

David Auerbach	Swarthmore
Darnel Degand	University of Pennsylvania
Hector E. Dimas	University of Pennsylvania
Ian Gelfand	University of Pennsylvania
Jason Gillman	University of Pennsylvania
Jolymar Gonzalez	University of Puerto Rico – Mayaguez
Kapil Kedia	University of Pennsylvania
Patrick Lu	Princeton University
Catherine Reynoso	Hampton University
Philip Schwartz	University of Pennsylvania

**LIST OF STUDENT PARTICIPANTS  
IN THE SUNFEST PROGRAM SINCE 1986  
(continued)**

**Summer, 1998**

Tarem Ozair Ahmed	Middlebury University
Jeffrey Berman	University of Pennsylvania
Alexis Diaz	Turabo University, Puerto Rico
Clara E. Dimas	University of Pennsylvania
David Friedman	University of Pennsylvania
Christin Lundgren	Bucknell University
Heather Anne Lynch	Villanova University
Sancho Pinto	University of Pennsylvania
Andrew Utada	Emory University
Edain (Eddie) Velazquez	University of Pennsylvania

**Summer, 1997**

Francis Chew	University of Pennsylvania
Gavin Haentjens	University of Pennsylvania
Ali Hussain	University of Pennsylvania
Timothy Moulton	University of Pennsylvania
Joseph Murray	Oklahoma University
O'Neil Palmer	University of Pennsylvania
Kelum Pinnaduwage	University of Pennsylvania
John Rieffel	Swarthmore College
Juan Carlos Saez	University of Puerto Rico, Cayey

**Summer, 1996**

Rachel Branson	Lincoln University
Corinne Bright	Swarthmore College
Alison Davis	Harvard University
Rachel Green	Lincoln University
George Koch	University of Pennsylvania
Sandro Molina	University of Puerto Rico-Cayey
Brian Tyrrell	University of Pennsylvania
Joshua Vatsky	University of Pennsylvania
Eric Ward	Lincoln University

**LIST OF STUDENT PARTICIPANTS  
IN THE SUNFEST PROGRAM SINCE 1986  
(continued)**

**Summer, 1995**

Maya Lynne Avent	Lincoln University
Tyson S. Clark	Utah State University
Ryan Peter Di Sabella	University of Pittsburgh
Oswaldo L. Figueroa	University of Puerto Rico-Humacao
Colleen P. Halfpenny	Georgetown University
Brandeis Marquette	Johns Hopkins
Andreas Olofsson	University of Pennsylvania
Benjamin A. Santos	University of Puerto Rico-Mayaguez
Kwame Ulmer	Lincoln University

**Summer, 1994**

Alyssa Apsel	Swarthmore College
Everton Gibson	Temple University
Jennifer Healy-McKinney	Widener University
Peter Jacobs	Swarthmore College
Sang Yoon Lee	University of Pennsylvania
Paul Longo	University of Pennsylvania
Laura Sivitz	Bryn Mawr College
Zachary Walton	Harvard University

**Summer, 1993**

Adam Cole	Swarthmore College
James Collins	University of Pennsylvania
Brandon Collings	Hamilton University
Alex Garcia	University of Puerto Rico
Todd Kerner	Haverford College
Naomi Takahashi	University of Pennsylvania
Christopher Rothey	University of Pennsylvania
Michael Thompson	University of Pennsylvania
Kara Ko	University of Pennsylvania
David Williams	Cornell University
Vassil Shtonov	University of Pennsylvania

**LIST OF STUDENT PARTICIPANTS  
IN THE SUNFEST PROGRAM SINCE 1986  
(continued)**

**Summer, 1992**

James Collins	University of Pennsylvania
Tabbatha Dobbins	Lincoln University
Robert G. Hathaway	University of Pennsylvania
Jason Kinner	University of Pennsylvania
Brenelly Lozada	University of Puerto Rico
P. Mark Montana	University of Pennsylvania
Dominic Napolitano	University of Pennsylvania
Marie Rocelie Santiago	Cayey University College

**Summer, 1991**

Gwendolyn Baretto	Swarthmore College
Jaimie Castro	University of Puerto Rico
James Collins	University of Pennsylvania
Philip Chen	University of Pennsylvania
Sanath Fernando	University of Pennsylvania
Zaven Kalayjian	University of Pennsylvania
Patrick Montana	University of Pennsylvania
Mahesh Prakriya	Temple University
Sean Slepner	University of Pennsylvania
Min Xiao	University of Pennsylvania

**Summer, 1990**

Angel Diaz	University of Puerto Rico
David Feenan	University of Pennsylvania
Jacques Ip Yam	University of Pennsylvania
Zaven Kalayjian	University of Pennsylvania
Jill Kawalec	University of Pennsylvania
Karl Kennedy	Geneva
Jinsoo Kim	University of Pennsylvania
Colleen McCloskey	Temple University
Faisal Mian	University of Pennsylvania
Elizabeth Penadés	University of Pennsylvania

**LIST OF STUDENT PARTICIPANTS  
IN THE SUNFEST PROGRAM SINCE 1986  
(continued)**

**Summer, 1989**

Peter Kinget	Katholiek University of Leuven
Chris Gerdes	University of Pennsylvania
Zuhair Khan	University of Pennsylvania
Reuven Meth	Temple
Steven Powell	University of Pennsylvania
Aldo Salzberg	University of Puerto Rico
Ari M. Solow	University of Maryland
Arel Weisberg	University of Pennsylvania
Jane Xin	University of Pennsylvania

**Summer, 1988**

Lixin Cao	University of Pennsylvania
Adnan Choudhury	University of Pennsylvania
D. Alicea-Rosario	University of Puerto Rico
Chris Donham	University of Pennsylvania
Angela Lee	University of Pennsylvania
Donald Smith	Geneva
Tracey Wolfsdorf	Northwestern University
Chai Wah Wu	Lehigh University
Lisa Jones	University of Pennsylvania

**Summer, 1987**

Salman Ahsan	University of Pennsylvania
Joseph Dao	University of Pennsylvania
Frank DiMeo	University of Pennsylvania
Brian Fletcher	University of Pennsylvania
Marc Loinaz	University of Pennsylvania
Rudy Rivera	University of Puerto Rico
Wolfram Urbanek	University of Pennsylvania
Philip Avelino	University of Pennsylvania
Lisa Jones	University of Pennsylvania

**Summer, 1986**

Lisa Yost	University of Pennsylvania
Greg Kreider	University of Pennsylvania
Mark Helsel	University of Pennsylvania

*University of Pennsylvania*  
Center for Sensor Technologies

SUNFEST

NSF REU Program  
Summer 2004

**THE IMPLEMENTATION OF THE SEGWAY ROBOTIC MOBILITY  
PLATFORM (RMP) FOR AUTONOMOUS NAVIGATION**

NSF Summer Undergraduate Fellowship in Sensor Technologies  
Benjamin Bau (Department of Electrical Engineering and Computer Science)-Massachusetts  
Institute of Technology  
Advisor: Professor Vijay Kumar and James Keller

**ABSTRACT**

A difficult problem in robotics is enabling a robot to navigate autonomously through a previously unexplored indoor environment. Part of this difficulty stems from the stringent requirements on the mobility and the power of a robotic platform. It is necessary that the platform has sufficient maneuverability to operate in a cluttered area and that it has sufficient power to carry the necessary sensors to operate autonomously. The Segway Robotic Mobility Platform (RMP) combines unusually high mobility with the power to carry a sufficient number of sensors to navigate in an indoor environment. This paper discusses how, using a laser range finder, a stereo camera, and the Segway's on-board encoders, the Segway RMP can be enabled to perform tasks of autonomous navigation while navigating through an area with obstacles.

## Table of Contents

**Section 1: Introduction**

**Section 2: Background**

**2.1: Segway Robotic Mobility Platform**

**2.2: Remote Objects Control Interface**

**Section 3: Mounting Sensors on the Segway**

**Section 4: Segway Blob Follower**

**Section 5: Segway Obstacle Avoider**

**5.1: A Preliminary Obstacle Avoider**

**5.2: Obstacle Avoidance with Mapping**

**Section 6: Current State of the Project**

**Section 7: Conclusions and Recommendations**

**Section 8: Acknowledgements**

**Section 9: References**

## 1. INTRODUCTION

One of the chief goals in robotics is to enable a robotic platform to navigate autonomously through an area with many potential, previously unknown obstacles. Even with the aid of such technologies as the global positioning system (GPS) and a variety of complementary sensors, this problem remains largely unsolved for even outdoor remote applications (for example, none of the competitors in the DARPA grand challenge this past year successfully completed the course). Indoors, the amount of space available for a robot to maneuver is often significantly decreased and the absence of a GPS signal makes it extremely difficult to pinpoint the robot's location. In order to enable a robot to successfully explore and navigate through the floor of an unknown building, one must seek to balance mobility with the ability to carry a sufficient number of sensors for the task.

At the General Robotics Automation, Sensing, and Perception (GRASP) Laboratory at the University of Pennsylvania, we sought to accomplish this task using a new form of vehicle technology, the Segway, which is unusually maneuverable for the amount of weight it can carry. This paper describes the process of equipping a Segway Robotic Mobility Platform (RMP) to perform autonomous navigation by enabling it to locate a colored object indoors and drive up to it while navigating around unspecified obstacles. This lays the groundwork for enabling robots to autonomously explore and operate in unmapped buildings with varying obstacles. Section 2 of this paper describes the Segway RMP, a test product developed based on the Segway HT technology for use as a robotic platform in the MARS2020 DARPA funded research initiative. Additionally, Section 2 provides background on the Remote Objects Control Interface (ROCI)[1] used by the GRASP laboratory to control all of its robots including the Segway RMP. Section 3 recounts the problems encountered in mounting sensors on the Segway due to its peculiar mode of movement and the design of a dynamic sensor platform in order to resolve these issues. Section 4 briefly describes the work done to enable the Segway to follow brightly colored objects autonomously using a stereo camera. Section 5 provides a description of two different methods of obstacle avoidance using a laser range finder. Section 6 describes the results of the implementation and testing of the Segway RMP as an autonomous robot. Finally, Section 7 contains conclusions and recommendations for future work on this project.

## 2. BACKGROUND

### 2.1 Segway Robotic Mobility Platform

The GRASP laboratory at the University of Pennsylvania received the Segway RMP as part of the MARS2020 project, which is funded by DARPA. The Segway RMP is configured by the manufacturer to follow external commands for its speed and turn rate. These external commands are transmitted via an onboard laptop computer which communicates with the RMP via a CAN bus. The Segway is special in that it is an automatically balancing, electrically powered, two-wheeled vehicle. Simply put, the Segway remains upright by accelerating in the direction that its platform is falling. Testing has led us to conclude that on certain terrains with low friction surfaces (ice, sand, mud, and dirt) this balancing mechanism becomes a liability because the Segway's attempts to accelerate in order to stay upright result in slippage and even greater loss

of control until it eventually falls. This has led us to conclude that the Segway is perfectly suited for indoor operations (rather than outdoors) where its biggest advantages, small foot-print (0.5 meters on a side), zero turning radius, and ability to carry well over one hundred pounds on its platform, make it perfectly suited for operating in a confined space. Whereas most robots equal to or superior to the Segway with respect to maneuverability in confined spaces are not powerful enough to carry the heavy sensors necessary for effective mapping and obstacle avoidance, the Segway's high payload capacity to size ratio makes it suited for the task of indoor autonomous navigation. Additionally, during indoor operation, the Segway rarely encounters the situations that make it most likely to lose traction, which could lead to loss of control and a crash. For example, indoors, the Segway is unlikely to encounter low-friction surfaces or bumpy terrain that interferes with its low-clearance [2].

The Segway RMP provided to the GRASP laboratory came with a simple program for sending commands to it and receiving data (*i.e.* wheel speeds and pitch angle) back from its encoders. A converter (wrapper) for this software was created in order to integrate it with the GRASP lab's software platform (see Section 2.2). Additionally, one of the first things I did upon arriving at the GRASP laboratory this summer was to write a simple user interface that allows the operator to see the commands being sent to the Segway and the readouts from the Segway's internal sensors. This interface (SegwayDashboard) also gave the user the ability to shut down the Segway, scale velocity and turn commands, and prevent commands from being sent to the Segway.

The University of Pennsylvania is not the only university currently working with the Segway RMP. Universities that are using the Segway RMP for similar purposes to the one in the GRASP laboratory include the Georgia Institute of Technology [3], Stanford University [4], and the University of Southern California [5]. In all three cases, these universities have mounted a SICK laser rangefinder on the Segway platform for the purposes of obstacle avoidance and other robotic applications such as terrain characterization. Likewise, this paper discusses how we mount and use a SICK laser rangefinder for obstacle avoidance. One dilemma that we address differently from these universities in mounting and operating the laser rangefinder and other sensors is in how we deal with the effect of the pitching of the Segway's platform on the observations made by the sensors mounted on it. Whereas, Georgia Tech corrects the error in distance measurements caused by this phenomenon by using pitch angle information provided from the Segway's internal encoders to mathematically correct for the Segway's pitching in software [3], we sought to resolve this issue by designing a new platform on which to mount sensors on the Segway (Section 3). Finally, while applications of the laser rangefinder might include terrain characterization, three dimensional area mapping, and supplying information to a remote, human operator, the main focus of the research covered in this paper is to equip the Segway RMP with an obstacle avoider effective enough to allow the Segway RMP to operate independently in a cluttered, unmapped indoor environment while attempting to accomplish a separate autonomous task.

## 2.2 Remote Objects Control Interface

Like the other robots in the MARS2020 project at the GRASP laboratory, the Segway is run using the Remote Objects Control Interface (ROCI) developed by the GRASP laboratory.

ROCI is a programming platform for robotic applications. Individual processes in ROCI are programmed as modules. For example, there is a module that receives commands from a joystick and a separate module that sends commands to the Segway. This means that modules can be used in a variety of combinations for various tasks. Modules are connected by pins that are responsible for transmitting data. These connections between modules are defined by XML files called tasks. Additionally, pins can connect various tasks allowing connections between processes running on different machines. One of the major advantages of ROCI is the extensibility of applications constructed within it and the reusability of their component modules. In short, since robotic applications are defined by which modules are connected, it is relatively simple to combine different simple robotic applications (such as following a colored object and obstacle avoidance) without writing any additional code. All that is needed is an XML task that connects the component modules in the correct fashion [2].

Fig. 1 shows an example of an assembly of ROCI modules that combines three different tasks: Task Joystick, Task SegwayRemote, and Task SegwayDashboard. When combined in this fashion, these tasks take in joystick commands in the Task Joystick, transmit these commands to a SegwayRemote task where they are changed into drive commands in the Joystick2Velocities module before finally sending them to the Segway module, which relays the commands to the Segway. Simultaneously, the Segway module is attached to a SegwayDashboard module, which provides a user on a different computer with a graphical user interface that displays options for controlling the Segway as well as data on its current behavior. While the Segway Remote task, which includes the Segway module, runs on the computer attached to the Segway, the Joystick and SegwayDashboard tasks can run on one or even two distinct computers.

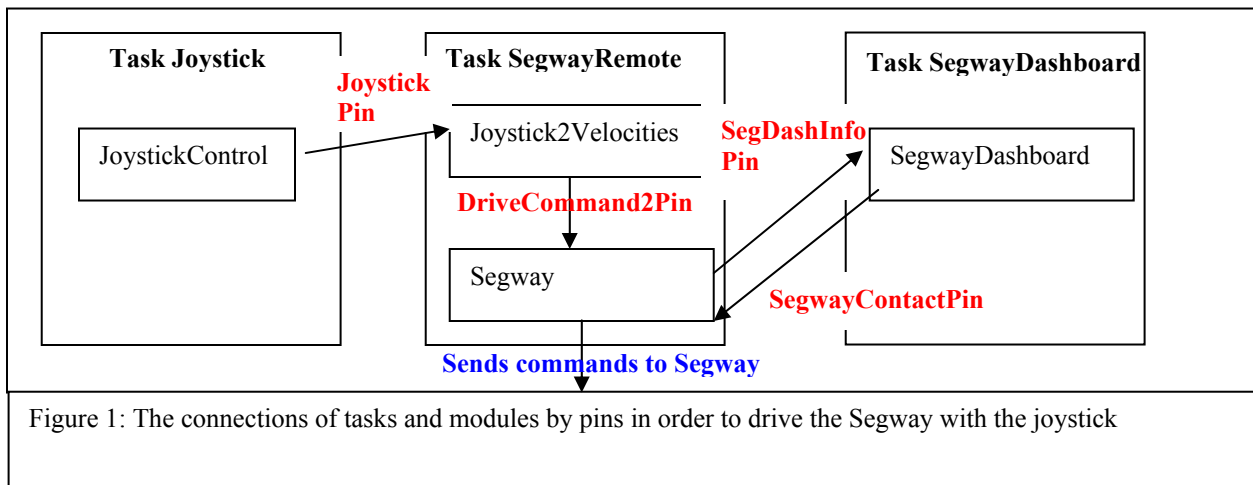


Figure 1: The connections of tasks and modules by pins in order to drive the Segway with the joystick

### 3. MOUNTING SENSORS ON THE SEGWAY

As described in Section 2.1, the built-in encoders from the Segway provide information on its speed, relative position, and orientation. However, in order to gather information about the space in which the Segway RMP is operating, it is necessary to mount additional sensors such as a camera and a laser range finder on its platform. Due to its balancing mechanism, the Segway's platform can tilt to significant angles when accelerating or having difficulty balancing. This severely inhibits the usefulness of sensors mounted on the Segway's platform in two ways. First of all, it makes locating an object detected by the sensors difficult because the distance measurements will be skewed by the sensor's varying orientation with respect to the ground. Second, the landscape that the sensor is viewing may change entirely. For example, a sensor that is supposed to look in the horizontal direction, which in most cases will be parallel to the ground, may end up observing the ground or the ceiling much of the time rather than the desired landscape. Figure 2 depicts the problem with mounting a sensor flat on the Segway's platform.

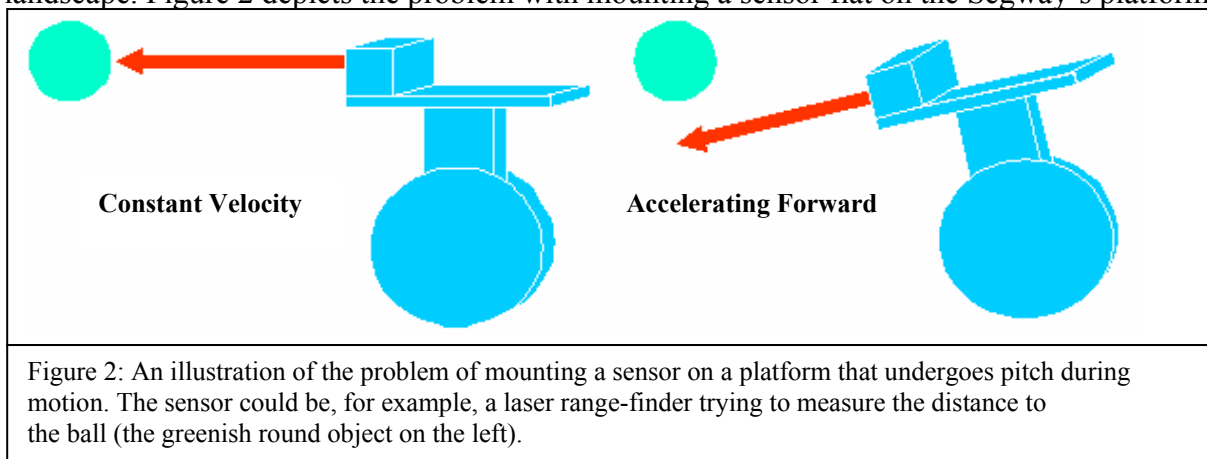
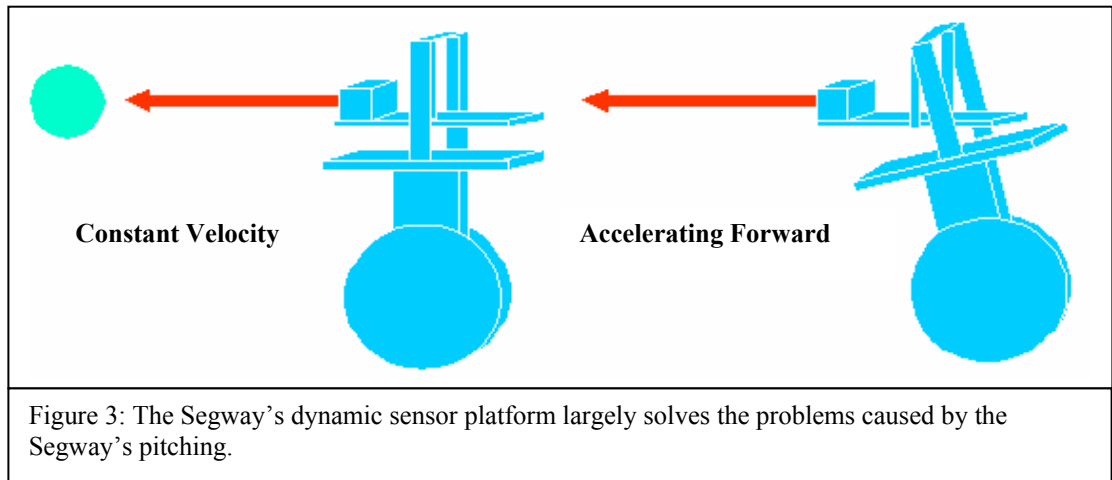


Figure 2: An illustration of the problem of mounting a sensor on a platform that undergoes pitch during motion. The sensor could be, for example, a laser range-finder trying to measure the distance to the ball (the greenish round object on the left).

Although the first problem could be solved in software by recording the Segway platform's pitch angle and using that information to correct for the error in the sensors' measurement of the distance, there is no software solution for the second problem (changing landscape of observation). Therefore, I opted to solve both problems at once by designing a passive, dynamically adjusting sensor platform which would always retain its horizontal orientation.

In designing the sensor platform, I chose to suspend the sensor platform as a pendulum and mount it on the Segway's platform. When the Segway's platform takes on a pitch angle, gravity causes the sensor platform to swing to the horizontal position. Although, it is true that when the platform moves it changes both the sensor's height off the ground and position with respect to the Segway's center, it is easy to compensate for these changes in distance mathematically, and the change in the sensor's frame of observation is insignificant compared to what would occur without the sensor platform. Figure 3 shows how this solution prevents the orientation of the sensor from changing.



In order to prevent oscillations as the sensor platform adjusts itself and to prevent the sensor platform from taking on a pitch angle of its own due to inertia when the Segway accelerates or decelerates, the motion of the sensor platform is damped with a commercially bought rotary dashpot (damper). Additionally, the position of the center of mass of the sensors on the sensor platform determines the angle that the platform maintains. For example, if the center of mass is positioned at the platform's center, then the sensor platform will maintain a horizontal orientation. Note that the height of the pivot and the amount of clearance of the sensor platform over the Segway's platform were calculated to allow the sensor platform to correct for pitch angles of over 30 degrees. The distance from pivot to sensor platform (the length of the arm of the pendulum) was chosen to be 19 inches in order to give plenty of room to place sensors on the platform. The minimum clearance necessary for a 20 inch long platform to adjust to a 30 degrees pitch angle (more than we ever expect to see during the course of regular indoor operation) without hitting the Segway platform is given by this formula:

$$height = \frac{2(arm)}{\sqrt{3}} - \frac{arm}{2} + 5\sqrt{3} \rightarrow clearance = height - arm \quad (1)$$

As can be seen from formula 1, the longer the arm is, the smaller the necessary clearance. For our prototype, the arm length is 19 inches, the height of the pivot above the Segway platform is 23 inches, and the clearance is 4 inches (as can be seen from plugging 19 inches in for the arm length in formula 1, anything over 3 inches of clearance is sufficient to handle a 30 degrees pitch angle without the sensor platform striking the Segway's platform).

Figure 4 shows the dynamic sensor platform mounted on the Segway carrying a LMS-200 laser range finder weighing 4.5 kilograms. In this case, the center of mass of the sensor and platform is in front of the pivot so the resting position of the platform gives the laser a slight angle downwards.

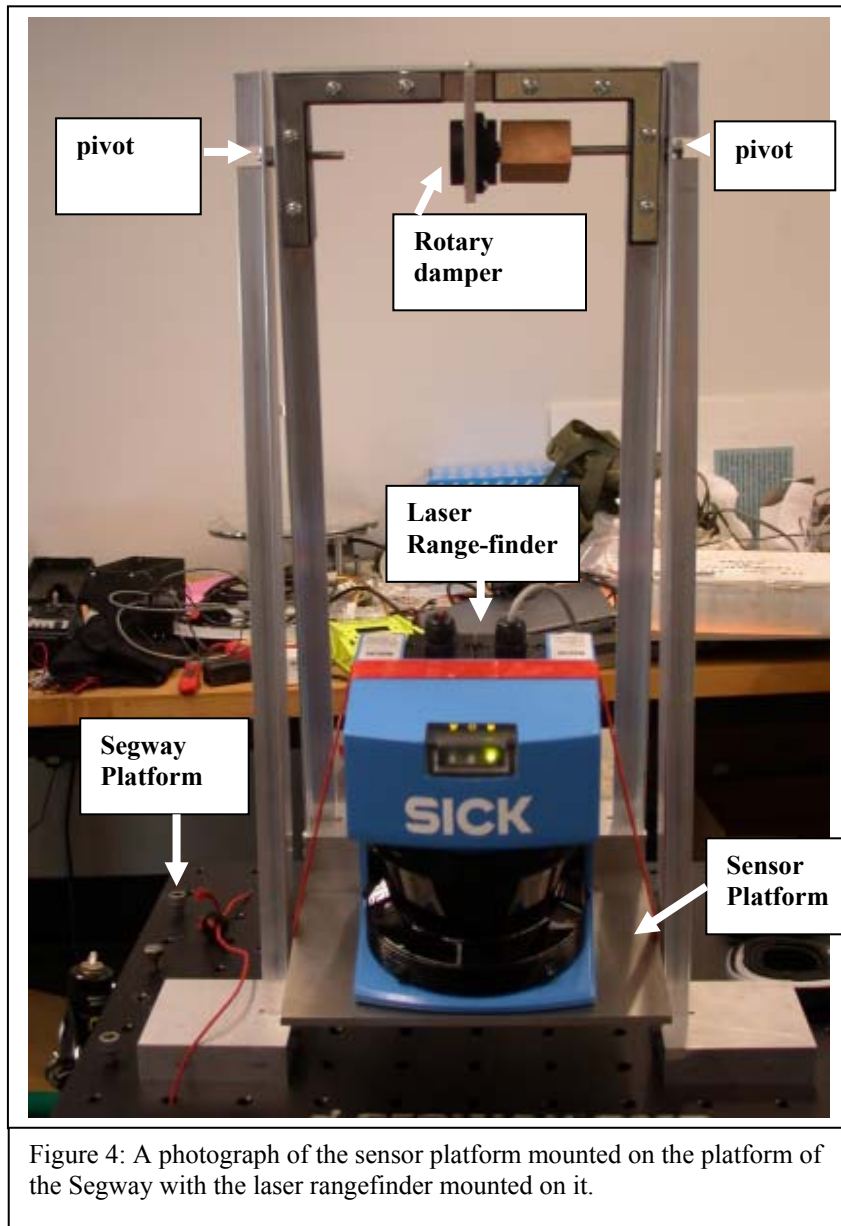


Figure 4: A photograph of the sensor platform mounted on the platform of the Segway with the laser rangefinder mounted on it.

#### 4. SEGWAY BLOB FOLLOWER

One of the sensors that can be mounted on the sensor platform is a stereo camera. This sensor is used to detect and locate brightly colored (orange, green, and pink) objects. Taking advantage of ROCI's (see Section 2.2) flexibility, we were able to use the same modules for identifying and calculating an object's distance from and angle to the camera as were used on another robotic platform-the Clodbuster (a small autonomous truck) [2]. Initially, I also used the same module to send drive commands to the Segway as was used to send commands to the Clodbuster in order to follow the object. Although this proved to work fairly well, the differences between the Segway and the Clodbuster eventually led me to redesign the way in which the drive commands were sent to the Segway based on the information provided by the camera about the object's location.

In the case of the Clodbuster, which is much smaller than the Segway, the costs of occasional erratic commands is less severe, both in terms of distance covered in the wrong direction and the types of crashes that may occur from a sudden wrong command, than they are for the Segway, which weighs approximately 130 lbs.

In the original system, upon receiving the estimated location of the object, a drive command was sent out which was proportional to the distance from the object. For example, when the object was five meters away from the Segway, the drive command would be larger than when it was two meters away. If the robot traveled to within a certain distance of the object (for example one meter) then it would be ordered to back up. Although typically estimates of the location of the object were on the mark, a few wrong estimates of an object's location could cause a wild response in the Segway's driving. These wrong estimations could be caused by the object not being quite the expected color or a simple change in lighting.

In order to smooth over these erratic measurements, I wrote a SegwayBlobFollower module that filtered the data before sending out drive commands. The module accomplished this task by collecting a number (specified by the user) of readings of the locations of points on the object (given by distance and angle) and comparing these readings with projected (extrapolated) distance and angle based on the Segway's velocity. Only measurements that were consistent with the projections were used to control the Segway. Moreover, by comparing the new measurements with the previous point chosen, an approximation of the rate of change of the distance and angle of the object with respect to the Segway is made and used to project the object's future location so that the next set of points can be filtered in the same manner.

In this way, data points that are egregiously wrong are likely to be ignored since only the one considered to be most "likely" is chosen from any given group. There are two major flaws in this approach, however. The first is that since multiple data observations have to be made before a drive command is determined the reaction time of the Segway is decreased in proportion to the number of data points that are collected in each group. Although unfortunate, this lag is dealt with by decreasing the speeds specified by the drive commands sent to the Segway. The second and more serious problem is that there are multiple sources of error in this method. These sources of error take three forms. The first is that the first data point cannot be checked against any projected position. Instead, it is simply the average of the first group of data points. A single outlier in this group would skew the original starting point, thus skewing future projections. The second source of error is that the estimates of rate of change are constant with respect to the moving Segway - not to any absolute point. In short, if either the Segway or the object is accelerating, then the projection will be incorrect. The third source of error is that if none of the points in the group are near the correct point, the point chosen from that group will then be wrong, as will be the rate of change estimates, causing future projections of the object's location to be wrong.

Although all of these are valid sources for concern, this algorithm tends to be self correcting. Operating under the premise that errors in the object's location are random or at least temporary, one can assume that even if the system begins to make incorrect projections of the object's position, it will eventually correct itself. In other words, if a projected location for the object is wrong, then it is unlikely that any of the locations in the group collected will match it. The point

chosen will therefore enforce a correction on future projections. For example, in the case where the object is accelerating away from the Segway, all the points in the group of measurements collected should be farther away than the projection would indicate. However, since the period between groups is not all that significant, the module will most likely choose a measurement that is close to correct (if one exists), and the resulting estimate of velocity will be greater than the previous one thus taking into account the acceleration of the object. For example, if the current distance to the blob is 5 meters and the estimated rate of change in distance is 3 m/s, then the projected distance to the blob after a second will be 8 meters. However, since the blob is accelerating with respect to the Segway, rather than any of the points taken in the next group being 8 meters, the module may get measurements of 11, 9, 13... meters. The blob follower will then choose 9 meters as the blob's location. Even if this is an underestimate of the distance to the blob, the new estimated speed will have increased taking into account the acceleration and forcing the projected value to be more in line with reality. Over the long term, any error should converge to zero as the general trend of the data forces projections to correspond with reality.

Although this blob follower has been written in software and preliminary tests show that it tends to perform at least as well as the original blob follower in locating and giving commands to follow the object, extensive testing has not been done on this module to see whether it actually is an improvement over the software previously used for Segway navigation.

## **5. SEGWAY OBSTACLE AVOIDER**

The Segway is equipped with a SICK laser rangefinder mounted on its sensor platform for the purposes of obstacle avoidance. The laser is capable of making a 180 degree scan of the area around it. In mounting the laser, I chose to direct it downwards so that on a completely clear plane, all of its readings except for the first and last one will hit the ground. Figures 5 and 6 show the necessary calculations for finding the expected distance to the ground for any angle in the laser's scan.

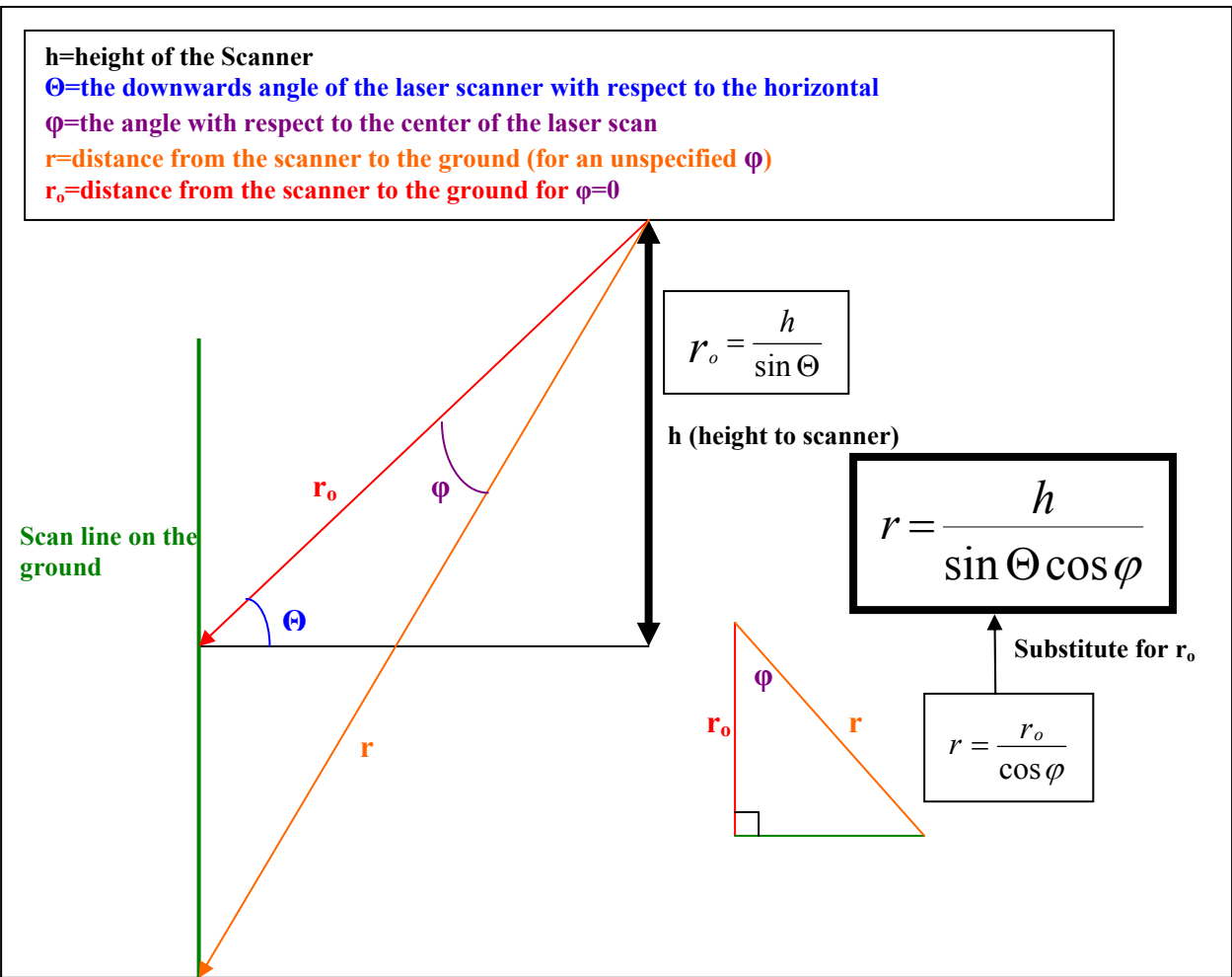


Figure 5: The plane between  $r_o$  and  $r$  is covered by the SICK laser. Shown are the calculations to determine the distance to the ground (assumes the ground is flat) as measured by the laser scanner in the absence of obstacles and holes as a function of the scan angle  $\varphi$ .

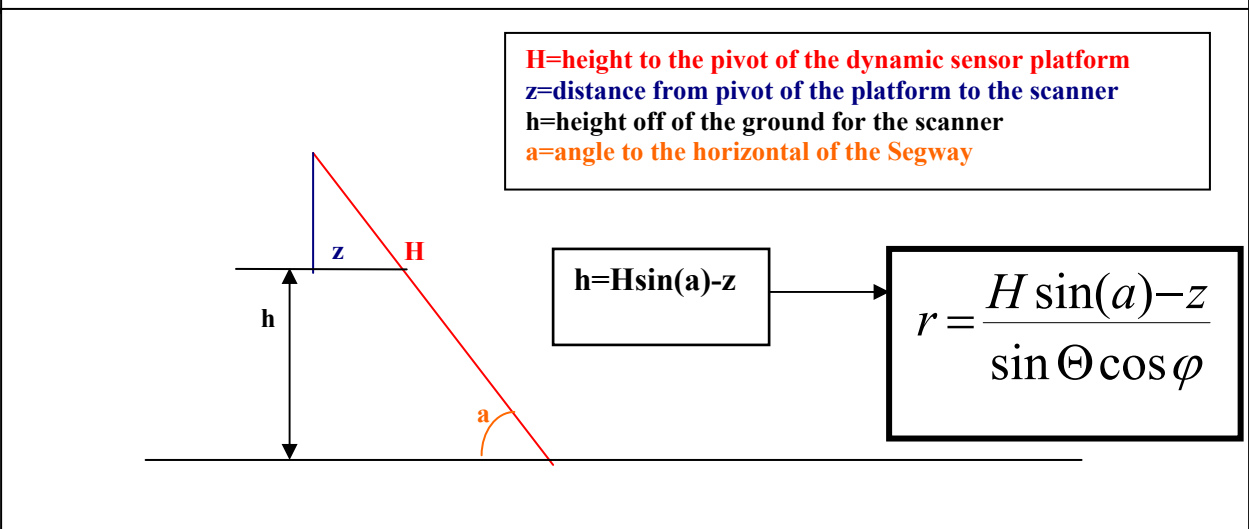


Figure 6: Refined calculation of the distance to the ground factoring in the pitch. This calculation accounts for a scanner mounted on the dynamic sensor platform

As the figures show, the expected distance to the floor for every scan is determined by the equation:

$$r = \frac{h}{\sin \Theta \cos \varphi}, \quad (2)$$

where  $h$  is the height of the laser from the ground,  $\Theta$  is the angle of the laser with respect to the horizontal, and  $\varphi$  is the angle in the laser's scan. Taking into account the Segway's pitch and the change in position of the laser on the dynamic sensor platform, the equation is modified to:

$$r = \frac{H \sin(a) - z}{\sin \Theta \cos \varphi}, \quad (3)$$

where  $a$  is the Segway's angle with respect to the horizontal,  $z$  is the distance to the pivot of the sensor platform from the laser, and  $H$  is the distance to the pivot from the bottom of the Segway.

Armed with this equation, for every data point given by the laser scan (angle and distance to object), we know whether the laser is detecting the ground, an obstacle, or a hole. If the scan returns the expected distance to the ground for that angle, then no obstacles were detected in that direction. On the other hand, should the laser's scan return a shorter distance than expected that means that there is an obstacle in that direction. Moreover, if the distance returned is longer than expected, then there is a hole in the ground in that direction. To allow for slight slopes and small obstacles that the Segway could easily roll over there is a +/- 0.1 meter margin of error before a reading is considered to be distinct from the ground. This precludes slopes larger than 10 degrees (which is near the maximum that the Segway RMP can handle). Since this obstacle avoider is intended primarily for indoor use, this limitation is not a serious one.

The algorithm above was used by both types of obstacle avoiders considered for this project. Section 5.1 describes the main obstacle avoider for this project. In section 5.2 are the outlines of an obstacle avoider that may eventually replace the design described in section 5.1. Although the laser range finder is an extremely accurate, active sensor, the fact that it only provides data on a part of a single plane leaves it vulnerable to several scenarios, listed in section 5.3.

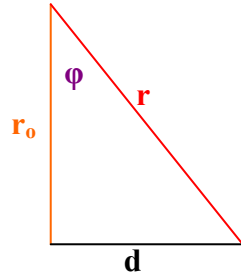
### 5.1 A Preliminary Obstacle Avoider

This obstacle avoider is passive as long as no obstacles are detected. In the absence of obstacles, it passes on the unmodified drive commands it receives from other modules. Upon detecting an obstacle, it ignores the drive commands it receives and issues its own commands until the obstacle is cleared.

The obstacle avoider detects an obstacle by checking whether the ground has been found for the range of angles that allow the Segway clearance to continue in a straight line from its present position. All readings for other angles are ignored because they are presumed not to interfere with the Segway's current motion. Figure 7, shows how to calculate the range of angles in the laser scan to check for obstacles.

Want to keep a width  $w$  clear-> angles of interest are:

$$2*d=w$$
$$r_o=h/\sin(\Theta)$$



$$w/2=r_o\sin(\varphi)$$

substitute for  $r_o$ :  $h\sin(\varphi)/(\sin(\Theta)\cos(\varphi))$

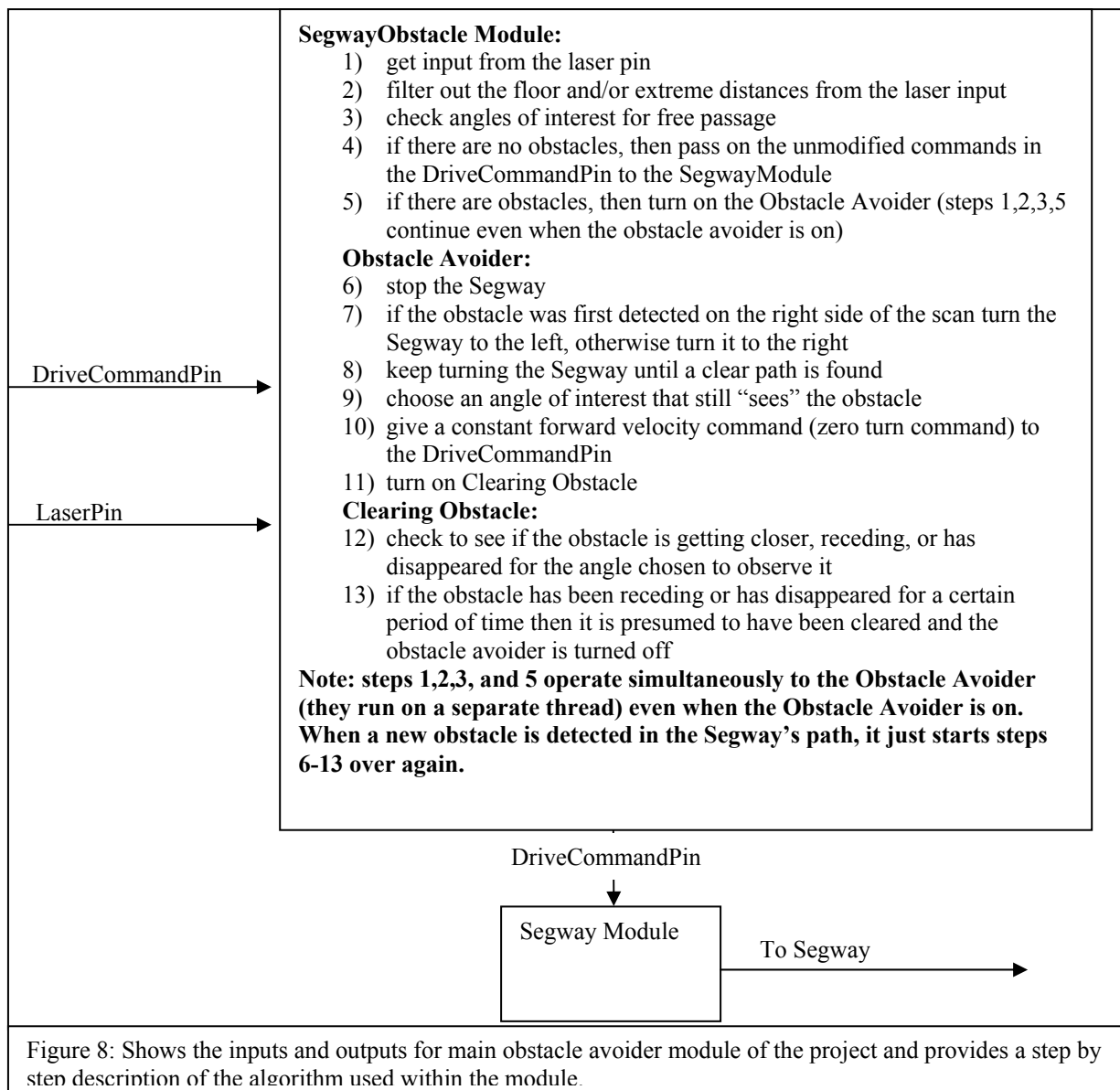
$$\varphi_1 = \tan^{-1} \frac{w\sin \Theta}{2h}$$

Figure 7: The calculation of the range of angles ( $-\varphi_1$  to  $\varphi_1$ ) needed to be checked to assure the presence of a gap of width  $w$  or greater that allows free motion of the Segway

The equation,

$$\varphi_1 = \tan^{-1} \frac{w\sin \Theta}{2h} \text{ (from } -\varphi_1 \text{ to } \varphi_1), \quad (4)$$

describes which angles should be checked to assure that a free passage of width  $w$  is available for the Segway to go through. Figure 8 describes the algorithm used by this module:



The obstacle avoiding algorithm follows these steps: (1) checks the laser data for an obstacle; (2) if there is no obstacle then the module passes on the unmodified drive commands to the Segway module (if the obstacle avoider is already on, then it sends the drive commands that it specifies) or if there is an obstacle turns on (restarts) the obstacle avoider. The following steps take place when the obstacle avoider has just been turned on: (3) stops the Segway; (4) turns the Segway at a constant speed until the laser data declares that the Segway can proceed in a straight line freely; (5) chooses an angle in the laser scan that still “sees” the obstacle; (6) the Segway is ordered to move forward with a constant velocity until the obstacle avoider is turned off or restarted; (7) the chosen angle is checked to see if the obstacle is getting closer, receding, or has disappeared; (8) if the obstacle has been receding or is no longer observed for a certain period of time then the obstacle avoider is turned off. Note that steps 1 and 2 operate concurrently to steps 5-8 so if the robot encounters an obstacle while obstacle avoiding, it simply restarts the obstacle avoider and

forgets about the prior obstacle. In this way, the algorithm deals with encountering additional obstacles while trying to avoid one. Also note that the reasoning behind observing the obstacle's distance and turning off the obstacle avoider when the obstacle has been receding or is no longer visible is that this observation indicates that the robot is about to pass a curve or corner in the obstacle or to leave it behind entirely. Therefore, the robot can either turn back towards its destination, having passed the obstacle, or at least choose a vector closer to the one desired if it has passed a corner or curve in the obstacle. The reason that the Segway continues in its straight line path for a period of time after the obstacle has been observed to have been cleared is that the laser rangefinder is observing the obstacle at a point ahead of the actual robot, so it observes that the obstacle will be cleared before the robot has actually cleared it. The additional time driving forward allows the robot to reach and pass the point at which it observes the obstacle to have been cleared. Figure 9 has a depiction of how the robot would act in encountering a single obstacle under this algorithm.

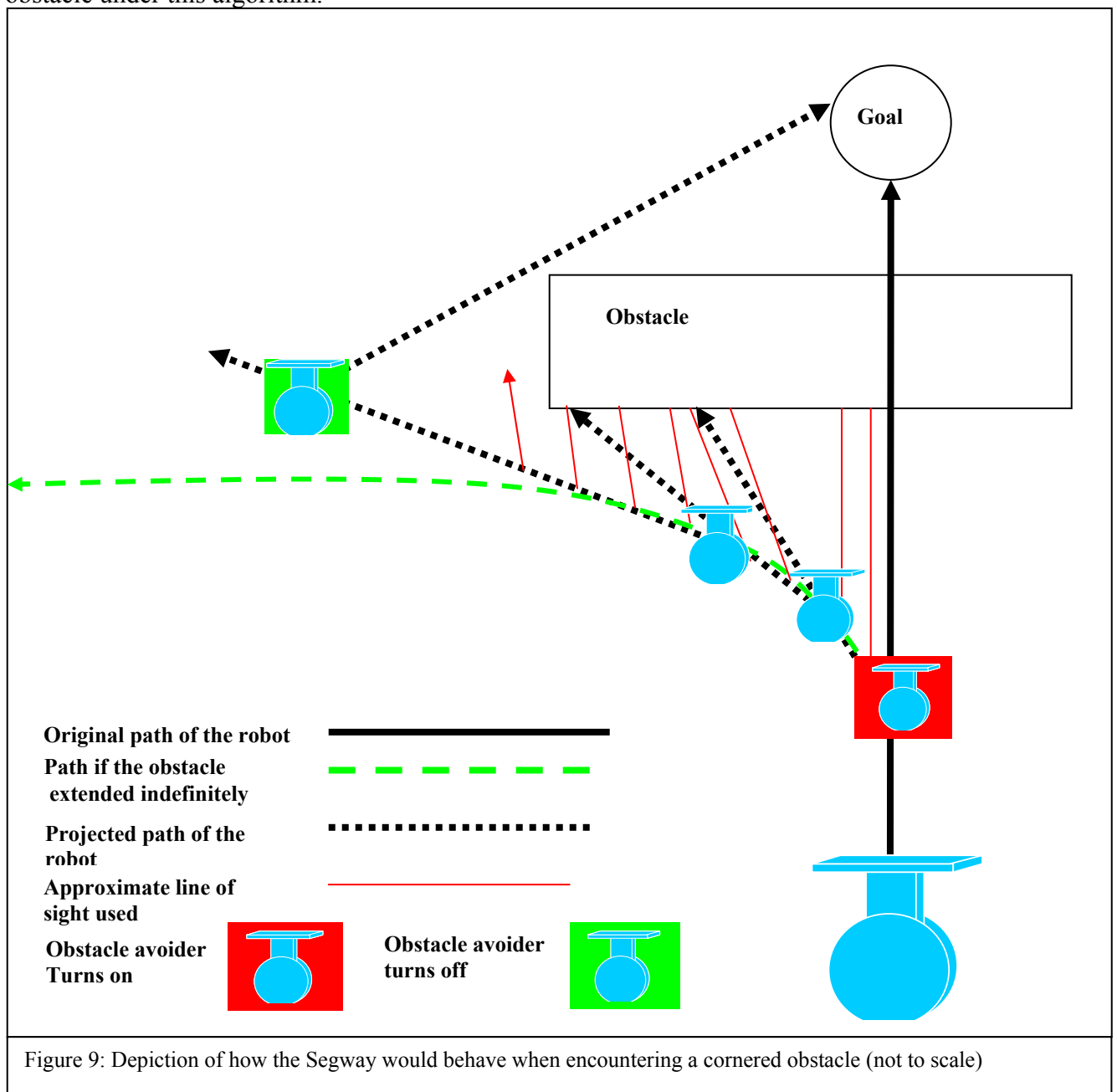


Figure 9: Depiction of how the Segway would behave when encountering a cornered obstacle (not to scale)

One of the flaws in this approach is that there is no awareness of the area in which the Segway is operating so there is no attempt by the module to chart an optimal course through all the obstacles recorded towards the goal. In other words, when the Segway is avoiding an obstacle, there is no awareness of the ultimate goal; it just wants to get around the obstacle at hand. In fact, the Segway may end up moving in a closed loop without ever reaching its target. Another problem is that there are scenarios where the robot could be caught in an infinite loop. Although a simple infinite loop can be ruled out by keeping the robot from choosing a trajectory 180 degrees trajectory from its current one when encountering an obstacle until that is determined to be the only available route, more complex infinite loops (for example, traveling in a circle around four points) can only be ruled out by implementing an obstacle avoider with mapping.

A flaw that should be corrected is that the Segway may already be turning away from the obstacle it views directly ahead under its regular drive commands but will still be sent into obstacle avoidance because the module always presumes that the robot is going straight ahead. Furthermore, currently, the module does not take into account the fact that the range of angles of interest (that could disrupt the Segway's path) increases the closer the object is to the machine. In the current configuration, the module only checks the range for a clear path at the distance that the laser scan reaches the floor. However, this is a much smaller range of angles than it would need to check for closer obstacles because the "rays" from the laser spread less for shorter distances. So a previously undetected obstacle that is very close to the Segway may be seen by the scanner but ignored because it is not in range

There are several ways to eliminate the problem of prematurely turning on the obstacle avoider. The first, and simplest, is to take advantage of the Segway's zero-turning radius to always have the Segway turn in place and then travel forward in a line. In that case, whenever the Segway is at risk of running into an obstacle, it is going straight. Alternatively, this problem could be solved by taking into account the current turn commands and speed in determining the range of angles from the scan to check for obstacles (if the Segway is turning to the right then check the same number of angles but in a range that is shifted to the right, of the center of the scan). The problem of missing close by obstacles can be eliminated by checking a wider range of angles for obstacles a short distance away and a decreasing range of angles from the scan for obstacles farther away. Although none of these solutions were implemented in the current obstacle avoidance module, it is likely that these improvements can be readily made. Unfortunately, there is no way to eliminate the rest of these problems without resorting to mapping (see Section 5.2).

As outlined earlier when encountering an obstacle, the Segway stops, then turns, then goes straight. At no point is it undergoing rotational and translational motion at the same time. This method was chosen because it provided the safest and simplest design. By stopping the Segway, we ensure that it has as much time as it needs to find an open vector in which to travel. Moreover, the magnitude of both the velocity and turn commands can be left as constant and need not be calculated based on sensor input (*i.e.* if the Segway is quickly approaching the obstacle it must decrease its translational velocity and increase the rate of its rotation). Attempting to have the Segway safely undergo dynamic navigation would require several additional layers of complexity in determining velocity and turn commands. At best, such a system could only match the current one in safety (preventing collisions). Given that the

processing speeds of the onboard computer rapidly decline with the addition of more sensors, such as the stereo-camera, the dynamic approach may currently be either infeasible or at least unsafe given our current computing power.

Tests indicate that the Obstacle Avoider described here works as intended. However, it has never been calibrated (the necessary measurements made) or tested for cases when the avoider is supposed to maneuver around holes in the nominal ground plane in addition to obstacles.

Note that this obstacle avoider deals fairly well with moving obstacles-it turns to avoid them just as it would avoid static obstacles and since it has no memory of obstacle location, it is not permanently affected by the obstacle's motion.

## 5.2 Obstacle Avoidance With Mapping

This obstacle avoider differs from the one in section 5.1 in that it plans its course around multiple obstacles rather than trying to explore one obstacle at a time. In essence, this obstacle avoider is made up of two parts: a mapper module and a navigator module. The area in which the Segway operates is mapped with a Cartesian grid. Upon starting, the Segway's location is set to be some point (currently the origin of the grid). The x and y coordinates of its goal are also set. From that point on, the Segway's position is calculated using its encoders, which provide integrated fore/aft distance and integrated yaw position. Drift in the information provided by these encoders, due to wheel slippage, is the major source of error in the mapping. Just as for the obstacle avoider described in section 5.1, the laser makes a reading and measurements that coincide with the ground are ignored. However, this time, all angles are checked and the ground distance to the obstacle from the Segway is determined using this equation:

$$d = \sqrt{r^2 - h^2}, \quad (5)$$

where the determination of r and h is described in Fig. 5. Using this distance and the angle in the laser scan and already knowing the Segway's x and y coordinates and its orientation, the x and y coordinate of the obstacle can be found and placed in the grid.

The map exists as a two-dimensional array with the addresses corresponding to the integer x and y coordinates. When an obstacle is detected it is placed in the container with the closest x and y coordinates. For example, an obstacle at (2.7, 3.1) goes in the [2, 3] container. Note that this method is inefficient in that each laser reading of an obstacle is treated separately. In short, every time the laser scan "sees" an obstacle in close to or the same location it will drop another recording of an obstacle into the container for that area rather than combining groups of readings into single obstacles. This could cause memory issues. Future improvements to this module should group obstacle readings for different locations that are close together into the single large obstacle that they probably form (or at least certainly would be as far as the robot is concerned). Ultimately, such a solution would be more efficient and elegant than the current one.

The obstacle avoider module receives an updated map and the Segway's location from the mapper module. It then attempts to plot a straight line between the Segway's current location and its goal. If there is an obstacle in the way on the map, the module determines whether it is more obstructive in the y or x direction. It then chooses a secondary goal with the same x or y

coordinate as the obstacle that appears to be reachable by a straight line on the map. For simplicity's sake, the Segway is either undergoing rotational or translational motion at any given time, not both. Once a safe line is determined the Segway turns onto a straight line to the new destination. If the destination is reached, then the Segway once more tries to make a straight line to its ultimate goal. If on the way to this secondary destination another obstacle appears on the updated map, then the Segway chooses another secondary destination and the prior one is thrown out. In this case, once the secondary destination is reached, the module again tries to plot a straight line route to the ultimate goal. In time, this method of choosing a route through the map should be changed to one where a full course is plotted with multiple way-points around all the known obstacles, not just the one of most immediate concern. Furthermore, search algorithms should be implemented to choose the most optimal trajectory based on a pre-defined cost function such as distance or time of travel.

To check whether any given line is safe, the contents of the grid spaces near the line are checked to ensure that no obstacles in them are within a certain margin of the Segway. In this way, there is some efficiency gain because only containers with contents that might possibly interfere with the current path are checked.

The most glaring problem with this obstacle avoider is that in its current implementation, an obstacle that is moving is recorded permanently on the map as blocking a certain area. In a busy environment this would render this obstacle avoider useless. An immediate, but somewhat complex, solution is to remove obstacles from the map as well as add them. However, this is not a viable alternative until the mapping mechanism is improved to the extent that the mapping groups whole areas together as obstacles rather than just individual points.

Although, this obstacle avoider has been implemented in software, it has never been tested with the Segway.

Figure 10, shows how the Segway would respond to an obstacle using this obstacle avoider.

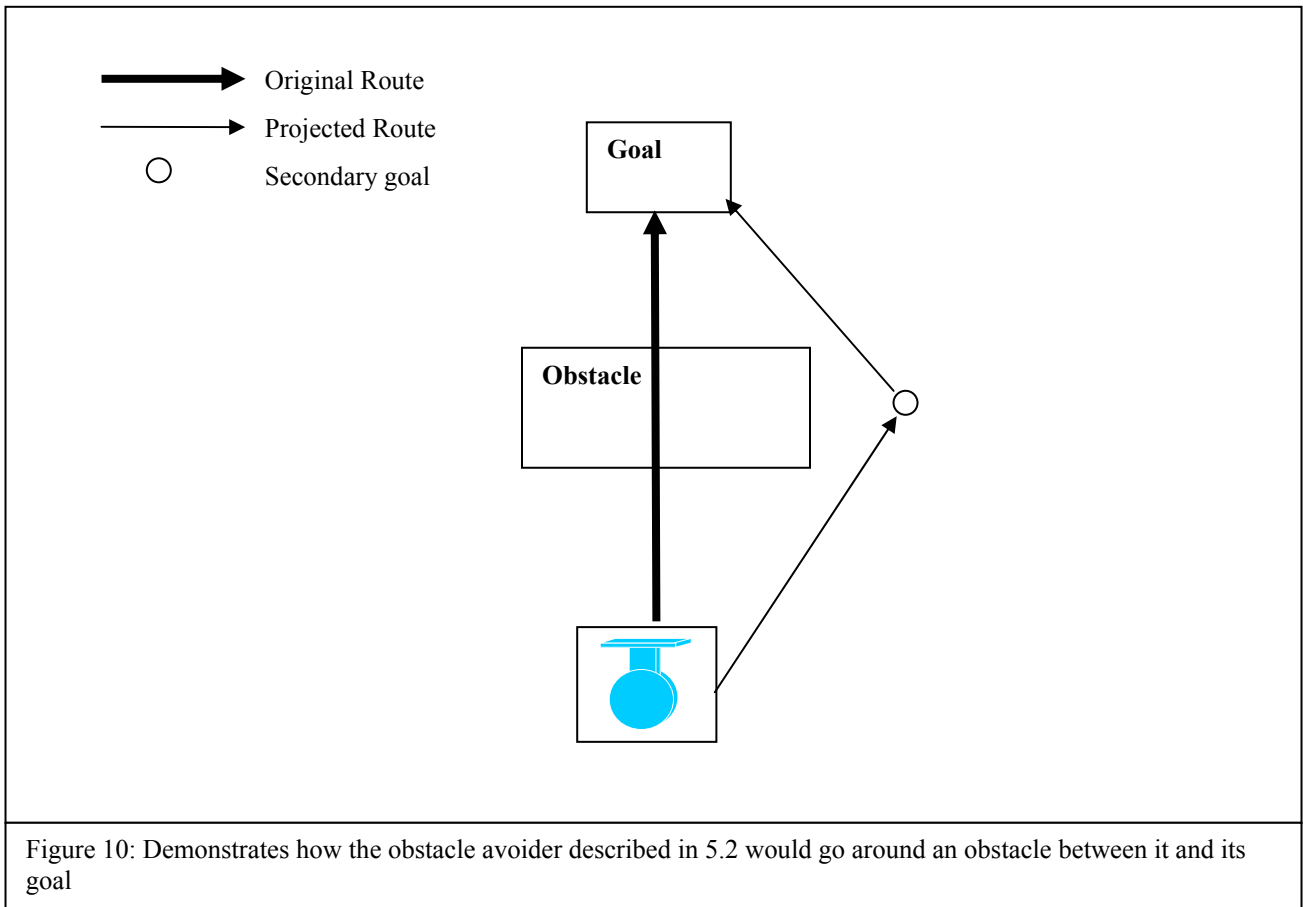
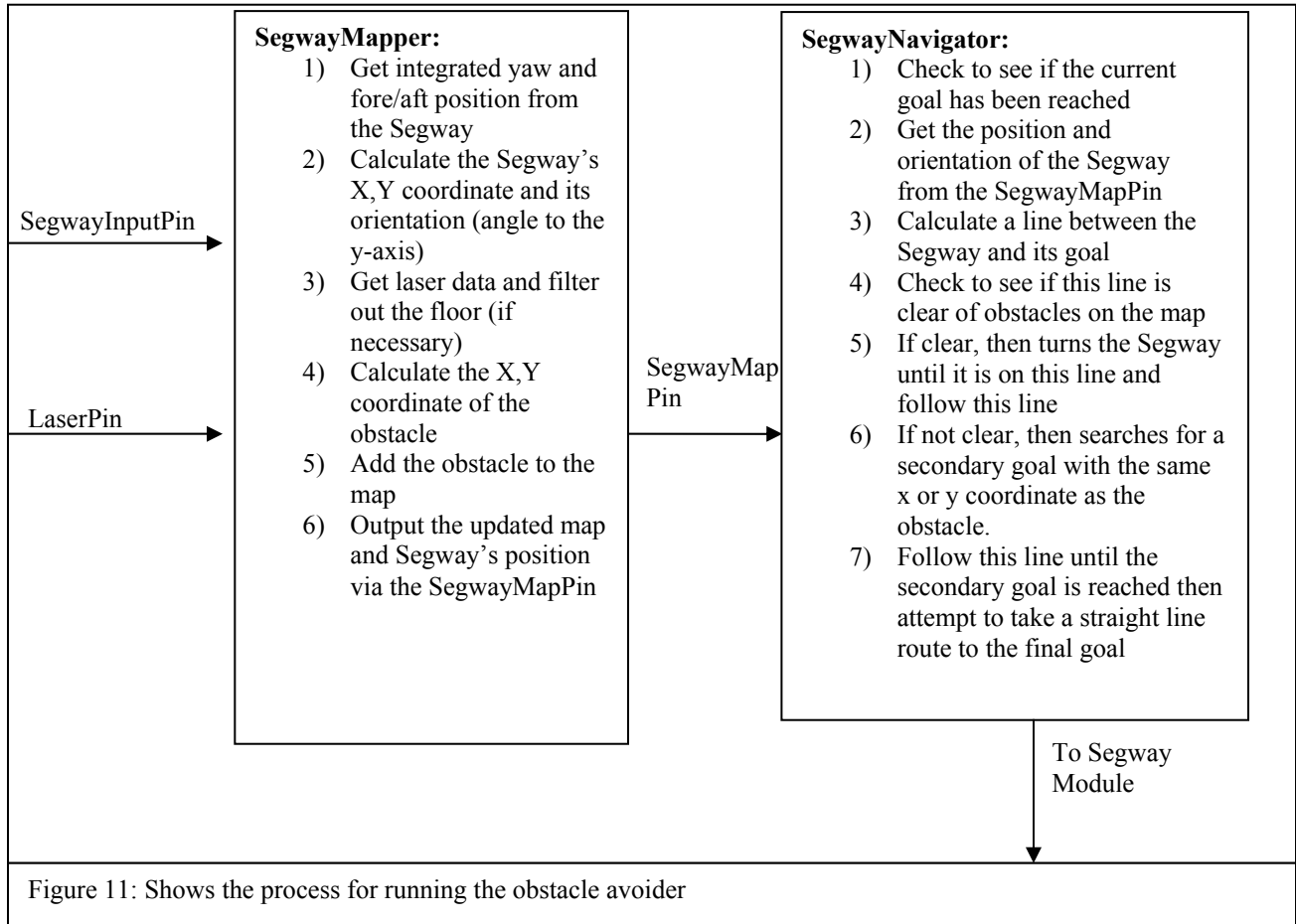


Figure 11 provides an outline of how this obstacle avoider works.



### 5.3 Problems With The Obstacle Avoider

Unfortunately, the first method of obstacle avoidance is fundamentally flawed. The simple fact is that with a two dimensional scan where the laser is mounted high above the ground, there is a great chance of the laser scan simply shooting over obstacles. With the passive obstacle avoider, the robot will see an obstacle to its side but since it is memory-less will not remember later that it should not turn in toward that obstacle. In the case of the second obstacle avoider, the robot will not hit an obstacle it has previously detected as long as the robot's coordinates are determined with a fair degree of accuracy. Therefore, when using an obstacle avoider with mapping, this problem is not so severe. Using the range-finder's 180 degrees scan, the robot will discover and map all obstacles it could possibly collide with before the range-finder starts shooting over them. In this case, the only requirement is that the robot starts out in an area free of obstacles that its laser might scan over.

At first, one might think that this problem could be easily solved simply by mounting the laser close enough to the ground so that the only obstacles it shoots over are those that the robot can roll over without trouble. Unfortunately, this introduces a whole new class of problems: the obstacles that it would shoot under. Particularly, indoors, the environment is not that of a plane world; the area in which the robot must operate is populated with tables, chairs, and benches

which a laser close to the ground will miss entirely. Ultimately, the use of a 3-d laser range-finder will completely eliminate this problem.

## **6. CURRENT STATE OF THE PROJECT**

During the course of this project, I successfully designed and mounted a dynamic sensor platform to compensate for potential difficulties in collecting data from sensors. Preliminary testing of the platform with a SICK laser range-finder and a stereo camera mounted on it shows that it does, in fact, provide a stable platform for mounting sensors on the Segway.

Additionally, there exists both a working prototype of a blob follower and an obstacle avoider that have undergone preliminary testing with the Segway. Currently the obstacle avoider has only been tested while receiving drive commands from a joystick. By replacing the joystick module with the modules used to develop drive commands for blob following in the XML file that defines an application in ROCI, the resulting application would allow the Segway to perform completely autonomous navigation by allowing it to attempt to follow a blob and avoid obstacles simultaneously. Early trials with putting this application together have indicated that the stereo camera consumes a significant portion of the Segway-based laptop's processing power, causing the computer to freeze when used in conjunction with the obstacle avoider. Cutting down on the camera's resolution seems to mitigate this problem, but it is not yet clear whether this is sufficient for autonomous operation given the throughput constraints of our current laptop computers.

Another problem involving the proposed autonomous navigation (obstacle avoidance while attempting to approach a blob of a certain color) is that currently the camera is flat-mounted on the sensor platform. This means that it faces in the direction that the Segway is facing. In many cases when trying to maneuver around obstacles, the Segway will have to turn away from the object it is attempting to approach. Just as a human would turn his head to look at the blob even while not walking directly towards it, the camera should have a pan mount so that it can turn with respect to the platform on which it is mounted in order to keep the object of interest in view. This would require some slight modifications in the modules related to locating the blob with respect to the Segway in order to correct for the camera's orientation.

As mentioned earlier, although the concept of a second, more advanced obstacle avoider with more potential for future improvement has been considered and I have begun implementing it, it has not yet been tested on the Segway and may require some modifications before it is a workable alternative to the current obstacle avoider. Also, since I do not know how quickly the encoders on the Segway will accumulate error this concept may not actually be a viable alternative at all. However, if the Segway's position can be tracked accurately, such an obstacle avoider would be a great improvement over the one currently employed.

Finally, as mentioned at the end of section 5.1, although the current obstacle avoider has been shown to work fairly well with respect to multiple obstacles, it has not undergone extensive testing in order to calibrate it most effectively. First, the avoider has not been calibrated to recognize and deal with holes and drop-offs since the mathematics require exact measurements of how the laser is mounted (in order to identify the location of the ground), and a final mounting

has not been developed yet. Second, extensive testing would be useful in helping to identify such variables as how far ahead obstacles should be detected and responded to. Also, testing might show that it is necessary to add more sophistication to interpreting the laser data than just filtering out the floor. It may be necessary to use the laser reading not only to determine the obstacle but to find out exactly how close it is in order to determine the response. At the end of section 5.1, I mentioned several problems with this obstacle avoider and sketched out potential solutions. Given time and testing all of these could be used to vastly improve its performance.

## **7. CONCLUSIONS AND RECOMMENDATIONS**

There are several steps that can be taken in the near future. First, the current obstacle avoider should undergo extensive testing to identify its weaknesses, to determine how exactly to mount the laser on the sensor platform, and to complete its calibration. Then, an attempt should be made to operate the blob follower in conjunction with the obstacle avoider and to streamline this process. If preliminary efforts in this direction are successful, then the camera should be mounted with its own motor so that it can rotate freely to track the target even when the Segway is not heading towards it. Additionally, the more complex obstacle avoider, which uses mapping, should be completed. For both concepts of obstacle avoiders, obstacles are assumed to be static. Future research into dealing with moving obstacles would also be beneficial.

In the long run, more mechanical improvements will be necessary to enable the Segway to be fully autonomous. The most important of these is to replace the current laser range-finder with one with 3-dimensional scanning ability, or to optimize an obstacle avoider that uses mapping.

The combination of maneuverability and onboard power gives the Segway great potential for autonomously navigated, indoor applications. One of the most significant drawbacks in mounting sensors directly fixed to the Segway, the pitching of its platform, can easily be resolved by constructing a sensor platform similar to the one outlined in this paper. Moreover, early preparations for the Segway to perform autonomous tasks such as blob following and obstacle avoidance are meeting with success and laying the groundwork for more advanced robotic applications.

## **8. ACKNOWLEDGMENTS**

I would like to thank my advisors Professor Vijay Kumar and James Keller at the GRASP laboratory at the University of Pennsylvania. Additionally, I would like to thank the rest of the GRASP lab staff and students. Finally, I would like to thank the National Science Foundation and the SUNFEST staff for giving me this research opportunity.

## 9. REFERENCES

1. Luiz Chaimowicz, Anthony Cowley, Vito Sabella, Camillo J. Taylor, ROCI: A Distributed Framework for Multi-Robot Perception and Control, Proc. 2003 IEEE/RSJ Intl. Conference on Intelligent Robots and Systems, Las Vegas, Nevada, USA, Oct. 2003, pp. 266-271.
2. Benjamin Bau, A Report on the Segway's Performance as a Robotic Mobility Platform, <http://www.cis.upenn.edu/marsteams/Segway/Segway%20site.htm>, 2003.
3. Tom Collins, Segway RMP Experiments at Georgia Tech, DARPA MARS Segway Workshop, <http://www.cc.gatech.edu/ai/robot-lab/segway/>, September 23, 2003.
4. The Segbot, <http://www.segbot.com>.
5. Andrew Howard, Denis F. Wolf and Gaurav S. Sukhatme, Towards Autonomous 3D Mapping in Urban Environments, [http://www.cres.usc.edu/pubdb\\_html/files\\_upload/393.pdf](http://www.cres.usc.edu/pubdb_html/files_upload/393.pdf).

*University of Pennsylvania*  
Center for Sensor Technologies

SUNFEST

NSF REU Program  
Summer 2004

**EXPERIMENTAL DEVELOPMENT OF THE MOBILE  
VESTIBULAR PLATFORM**

NSF Summer Undergraduate Fellowship in Sensor Technologies  
Alexander H. Chang (Comp. and Telecom. Engineering) – University of Pennsylvania  
Microsoft Sunfest Fellow  
Advisor: Dr. Daniel D. Lee

**ABSTRACT**

Cable robotics is an emerging research field in robotics which has the potential to be applied to a variety of practical purposes and tasks. Applications dealing with short distance transportation of hazardous materials as well as the handling of and interaction around these materials are several of the major tasks that can be handled efficiently and safely by cable robots, reducing the risk to employee lives as well as the need for more complex methods to accomplish the same task. Environmental monitoring of deep mines, hostile environments, and other locations inaccessible or uninhabitable by humans is another very realistic and viable application of cable robotics, allowing for the current sensory information about a remote location to be known at any time. Because of the simplistic nature of the design of cable robots, entire networks can also be implemented in order to cooperate with one another with the purpose of completing a particular task and reacting to sudden changes in sensory data extracted from the surrounding environment.

The particular robot being developed in this project is a versatile, cable driven robotic platform capable of movement in a three-dimensional space, and is named the mobile vestibular platform (MVP). It is designed to be versatile in that the system can easily accommodate several different sensory functions, while also being low budget and light weight. The particular implementation used allows for high precision motor control and thus higher precision in the movement of the robotic platform through space, while a Matlab program handles calculation tasks and remote operation of the platform from a central processing PC.

## Table of Contents

<b>SECTION 1: INTRODUCTION</b>	<b>pg. 3</b>
<b>SECTION 2: A General Overview of the Cable Robot System</b>	<b>pg. 6</b>
2.1 Command Terminal Overview	pg. 6
2.2 Mobile Platform (End-effector) Overview	pg. 7
<b>SECTION 3: Mech. Design of the MVP System</b>	<b>pg. 7</b>
3.1 Suspension Cables	pg. 7
3.2 Cable Mount Locations	pg. 9
3.3 Platform Design	pg. 11
<b>SECTION 4: Elec. Design of the MVP System</b>	<b>pg. 12</b>
4.1 Components	pg. 12
4.2 PCB Design	pg. 16
4.3 Flowchart of the Electrical System	pg. 16
4.4 Problems/Issues	pg. 17
4.5 Completed MVP End-Effector	pg. 19
<b>SECTION 5: Soft. Design of the MVP System</b>	<b>pg. 19</b>
5.1 Mobile Platform End-Effector System Software	pg. 20
5.2 Command Terminal Software	pg. 20
<b>SECTION 6: DISCUSSIONS AND CONCLUSIONS</b>	<b>pg. 22</b>
6.1 Foreseeable System Issues	pg. 22
6.2 Future Work	pg. 22
<b>SECTION 7: RECOMMENDATIONS</b>	<b>pg. 24</b>
<b>SECTION 8: ACKNOWLEDGEMENTS</b>	<b>pg. 24</b>
<b>SECTION 9: REFERENCES</b>	<b>pg. 25</b>
<b>APPENDIX A: MVP - End-Effector System Software</b>	<b>pg. 26</b>
<b>APPENDIX B: MVP - Command Terminal System Software</b>	<b>pg. 37</b>

## 1. INTRODUCTION

The field of research in cable robotics has been gathering increasing attention due to the growing number of applications to which this field can be applied. Cable robots present several advantages in different applications due to their fundamental methods of operation, making them more suitable than other types of robots for several applications. This emerging field deals with the development of a form of robotics in which a central platform, or end-effector, is suspended by several cables, each of which is anchored to a stationary point in the surrounding environment. [3] The end-effector is so-named because it is the component performing the primary task of the robotic system and therefore is the only module of the system supporting the equipment needed for the particular primary task. It is moved from one point to another in three dimensional space by changing the lengths of the cable by which it is supported. This particular fundamental operation of the system is performed by actuators, or motors, that rotate the spools to which the suspension cables are attached. [2] The mobile vestibular platform (MVP) that was developed in this project is a particular example of a cable robot design. Its physical and mechanical aspects are shown in figure 1.

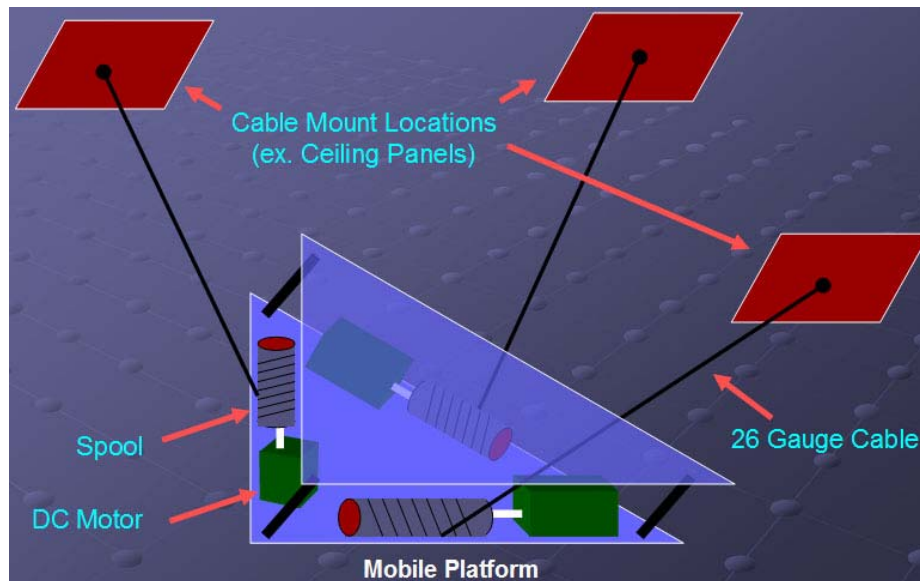


Fig. 1: Diagram of mechanical aspects of mobile vestibular platform end-effector

Several key properties of cable robots allow them significantly greater capabilities than other types of robotics. Because of their suspension by cables to stable points in the surrounding environment, cable robots have the capability to move in three dimensions, thus allowing them to move in efficient trajectories that other robots, constrained to movement in a plane, cannot employ. In this way, complex terrain and ground obstacles do not play a significant factor in the problem of moving from any point A to another point B, especially since obstructions and obstacles in the volume above a ground surface are much less common than those that may occur on the ground surface. In addition, the capability of movement in a third dimension allows for a much larger volume in which the robotic system may perform its tasks or work. Thus, this space or volume, constituting all of the points in the three-dimensional space to which the end-effector may travel, is defined as the *workspace* [4]. In addition to this, the robotic system can be

designed to be modular as well as extremely versatile, in many ways. Modularity allows for easy and quick repair and maintenance of the robotic system. The versatility of the cable robot is evident in designs where the end-effector is the only component performing the primary function within the robot's environment. Different end-effectors may be installed, or the equipment on the end-effectors changed, to allow for different tasks to be performed, such as sensory data collection, object transportation, etc. Also, cable robot design need not be tailored to the environment at hand, since the suspension cable mounts may be installed to any stationary location, after which initial setup and calibration of the system will "customize" the system to its particular environment.

This type of robotic system is appropriate for situations in which simple tasks or routines must be performed with precision in environments that are not particularly suitable or safe for human interaction. For instance, routine measurements of environmental properties, such as gaseous air content or temperature, in deep mines is one application to which cable robots are well-suited. Another realistic and practical application of cable robots is the manipulation and short distance transportation of hazardous materials, whether in a disposal or research environment, which would require a system that is extremely robust as well as reliable and precise. Another reason for the increasing interest in cable robotics is its suitability to future applications and problems. For instance, one possible future use of the cable robot would be in the monitoring and surveillance of the exterior region of a space shuttle or station, as well as the execution of simple operations such as object retrieval and data collection.

Several models of cable robots are currently in existence and are used in industries for which they were designed. One well-known example is the SkyCam (figure 2, left), which is a camera suspended by three very thin, but extremely robust, Kevlar-braided cables. The .25 mm diameter and reliability of the Kevlar-braided suspension cables allow the end-effector, the camera, to be transported at speeds up to 28 mph [1]. Due to the fact that this system transports a known, constant load, as opposed to a varying one such as in the application of waste disposal, its capabilities are easily determined and relatively stable. This property of SkyCam, however, is not always the case, as is evident in another well-known cable robot model, RoboCrane (figure 2, right), which is an industrial cable robot developed by the National Institute of Standards and Technology (NIST). Due to its extreme robustness, it can perform tasks dealing with variably heavy loads, such as warehouse item management and aircraft maintenance. [1]

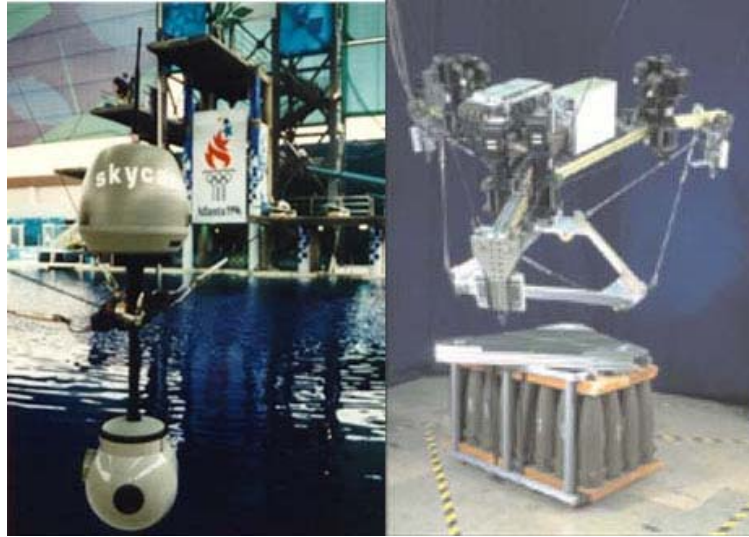


Fig. 2: SkyCam (left) and NIST RoboCrane (right)

The cable robot developed in this project is geared largely toward providing sensor mobility in a variety of environments, independent of the local or surrounding terrain, with the exception of the necessary stable cable mount locations. It was envisioned to be both light weight, to allow for operation in a wider gamut of environments, and low cost, so that entire sensory networks can be developed with these mobile platforms as sensory nodes for a variety of different sensory data and equipment. The intended purpose of the mobile vestibular platform necessitates the incorporation of several essential properties in order for the system to be practical and widely used. Versatility is one important aspect; the system should accommodate several different sensory functions at once and also be readily and quickly modified to support other functions and equipment. Another property needed for this particular system is precision mobility. The mobile platform is the means by which a general variety of light weight sensory equipment will be made mobile. As a result, the system's operations will be required to be precise enough in its movements so that that functions such as locating sources of sensory data (for example sound, light, chemicals sources, etc.) can be accomplished efficiently. This was done by incorporating precision motor controller IC's, which maintain precise tracking of motor position and movement related quantities, into the electrical system of the platform. In addition to the mobile platform and its own software/hardware control system, another remote terminal control system was implemented in a Matlab GUI application, allowing users to remotely control most higher-level functions of the platform as well as some basic functions for system debugging purposes.

A general overview describing the hardware and software systems that are implemented on the mobile vestibular platform system is first presented, in section 2. Section 3 provides a brief description of the mechanical system of the mobile platform end-effector, in order to give the reader an idea of the physical aspects of the system. Also, a description of the electrical system is presented in detail in section 4, summarizing the function of each component as well as revealing some of the problems encountered in the overall electrical system. In addition, several of the approaches taken to attempt to solve the different obstacles encountered are discussed. Finally, the programming/software aspect of this system is illustrated in two parts, one for the

microcontroller program controlling the end-effector, and one for the Matlab GUI program controlling the command terminal, both in section 5. The justification for the functions implemented in each of these two modules of code is also provided. In the end, some apparent issues of the mobile vestibular platform system as well as recommended solutions and future work are discussed.

## 2. A GENERAL OVERVIEW OF THE CABLE ROBOT SYSTEM

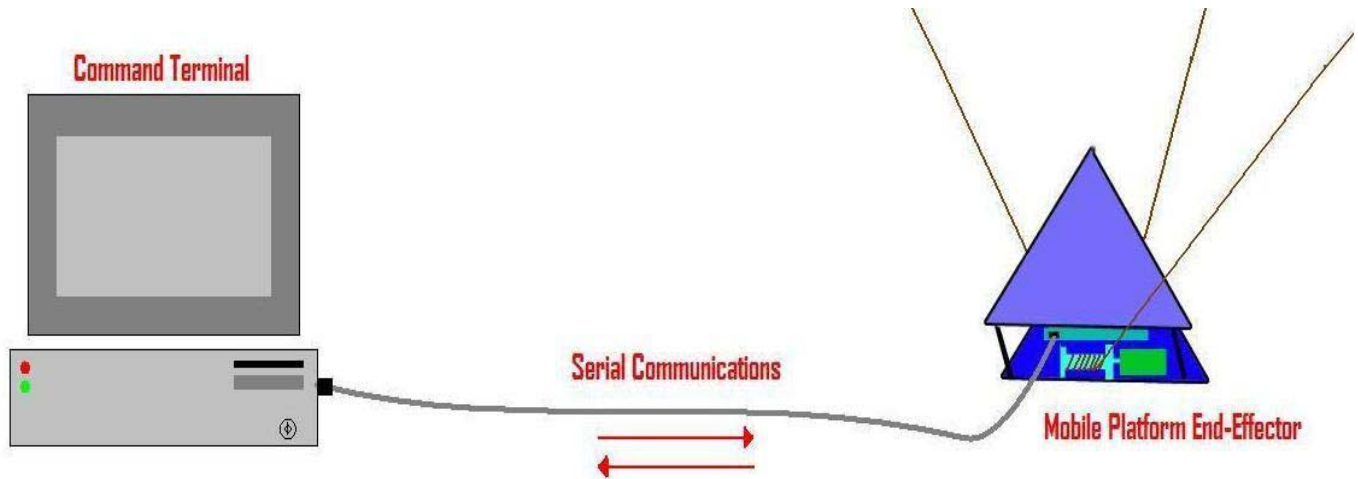


Fig. 3: Image of serial connection between command terminal and moving mobile platform

The MVP system being developed in this program is essentially a low-cost cable robot that is intended for use in tasks involving sensory data collection. The design was such that the cable robot system could be applied to a variety of environments, given the existence of the necessary number of stable cable mount locations. As a result, the environment in which this system could be used to collect sensory data did not play a large role as a variable in determining the design of the robot. In addition, the type of sensory equipment intended for use on this particular robot was limited to a relatively light weight, which also influenced both the mechanical and electrical design. Together, all of constraints as well as the intended purpose of the system led to a unique design compared to existing cable robots. The particular cable robot system that was developed in this program consists primarily of two physical entities. One was the mobile platform itself, serving as the end-effector of the system, and the other, less obvious, component was the PC running the Matlab GUI application from which the user can issue commands to the platform. The PC is referred to as the command terminal of the cable robot system. Both of these components of the mobile vestibular platform system are shown in figure 3, illustrating the mutual communication between the two.

### 2.1 Command Terminal Overview

Any PC, with Mathworks' Matlab Release 13 installed on it and at least one serial port, can be turned into the command terminal, with command terminal software installed. The command terminal PC runs a Matlab GUI application that was created with Matlab's Graphical User Interface Design Environment (GUIDE) to allow a user easy manipulation of the mobile vestibular platform system, while hiding the complexities of the calculations and communication that are required to carry-out those operations. The Matlab command terminal GUI application

allows operation of the system on different levels in that the user may command the mobile platform to move as a whole unit to different locations, or it may issue commands to perform more fundamental operations, such as the movement of one or more motors individually. From this command terminal, the user may also check the status of different components of the system as well as monitor overall system status. A very long serial cable connected the command terminal and the mobile platform to enable serial communication. The main objectives of creating the command terminal was, not only allow to the user easy control over the operations of the mobile platform, but to also provide a remote method of control of the platform. This is essential in situations where the platform cannot easily be reached for maintenance or manual control, which may be a large majority of the time since the mobile platform is most suitable for implementation in environments that are hostile or that make frequent access impractical.

## **2.2 Mobile Platform (End-Effector) Overview**

The bulk of the design of the system was concentrated on the mobile platform. Mechanical, electrical, and software design were needed in order to effectively implement the system. Later sections will elaborate, in much more detail, the mechanical, electrical, and software aspects of the design of the mobile platform. The mobile platform, in this system, is the end-effector of the cable robot where the sensory equipment is to be attached. The mobile platform provides mobility to the attached sensory equipment. In essence, it ‘houses’ the sensory equipment, while also providing mobility, and thus justifies the term “vestibular” in its name since it acts much like a car or train vestibule, transporting the equipment onboard. The platform has the ability to move in three dimensional space, within a volume limited only by the placement of its cable mounts. In addition, because of its mechanical design, it has the ability to change its relative orientation. For example, instead of being constantly horizontal with the ground surface, it can operate at variable angles, such as forty-five degrees relative to the surface, and thus has some limited rotational capability. The mobile platform is very modular, with the onboard microcontroller controlling all fundamental operations of the various components. It only requires commands, in a pre-determined format, to be issued to it serially in order to execute operations or sequences of operations to perform a task.

## **3. MECHANICAL DESIGN OF THE MOBILE VESTIBULAR PLATFORM SYSTEM**

One of the main objectives was to make the mobile platform design light-weight. With the mobile platform supported by a given number of cables, each with equivalent and constant maximum torque capabilities, each amount less than the mobile platform end-effector can weigh is an additional amount of weight more that can be allocated to sensory equipment. Using sensory equipment with greater weight generally means allowing more complex equipment with greater capabilities, which increases the effectiveness and applicability of the cable robot system as a whole. This section discusses several other mechanical properties of the mobile vestibular platform that may seem relatively insignificant at first, but allow the mobile platform several unique properties.

### **3.1 Suspension Cables**

There are several design issues that affect the operational capabilities of a cable robot system. An obvious consideration is the number of cables from which to suspend the mobile platform end-effector. The minimum number of cables needed to suspend an end-effector is directly related to the number of degrees of freedom desired. For example, if the platform is restricted to only moving along one line in space, then a minimum of two cables are needed; one cable to move the end-effector in one direction along the line and another cable to move it in the opposite direction along the same line. In general,  $n+1$  cables are required in order allow the system to operate with  $n$  degrees of freedom. More generally, for  $n$  degrees of freedom, a system requires  $n+1$  magnitude-varying, yet directionally-constant forces acting upon it [1]. This means that the force of gravity itself can serve as a sufficient surrogate for an additional cable, along the same direction as the force of gravity. In the particular cable robot design outlined in this paper, for example, only three physical cables are used to suspend and move the platform, yet the system can still perform movements through three dimensional space. With three degrees of freedom, the system requires  $3+1 = 4$  forces acting upon it. They are provided by the three physical cables plus the force of gravity, pulling the platform toward the center of mass of the Earth.

This particular design, where fewer physical cables are used, than are required for a system operating with a particular number of degrees of freedom, is defined as an *under-constrained* system (shown in figure 4, right). In other applications, such as the futuristic space station application proposed, in which the cable robot is used to survey the exterior of a space shuttle or station, the negligible overall force of gravity in any particular direction necessitates a fourth force to allow three dimensional movement in the region outside a space craft. [1] This can be accomplished, perhaps, by some type of onboard propulsion system. This type of system, in which all of the forces required for the particular number of degrees of freedom are implemented by system-controlled forces (ie. cables, constant propulsion devices) is defined as a *fully-constrained* system (shown in figure 4, left). [1] The mobile vestibular platform system could have been designed as a fully-constrained system. However, adding another suspension cable by which to manipulate movement of the mobile platform increases the complexity of the program and also requires more equipment on the platform, increasing the weight and cost. Since the force of gravity serves as a sufficient fourth force, to allow three degrees of freedom, the inclusion of a fourth cable in the direction of gravity was justifiably neglected in the design.

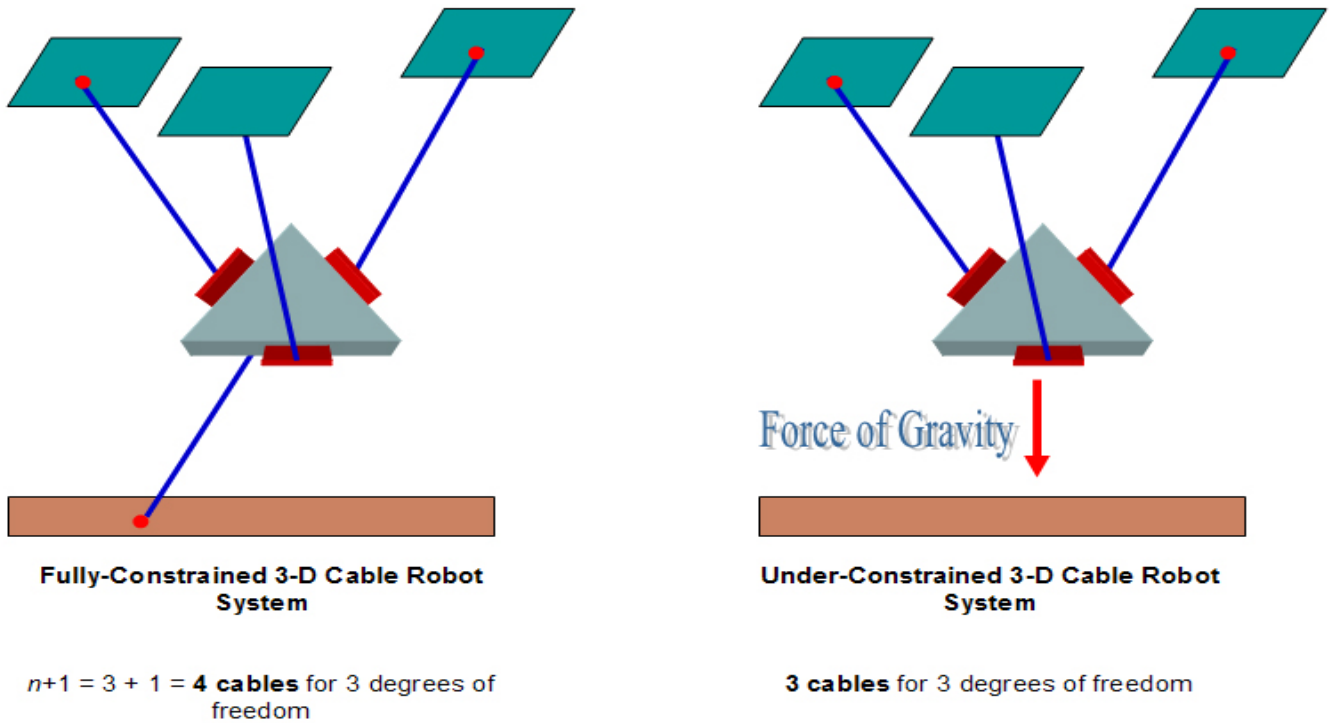


Fig. 4: Right: Under-constrained MVP system versus, Left: full-constrained MVP system

### 3.2 Cable Mount Locations

Related to the number of cables is the placement or the mounting locations of the cables on the mobile platform itself. Different on-platform, cable-mounting orientations allow different capabilities for the robotic system. For example, mounting all of the suspension cables on the periphery of the end-effector allows more stability against external disturbances, such as strong winds, collisions with other moving objects, during system operations. This is illustrated in figure 5 (right), where a strong wind can cause a point-mass cable mounting configured end-effector to sway from side to side severely. The image on the left in figure 5 displays the relatively little effect the same wind disturbance can have on a peripherally cable mounted end-effector. Also, peripheral mounting of the suspension cables on the end-effector allows for control over its orientation, allowing a mobile platform to orient itself parallel to different relative angular surfaces as needed. An alternative to peripheral orientation of the on-platform cable mounts is mounting the suspension cables at the center of mass of the platform, called point-mass mounting of the cables [4]. The advantage of this method is that there is no ‘wobbling’ of the platform as it is moved from one location to another. Wobbling is an issue using the peripheral orientation. [4]

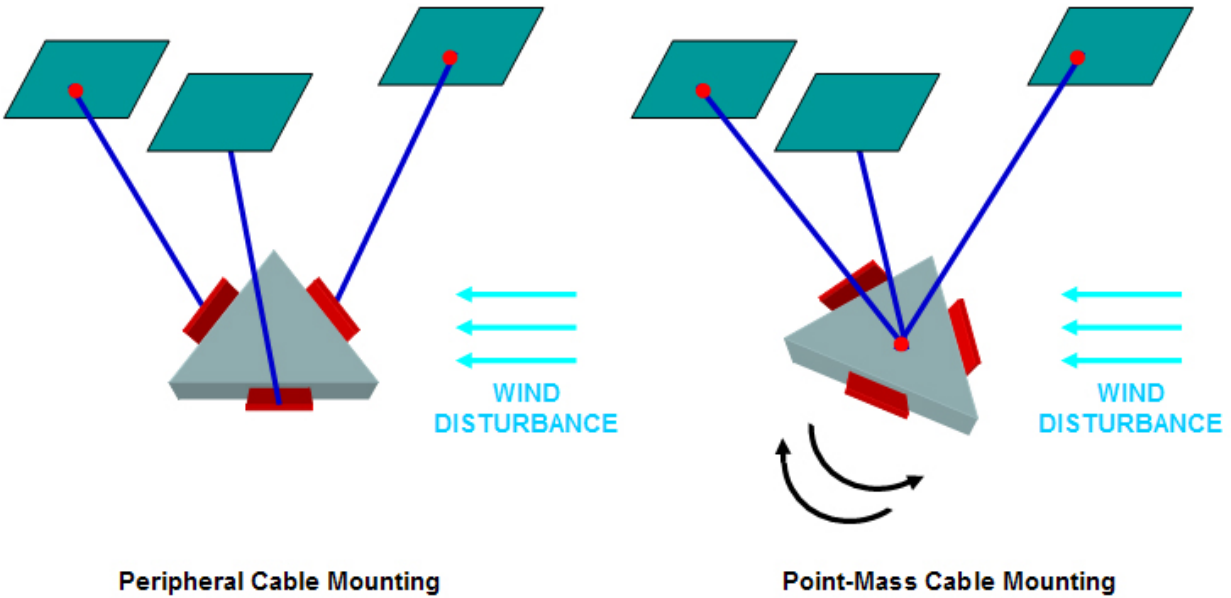


Fig. 5: Comparison of cable mount locations (Left: Peripheral Mounting, Right: Point-Mass Mounting)

‘Wobbling’ occurs when changing cable lengths, cause the platform to change its angular orientation continuously during movement. This occurs because with any given trajectory, the cable lengths may be required to change nonlinearly with time, in order to move the platform from one point to another. The ‘wobbling’ effect occurs when the system is operated or programmed assuming that the cables lengths should change linearly, as opposed to nonlinearly, with time. Figure 6 displays this effect with trajectory 1, where when moving the platform from point A to point B, the cable length,  $L$ , does not change. However, because of this, the part of the end-effector connected to this cable, will dip lower than other cable connections to the end-effector. A desired trajectory would be trajectory 2, in figure 6, where a straight path is followed from point A to point B. However, this path requires non-linear change in the cable length,  $L$ , as the end-effector travels from point A to point B. With multiple cables being used to control a platform, this effect can occur for each cable, each with different degrees of severity, depending upon the trajectory specified. With a center of mass configuration, however, a platform can have only one orientation due to the force of gravity, and thus it is not subject to ‘wobbling’ (assuming the center of mass remains constant). Thus with the center of mass configuration, no complexity has to be taken into account to minimize the ‘wobbling’ effect.

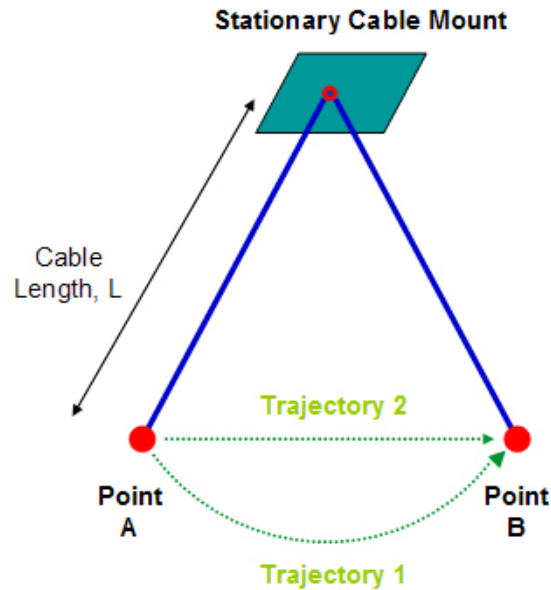


Fig. 6: Illustration of non-linear (Trajectory 2) versus linear (Trajectory 1) cable length actuation along one cable during platform movement

In the mobile vestibular platform, the suspension cables were mounted on the periphery of the platform, near the motors. As a result, the wobbling effect will play a factor in system performance, however, it can be approximately compensated for in the software of the command terminal running the Matlab GUI, the system which can handle the processing of this task most efficiently. Assigning this processing task to the command terminal PC significantly reduces the additional negative complexity that would otherwise be thrown onto the on-platform microcontroller, which is much less efficient in handling such operations.

### 3.3 Platform Design

The mobile platform that was designed for use as the end-effector in this system is a two-tiered, light-weight plastic structure. The two-tiered structure allows for protection of the equipment housed inside. This is useful as the environment in which the system may be operating is unknown. As a result, the components providing functionality to the system are hidden as well as protected from potential collisions. Also, the two-tiered structure allows for more flexibility in placing sensory and other communications-related equipment. Basically, there's more surface area on which to mount components. Both tiers of the mobile platform are equilateral triangles, which allows sensory equipment to be mounted symmetrically, aiding future platform operations that are dependent upon the comparison of data collected at different locations, such as in the task of locating the source of a type of data.

The three motors, which actuate the lengths of each of the three suspension cables, are mounted on the peripheral edges of the triangular platform, in between the two tiers. This particular placement of the cable length actuators, or motors, is different from many other conventional or past developed cable robot systems. The motors are not mounted to the stable cable mounting locations in the environment, but rather, they are mounted on the end-effector. Also, the suspension cable mounts in the environment (as opposed to on the end-effector) are

simply permanent attachments of the cable to the stable mount location, such as a ceiling or pole. There are several advantages to the placement of all of the motors on the mobile platform. First, the microcontroller on the platform has full control of the motors and thus its movements, making it very modular. In addition, when the system is used in difficult-to-reach locations, the motors can easily be replaced or maintained by having the mobile platform move to the most convenient location. When the motors are mounted to remote stable locations within the environment, repairing or replacing the motors can be very difficult. In addition, for remotely-mounted motors, a separate method of communication from a command terminal is needed. In the mobile vestibular platform, communication is accomplished through a single serial cable from the command terminal to the mobile platform.

#### **4. ELECTRICAL DESIGN OF THE MOBILE VESTIBULAR PLATFORM SYSTEM**

The electrical system that controls the mobile platform and its components is a relatively simple, modular system, consisting of components (IC's) that each perform a unique task in the operation of the mobile platform. The on-board microcontroller acts as the processing center for the mobile platform, directly receiving serial communications as well as issuing the commands to operate the rest of the components of the board. In addition to this, the program to control the microcontroller, and thus the entire mobile platform electrical system, was permanently installed in the system, reducing the end-effector system's reliance on other external systems by allowing it the capability to perform all of the basic operations independently. The following sections give a detailed description of the role of the various components of the mobile platform's electrical system and explain the relationships among them. Also discussed are the problems and obstacles encountered in developing the electrical aspects of the mobile vestibular platform system, and how they were solved.

##### **4.1 Components**

Adapt11C24DX Microcontroller Board with Embedded Motorola M68HC11 Microcontroller:

The Adapt11C24DX microcontroller board, with its embedded M68HC11 microcontroller, is the microcontroller unit (MCU) used on-board the mobile platform to control all the fundamental operations of the platform. It is also the board to which the serial cable is connected to receive communication from the command terminal. The mobile platform control program, to be run by the MCU, is compiled and the resulting machine code loaded into the on-board memory of the Adapt11C24DX microcontroller board. This control program is then executed by the MCU, allowing it to process the commands received serially and to execute the operations needed to carry out those commands received. The MCU controls the LM629 IC's, or precision DC motor controller IC's, to be explained momentarily, instructing them to execute the desired procedures to correctly operate the DC motors. The microcontroller essentially acts as the mobile platform's personal processing unit, which is what gives the mobile platform its modularity. Much like a computer with many peripheral modules being controlled by a central processing unit (CPU), the mobile platform also consists of many peripheral components or IC's which are controlled, directly or indirectly, by the MCU. The microcontroller relies only on commands issued from an external source in order to perform its basic operations of controlling the motion of the three motors. After receiving commands from the command terminal, it

communicates with the LM629 IC's through several I/O pins to issue the proper instructions. A modular diagram of the on-board peripheral components of the microcontroller board is shown in figure 7, below.

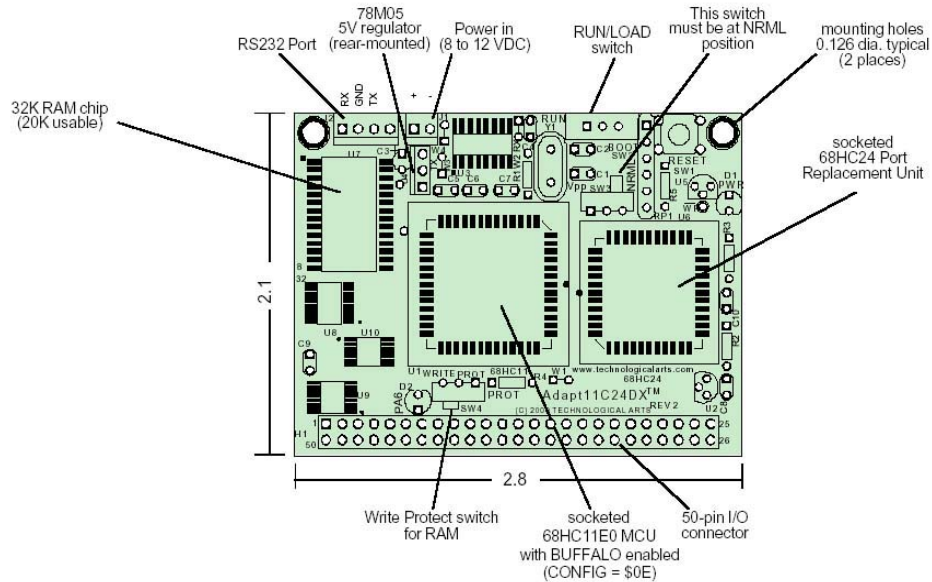


Fig. 7: Adapt11C24DX microcontroller board with embedded Motorola M68HC11 MCU

An advantageous feature of the Adapt11C24DX microcontroller board is that it contains 32K of electrically erasable programmable memory (EEPROM). This is a type of ROM that can be cleared, modified, and written through special procedures. Anything stored in EEPROM is not erased when the power supply is disrupted, as opposed to random access memory (RAM), where any type of power disruption wipes out all contents of the memory. This capability of the microcontroller board is a major contributor to making the mobile platform more modular, since the program to be run by the microcontroller does not need to be reloaded every time the power to the mobile platform system is reconnected or upon every start-up of the system.

National Semiconductor LM629N-6 Precision DC Motor Controller:

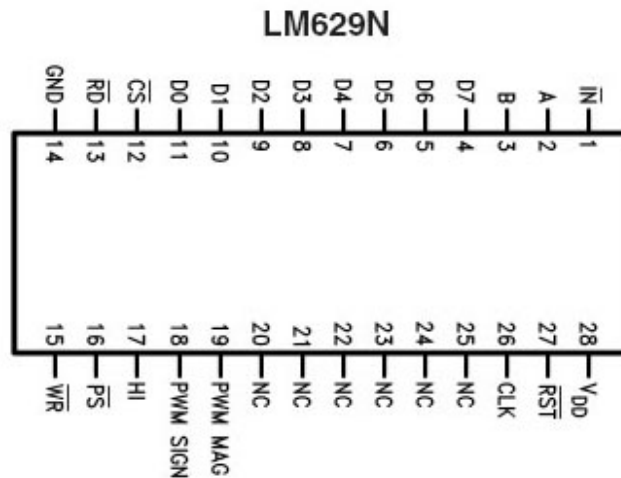


Fig. 8: LM629N-6 Precision DC Motor Controller IC

The LM629N-6 (figure 8) is, as its name implies, a high precision DC motor controller. This precision DC motor controller IC plays a large role by carrying out an entire aspect of the mobile platform electrical system, which is the precise control of the motor system. It can control the motion of a DC motor with significant precision in revolutions per second. The LM629 IC itself acts as a limited microprocessor, receiving and executing commands, although in reality it doesn't perform any processing. It is capable of receiving commands from its data lines. To put it simply, the fundamental commands it can perform allow it to receive an angular position to which to move the motor as well as an angular velocity and acceleration at which to move the motor. When the IC has received this information from the data lines, and is then commanded to execute the position change of the motor, it produces a pulse width modulated (PWM) signal to drive the motor to the intended position. In addition to this, the LM629 has two pins to receive optical encoder feedback from the motor, which provides a precise indication of the current position of the motor through the use of a quadrature amplitude encoded signal. With this two-line signal, the LM629 can make adjustments to the PWM signal being sent to the DC motor in order to speed it up, slow it down, or stop it, so that the desired position, velocity, and acceleration parameters are met as closely as possible. In this way, much of the processing needed to produce and adjust the necessary PWM signals, as well as the calculations to process the optical encoder feedback, are lifted off of the shoulders of the M68HC11 microcontroller on the platform, and automated in the LM629 IC instead. In addition, a large portion of the code and complexity that would otherwise have to be programmed and loaded into the microcontroller board's memory can be cut out.

National Semiconductor LMD18201T P+ H-Bridge:

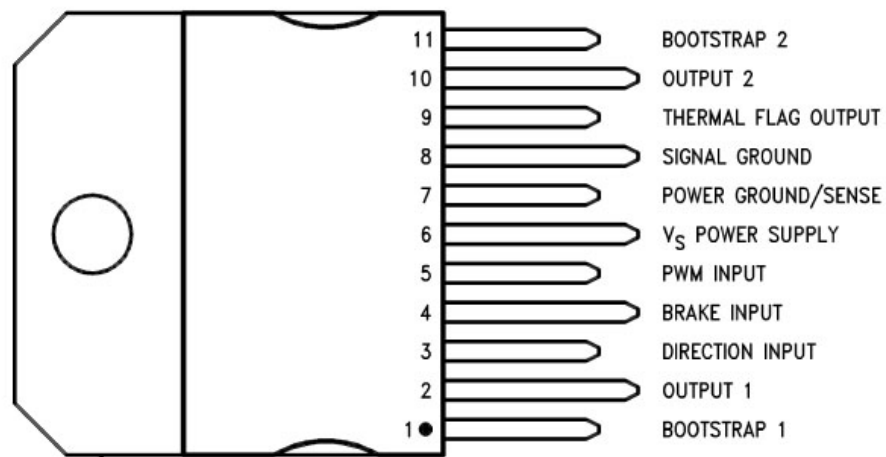


Fig. 9: LMD18201T P+ H-Bridge DC Motor Driver

Although the LM629 precision DC motor controller produces the PWM signal to operate the DC motors at the desired angular velocity and acceleration to reach the desired angular position, the signal power is relatively low since the IC's themselves cannot draw too much current without burning out. As a result, the PWM signals produced by the precision motor

controllers must be current-amplified in order to drive the DC motors. This is accomplished by the LMD 18201T P+ H-Bridge DC motor drivers. Given an input PWM signal, the H-bridge IC takes that PWM signal and produces the same PWM signal but at a higher voltage and current. For example, in this system the LM629 produces a PWM signal with a peak voltage of 5 V. The H-bridge takes that signal and amplifies it to a peak voltage of 12 V, while still maintaining the time characteristics of the signal and allowing the current drawn by the DC motor, from the H-bridge, to be increased significantly, giving the DC motors the necessary power to effectively actuate the mobile platform. The LMD18201T IC also has several other features such as a brake pin, which causes a signal of 0 V DC to be sent to the DC motor, immediately stopping any signal driving the DC motor. Another pin of the H-bridge, directly used by the LM629 precision DC motor controller, is the direction pin. This pin toggles the polarity of the PWM signal produced by the H-bridge and driving the DC motor. As a result, when the LM629 needs to do so, the DC motor will be driven in the opposite direction and thus will move with a negative, or reverse angular velocity. The DC motor controls the lengths of the cables by which the mobile platform is suspended and thus, the cables must be able to be reeled in and out in order to allow free movement of the mobile platform anywhere in a three dimensional space. In a more simplified model, the LMD18201T H-bridge can be thought of as a PWM signal amplifier, which receives the low voltage-current PWM signal from the LM629 precision DC motor controller, and amplifies this signal to the necessary characteristics in order to directly drive the DC motors.

Maxon DC Motor with Quadrature Amplitude Optical Encoder Feedback:



Fig. 10: Maxon DC Motor with Optical Encoder Positioning Feedback

While the LM629 precision motor controllers send PWM signals to the H-bridges, the H-bridges in turn send their output PWM signals directly to the Maxon DC motors, shown in figure 10. These motors wind and unwind the spools to which they are attached to lengthen or shorten suspension cables, allowing the mobile platform to change its position in three dimensional space. These DC motors, manufactured by Maxon, are also equipped with optical encoder feedback, allowing precise determination of the DC motor's operation or movement. Put simply, the optical encoder system produces two signals or channels that are sent back to the LM629 precision motor controller. The optical encoder feedback signals are quadrature amplitude encoded signals from which increments in the smallest rotational unit (which is determined by the precision of the optical encoder system) can be determined as well as the direction of rotation. The optical encoder system measures these increments in rotational units by optically

monitoring the rotational component of the DC motor. As a result, the data sent to the LM629 from the optical encoder of the DC motor allows for a measure of the real physical change in angular position of the DC motor, allowing the LM629 IC to make the necessary adjustments to the PWM signal driving the DC motor. In this way, there is a feedback loop from the DC motor output to the LM629 precision motor controller, so that adjustments can be made to follow the specified trajectory as closely as possible. In addition to this, this feedback from the DC motors allows the LM629 to make adjustments so that the DC motor stays in the same position once it has reached the desired angular position. When the platform has moved to its final position and must stay stationary in that position, the DC motor optical encoder feedback will provide the necessary data to the LM629 so that adjustments may be made in the PWM signal sent to the DC motor, to maintain the motor in the same position despite opposing torque from the load, which may be the platform itself along with other equipment.

## 4.2 PCB Design

The electrical system of the mobile platform was first implemented and tested on a series of proto-boards, with all of the motors connected. The circuit that was assembled on the proto-boards was exactly equivalent to the electrical system to be implemented on the two-tiered mobile platform. However, because the proto-board circuit required the use of almost three proto-boards, each being rather heavy, the equivalent circuit was implemented and laid out on a printed circuit board (PCB), on which all of the components needed for the circuit could easily and robustly be soldered. This greatly reduced the weight of the circuit and also allowed for it to be made much more compact in order to better fit on the mobile platform. In addition, all of the lines that were used to connect the proto-board components were readily capable of being accidentally removed, making the idea of using a PCB much more favorable. Two PCB designs were laid out, the first having dimensions of approximately 3.8 x 4.5 inches, and the second (shown in figure 11) much more compact with dimensions of approximately 3.6 x 3.9 inches. The second PCB layout significantly cut down on excess area and therefore seemed like the obvious choice to have manufactured. Problems caused by the particular PCB design used are discussed in section 4.4.

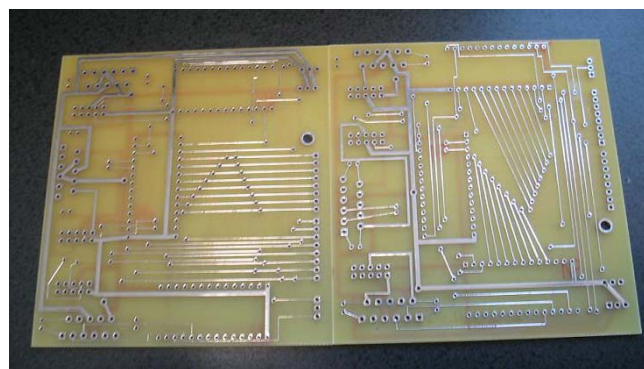


Fig. 11: Mobile Platform End-Effector System PCB

### 4.3 Flowchart of the Electrical System

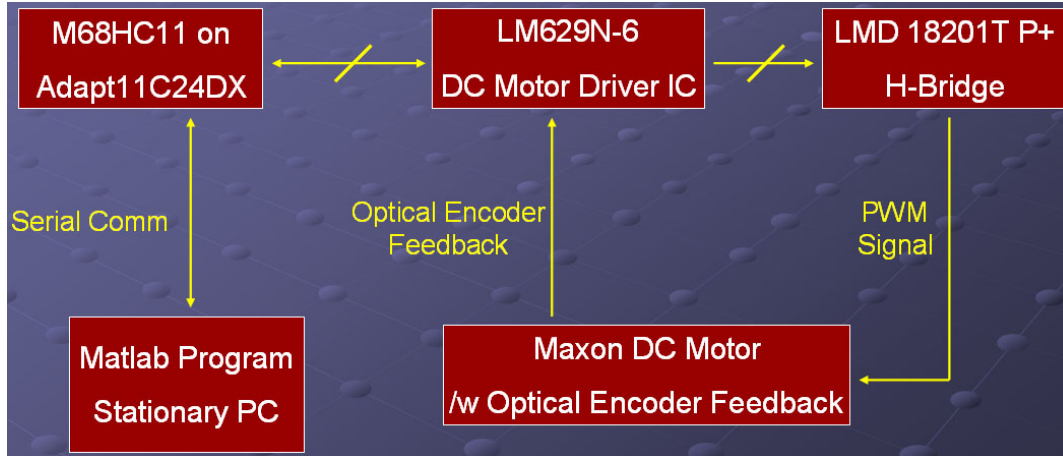


Fig. 12: Mobile Vestibular Platform Electrical System Flowchart

Figure 12 is the flowchart that corresponds to the software/hardware system developed for this cable robot system. Beginning with the Adapt11C24DX microcontroller board, we can see that this component communicates with the LM629 precision DC motor controller IC through several lines (data and command). The microcontroller follows the protocols required in order to issue byte commands to the LM629. The LM629 then communicates with the H-bridge by sending it a PWM signal, with which the DC motor should be driven, and a direction signal. The H-bridge, in turn, takes these two signals and produces a two channel PWM signal equivalent to the one received from the LM629, but voltage and current amplified sufficiently enough to drive the DC motor. These two PWM output channels directly drive the Maxon DC motor. From here, the optical encoder feedback system produces a two channel quadrature amplitude encoded signal that is sent back to the LM629, which then uses this signal to keep track of the current real angular position, velocity, and acceleration of the motor. With this information, the LM629 then makes the necessary adjustments to the PWM signal in order that the trajectory programmed into the LM629, by the microcontroller, is followed as closely as possible.

### 4.4 Problems/Issues

Of all of the problems and obstacles that have arisen during the development of the mobile vestibular platform system, the most persistent and difficult to debug problems, by far, were related to the electrical circuit for the mobile platform. Many of these problems seemed to be related to interference with the LM629 precision DC motor controller IC's. The circuit first developed, on a series of proto-boards, was found to consistently operate correctly, as opposed to the PCB circuit. The proto-board circuit was very well organized and easy to debug. In addition to this, all of the lines were well isolated simply due to the nature of proto-board. Therefore, this circuit was compared to the PCB circuit in an effort to determine the sources of various problems. Of all of the problems encountered during the development stages, the most interesting two are discussed below.

Floating LM629 Data Lines:

The first interesting issue encountered was a problem that occurred on the proto-board circuit. One motor could run by itself, however, when multiple motors were run, they operated in a very sporadic and random way, clearly not following the intended trajectory. Because this only occurred with multiple motors being run, or multiple LM629's being operated at the same time, it was deduced that the problem lay with the LM629's somehow causing interference with one another. However, the LM629's were connected to one another only through the control and data lines. Only the data lines were occasionally left to "float" (a situation in which no particular voltage is applied over the lines and thus random signals may travel). It was hypothesized that operating LM629's created unintentional signals over these 'floating' data lines, and those signals were interfering with the operation of other LM629 IC's. The microcontroller program was modified so that control over the control and data lines to the LM629's was 'tighter'; whenever control or data lines were not used by the microcontroller, they were set to a definite value (0 V or 5 V). This seemed to solve this particular problem on the proto-board circuit.

#### Electro-magnetic Interference (EMI):

Electro-magnetic interference was probably the most time consuming issue encountered. EMI occurred in several ways, requiring major modifications to be made to the PCB circuit. In the mobile platform electrical system, there are two power lines and a ground line. The first power line is the 5 V line, which powers the LM629's, the optical encoders on each DC motor, the microcontroller, and any other component powered through the microcontroller. The second power line is the 12 V line, which is used only to power the H-bridges, driving the DC motors. The issue arises with the H-bridges, which produce a high voltage, high current PWM signal. This signal varies from 0 V, and thus 0 A current, to 12 V with a correspondingly high current capable of reaching 1 A. Because a PWM signal is produced by the H-bridge, the current drawn from the 12 V line must vary rapidly over a large range of 0 A to 3 A in the worst case, since three H-bridges are driving three motors simultaneously and are powered by the same 12 V power line. Thus, we can assume that a large amount of EMI is produced along the 12 V power line. The negative effects of the EMI, produced along the 12 V line, were seen in several places on the PCB, determined through experimentation. The first place where this was a problem was where the 12 V and 5 V lines ran a long length of the board in very close proximity. The result was that the 5 V line became affected by the EMI produced, causing the LM629's to reset and behave erratically in driving the motor. Another place where this problem occurred was in the close proximity of the H-bridges and LM629's. It seemed that the PWM produced at the output of the H-bridges was located very close to the LM629's creating internal disturbances within the LM629 IC's themselves, and causing internal registers to store incorrect values. Furthermore, placing a 12 V line wire directly over an LM629 also caused it to operate incorrectly, making the DC motors operate with seemingly random trajectories, further supporting the hypothesis of EMI being the source of several problems. On the complete prototype of the mobile platform, these issues were carefully dealt with. For example, the 12 V line was disconnected from the PCB and all components requiring the 12 V power line were also removed and isolated to another region, away from any 5 V power lines and LM629 IC's. This required extensive manual modifications to the PCB as well as a new bread-board circuit to be soldered together with the sole purpose of isolating the 12 V line and its components from the rest of the circuit. The EMI problem also played a role in the physical placement of the components on the final prototype of the mobile

platform, since now some components were restricted in how close they could physically be to other specific components.

#### 4.5 Completed Mobile Platform End-Effector

The completed mobile vestibular platform system's end-effector is displayed in figure 13, below. The Adapt11C24DX microcontroller can be seen on the top tier of the platform with the PCB, holding the LM629's behind it. A separate soldered bread board can be seen on the right side of the top tier of the platform, to which the motor's connect and on which the 5 V and 12 V lines can be isolated. The bottom tier contains the three motors with their spools and cables attached to each. The H-bridges, on their own PCB's can be seen here, each under the spool belonging to motor which the H-bridge controls.

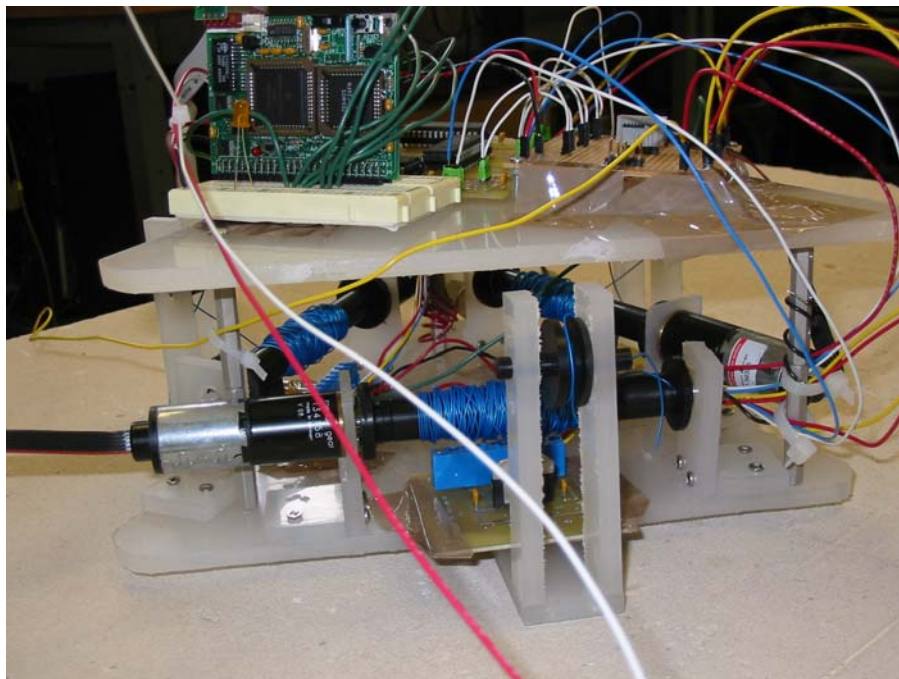


Fig. 13: Complete End-Effector of the Mobile Vestibular Platform System

### 5. SOFTWARE SYSTEM OF THE MOBILE VESTIBULAR PLATFORM SYSTEM

All electrical components of the mobile vestibular platform system are controlled by two software modules. One module is the mobile platform system program that controls all operations of the mobile platform system through the Motorola M68HC11 microcontroller. This program was coded using Technological Arts' ICC11 software, in C, and was compiled and downloaded to the EEPROM module piggy-backed on the Adapt11C24DX microcontroller board, using Technological Arts' MicroLoad program. This particular program is modular in the sense that it does not rely on external systems in order to perform the basic functions to operate the mobile platform, such as operating the DC motors to run specific trajectories. The other program module is the Matlab GUI application which acts as the command terminal from which a user can remotely operate several different functions of the mobile platform. This module was programmed using Matlab's Graphical User Interface Development Environment (GUIDE) and

is run by Matlab to communicate instructions and data to and from the mobile platform through the PC's serial port.

## **5.1 Mobile Platform End-Effector System Software**

This program was written largely in order to allow the Adapt11C24DX microcontroller board to program and operate the LM629 precision DC motor controller IC. The program for this module can be found in Appendix A. It contains several functions, which perform simple but frequently used operations such as writing command bytes to and reading data bytes from the LM629 IC. Several hierarchically higher functions use the basic command and data writing and reading functions in order to perform specific tasks such as programming a specific trajectory into the LM629 or reading the many registers that provide information bytes indicating the status of the precision DC motor controller IC. For example, there are functions that issue commands to the LM629 in order to read the various status registers such as chip status, current real position of the motor, temporal desired position of the motor, current real velocity of the motor, temporal desired velocity of the motor, etc. The LM629 is a very complex IC with many different functions and capabilities and thus, it makes sense that the mobile platform system program would require many functions in order to cover all of the operations the LM629 is capable of. In addition to this, the program is also responsible for the control of all three motors of the mobile platform.

The mobile platform system, however, will not perform any functions without the commands to do so. The commands needed to carry out operations are received through the serial port on the microcontroller board. A baud rate of 19200 bps is used to transfer commands and data between the remote user command terminal and mobile platform system, with a specific format that is hard-coded in the mobile platform system software. Because the commands are received through the serial port using the RS-232 protocol and use a specific format and set of text commands, the commands can be issued from any source or program with access to a serial port and the correct format. This makes the mobile platform system itself largely modular and capable of being used as a component in other, perhaps larger or upgraded, systems.

## **5.2 Command Terminal Software**

The other software module used in the mobile vestibular platform system, as mentioned above, is the remote user command terminal program. Whereas the mobile platform system software handles the processing and execution of instructions to perform basic functions on the mobile platform, the command terminal program processes and executes direct commands from the user, requiring more complex computation as well as more complex sequences of instruction to be issued to the mobile platform system. For instance, there are fields in the command terminal GUI, shown in figure 14, that allow the user to move the mobile platform from its current position in three dimensional space to a new position by entering the new coordinates into the proper fields of the GUI. The GUI then takes all of the data from the proper fields and performs the calculations to determine the change in each cable length that must occur and then the trajectory that should be taken by each motor to change the cable lengths. Thus it must calculate the number of basic rotational units for each motor in order to change the cable lengths to the desired lengths. These calculations depend upon several initial factors including the

dimensions of the platform, the positions of the motors, and the positions of the stable external cable mounts. The center of the mobile platform at its initial position upon powering up the system is considered to be the origin and all initial positions of the cable mounts must be measured relative to that origin. The cable mount locations relative to the origin must be entered into the GUI upon powering up the system, before any platform movements commands are issued from the GUI. All other initial data required, such as the platform dimensions and motor positions are already hard-coded into the GUI application calculations. Upon completing the required calculations, the Matlab GUI application sends the appropriate text commands to the mobile platform system which instructs the motors to operate properly in order to move the platform to the desired location. The software source code for the command terminal module can be found in Appendix B. It was coded using Matlab's own programming syntax.

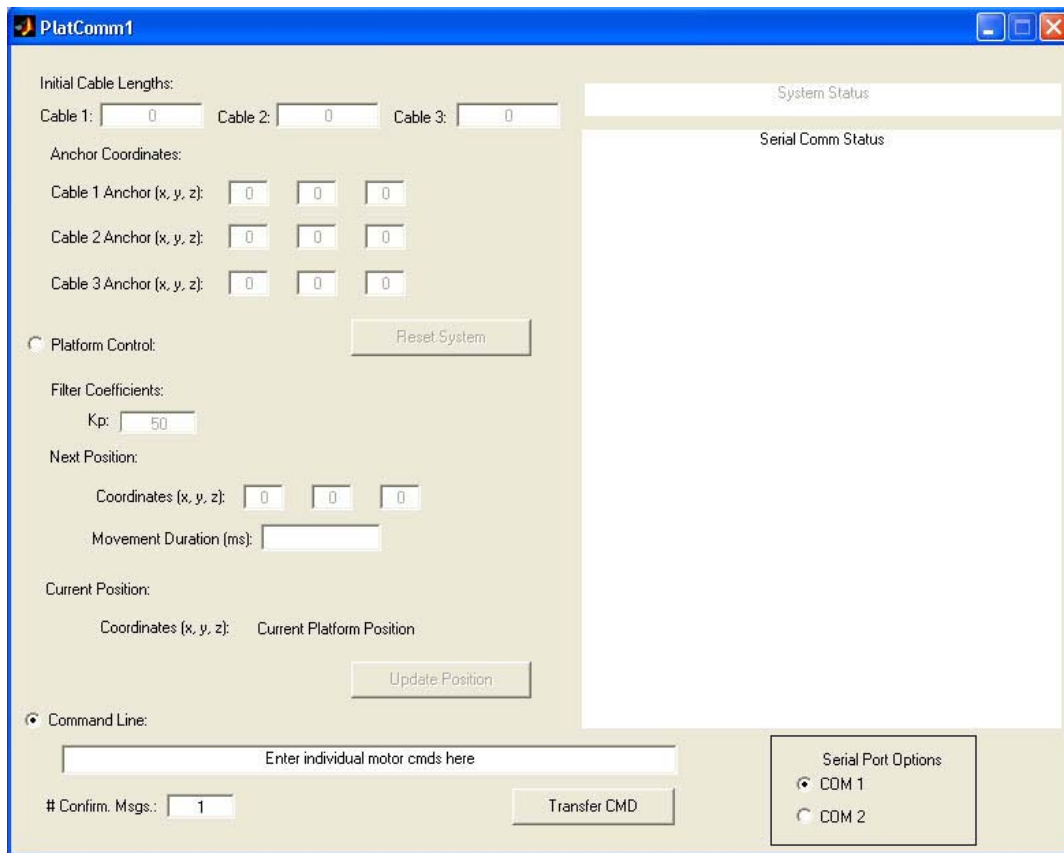


Fig. 14: Remote User Command Terminal GUI, developed in Matlab using GUIDE

The major advantage obtained by using this command terminal Matlab GUI is the reduction in calculations that the M68HC11 microcontroller would otherwise have to perform. In addition, the calculations needed to be performed are floating point (or decimal) calculations. These calculations require significantly more processing power to complete. Since the calculations performed by the Matlab GUI are largely floating point calculations, putting this extra work on the shoulders of the microcontroller would undoubtedly cause the system to run more slowly, likely resulting in a lag between the time the user enters a command and the time the mobile platform actually begins to move. This severity of this problem would likely be amplified in the future, when more complex algorithms are implemented to reduce other unintended behaviors of

the platform. By having the Matlab GUI perform all of the required floating point calculations for moving the mobile platform between coordinates, the calculations can be done much faster, since the PC has much greater processing power than the microcontroller.

One other aspect of the Matlab GUI command terminal application is that it allows the user to enter text commands to be sent through the serial port directly to the mobile platform. Although the user must be familiar with the command format and commands that can be sent to the mobile platform to execute these commands, this capability of the GUI allows the user an easy method to control hierarchically lower functions of the mobile platform such as operating each motor individually as well as changing different parameters used by the LM629's and checking the status of the system through the LM629's status registers. This has been very useful for debugging and minor adjustment purposes on the mobile platform.

## **6. DISCUSSION AND CONCLUSIONS**

A large portion of the development of the mobile vestibular platform system was spent debugging and determining the source of problems in the circuit. However, a good deal of work was accomplished in the development of this system, with various modifications in the original design being made in the electrical system of the mobile platform. Testing of various operations of the mobile platform raises some issues that may be potential problems in the future. There are also many more features that could be implemented in the mobile vestibular platform system, in both hardware as well as software, to make it more applicable to different tasks and convenient to operate.

### **6.1 Foreseeable System Issues**

In surveying and evaluating the operation of the mobile vestibular platform system, a couple of potential sources of future problems arise. These problems occur in both the mechanical as well as electrical realm of the mobile platform design. First, in the mechanical design, the suspension cables currently used are very thin wires, which are relatively easy to break or stretch. With stretching occurring frequently in the suspension cables, commands issued to move the mobile platform to a particular position in three dimensional space will become less accurate since the stretching will gradually cause the mobile platform to deviate from its desired 'stationary' position. In the electrical design of the system, the mobile platform currently uses two external power supplies to power itself, one for the 5 V supply and one for the 12 V supply. This is due to the fact that even when the 5 V supply is drawn from the output of a voltage regulator supplied with the 12 V line, EMI still causes significant problems and thus, two separate power supplies are used instead. Eventually, the mobile platform will have to operate with an on-board power supply such as a battery. This may become troublesome if the same problem with interference arises. Having two separate power supplies for these two voltages, on-board the mobile platform, is impractical since it would significantly increase the load being operated by the motors.

## 6.2 Future Work

There is an endless supply of ideas that can be applied to the mobile vestibular platform system to enhance as well as to apply it. These ideas apply both to the hardware and the software aspects of this cable robot system.

Of these, several were for this research program but were not completed. The first is infrared (IR) remote control of the mobile platform. With an IR detector in the mobile platform electrical system, the on-board microcontroller could detect and measure pulse widths from an IR remote control, and decode the pulse sequences received to determine which button on the IR remote control was pressed. Based on the button pressed, the microcontroller can then execute a function associated with that particular remote control button. This would be useful for manual adjustment of individual motors while surveying the operation of the motor from a location other than the remote user command terminal. This method of adjustment could be a useful, temporary solution to re-align the mobile platform to a horizontal position parallel to the ground, when stretching cable lengths alter this. In addition, other buttons on the remote can be applied to operate future components aboard the mobile platform.

Another enhancement to the system is a software solution to the ‘wobbling’ effect, explained in section 3.2, where cable mount locations on the mobile platform end-effector are discussed. A software solution to this problem can be implemented in the Matlab GUI command terminal application. When a user enters a new coordinate for the mobile platform, the Matlab program can take the trajectory from the mobile platform’s current position to the new position and divide it into several unit divisions along the trajectory. Then, the Matlab GUI can issue a separate trajectory command to the mobile platform for each of these unit divisions along the overall intended platform path until the desired position is reached. As a result, the ‘wobbling’ effect will be greatly reduced because it will only occur in the continuous transition for each of these small unit path divisions, which will barely be noticeable. The downside is that the same set of floating point calculations will have to be made for each of these small platform movements along the path to the destination position, whereas only one set of calculations would otherwise have to be made for one continuous movement of the platform from the current position to the destination position. However, this does not pose a significant problem since these calculations are performed on a PC with significant processing power. Each set of calculations will be computed before the mobile platform is even nearly completed executing the trajectory for the previous path division.

One final additional feature that would have been rather exciting to implement on the mobile vestibular platform system would be some type of sensory equipment, such as an IR detector. Several IR detectors could be installed on the bottom of the mobile platform, with each connected to an A/D converter on the microcontroller board. As a result, the microcontroller would collect and process the data from these IR sensors and act according to a pre-programmed algorithm. For instance, it would have been very interesting to program the mobile platform system to follow an IR emitter within its reachable space. A simple algorithm to implement and test would be to instruct the mobile platform to move in the direction of the IR detector which detected the strongest IR signal from the emitter, allowing the mobile platform to approximately follow an IR emitting source.

There are an endless number of possibilities for enhancements and applications of the mobile vestibular platform. It will be interesting to see how this field of robotics develops in the future and how readily cable robot systems will be applied to a variety of environments including industrial, military, and domestic households. The unique capabilities that are made possible by the fundamental mechanical design of the cable robot make it a very suitable alternative to conventional wheeled robots, for use in a variety of applications and tasks in the real world and probably even more in the future.

## **7. RECOMMENDATIONS**

I have a few recommendations which I believe may be of use for future development of the mobile vestibular platform system. Many of the recommendations relate to the issue protecting the electrical system of the mobile platform from the unwanted effects resulting from electromagnetic interference (EMI). One possible solution to this problem is to isolate each LM629, H-bridge, and DC motor connector on a different PCB. From past experimentation, it seemed that operating one LM629 and H-bridge set on a PCB did not cause problems. This is a solution that currently being experimentally implemented for the mobile platform end-effector system. Another benefit from this is added modularity of the electrical circuit of the system. With this design, if more suspension cables, and thus LM629's and their H-bridges, are to be added to the cable robot system, it can be done simply by using another one of these PCB's, containing only a set of components to operate a single motor.

Another simpler recommendation, relating to the PCB design, would be to have the PCB's manufactured with an epoxy coating, in order to prevent accidentally applying voltages from hanging wires to incorrect lines. This is a simple recommendation in order to help safe guard against burning out the LM629's which occurred quite often and became somewhat expensive, due to the 12 V line being so close to the 5 V line on the PCB, with both lines exposed and unprotected by any type of non-conducting coating.

Finally, it may be useful to use fishing wire, which can sustain significantly more tension than the cable currently used, as the suspension cables. The cables used now were originally intended to supply the voltage-current needed by the system. However, since this method is no longer used, the suspension cables can be replaced with fishing wire which is less susceptible to stretching and can support significantly heavier loads.

## **8. ACKNOWLEDGMENTS**

This research program has offered me the opportunity to experience ten weeks of intense research and development in a field I previously had little knowledge about. I feel I have grown greatly and have also gained invaluable experience in the research and development process. An academic knowledge in electric circuits and systems as well as programming is largely the only thing I brought with me into the program. However, I have come out having learned many skills and concepts through from research, lab experience, and my own mistakes due to lack of

experience. I would like to thank the National Science Foundation's Research Experience for Undergraduates program for their support of the SUNFEST Undergraduate Research Program at the University of Pennsylvania. I would also like to recognize the financial support of the Microsoft Corporation.

Much appreciation and many thanks also go to my advisor, Dr. Daniel Lee, for his invaluable support, time, patience, and advice in helping a relatively un-experienced undergraduate student learn the ropes of the research and development process.

Furthermore, I'd also like to thank the graduate students Chintan Cadala and Mubeen Bhatti, working under Dr. Daniel Lee, for their support and patience in helping me become acquainted with the project as well as for their suggestions and advice.

## 9. REFERENCES

1. Bosscher, P., Ebert-Uphoff, I., Lipkin, H., Riechel, A. (2003) Concept Paper: Cable-Driven Robots for Use in Hazardous Environments.  
[http://www.google.com/url?sa=U&start=1&q=http://robot.me.gatech.edu/~paul/papers/RSHE2004\\_concept\\_paper.pdf&e=747](http://www.google.com/url?sa=U&start=1&q=http://robot.me.gatech.edu/~paul/papers/RSHE2004_concept_paper.pdf&e=747)
2. Ebert-Uphoff, I., Voglewede, P. (2004) On the Connections Between Cable-Driven Robots, Parallel Manipulators and Grasping.  
[http://robot.me.gatech.edu/~phil/downloads/ICRA2004\\_connections.pdf](http://robot.me.gatech.edu/~phil/downloads/ICRA2004_connections.pdf)
3. Oh, S., Mankala, K., Agrawal, S., Albus, J., Dynamic Modelling and Robust Controller Design of a Two-Stage Parallel Cable Robot, Proc. 2004 IEEE ICRA Conf., New Orleans, LA, USA, April 2004, pp. 3678-3683.  
[http://ieeexplore.ieee.org/xpl/abs\\_free.jsp?arNumber=1308830](http://ieeexplore.ieee.org/xpl/abs_free.jsp?arNumber=1308830)
4. Riechel, A., Ebert-Uphoff, I. (2003) Force-Feasible Workspace Analysis for Underconstrained, Point-Mass Cable Robots.  
[http://www.google.com/url?sa=U&start=1&q=http://robot.me.gatech.edu/~andrew/ffw\\_paper3.pdf&e=747](http://www.google.com/url?sa=U&start=1&q=http://robot.me.gatech.edu/~andrew/ffw_paper3.pdf&e=747)

## APPENDIX A: Mobile Vestibular Platform - End-Effector System Software

### PLTFRM2.C

(Source Code in C, to be compiled in ImageCraft's ICC11 for download to Technological Arts' Adapt11C24DX Microcontroller Board with Embedded Motorola M68HC11 Microcontroller)

```
#include <hc11.h>
#include <ctype.h>
#include <string.h>

#define BAUD19200 0x03
#pragma interrupt_handler TOIISR
/*
#pragma interrupt_handler IC1ISR
#pragma interrupt_handler IC2ISR
#pragma interrupt_handler IC3ISR
*/
unsigned int byte = 0;
unsigned int STATUS = 0;
unsigned int choice = 0;
unsigned int cur_Motor = 0;

unsigned int input = 0;
char msg_rcv[100];
unsigned int msg_length = 0;
unsigned int loop = 0;

unsigned long int n_position = 0;
unsigned long int n_velocity = 0;
unsigned long int n_acceleration = 0;
unsigned int n_filter_kp = 0;

unsigned int count = 0;

void TOIISR() {

    TFLG2 &= 0x80;                //clearing TOF to enable further interrupts

    if (count % 32 == 0)
        if (PORTA & 0x10)
            PORTA &= 0xEF;
        else
            PORTA |= 0x10;

    count++;
}

void main() {

    int x = 0;
    setbaud(BAUD19200);

    TMSK2 |= 0x80;                //locally enable TOI
```

```

asm("CLI");

PORTB = 0xFE; //set all control lines high and select motor #1
run_HDW_RSTSEQ();

while(1) {
    msg_length = 0;
    x = 0;
    n_position = 0;
    n_velocity = 0;
    n_acceleration = 0;
    n_filter_kp = 0;

    DDRC = 0xFF;

    input = getchar();
    while (input != 10 && input != 13) { //get serial comm msg
        msg_rcv[msg_length] = input;
        msg_length++;
        input = getchar();
    }

    putline("Received CMD: ", 14); //echo/confirm serial comm msg
    while (x < msg_length) {
        putchar(msg_rcv[x]);
        x++;
    }
    putchar(10); //line feed delimiter

    if (msg_rcv[0] == 'c') {
        cur_Motor = (msg_rcv[1] - '0');
    }
    else if (msg_rcv[0] == 'r') {
        putline("RESETTING ALL MOTOR LM629's ...", 30);
        putchar(10);
        if (run_HDW_RSTSEQ()) {
            putline("ALL MOTORS RST SUCCESSFUL", 25);
            putchar(10);
        }
        else {
            putline("ALL MOTORS RST FAILED", 21);
            putchar(10);
        }
        continue;
    }

    loop = 3;

    if (msg_rcv[loop] == 'p') {
        loop++;
        while (isdigit(msg_rcv[loop])) {
            n_position = n_position * 10 + (msg_rcv[loop] - '0');
            loop++;
        }
        loop++;
    }
}

```

```

        if (msg_rcv[loop] == 'v') {
            loop++;
            while(isdigit(msg_rcv[loop])) {
                n_velocity = n_velocity*10 + (msg_rcv[loop]-'0');
                loop++;
            }
            loop++;
        }

        if (msg_rcv[loop] == 'a') {
            loop++;
            while(isdigit(msg_rcv[loop])) {
                n_acceleration = n_acceleration*10 + (msg_rcv[loop]-'0');
                loop++;
            }
            loop++;
        }
        LOAD_TRAJ(n_position, n_velocity, n_acceleration);
    }

else if (msg_rcv[loop] == 'r' && msg_rcv[loop+1] == 'e') {
    putline("RESETTING CURRENT MOTOR LM629 #: ", 33);
    putchar(cur_Motor + '0');
    putchar(10);
    if (run_SFTW_RSTSEQ()) {
        putline("MOTOR RST SUCCESSFUL", 25);
        putchar(10);
    }
    else {
        putline("MOTOR RST FAILED", 21);
        putchar(10);
    }
}

else if (msg_rcv[loop] == 'l' && msg_rcv[loop+1] == 'f') {
    loop += 2;
    while(isdigit(msg_rcv[loop])) {
        n_filter_kp = n_filter_kp*10 + (msg_rcv[loop]-'0');
        loop++;
    }
    loop++;
    LOAD_FILTER(n_filter_kp);
}

else if (msg_rcv[loop] == 'r' && msg_rcv[loop+1] == 's') {
    RD_SIGS();
}

else if (msg_rcv[loop] == 'r' && msg_rcv[loop+1] == 'p') {
    RD_RPOS();
}

else if (msg_rcv[loop] == 'd' && msg_rcv[loop+1] == 'p') {
    RD_DPOS();
}

```

```

        else if (msg_rcv[loop] == 'r' && msg_rcv[loop+1] == 'v') {
            RD_RVEL();
        }

        else if (msg_rcv[loop] == 'd' && msg_rcv[loop+1] == 'v') {
            RD_DVEL();
        }

        else if (msg_rcv[loop] == 's' && msg_rcv[loop+1] == 'a') {
            run_SampleTraj();
        }

        else if (msg_rcv[loop] == 's' && msg_rcv[loop+1] == 'm') {
            STT_MOTOR();
        }

        for (x=0; x < msg_length; x++) //clear msg_rcv array so prev msg doesn't interfere
            msg_rcv[x] = '\0';
    }
}

void putline(char* msg_str, int length) {
    int i = 0;

    for (i = 0; i < length; i++)
        putchar(msg_str[i]);
}

void putNum(unsigned int number) { //puts numbers in character format to serial

    putchar(number/10000 + '0');
    number %= 10000;
    putchar(number/1000 + '0');
    number %= 1000;
    putchar(number/100 + '0');
    number %= 100;
    putchar(number/10 + '0');
    number %= 10;
    putchar(number + '0');
}

void wait_BUSY() { //loops until LM629 NOT busy

    STATUS = 0x01;
    DDRC = 0x00;

    while (STATUS & 0x01) {
        PORTB &= 0xDF; //PB5 = PS low
        PORTB &= 0x7F; //PB7 = RD low

        STATUS = PORTC; //read STATUS byte

        PORTB |= 0x80; //PB7, RD high
        PORTB |= 0x20; //PB5, PS high
    }
}

```

```

        DDRC = 0xFF;                //give data line control back to HC11
    }

void chk_STATUS() {                //immediate update of STATUS value from LM629

    DDRC = 0x00;

    chng_Motor(cur_Motor);        //CS low
    PORTB &= 0xDF;                //PB5 = PS low
    PORTB &= 0x7F;                //PB7 = RD low

    STATUS = PORTC;

    PORTB |= 0x80;                //PB7, RD high
    PORTB |= 0x20;                //PB5, PS high
    chng_Motor(0);                //CS high

    DDRC = 0xFF;                //give data line control back to HC11
}

void write_CMD(int CMD) {

    DDRC = 0xFF;
    PORTC = CMD;

    chng_Motor(cur_Motor);        //CS low
    PORTB &= 0xDF;                //PB5 = PS low
    PORTB &= 0xEF;                //PB4 = WR low
    PORTB |= 0x10;                //PB4 = WR high
    PORTB |= 0x20;                //PB5 = PS high
    wait_BUSY();
    chng_Motor(0);                //CS high
}

void write_DATA(unsigned int DATA_MS, unsigned int DATA_LS) {

    DDRC = 0xFF;

    chng_Motor(cur_Motor);        //CS low
    PORTB |= 0x20;                //PB5, PS high
    PORTC = DATA_MS;
    PORTB &= 0xEF;                //PB4 = WR low
    PORTB |= 0x10;                //PB4 = WR high

    PORTC = DATA_LS;
    PORTB &= 0xEF;                //PB4 = WR low
    PORTB |= 0x10;                //PB4 = WR high
    wait_BUSY();
    chng_Motor(0);                //CS high
}

unsigned int read_DATA() {
    unsigned int DATA = 0;

    DDRC = 0x00;

```

```

    chng_Motor(cur_Motor);           //CS low
    PORTB |= 0x20;                    //PB5, PS high
    PORTB &= 0x7F;                    //PB7 = RD low
    PORTB |= 0x80;                    //PB7, RD high
    DATA = PORTC;
    DATA = DATA << 8;

    PORTB &= 0x7F;                    //PB7 = RD low
    PORTB |= 0x80;                    //PB7, RD high
    DATA += PORTC;
    wait_BUSY();
    chng_Motor(0);                    //CS high

    DDRC = 0xFF;

    return DATA;
}

void LOAD_FILTER(unsigned int Kp) {

    putline("*** LOADING NEW FILTER COEFF: ", 30);
    putNum(Kp);
    putchar(10);

//    wait_BUSY();
    write_CMD(0x1E);           //LFIL; load filter coeff cmd

    write_DATA(0x00, 0x08); //derivative sample rate, load Kp filter coeff

    write_DATA(0x00, Kp);

//    putline("UPDATING FILTER DATA (UDF)", 26);

    write_CMD(0x04);           //UDF

    putline("FILTER UPDATE COMPLETE!", 23);
    putchar(10);
}

void LOAD_TRAJ(unsigned long int position, unsigned long int velocity, unsigned long int acceleration) {
    unsigned int vel_MSW = 0;
    unsigned int vel_LSW = 0;
    unsigned int acc_MSW = 0;
    unsigned int acc_LSW = 0;
    unsigned int pos_MSW = 0;
    unsigned int pos_LSW = 0;

    acc_MSW = ((acceleration >> 16) & 0x0000FFFF);
    acc_LSW = (acceleration & 0x0000FFFF);

    vel_MSW = ((velocity >> 16) & 0x0000FFFF);
    vel_LSW = (velocity & 0x0000FFFF);

    pos_MSW = ((position >> 16) & 0x0000FFFF);
    pos_LSW = (position & 0x0000FFFF);
}

```

```

putline("*** LOADING NEW TRAJECTORY (format MS_WORD*2^16+LS_WORD): ", 56);
putline("pos_MSW: ", 9);
putNum(pos_MSW);
putline(" pos_LSW: ", 10);
putNum(pos_LSW);
putline(" vel_MSW: ", 10);
putNum(vel_MSW);
putline(" vel_LSW: ", 10);
putNum(vel_LSW);
putline(" accel_MSW: ", 12);
putNum(acc_MSW);
putline(" accel_LSW: ", 12);
putNum(acc_LSW);
putchar(10);

// wait_BUSY();
write_CMD(0x1F); //LTRJ; load trajectory cmd

write_DATA(0x00, 0x2B);

write_DATA((acc_MSW >> 8) & 0x00FF, acc_MSW & 0xFF);
write_DATA((acc_LSW >> 8) & 0x00FF, acc_LSW & 0xFF);
write_DATA((vel_MSW >> 8) & 0x00FF, vel_MSW & 0xFF);
write_DATA((vel_LSW >> 8) & 0x00FF, vel_LSW & 0xFF);
write_DATA((pos_MSW >> 8) & 0x00FF, pos_MSW & 0xFF);
write_DATA((pos_LSW >> 8) & 0x00FF, pos_LSW & 0xFF);

putline("NEW TRAJECTORY DATA LOADED", 26);
putchar(10);
}

void STT_MOTOR() {
putline("EXECUTING CMD TO STT MOTOR: ", 28);
putNum(cur_Motor);
putchar(10);

// wait_BUSY();
write_CMD(0x01); //STT; start motor motion cmd
}

void run_SampleTraj() {
//===== LOAD FILTER COEFFICIENTS =====
// wait_BUSY();
write_CMD(0x1E); //LFIL; load filter coefficients command

write_DATA(0x00, 0x08); //begin load filter control word

write_DATA(0x00, 0x30); //begin load kp word

write_CMD(0x04); //UDF; update filter command
}

```

```

//===== LOAD TRAJECTORY DATA =====
    write_CMD(0x1F);                //LTRJ; load trajectory command

    write_DATA(0x00, 0x2A);        //begin load trajectory control word

    write_DATA(0x00, 0x00);        //begin load acc int word

    write_DATA(0x00, 0x02);        //begin load acc frac word

    write_DATA(0x00, 0x01);        //begin load vel int word

    write_DATA(0x34, 0x6E);        //begin load vel fract word

    write_DATA(0x00, 0x00);        //begin load position MS word

    write_DATA(0xAF, 0x40);        //begin load position LS word

    write_CMD(0x01);                //STT; Start motion command

    putline("Starting pre-programmed sample traj ...", 39);
    putchar(10);
//=====
}

void HDW_RSET() {                  //READ STATUS BYTE

    DDRC = 0x00;                  //set to read input status byte

    PORTB &= 0xBF;                //PB6 = RST low
    TOC3 = TCNT + 3500;
    TFLG1 &= 0x20;
    while (!(TFLG1 & 0x20)); //hold RST low for more than 8 clk cycles
    PORTB |= 0x40;                //PB6 = RST high

    TFLG1 &= 0x20;
    TOC3 = TCNT + 7000;
    while (!(TFLG1 & 0x20)); //wait for 1.5 ms after RESET
}

int run_HDW_RSTSEQ() {

    int rst_stat = 0;
    int motor = 1;
    int rst_failed = 0;

    HDW_RSET();

    for (motor = 1; motor <= 3; motor++) {
        cur_Motor = motor;
        chk_STATUS();
        if (STATUS == 0xC4 || STATUS == 0x84)
            rst_stat = 1;
        else {
            rst_stat = 0;
        }
    }
}

```

```

//      wait_BUSY();
        write_CMD(0x1D);                                //RSTI; reset interrupts command

        write_DATA(0x00, 0x00);                        //reset all interrupts

        chk_STATUS();
        if((STATUS == 0x80 || STATUS == 0xC0) && rst_stat == 1)
            rst_stat = 1;
        else {
            rst_stat = 0;
        }
        if(rst_stat == 0)
            rst_failed = 1;
    }
    return !(rst_failed);
}

int run_SFTW_RSTSEQ() {
    int rst_stat = 0;

//      wait_BUSY();
        write_CMD(0x00);

        TFLG1 &= 0x20;
        TOC3 = TCNT + 7000;
        while (!(TFLG1 & 0x20)); //wait for 1.5 ms after RESET

        chk_STATUS();

        if (STATUS == 0xC4 || STATUS == 0x84)
            rst_stat = 1;
        else {
            rst_stat = 0;
        }

        write_CMD(0x1D);                                //RSTI; reset interrupts command

        write_DATA(0x00, 0x00);                        //reset all interrupts

        chk_STATUS();
        if((STATUS == 0x80 || STATUS == 0xC0) && rst_stat == 1)
            rst_stat = 1;
        else {
            rst_stat = 0;
        }
        return rst_stat;
}

void RD_SIGS() {
    unsigned int signals = 0;

//      wait_BUSY();
        chk_STATUS();
        write_CMD(0x0C);                                //RDSIGS; load read signals reg command

```

```

signals = read_DATA();

putline("READ SIGNALS (MSB -> LSB): ", 27);
putNum((signals >> 8) & 0x00FF);
putchar(' ');
putNum(signals & 0x00FF);
putchar(10);
}

void RD_RPOS() {
    unsigned int signals_MSW = 0;
    unsigned int signals_LSW = 0;
    int i = 0;

//    wait_BUSY();

    write_CMD(0x0A);                //RDRP; load read real position reg command

    signals_MSW = read_DATA();

    signals_LSW = read_DATA();

    putline("READ REAL POS (MSW -> LSW): ", 28);
    for (i = 0; i < 16; i++)
        putchar(((signals_MSW >> (15 - i)) & 0x0001) + '0');

    putchar(' ');

    for (i = 0; i < 16; i++)
        putchar(((signals_LSW >> (15 - i)) & 0x0001) + '0');

    putline(" = ", 3);
    putNum(signals_MSW);
    putchar(' ');
    putNum(signals_LSW);
    putchar(10);
}

void RD_DPOS() {
    unsigned int signals_MSW = 0;
    unsigned int signals_LSW = 0;
    int i = 0;

//    wait_BUSY();

    write_CMD(0x08);                //RDRP; load read real position reg command

    signals_MSW = read_DATA();

    signals_LSW = read_DATA();

    putline("READ DESIRED POS (MSW -> LSW): ", 31);
    for (i = 0; i < 16; i++)
        putchar(((signals_MSW >> (15 - i)) & 0x0001) + '0');

    putchar(' ');

```

```

    for (i = 0; i < 16; i++)
        putchar(((signals_LSW >> (15 - i)) & 0x0001) + '0');

    putline(" = ", 3);
    putNum(signals_MSW);
    putchar(' ');
    putNum(signals_LSW);
    putchar(10);
}

void RD_RVEL() {
    unsigned int signals_MSW = 0;
    int i = 0;

    //    wait_BUSY();

    write_CMD(0x0B);                //RDRP; load read real position reg command

    signals_MSW = read_DATA();

    putline("READ REAL VEL: ", 15);
    for (i = 0; i < 16; i++)
        putchar(((signals_MSW >> (15 - i)) & 0x0001) + '0');

    putline(" = ", 3);
    putNum(signals_MSW);
    putchar(10);
}

void RD_DVEL() {
    unsigned int signals_MSW = 0;
    unsigned int signals_LSW = 0;
    int i = 0;

    //    wait_BUSY();

    write_CMD(0x07);                //RDRP; load read real position reg command

    signals_MSW = read_DATA();

    signals_LSW = read_DATA();

    putline("READ DESIRED VEL (MSW -> LSW): ", 31);
    for (i = 0; i < 16; i++)
        putchar(((signals_MSW >> (15 - i)) & 0x0001) + '0');

    putchar(' ');

    for (i = 0; i < 16; i++)
        putchar(((signals_LSW >> (15 - i)) & 0x0001) + '0');

    putline(" = ", 3);
    putNum(signals_MSW);
    putchar(' ');
}

```

```

        putNum(signals_LSW);
        putchar(10);
    }

void chng_Motor(int m_num) {

    switch (m_num) {
        case 0: //all LM629's off
            PORTB |= 0x01;
            PORTB |= 0x02;
            PORTB |= 0x04;
        case 1: //LM629 #1 on, PB0
            PORTB &= 0xFE;
            PORTB |= 0x02;
            PORTB |= 0x04;
            break;
        case 2: //LM629 #2 on, PB1
            PORTB |= 0x01;
            PORTB &= 0xFD;
            PORTB |= 0x04;
            break;
        case 3: //LM629 #3 on, PB2
            PORTB |= 0x01;
            PORTB |= 0x02;
            PORTB &= 0xFB;
            break;
        default:
            break;
    }
}

#include "vectors.c"

```

## APPENDIX B: Mobile Vestibular Platform – Command Terminal System Software

### PLATCOMM1.M

**(Programmed using Mathworks' Matlab's Graphical User Interface Development Environment)**

```

function varargout = PlatComm1(varargin)
% PLATCOMM1 M-file for PlatComm1.fig
%   PLATCOMM1, by itself, creates a new PLATCOMM1 or raises the existing
%   singleton*.
%
%   H = PLATCOMM1 returns the handle to a new PLATCOMM1 or the handle to
%   the existing singleton*.
%
%   PLATCOMM1('CALLBACK',hObject,eventData,handles,...) calls the local
%   function named CALLBACK in PLATCOMM1.M with the given input arguments.
%
%   PLATCOMM1('Property','Value',...) creates a new PLATCOMM1 or raises the
%   existing singleton*. Starting from the left, property value pairs are
%   applied to the GUI before PlatComm1_OpeningFunction gets called. An
%   unrecognized property name or invalid value makes property application

```

```

% stop. All inputs are passed to PlatComm1_OpeningFcn via varargin.
%
% *See GUI Options on GUIDE's Tools menu. Choose "GUI allows only one
% instance to run (singleton)".
%
% See also: GUIDE, GUIDATA, GUIHANDLES

% Edit the above text to modify the response to help PlatComm1

% Last Modified by GUIDE v2.5 19-Jul-2004 11:05:31

% Begin initialization code - DO NOT EDIT
gui_Singleton = 1;
gui_State = struct('gui_Name',    mfilename, ...
                  'gui_Singleton', gui_Singleton, ...
                  'gui_OpeningFcn', @PlatComm1_OpeningFcn, ...
                  'gui_OutputFcn', @PlatComm1_OutputFcn, ...
                  'gui_LayoutFcn', [] , ...
                  'gui_Callback', []);
if nargin & isstr(varargin{1})
    gui_State.gui_Callback = str2func(varargin{1});
end

if nargout
    [varargout{1:nargout}] = gui_mainfcn(gui_State, varargin{:});
else
    gui_mainfcn(gui_State, varargin{:});
end
% End initialization code - DO NOT EDIT

% --- Executes just before PlatComm1 is made visible.
function PlatComm1_OpeningFcn(hObject, eventdata, handles, varargin)
% This function has no output args, see OutputFcn.
% hObject    handle to figure
% eventdata  reserved - to be defined in a future version of MATLAB
% handles    structure with handles and user data (see GUIDATA)
% varargin   command line arguments to PlatComm1 (see VARARGIN)

% Choose default command line output for PlatComm1
handles.output = hObject;

% Update handles structure
guidata(hObject, handles);

% UIWAIT makes PlatComm1 wait for user response (see UIRESUME)
% uiwait(handles.figure1);
global Serial_COM;
global edit_SysStatTxt;
edit_SysStatTxt = 'System Status';
Serial_COM = 'COM1';

set(handles.radio_cmd, 'Value', 1);
off = [handles.radio_platform];
mutual_exclude(off);

```

```

update_radioEnables(2, handles);

% --- Outputs from this function are returned to the command line.
function varargout = PlatComm1_OutputFcn(hObject, eventdata, handles)
% varargout cell array for returning output args (see VARARGOUT);
% hObject handle to figure
% eventdata reserved - to be defined in a future version of MATLAB
% handles structure with handles and user data (see GUIDATA)

% Get default command line output from handles structure
varargout{1} = handles.output;

% ***** Unused/Unmodified Code *****
% --- Executes during object creation, after setting all properties.
function edit_cmd_CreateFcn(hObject, eventdata, handles)
% hObject handle to edit_cmd (see GCBO)
% eventdata reserved - to be defined in a future version of MATLAB
% handles empty - handles not created until after all CreateFcns called

% Hint: edit controls usually have a white background on Windows.
% See ISPC and COMPUTER.
if ispc
    set(hObject,'BackgroundColor','white');
else
    set(hObject,'BackgroundColor',get(0,'defaultUicontrolBackgroundColor'));
end

function edit_cmd_Callback(hObject, eventdata, handles)
% hObject handle to edit_cmd (see GCBO)
% eventdata reserved - to be defined in a future version of MATLAB
% handles structure with handles and user data (see GUIDATA)

% Hints: get(hObject,'String') returns contents of edit_cmd as text
% str2double(get(hObject,'String')) returns contents of edit_cmd as a double

% --- Executes during object creation, after setting all properties.
function edit_filter_kp_CreateFcn(hObject, eventdata, handles)
% hObject handle to edit_filter_kp (see GCBO)
% eventdata reserved - to be defined in a future version of MATLAB
% handles empty - handles not created until after all CreateFcns called

% Hint: edit controls usually have a white background on Windows.
% See ISPC and COMPUTER.
if ispc
    set(hObject,'BackgroundColor','white');
else
    set(hObject,'BackgroundColor',get(0,'defaultUicontrolBackgroundColor'));
end

function edit_filter_kp_Callback(hObject, eventdata, handles)

```

```

% hObject handle to edit_filter_kp (see GCBO)
% eventdata reserved - to be defined in a future version of MATLAB
% handles structure with handles and user data (see GUIDATA)

% Hints: get(hObject,'String') returns contents of edit_filter_kp as text
% str2double(get(hObject,'String')) returns contents of edit_filter_kp as a double

```

```

% --- Executes during object creation, after setting all properties.
function edit_coord_x_CreateFcn(hObject, eventdata, handles)
% hObject handle to edit_coord_x (see GCBO)
% eventdata reserved - to be defined in a future version of MATLAB
% handles empty - handles not created until after all CreateFcns called

```

```

% Hint: edit controls usually have a white background on Windows.
% See ISPC and COMPUTER.
if ispc
    set(hObject,'BackgroundColor','white');
else
    set(hObject,'BackgroundColor',get(0,'defaultUicontrolBackgroundColor'));
end

```

```

function edit_coord_x_Callback(hObject, eventdata, handles)
% hObject handle to edit_coord_x (see GCBO)
% eventdata reserved - to be defined in a future version of MATLAB
% handles structure with handles and user data (see GUIDATA)

```

```

% Hints: get(hObject,'String') returns contents of edit_coord_x as text
% str2double(get(hObject,'String')) returns contents of edit_coord_x as a double

```

```

% --- Executes during object creation, after setting all properties.
function edit_coord_y_CreateFcn(hObject, eventdata, handles)
% hObject handle to edit_coord_y (see GCBO)
% eventdata reserved - to be defined in a future version of MATLAB
% handles empty - handles not created until after all CreateFcns called

```

```

% Hint: edit controls usually have a white background on Windows.
% See ISPC and COMPUTER.
if ispc
    set(hObject,'BackgroundColor','white');
else
    set(hObject,'BackgroundColor',get(0,'defaultUicontrolBackgroundColor'));
end

```

```

function edit_coord_y_Callback(hObject, eventdata, handles)
% hObject handle to edit_coord_y (see GCBO)
% eventdata reserved - to be defined in a future version of MATLAB
% handles structure with handles and user data (see GUIDATA)

```

```

% Hints: get(hObject,'String') returns contents of edit_coord_y as text
% str2double(get(hObject,'String')) returns contents of edit_coord_y as a double

```

```

% --- Executes during object creation, after setting all properties.
function edit_coord_z_CreateFcn(hObject, eventdata, handles)
% hObject handle to edit_coord_z (see GCBO)
% eventdata reserved - to be defined in a future version of MATLAB
% handles empty - handles not created until after all CreateFens called

% Hint: edit controls usually have a white background on Windows.
% See ISPC and COMPUTER.
if ispc
    set(hObject,'BackgroundColor','white');
else
    set(hObject,'BackgroundColor',get(0,'defaultUicontrolBackgroundColor'));
end

```

```

function edit_coord_z_Callback(hObject, eventdata, handles)
% hObject handle to edit_coord_z (see GCBO)
% eventdata reserved - to be defined in a future version of MATLAB
% handles structure with handles and user data (see GUIDATA)

% Hints: get(hObject,'String') returns contents of edit_coord_z as text
% str2double(get(hObject,'String')) returns contents of edit_coord_z as a double

```

```

% --- Executes during object creation, after setting all properties.
function edit_num_rcvmsgs_CreateFcn(hObject, eventdata, handles)
% hObject handle to edit_num_rcvmsgs (see GCBO)
% eventdata reserved - to be defined in a future version of MATLAB
% handles empty - handles not created until after all CreateFens called

% Hint: edit controls usually have a white background on Windows.
% See ISPC and COMPUTER.
if ispc
    set(hObject,'BackgroundColor','white');
else
    set(hObject,'BackgroundColor',get(0,'defaultUicontrolBackgroundColor'));
end

```

```

function edit_num_rcvmsgs_Callback(hObject, eventdata, handles)
% hObject handle to edit_num_rcvmsgs (see GCBO)
% eventdata reserved - to be defined in a future version of MATLAB
% handles structure with handles and user data (see GUIDATA)

% Hints: get(hObject,'String') returns contents of edit_num_rcvmsgs as text
% str2double(get(hObject,'String')) returns contents of edit_num_rcvmsgs as a double

```

```

% --- Executes during object creation, after setting all properties.
function edit_cable1_CreateFcn(hObject, eventdata, handles)
% hObject handle to edit_cable1 (see GCBO)
% eventdata reserved - to be defined in a future version of MATLAB

```

```

% handles empty - handles not created until after all CreateFcns called

% Hint: edit controls usually have a white background on Windows.
% See ISPC and COMPUTER.
if ispc
    set(hObject,'BackgroundColor','white');
else
    set(hObject,'BackgroundColor',get(0,'defaultUicontrolBackgroundColor'));
end

function edit_cable1_Callback(hObject, eventdata, handles)
% hObject handle to edit_cable1 (see GCBO)
% eventdata reserved - to be defined in a future version of MATLAB
% handles structure with handles and user data (see GUIDATA)

% Hints: get(hObject,'String') returns contents of edit_cable1 as text
% str2double(get(hObject,'String')) returns contents of edit_cable1 as a double

% --- Executes during object creation, after setting all properties.
function edit_cable2_CreateFcn(hObject, eventdata, handles)
% hObject handle to edit_cable2 (see GCBO)
% eventdata reserved - to be defined in a future version of MATLAB
% handles empty - handles not created until after all CreateFcns called

% Hint: edit controls usually have a white background on Windows.
% See ISPC and COMPUTER.
if ispc
    set(hObject,'BackgroundColor','white');
else
    set(hObject,'BackgroundColor',get(0,'defaultUicontrolBackgroundColor'));
end

function edit_cable2_Callback(hObject, eventdata, handles)
% hObject handle to edit_cable2 (see GCBO)
% eventdata reserved - to be defined in a future version of MATLAB
% handles structure with handles and user data (see GUIDATA)

% Hints: get(hObject,'String') returns contents of edit_cable2 as text
% str2double(get(hObject,'String')) returns contents of edit_cable2 as a double

% --- Executes during object creation, after setting all properties.
function edit_cable3_CreateFcn(hObject, eventdata, handles)
% hObject handle to edit_cable3 (see GCBO)
% eventdata reserved - to be defined in a future version of MATLAB
% handles empty - handles not created until after all CreateFcns called

% Hint: edit controls usually have a white background on Windows.
% See ISPC and COMPUTER.
if ispc
    set(hObject,'BackgroundColor','white');

```

```

else
    set(hObject,'BackgroundColor',get(0,'defaultUicontrolBackgroundColor'));
end

```

```

function edit_cable3_Callback(hObject, eventdata, handles)
% hObject   handle to edit_cable3 (see GCBO)
% eventdata reserved - to be defined in a future version of MATLAB
% handles   structure with handles and user data (see GUIDATA)

% Hints: get(hObject,'String') returns contents of edit_cable3 as text
%       str2double(get(hObject,'String')) returns contents of edit_cable3 as a double

```

```

% --- Executes during object creation, after setting all properties.
function edit_cable1_x_CreateFcn(hObject, eventdata, handles)
% hObject   handle to edit_cable1_x (see GCBO)
% eventdata reserved - to be defined in a future version of MATLAB
% handles   empty - handles not created until after all CreateFns called

```

```

% Hint: edit controls usually have a white background on Windows.
%       See ISPC and COMPUTER.
if ispc
    set(hObject,'BackgroundColor','white');
else
    set(hObject,'BackgroundColor',get(0,'defaultUicontrolBackgroundColor'));
end

```

```

function edit_cable1_x_Callback(hObject, eventdata, handles)
% hObject   handle to edit_cable1_x (see GCBO)
% eventdata reserved - to be defined in a future version of MATLAB
% handles   structure with handles and user data (see GUIDATA)

% Hints: get(hObject,'String') returns contents of edit_cable1_x as text
%       str2double(get(hObject,'String')) returns contents of edit_cable1_x as a double

```

```

% --- Executes during object creation, after setting all properties.
function edit_cable1_y_CreateFcn(hObject, eventdata, handles)
% hObject   handle to edit_cable1_y (see GCBO)
% eventdata reserved - to be defined in a future version of MATLAB
% handles   empty - handles not created until after all CreateFns called

```

```

% Hint: edit controls usually have a white background on Windows.
%       See ISPC and COMPUTER.
if ispc
    set(hObject,'BackgroundColor','white');
else
    set(hObject,'BackgroundColor',get(0,'defaultUicontrolBackgroundColor'));
end

```

```

function edit_cable1_y_Callback(hObject, eventdata, handles)

```

```

% hObject handle to edit_cable1_y (see GCBO)
% eventdata reserved - to be defined in a future version of MATLAB
% handles structure with handles and user data (see GUIDATA)

% Hints: get(hObject,'String') returns contents of edit_cable1_y as text
% str2double(get(hObject,'String')) returns contents of edit_cable1_y as a double

```

```

% --- Executes during object creation, after setting all properties.
function edit_cable2_x_CreateFcn(hObject, eventdata, handles)
% hObject handle to edit_cable2_x (see GCBO)
% eventdata reserved - to be defined in a future version of MATLAB
% handles empty - handles not created until after all CreateFcns called

```

```

% Hint: edit controls usually have a white background on Windows.
% See ISPC and COMPUTER.
if ispc
    set(hObject,'BackgroundColor','white');
else
    set(hObject,'BackgroundColor',get(0,'defaultUicontrolBackgroundColor'));
end

```

```

function edit_cable2_x_Callback(hObject, eventdata, handles)
% hObject handle to edit_cable2_x (see GCBO)
% eventdata reserved - to be defined in a future version of MATLAB
% handles structure with handles and user data (see GUIDATA)

```

```

% Hints: get(hObject,'String') returns contents of edit_cable2_x as text
% str2double(get(hObject,'String')) returns contents of edit_cable2_x as a double

```

```

% --- Executes during object creation, after setting all properties.
function edit_cable2_y_CreateFcn(hObject, eventdata, handles)
% hObject handle to edit_cable2_y (see GCBO)
% eventdata reserved - to be defined in a future version of MATLAB
% handles empty - handles not created until after all CreateFcns called

```

```

% Hint: edit controls usually have a white background on Windows.
% See ISPC and COMPUTER.
if ispc
    set(hObject,'BackgroundColor','white');
else
    set(hObject,'BackgroundColor',get(0,'defaultUicontrolBackgroundColor'));
end

```

```

function edit_cable2_y_Callback(hObject, eventdata, handles)
% hObject handle to edit_cable2_y (see GCBO)
% eventdata reserved - to be defined in a future version of MATLAB
% handles structure with handles and user data (see GUIDATA)

```

```

% Hints: get(hObject,'String') returns contents of edit_cable2_y as text
% str2double(get(hObject,'String')) returns contents of edit_cable2_y as a double

```

```

% --- Executes during object creation, after setting all properties.
function edit_cable2_z_CreateFcn(hObject, eventdata, handles)
% hObject    handle to edit_cable2_z (see GCBO)
% eventdata  reserved - to be defined in a future version of MATLAB
% handles    empty - handles not created until after all CreateFens called

% Hint: edit controls usually have a white background on Windows.
%       See ISPC and COMPUTER.
if ispc
    set(hObject,'BackgroundColor','white');
else
    set(hObject,'BackgroundColor',get(0,'defaultUicontrolBackgroundColor'));
end

function edit_cable2_z_Callback(hObject, eventdata, handles)
% hObject    handle to edit_cable2_z (see GCBO)
% eventdata  reserved - to be defined in a future version of MATLAB
% handles    structure with handles and user data (see GUIDATA)

% Hints: get(hObject,'String') returns contents of edit_cable2_z as text
%       str2double(get(hObject,'String')) returns contents of edit_cable2_z as a double

% --- Executes during object creation, after setting all properties.
function edit_cable3_x_CreateFcn(hObject, eventdata, handles)
% hObject    handle to edit_cable3_x (see GCBO)
% eventdata  reserved - to be defined in a future version of MATLAB
% handles    empty - handles not created until after all CreateFens called

% Hint: edit controls usually have a white background on Windows.
%       See ISPC and COMPUTER.
if ispc
    set(hObject,'BackgroundColor','white');
else
    set(hObject,'BackgroundColor',get(0,'defaultUicontrolBackgroundColor'));
end

function edit_cable3_x_Callback(hObject, eventdata, handles)
% hObject    handle to edit_cable3_x (see GCBO)
% eventdata  reserved - to be defined in a future version of MATLAB
% handles    structure with handles and user data (see GUIDATA)

% Hints: get(hObject,'String') returns contents of edit_cable3_x as text
%       str2double(get(hObject,'String')) returns contents of edit_cable3_x as a double

% --- Executes during object creation, after setting all properties.
function edit_cable3_y_CreateFcn(hObject, eventdata, handles)
% hObject    handle to edit_cable3_y (see GCBO)
% eventdata  reserved - to be defined in a future version of MATLAB

```

```

% handles empty - handles not created until after all CreateFcns called

% Hint: edit controls usually have a white background on Windows.
% See ISPC and COMPUTER.
if ispc
    set(hObject,'BackgroundColor','white');
else
    set(hObject,'BackgroundColor',get(0,'defaultUicontrolBackgroundColor'));
end

function edit_cable3_y_Callback(hObject, eventdata, handles)
% hObject handle to edit_cable3_y (see GCBO)
% eventdata reserved - to be defined in a future version of MATLAB
% handles structure with handles and user data (see GUIDATA)

% Hints: get(hObject,'String') returns contents of edit_cable3_y as text
% str2double(get(hObject,'String')) returns contents of edit_cable3_y as a double

% --- Executes during object creation, after setting all properties.
function edit_cable3_z_CreateFcn(hObject, eventdata, handles)
% hObject handle to edit_cable3_z (see GCBO)
% eventdata reserved - to be defined in a future version of MATLAB
% handles empty - handles not created until after all CreateFcns called

% Hint: edit controls usually have a white background on Windows.
% See ISPC and COMPUTER.
if ispc
    set(hObject,'BackgroundColor','white');
else
    set(hObject,'BackgroundColor',get(0,'defaultUicontrolBackgroundColor'));
end

function edit_cable3_z_Callback(hObject, eventdata, handles)
% hObject handle to edit_cable3_z (see GCBO)
% eventdata reserved - to be defined in a future version of MATLAB
% handles structure with handles and user data (see GUIDATA)

% Hints: get(hObject,'String') returns contents of edit_cable3_z as text
% str2double(get(hObject,'String')) returns contents of edit_cable3_z as a double

% --- Executes during object creation, after setting all properties.
function edit_cable1_z_CreateFcn(hObject, eventdata, handles)
% hObject handle to edit_cable1_z (see GCBO)
% eventdata reserved - to be defined in a future version of MATLAB
% handles empty - handles not created until after all CreateFcns called

% Hint: edit controls usually have a white background on Windows.
% See ISPC and COMPUTER.
if ispc
    set(hObject,'BackgroundColor','white');

```

```

else
    set(hObject,'BackgroundColor',get(0,'defaultUicontrolBackgroundColor'));
end

```

```

function edit_cable1_z_Callback(hObject, eventdata, handles)
% hObject    handle to edit_cable1_z (see GCBO)
% eventdata  reserved - to be defined in a future version of MATLAB
% handles    structure with handles and user data (see GUIDATA)

% Hints: get(hObject,'String') returns contents of edit_cable1_z as text
%       str2double(get(hObject,'String')) returns contents of edit_cable1_z as a double

```

```

% --- Executes during object creation, after setting all properties.
function edit_move_duration_CreateFcn(hObject, eventdata, handles)
% hObject    handle to edit_move_duration (see GCBO)
% eventdata  reserved - to be defined in a future version of MATLAB
% handles    empty - handles not created until after all CreateFcns called

```

```

% Hint: edit controls usually have a white background on Windows.
%       See ISPC and COMPUTER.
if ispc
    set(hObject,'BackgroundColor','white');
else
    set(hObject,'BackgroundColor',get(0,'defaultUicontrolBackgroundColor'));
end

```

```

function edit_move_duration_Callback(hObject, eventdata, handles)
% hObject    handle to edit_move_duration (see GCBO)
% eventdata  reserved - to be defined in a future version of MATLAB
% handles    structure with handles and user data (see GUIDATA)

% Hints: get(hObject,'String') returns contents of edit_move_duration as text
%       str2double(get(hObject,'String')) returns contents of edit_move_duration as a double

```

```

% --- Executes during object creation, after setting all properties.
function edit_systemstat_CreateFcn(hObject, eventdata, handles)
% hObject    handle to edit_systemstat (see GCBO)
% eventdata  reserved - to be defined in a future version of MATLAB
% handles    empty - handles not created until after all CreateFcns called

```

```

% Hint: edit controls usually have a white background on Windows.
%       See ISPC and COMPUTER.
if ispc
    set(hObject,'BackgroundColor','white');
else
    set(hObject,'BackgroundColor',get(0,'defaultUicontrolBackgroundColor'));
end

```

```

% ***** End Unused/Unmodified Code *****

```

```

% --- Disables all appropriate radio buttons
function mutual_exclude(off)
set(off,'Value',0)

% --- Enables/Disables all uicontrols appropriately to what radio buttons are enabled
function update_radioEnables(radius_choice, handles)

if (radius_choice == 2)
    cmd_enable = 'on';
    plat_enable = 'off';
elseif (radius_choice == 1)
    cmd_enable = 'off';
    plat_enable = 'on';
end

set(handles.push_transfer, 'Enable', cmd_enable);
set(handles.edit_num_rcvmsgs, 'Enable', cmd_enable);
set(handles.edit_cmd, 'Enable', cmd_enable);
set(handles.edit_filter_kp, 'Enable', plat_enable);
set(handles.edit_coord_x, 'Enable', plat_enable);
set(handles.edit_coord_y, 'Enable', plat_enable);
set(handles.edit_coord_z, 'Enable', plat_enable);
set(handles.push_rst_sys, 'Enable', plat_enable);
set(handles.push_update_pos, 'Enable', plat_enable);
set(handles.edit_cable1, 'Enable', plat_enable);
set(handles.edit_cable2, 'Enable', plat_enable);
set(handles.edit_cable3, 'Enable', plat_enable);
set(handles.edit_cable1_x, 'Enable', plat_enable);
set(handles.edit_cable1_y, 'Enable', plat_enable);
set(handles.edit_cable1_z, 'Enable', plat_enable);
set(handles.edit_cable2_x, 'Enable', plat_enable);
set(handles.edit_cable2_y, 'Enable', plat_enable);
set(handles.edit_cable2_z, 'Enable', plat_enable);
set(handles.edit_cable3_x, 'Enable', plat_enable);
set(handles.edit_cable3_y, 'Enable', plat_enable);
set(handles.edit_cable3_z, 'Enable', plat_enable);
set(handles.edit_systemstat, 'Enable', plat_enable);

% --- Executes on button press in radio_cmd.
function radio_cmd_Callback(hObject, eventdata, handles)
% hObject    handle to radio_cmd (see GCBO)
% eventdata  reserved - to be defined in a future version of MATLAB
% handles    structure with handles and user data (see GUIDATA)
off = [handles.radio_platform];
mutual_exclude(off);

set(hObject, 'Value', 1);

update_radioEnables(2, handles);      %enable radio_platform related uicontrols
% Hint: get(hObject,'Value') returns toggle state of radio_cmd

% --- Executes on button press in radio_platform.
function radio_platform_Callback(hObject, eventdata, handles)

```

```

% hObject handle to radio_platform (see GCBO)
% eventdata reserved - to be defined in a future version of MATLAB
% handles structure with handles and user data (see GUIDATA)
off = [handles.radio_cmd];
mutual_exclude(off);

set(hObject, 'Value', 1);

update_radioEnables(1, handles); %enable radio_cmd related uicontrols
% Hint: get(hObject,'Value') returns toggle state of radio_platform

% --- Executes on button press in push_transfer.
function push_transfer_Callback(hObject, eventdata, handles)
% hObject handle to push_transfer (see GCBO)
% eventdata reserved - to be defined in a future version of MATLAB
% handles structure with handles and user data (see GUIDATA)

%-----BEGIN CODE TO BE DELETED-----
if (strcmp(get(handles.edit_cmd, 'String'), 'run test protocol'))
    send_MSG('r', 3, handles);
    send_MSG('c1 sa', 2, handles);
    set(handles.edit_systemstat, 'Enable', 'on');
    count = 0;
    tempString = ' ';
    while (~strcmp(get(handles.edit_cmd, 'String'), 'stop'))
        count = count + 1;
        send_MSG('c1 rs', 2, handles);
        for loop = 1:4
            inputString = get(handles.text_serialstat, 'String');
            tempString = [tempString, num2str(count), 13, inputString(loop, :), 13];
        end
        send_MSG('c1 rp', 2, handles);
        for loop = 1:5
            inputString = get(handles.text_serialstat, 'String');
            tempString = [tempString, inputString(loop, :), 13];
        end
        send_MSG('c1 dp', 2, handles);
        for loop = 1:5
            inputString = get(handles.text_serialstat, 'String');
            tempString = [tempString, inputString(loop, :), 13];
        end
        inputString = get(handles.edit_systemstat, 'String');
        set(handles.edit_systemstat, 'String', [inputString, 10, tempString]);
    end
    while (~strcmp(get(handles.edit_cmd, 'String'), 'done'))
        end
        set(handles.edit_systemstat, 'Enable', 'off');
    else
        %-----END CODE TO BE DELETED-----
        send_MSG(get(handles.edit_cmd, 'String'), str2num(get(handles.edit_num_rcvmsgsgs, 'String')), handles);
    end

% --- Executes on button press in radio_com1.
function radio_com1_Callback(hObject, eventdata, handles)

```

```

% hObject   handle to radio_com1 (see GCBO)
% eventdata reserved - to be defined in a future version of MATLAB
% handles   structure with handles and user data (see GUIDATA)
off = [handles.radio_com2];
mutual_exclude(off);
set(hObject, 'Value', 1);
Serial_COM = 'COM1';
% Hint: get(hObject,'Value') returns toggle state of radio_com1

% --- Executes on button press in radio_com2.
function radio_com2_Callback(hObject, eventdata, handles)
% hObject   handle to radio_com2 (see GCBO)
% eventdata reserved - to be defined in a future version of MATLAB
% handles   structure with handles and user data (see GUIDATA)
off = [handles.radio_com1];
mutual_exclude(off);
set(hObject, 'Value', 1);
Serial_COM = 'COM2';
% Hint: get(hObject,'Value') returns toggle state of radio_com2

% --- Executes on button press in push_rst_sys.
function push_rst_sys_Callback(hObject, eventdata, handles)
% hObject   handle to push_rst_sys (see GCBO)
% eventdata reserved - to be defined in a future version of MATLAB
% handles   structure with handles and user data (see GUIDATA)
global cable1_length;
global cable2_length;
global cable3_length;
global anchor1_pos;
global anchor2_pos;
global anchor3_pos;
global cur_plat_pos;

cable1_length = str2num(get(handles.edit_cable1, 'String'));
cable2_length = str2num(get(handles.edit_cable2, 'String'));
cable3_length = str2num(get(handles.edit_cable3, 'String'));

anchor1_pos = [str2num(get(handles.edit_cable1_x, 'String')) str2num(get(handles.edit_cable1_y, 'String'))
str2num(get(handles.edit_cable3, 'String'))];
anchor2_pos = [str2num(get(handles.edit_cable2_x, 'String')) str2num(get(handles.edit_cable2_y, 'String'))
str2num(get(handles.edit_cable2_z, 'String'))];
anchor3_pos = [str2num(get(handles.edit_cable3_x, 'String')) str2num(get(handles.edit_cable3_y, 'String'))
str2num(get(handles.edit_cable3_z, 'String'))];
cur_plat_pos = [0 0 0];
set(handles.statictxt_cur_coord, 'String', num2str(cur_plat_pos));

send_MSG('r', 3, handles);    %RST all LM629's to initialize position registers -> cur pos = home pos
set(handles.text12, 'String', 'Current Cable Lengths: ');

% --- Executes on button press in push_update_pos.
function push_update_pos_Callback(hObject, eventdata, handles)
% hObject   handle to push_update_pos (see GCBO)
% eventdata reserved - to be defined in a future version of MATLAB

```

```

% handles  structure with handles and user data (see GUIDATA)
global cur_plat_pos;
global edit_SysStatTxt;

filter_coeff_kp = str2num(get(handles.edit_filter_kp, 'String'));
move_duration = str2num(get(handles.edit_move_duration, 'String'));
next_plat_pos = [str2num(get(handles.edit_coord_x, 'String')) str2num(get(handles.edit_coord_y, 'String'))
str2num(get(handles.edit_coord_z, 'String'))];
d_plat_pos = next_plat_pos - cur_plat_pos;

d_cable1_length = num2str(sqrt((anchor1_pos(1)-d_plat_pos(1)-cur_plat_pos(1))^2 + (anchor1_pos(2)-
d_plat_pos(2)-cur_plat_pos(2)+PTFM_L/4)^2 + (anchor1_pos(3)-d_plat_pos(3)-cur_plat_pos(3))^2) -
sqrt((anchor1_pos(1)-cur_plat_pos(1))^2 + (anchor1_pos(2)-cur_plat_pos(2)+PTFM_L/4)^2 + (anchor1_pos(3)-
cur_plat_pos(z))^2));
d_cable2_length = num2str(sqrt((anchor2_pos(1)-d_plat_pos(1)-cur_plat_pos(1)-PTFM_L/(8*sqrt(3)))^2 +
(anchor2_pos(2)-d_plat_pos(2)-cur_plat_pos(2)-PTFM_L/8)^2 + (anchor2_pos(3)-d_plat_pos(3)-
cur_plat_pos(3))^2) - sqrt((anchor2_pos(1)-cur_plat_pos(1)-PTFM_L/(8*sqrt(3)))^2 + (anchor2_pos(2)-
cur_plat_pos(2)-PTFM_L/8)^2 + (anchor2_pos(3)-cur_plat_pos(3))^2));
d_cable3_length = num2str(sqrt((anchor3_pos(1)-d_plat_pos(1)-cur_plat_pos(1)-PTFM_L/(8*sqrt(3)))^2 +
(anchor3_pos(2)-d_plat_pos(2)-cur_plat_pos(2)+PTFM_L/8)^2 + (anchor3_pos(3)-d_plat_pos(3)-
cur_plat_pos(3))^2) - sqrt((anchor3_pos(1)-cur_plat_pos(1)-PTFM_L/(8*sqrt(3)))^2 + (anchor3_pos(2)-
cur_plat_pos(2)+PTFM_L/8)^2 + (anchor3_pos(3)-cur_plat_pos(3))^2));

%convert from inches to cnts
d_cable1_length = d_cable1_length*925/1.884;
d_cable2_length = d_cable2_length*925/1.884;
d_cable3_length = d_cable3_length*925/1.884;

d_cable1_vel = num2str((d_cable1_length / move_duration / (1024.0 / 1000.0))*65536);
d_cable2_vel = num2str((d_cable2_length / move_duration / (1024.0 / 1000.0))*65536);
d_cable3_vel = num2str((d_cable3_length / move_duration / (1024.0 / 1000.0))*65536);

d_cable1_accel = num2str(d_cable1_vel/(1500/1000*1024));          %accelerate to max velocity over 1.5 s = 1500
ms = 1536 samples
d_cable2_accel = num2str(d_cable2_vel/(1500/1000*1024));
d_cable3_accel = num2str(d_cable3_vel/(1500/1000*1024));

msg_SysStat1 = ['Commencing Platform Movement: Pos Changes (cnts) -> Cable1: ', d_cable_length, ' Cable2: ',
d_cable2_length, ' Cable3: ', d_cable3_length, 10];
msg_SysStat2 = ['Approximate Vel(s) (cnts/smpl) -> Cable1: ', d_cable1_vel, ' Cable2: ', d_cable2_vel, ' Cable3: ',
d_cable3_vel, 10];
msg_SysStat3 = ['Accel(s) (cnts/smpl/smpl) -> Cable1: ', d_cable1_accel, ' Cable2: ', d_cable2_accel, ' Cable3: ',
d_cable3_accel, 10];
edit_SysStatTxt = [edit_SysStatTxt, 10, msg_SysStat1, msg_SysStat2, msg_SysStat3];

send_MSG(['c1 lf', filter_coeff_kp], 3, handles);
send_MSG(['c1 p', d_cable1_length, ' v', d_cable1_vel, ' a', d_cable1_accel], 3, handles);
send_MSG(['c2 lf', filter_coeff_kp], 3, handles);
send_MSG(['c2 p', d_cable2_length, ' v', d_cable2_vel, ' a', d_cable2_accel], 3, handles);
send_MSG(['c3 lf', filter_coeff_kp], 3, handles);
send_MSG(['c3 p', d_cable3_length, ' v', d_cable3_vel, ' a', d_cable3_accel], 3, handles);

send_MSG('c1 sm', 2, handles);
send_MSG('c2 sm', 2, handles);
send_MSG('c3 sm', 2, handles);

```

```

% --- Executes procedure to send msg to HC11
function send_MSG(msg, num_rcvmsgs, handles)
global Serial_COM;

static_SerTxt = 'Serial Comm Status';

if (strcmp(Serial_COM, 'COM1'))
    HC11 = serial('COM1');
elseif (strcmp(Serial_COM, 'COM2'))
    HC11 = serial('COM2');
end

HC11.BaudRate = 19200;
fopen(HC11);
fprintf(HC11, msg);

for cur_msg_num = 1:num_rcvmsgs
    HC11_from = fscanf(HC11);
    static_SerTxt = [static_SerTxt, 10, HC11_from];
    set(handles.text_serialstat, 'String', static_SerTxt);
end
delete(HC11);
clear HC11;

% --- Code to prevent user from altering system status reporting txt
function edit_systemstat_Callback(hObject, eventdata, handles)
% hObject   handle to edit_systemstat (see GCBO)
% eventdata reserved - to be defined in a future version of MATLAB
% handles   structure with handles and user data (see GUIDATA)
global edit_SysStatTxt

set(handles.edit_systemstat, 'String', editSysStatTxt);
% Hints: get(hObject,'String') returns contents of edit_systemstat as text
%       str2double(get(hObject,'String')) returns contents of edit_systemstat as a double

```

*University of Pennsylvania*  
Center for Sensor Technologies

SUNFEST

NSF REU Program  
Summer 2004

**VISUALIZATION OF REACHABILITY GRAPHS IN  
HYBRID SYSTEMS**

NSF Summer Undergraduate Fellowship in Sensor Technologies  
Seth Charlip-Blumlein, Electrical Engineering – University of Pennsylvania  
Microsoft Sunfest Fellow  
Advisor: Professor Vijay Kumar

**ABSTRACT**

Hybrid Systems is a control technique that is used in robotics. It combines sets of continuous differential equations with a discrete system that adjusts them based on multiple criteria, and uses this to simulate or control a system. The BIOCharon team takes this technique and uses it to simulate biological systems. These systems can contain many variables, and the end result of the simulation is a state space that is not easily understandable or viewable. GGV (short for Gridded Graph Viewer) is a program that allows a user to do specific "reachability analysis" on the system as well as presents a good visualization for it.

## **Table of Contents**

- 1. Introduction**
- 2. Definitions**
  - 2.1 N-tangle**
  - 2.2 Directed Graph**
  - 2.3 Gridded Graph**
  - 2.4 Reachability Graph**
- 3. Gridded Graph Viewer (GGV)**
  - 3.1 Reachability Analysis**
  - 3.2 Graph Visualization**
  - 3.3 The GGV Graphical User Interface**
- 4. Acknowledgments**

## 1. INTRODUCTION

The hybrid systems technique is built around the concept of combining discrete modeling techniques with continuous ones. Not all systems can be successfully modeled with only one of these techniques: some systems will be accurate for a time but will break down and lose their accuracy after a certain amount of time. The hybrid systems approach solves these problems by combining continuous and discrete systems into a powerful modeling technique that is capable of handling most any type of system.

A hybrid system is constructed from several elements. The most important element is the set of  $N$  variables that make up an  $N$ -dimensional state space. These variables are chosen to be significant in terms of the simulation (for example, in a biological simulation, they would be chosen as substance concentrations or other important values). The system also contains a finite state machine, defined in order to transition between states when one or more variables satisfy certain conditions. Lastly, each state contains a set of differential equations that govern the behavior of the system in that particular state.

The system is simulated as follows. Each variable in the state space is partitioned into slices, making  $N$ -dimensional surfaces. The sets of differential equations can be thought of as vector fields throughout the state space, and thus the flux of the vector fields through the surfaces can be calculated. If we consider the spaces bounded by the surfaces as nodes in a directed graph, a directed edge can be made between nodes based on how much flux there is between adjacent surfaces. Doing this for all of the surfaces in the state space results in a directed graph, which is the input to GGV (the graph analysis program).

## 2. DEFINITIONS

This section is devoted to defining some key terms that are needed to explain the functionality of GGV.

### 2.1 N-tangle

An  $N$ -tangle is an extension of a rectangle into  $N$  dimensions. An  $N$ -tangle is defined by two vectors: one designating the smallest point of the rectangle and one designating the biggest. The  $N$ -tangle itself is the set of all points that are both greater than or equal to the small vector and less than or equal to the big vector.

### 2.2 Directed Graph

A directed graph is composed of two sets: a set of nodes and edges. A node is a point in the graph, and in practical applications, it has a piece of information attached to it (sometimes a name, sometimes something more informative). An edge in a directed graph has a starting node and an ending node, and may only be traversed in one direction.

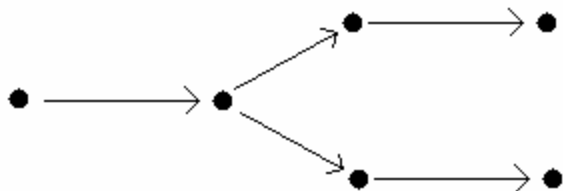


Figure 1: Example of a Directed Graph

### 2.3 Gridded Graph

A gridded graph is a directed graph for which each node is associated with a different N-tangle. Edges between nodes may only exist if the N-tangles of the start and end nodes are adjacent to each other.

A gridded graph is given as input into GGv.

### 2.4 Reachability Graph

A reachability graph is a directed graph that is created based on a starting graph and a starting node. A reachability graph contains the subgraph of all nodes and all edges that can be reached from the starting node. There are several algorithms that can be run to extract a reachability graph.

Breadth first search is an algorithm that is run on a graph in order to determine what nodes are reachable from a particular starting node. The breadth first search (BFS from now on) that GGv uses is different from the usual definition of breadth first search. It takes 3 parameters: the graph to be searched, a starting node, and an integer to designate the maximum number of links in the graph.

The algorithm runs as follows. Beginning with the starting node, the algorithm adds the starting node, all outgoing edges and the end nodes of those edges to a new graph. It continues to do this for the newly added nodes until the new nodes are further away from the starting node than the threshold allows or that there are no new nodes to add. Once either of these conditions have been fulfilled, the algorithm terminates and returns the newly created graph.

This algorithm can be retrofitted to search in reverse quite simply and efficiently. Instead of using the outgoing edges of newly added nodes, the algorithm can use the incoming edges. This allows BFS to create the reverse graph.

## 3. GGv

### 3.1 Reachability Analysis

One of GGV's main functions is to do reachability analysis. At startup, GGV reads in a gridded graph from a file. It then allows the user to select the starting node and, once this is done, it generates the new reachability graph using the selected base node.

Since the graphs can sometimes be difficult to visualize, GGV allows you to ask reachability questions of the form "Is node X reachable from the current base node?" or "Is it possible to reach the current base node from node Y?".

### 3.2 Visualization

The other major function of GGV is to visualize these gridded graphs in a helpful way. The best way to do this is to project all of the N-tangle nodes down into 2-dimensions (based on 2 variables chosen by the user), plot the nodes in these 2 dimensions, and look at many of these plots at the same time. This is how GGV displays the gridded graphs. It also allows the ability to mask nodes, gain node information by mousing over a node, as well as other possibilities.

### 3.3 The GGV Graphical User Interface

The following images were captured based on a simulation run by the BIOCharon team. It is a system with 5 variables, 3125 nodes and approximately 15000 edges.

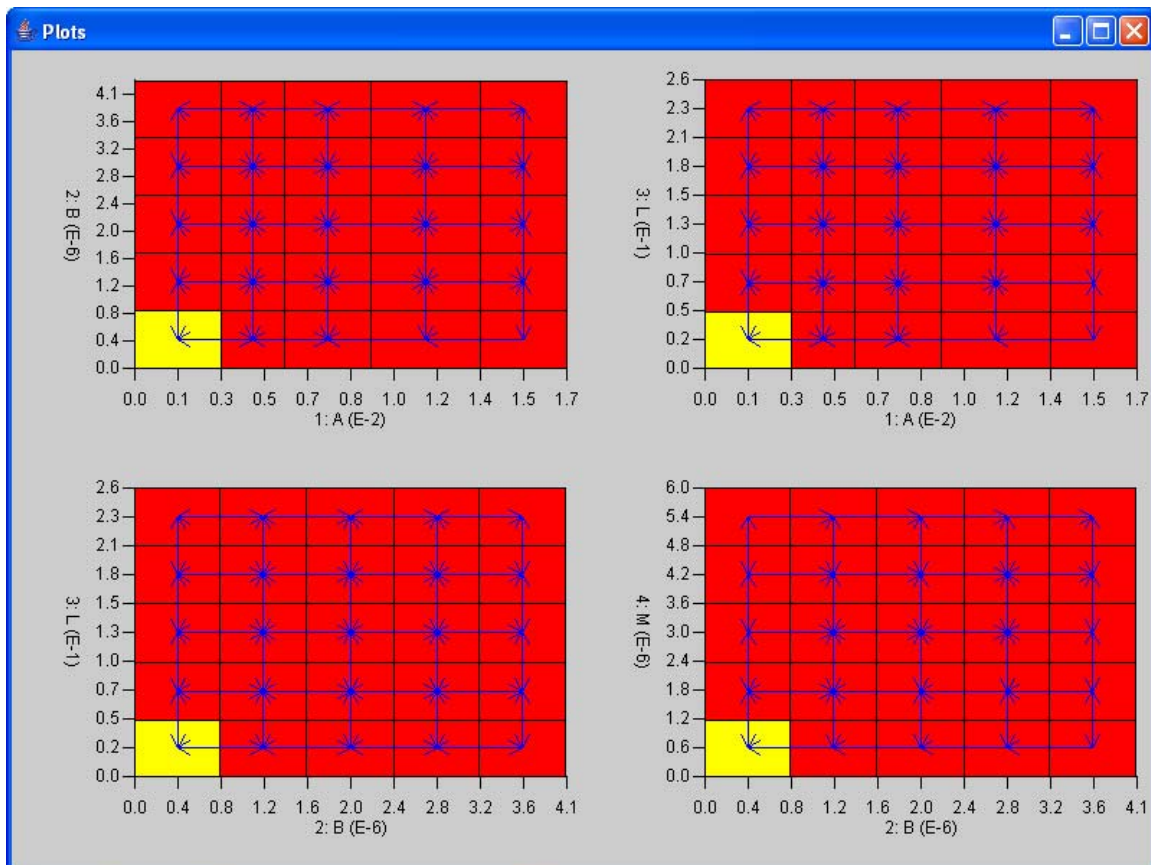


Figure 2: GGV Plots Window

Figure 2 is the GGV plots window, where the plots are displayed. The yellow rectangles represent the N-tangle of the current base node and the red rectangles represent the reachable nodes. The blue arrows are the visible edges (but only the ones where the start and end nodes differ only in the plotted dimension).

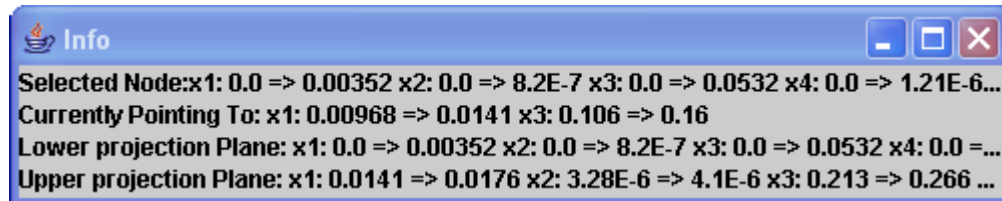


Figure 3: GGV Information Window

Figure 3 is the GGV Information window. It lists the currently selected node, the node that the user is currently pointing to with the mouse, as well as the upper and lower projection planes. Any node that is greater than the upper projection plane or less than the lower projection plane is not drawn on the plot (these planes are unique to the individual plots).

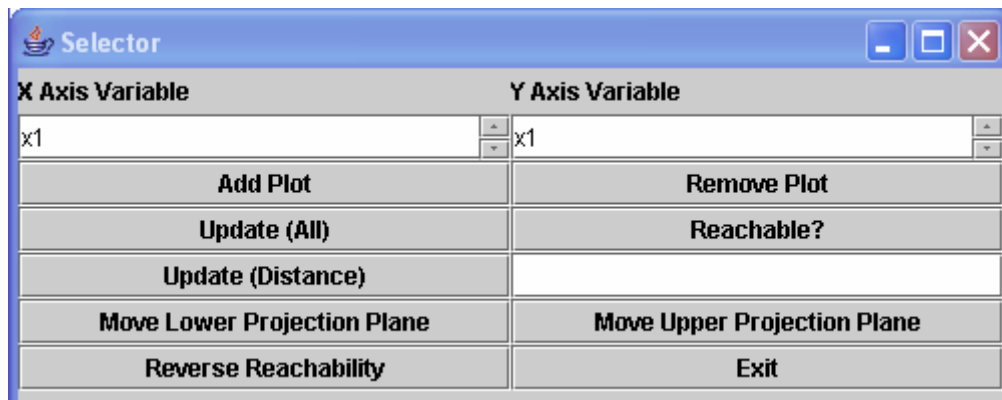


Figure 4: GGV Plot Selector and Manipulation Window

Figure 4 is where most of the user interaction takes place. Here, the user can add and remove plots from the plot window, update the graph for a new base node or limit the number of links in the reachability graph (as mentioned in section 2.4) as well as moving the projection planes and reversing the reachability graphs.

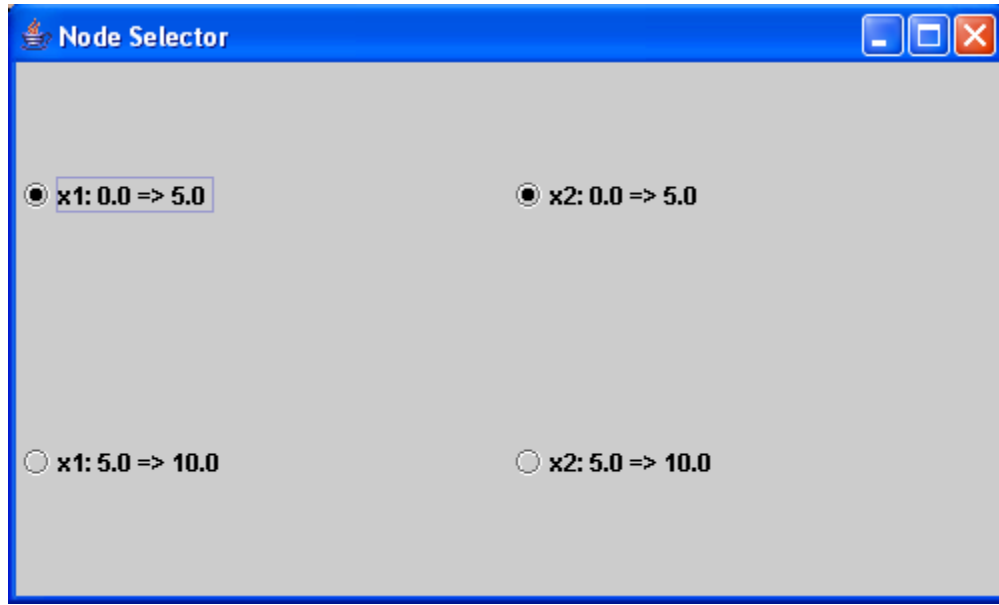


Figure 5: GGV Node Selector Window

Figure 5 is the GGV node selector window (the figure is from a different, much smaller, 2 variable model than the 3125 node model). It is used to select new base nodes, ask the reachability questions (from section 3.1), as well as move the projection planes.

#### 4. ACKNOWLEDGMENTS

Several people made this project possible and helped me in its realization. Peter Finin helped me a great deal in understanding hybrid systems and reachability analysis, as well as helped me with general coding and input issues. Adam Halsasz and Oleg Sokolsky were also very helpful in pointing me in the right direction on the project. I would also like to thank Professors Vijay Kumar and Jan Van der Spiegel for making this internship possible, as well as the generous people at the Microsoft Corporation for funding my project. They have all been very supportive and helpful over the course of this project and I extend my most sincere thanks to all of them.

*University of Pennsylvania*  
Center for Sensor Technologies

SUNFEST

NSF REU Program  
Summer 2004

**CONQUERING TISSUE-SENSOR CONTACT**  
*-- for A Breast Cancer Detector*

NSF Summer Undergraduate Fellowship in Sensor Technologies  
Ling Dong (Biomedical Engineering) – University of Rochester  
Advisor: Dr. Britton Chance

**ABSTRACT**

Current imaging diagnostic techniques demand better detection methodology to non-invasively monitor the angiogenesis of breast cancer. One of the emerging imaging techniques is to use near infrared (NIR) light to image the biophysical signs of cancerous tumor cells using optical spectroscopy. Two of the problems that arise from implementing such a method are optode-tissue coupling while fitting the contours of the breast and pressure equalization. The purpose of this project is to build upon the previous work in fabricating a device to counteract the two problems. Over the 10-week span of the SUNFEST program, an improved breast cancer detection probe has been designed, built, and validated.

This new prototype introduces two new components: Poron Quick Recovery Polyurethane Foam and a rigid delrin backing plate. The foam allows localized articulation at specific sites to fit the contours of the breast while the rigid plate aids in equalizing the pressures. Another vital advance of this device is implementation of an improved photodiode with 9.7mm \* 9.7mm active area, which permits a high signal-to-noise ratio. Experiments have been conducted to validate this prototype and they have shown promising results. The next stage will involve clinical trials in monitoring angiogenesis *in-vivo*.

## Table of Contents

<b>1.</b>	<b>Introduction</b>	<b>3</b>
<b>2.</b>	<b>Background</b>	<b>3</b>
<b>2.1</b>	<b>Identify the Scale of Force and Equipment Dimensions</b>	<b>4</b>
<b>3.</b>	<b>Possible Solutions</b>	<b>5</b>
<b>3.1</b>	<b>A Preliminary Design</b>	<b>5</b>
<b>3.1.1</b>	<b>Pros and Cons of the Preliminary Design</b>	<b>5</b>
<b>3.2</b>	<b>The Ultimate Design</b>	<b>6</b>
<b>3.2.1</b>	<b>Materials Chosen</b>	<b>6</b>
<b>4.</b>	<b>Fabrication of the Probe</b>	<b>7</b>
<b>5.</b>	<b>Experimental Setup</b>	<b>9</b>
<b>6.</b>	<b>Experimental Results</b>	<b>10</b>
<b>7.</b>	<b>Discussion</b>	<b>11</b>
<b>8.</b>	<b>Recommendation And Conclusions</b>	<b>12</b>
<b>9.</b>	<b>Acknowledgement</b>	<b>13</b>
<b>10.</b>	<b>References</b>	<b>13</b>

## 1. INTRODUCTION

Breast cancer is the most malignant tumor and the leading cause of cancer death in the western world [1]. Early detection of breast cancer, which helps reduce the need for therapeutic treatment and minimizes pain and suffering, plays an essential role in reducing the mortality rate[2]. Current screening techniques for cancer detection include X-ray mammography, magnetic resonance imaging (MRI), and ultrasound [3] [4] [6]. However, due to morphologic similarity between benign and malignant lesions, these imaging modalities become less useful [7]. Consequently, most technicians resort to biopsies for definitive diagnosis. However, up to 80% of patients who undergo breast biopsies were discovered negative for malignancy [5]. Therefore, a better diagnostic technique is needed to prevent unnecessary biopsies, which cause patients to suffer from both physical and emotional trauma.

One of the emerging imaging modalities that show promising results of illuminating the biochemical processes of tissue is using near infrared (NIR) light as a source to non-invasively monitor angiogenesis with diffuse spectroscopic techniques. When practicing this technique, several problems arise; two of them are addressed by this project: optode-tissue coupling and pressure equalization throughout the surface of the breast.

## 2. BACKGROUND

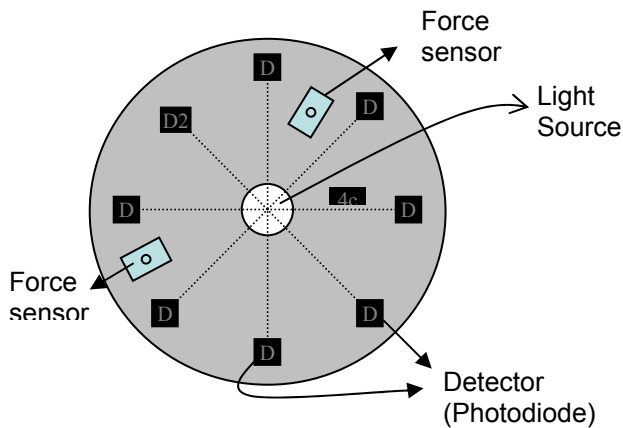


**Figure 1 - The bottom view of the earlier breast cancer detection probe with an LED in the middle, which is flanked by 8 detectors to pick up the light information.**

Earlier probe uses eight detectors, which are arranged in a circle, as illustrated in Figure 1. An LED is embedded in the middle of the probe to emit lights with three different wavelengths: 730nm, 805nm, and 850nm. This probe incorporates two force sensors to measure the pressures experienced in the vicinity of the detectors. Experimental trials show that it's almost impossible to equalize pressure using only two sensors in such a probe. The fact that this device is hand-held increases the complexity of equalizing the forces, due to human hand trembling, difficulty in coordinating the forces exerted by each finger, and the high sensitivity of the force sensors.

Since the bottom of the probe makes direct contact with the breast skin, the placement and orientation of the force sensors causes a problem. The force sensor has a small metal ball protruding that pushes against the breast tissue, thereby imposing a point contact with the breast; this point contact induces pain on the breast under a relatively high pressure, even within the desire range of examination. In addition, this probe does not have any necessary components to avoid the air bubbles in-between the detectors and the skin.

The goal of this project is to build on the existing probe and improve it by eliminating the voids and the point contact with the breast tissue. In addition to addressing the two problems, affordability is also a goal of this project.

## 2.1 Identify the Scale of Force and Equipment Dimensions

Although the relationship between the importance of the exerted force on the breast surface and the accuracy of the cancerous cell detection has not yet been discovered, a study has been conducted to test the relationship between patient comfort level and blood pressure. It found that pressures of 60 mmHg and above result in insufficient blood supply to the tumor cells, which in turn result in inaccuracy of tumor detection as well as patient discomfort. A blood pressure of 10mmHg gives an optimal outcome for cancer detection under normal blood supply. Figure 2 illustrates the relationship between the size of the breast and the amount of weight applied to the breast at 10mmHg. The graph shows that the typical amount of weight to apply to the breast at 10mmHg falls between 50g to 350g, regardless of breast size. Therefore, for the scope of this project, the desired force applied to the breast surface should roughly be 0.49N to 3.5N, assuming gravitational acceleration.

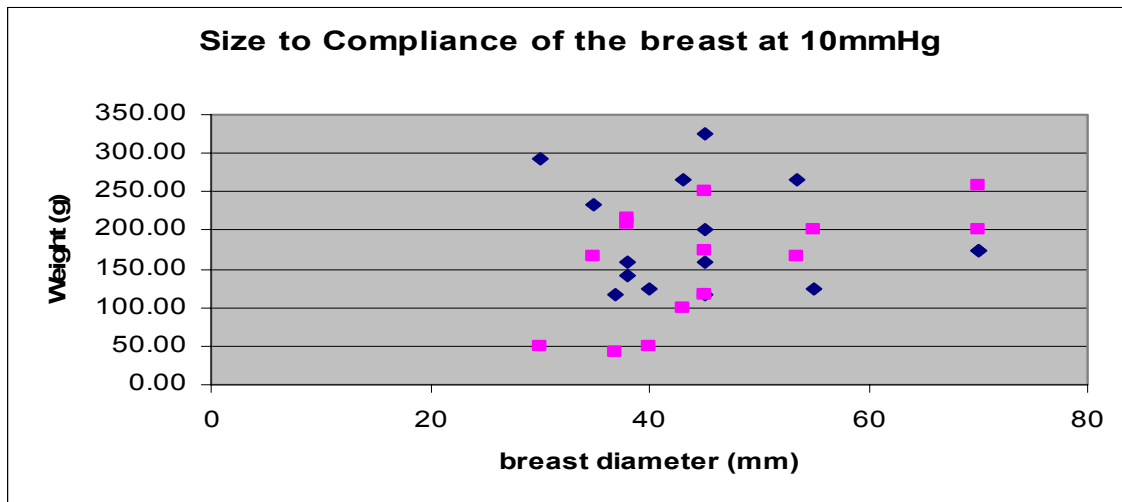


Figure 2 – A plot illustrating the relationship between the size of the breast and its compliance at 10mmHg pressure. This graph shows that the amount of mass applied to the breast is within 50g to 350g regardless of the size and firmness of the breast.

The photodiode and force sensor are approximately 10mm x 10mm x 1mm and 5.78mm\*9.28mm\*3.30mm, respectively. Knowing the scale of force and dimensions of

the necessary equipment crystallizes the problems of this project, making them easier to attack.

### 3. POSSIBLE SOLUTIONS

Solutions to the problems must meet the following conditions: the probe must be an appropriate size to be hand-held; each sensors should detect similar, if not identical, force per unit area; and the probe must fit the contours of the breast.

#### 3.1 A Preliminary Design

To equalize the pressures, programming may be the most convenient solution. A system incorporating a force sensor, an actuator and a microcontroller can be designed such that a threshold force is quantified prior to programming. The microcontroller can be programmed to communicate with the actuator and command it to exert a force on the force sensor, which pushes on the detector. Feedback is provided by the force sensor, which pushes on the detector. Feedback is provided by the force sensor, which feeds the force information to the microcontroller. A basic sketch of this design system and the schematic of its working loop are shown in Figure 3. The actuator pushes the force sensor forward until the threshold has been reached. If the microcontroller detects that the force has not reached the specified threshold, it asks the actuator to stop pushing and maintain this amount of force.

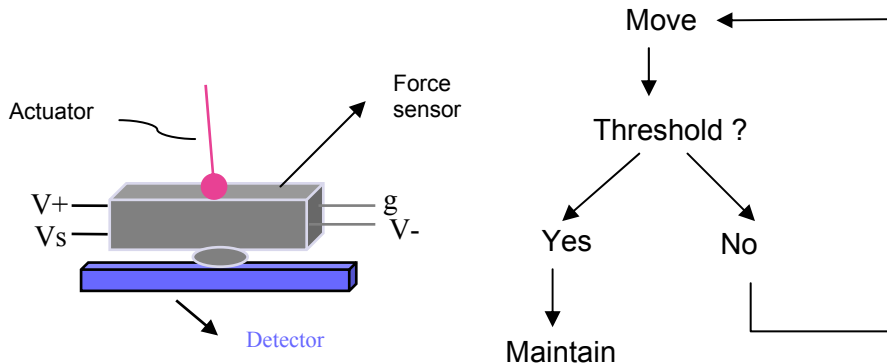


Figure 3 – A rough drawing of the preliminary design and an illustration of how this system works.

##### 3.1.1 Pros and Cons of the Preliminary Design

Although the idea of programming simplifies equalization and eliminates the need to exert a force from human hands, its consequent problems seem to outweigh the benefits. One problem is overshooting the necessary force; this system cannot cope if the actuator exerts a force greater than the threshold. However, an immediate difficulty is to find an actuator that is small enough – preferably the size of the detectors - yet has the ability to produce a 1mm to 3 mm stroke and to block an approximated 3N of force, which was discussed in detail in section 2.1. A displacement of approximately 1mm to 3mm is assumed to be enough to deform the breast tissue for a reliable result from the photodiodes.

Another problem associated with this system might be keeping the probe in place. According to Newton's Law, when the probe is exerting a force on the breast, the breast is pushing the same amount of force back to the probe. The only counteracting force to the force exerted by the actuators comes from the weight of the probe itself, which might not be enough to prevent it from sliding off the breast. It's possible that the probe will slide far off to the sides of the breast, due to the actuated forces, causing the detectors to totally lose contact with the breast tissue. Since this design solves the problem by bringing out more problems, it is not ideal.

### 3.2 The Ultimate Design

A more practical and economical solution to the challenges faced by this project is to use foam, which is readily available to replace actuators, which are expensive and also hard to locate. The elastic property of foam allows compression and decompression, which is lacking in the preliminary design. A rigid backing plate is employed to accomplish the goal of pressure equalization. Although the forces might not be exactly the same at each of the eight sites, they should be close to each other with the aid of a rigid plate.

Figure 4 shows the basic layout of this design. The force sensor is on top of the photodiode such that the force experienced by the photodiode can be directly passed on to the force sensor for a more accurate analysis. The foam cushions between the force sensor and photodiode allow the diode to maneuver around and fit the contours of the breast.

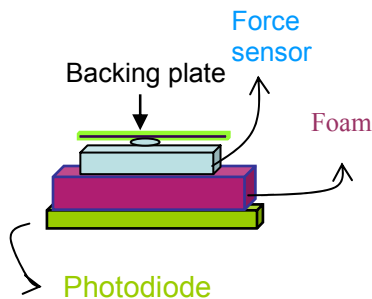


**Figure 4 – A representative unit of the eight sites in the final design. The major components to this unit are labeled.**

#### 3.2.1 Materials Chosen

A vital and innovative component for this system is the foam and the backing plate, which work in combination to meet the design constraint. The Poron Quick Recovery Polyurethane Foam chosen allows instant recovery when compressed. This foam is made of an ether and ester blend that permits high-cycle compression loads. It has a firmness of 1-5 psi, which is relatively soft. To confirm that the Poron Polyurethane Foam has the characteristics needed for the probe, a simple experiment was conducted to examine the compliance of the foam. The experiment was performed by adding forces to the foam incrementally and observing the relationship between the grams of mass applied and the displacements. A plot demonstrating their linear relationship is shown in Figure 5. Since the data shows that the foam does not undergo

plasticity within the desired range of force (100g = .98N, assuming gravitational acceleration), it is appropriate for this system.

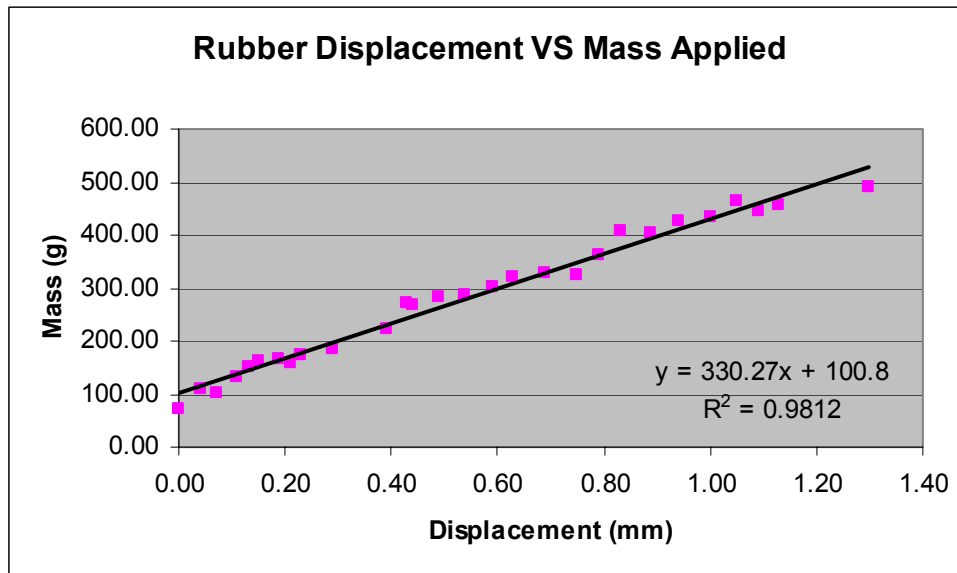


**Figure 5 – Plotting of the foam’s displacements versus the corresponding masses applied. This graph shows that this foam is appropriate to be used in the probe.**

The material for the backing plate is delrin, which is rigid enough to spread the concentrated forces evenly to the eight sites. The force sensors used are the same as the ones in the older probe except that the point contact has been changed from skin to the backing plate. The photodiode chosen is FDS1010 supplied by Thorlabs; it has an active area of 9.7mm \* 9.7mm which permits a higher signal to noise ratio than the OPT101 photodiode used previously, thereby allowing for a more accurate signal output.

#### **4. FABRICATION OF THE PROBE**

A completed prototype requires eight force sensors and eight photodiodes. For simplicity and testing purposes, only two of each are included in this prototype. The original design model drills two holes on the backing plate for the cable wires to go out through the plate allowing circuitry for the force sensors and the photodiodes to be connected outside the probe. This model was built at the machine shop, based on the design specifications, so that multiple probes can easily be fabricated if desired. The probe itself was molded using silicone rubber, because it is widely used for medical applications [8]. Figure 6 shows a cross-section of the probe to help in visualizing each of the eight units. The foam protrudes approximately 2mm from the bottom surface of the probe to free itself from encasing inside the probe, enabling the photodiodes to tilt. This length of the protrusion can be adjusted by stacking the foam of different sizes to different thicknesses. The foam avoids the spaces between the photodiodes and the skin by allowing for pressure changes without losing contact between the two.

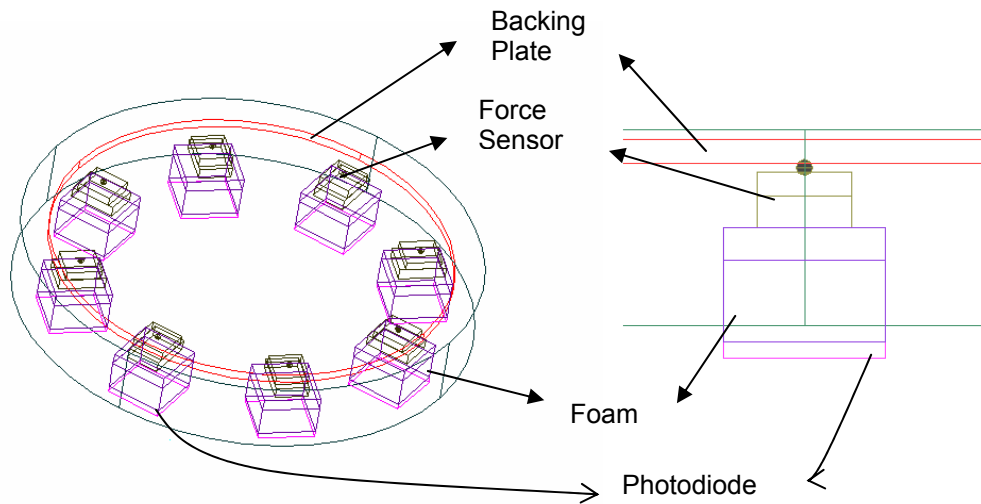


**Figure 6 – Three dimensional view of the probe from a 45 degree angle from the x-y plane and a side view of one of the eight sites in the probe.**

A differential circuit was built on a chip to amplify the output signal from the force sensors. This circuitry was designed with a gain up to the order of 20. The built-in Wheatstone bridge circuit in the force sensor transduces a potential difference across the outputs of the sensor whenever the metal ball is depressed and a force is detected. The circuit amplifies this voltage difference 20 times to eliminate the noise from the internal impedances of the force sensor and displays the reading on a digital voltmeter.

The circuitry for the photodiodes, which was built previously for a senior design course, serves as a converter to transform the current to voltage and amplifies the output. An RC low-pass filter using 8pF and 1MΩ resistors was also included in the circuit after the output voltage amplification to eliminate high-frequency noise.

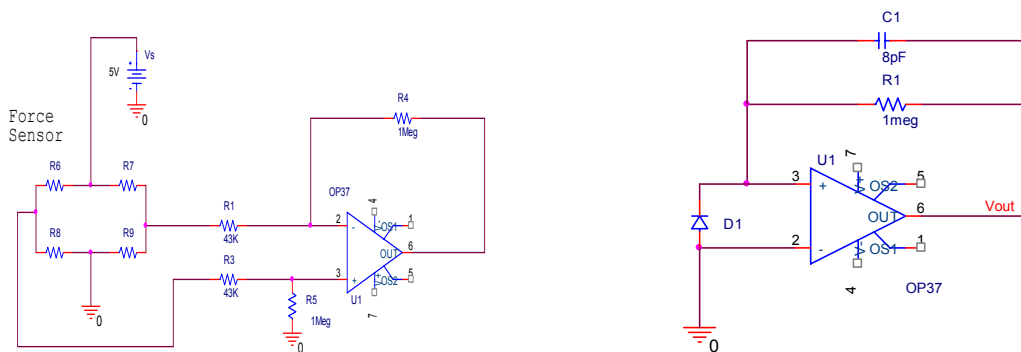


**Figure 7 – Circuits used for the probe. The differential circuit on the left is for the voltage output of force sensors and the circuit on the right acts as an RC low-pass filter for the output of photodiodes.**

Soldering also plays a major role in fabricating the probe. The four leads of the force sensors need to be bent upwards to fit the rectangular cases of the probe before soldering the wires. Epoxy was applied to all the soldering sites of the wires to prevent

detachment of wires. All the circuits were tested on a breadboard and later transformed onto a chip by soldering.

## 5. EXPERIMENTAL SETUP

Three experiments were conducted to examine the operational behavior of the probe. The major components for the experimental setup were labeled in Figure 8. These components include: a power supply for the force sensor circuit, a control box to convert the output signal from the photodiodes to a computer program, and a laptop for display. The output from the force sensors was displayed on the digital voltmeters on a circuit board, whereas the voltage output from the two photodiodes was displayed on a laptop screen via a control box. Three filters with different absorbance were used for the first preliminary test; objects with known masses and five sand bags of about 100 grams each were prepared for the second and third tests as sources of force.

The first experiment was performed specifically to examine the photodiodes' sensitivity to absorbance of the filter paper. The second experiment measured the behavior of the force in response to added weight. The third experiment involved a human subject to test how well the photodiode could respond to incremental weights when testing the probe on the human skin. During the third experiment, the subject was on a supine position with the probe on her abdomen area, which resembles the breast in its fatty characteristic.

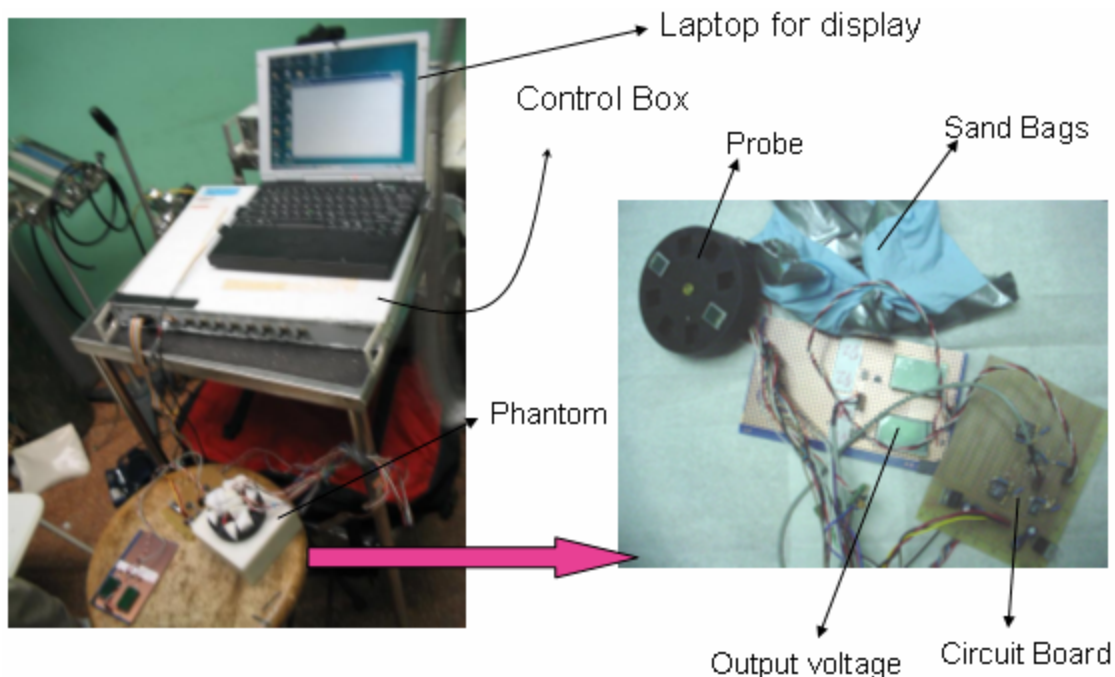


**Figure 8 – Components for the experimental setup are labeled above on the figure. The picture on the right is an enlarged view of the probe and the sensor circuit.**

## 6. EXPERIMENTAL RESULTS

The result from the standardized filter test is graphed in Figure 9, which plots the output signal from the photodiodes in mVs against the number of points recorded. Data collection started with a baseline without any light filtration and proceeded by testing the probe on three filter papers with absorbance  $0.1\text{mm}^{-1}$ ,  $0.2\text{mm}^{-1}$ , and  $0.3\text{mm}^{-1}$ .

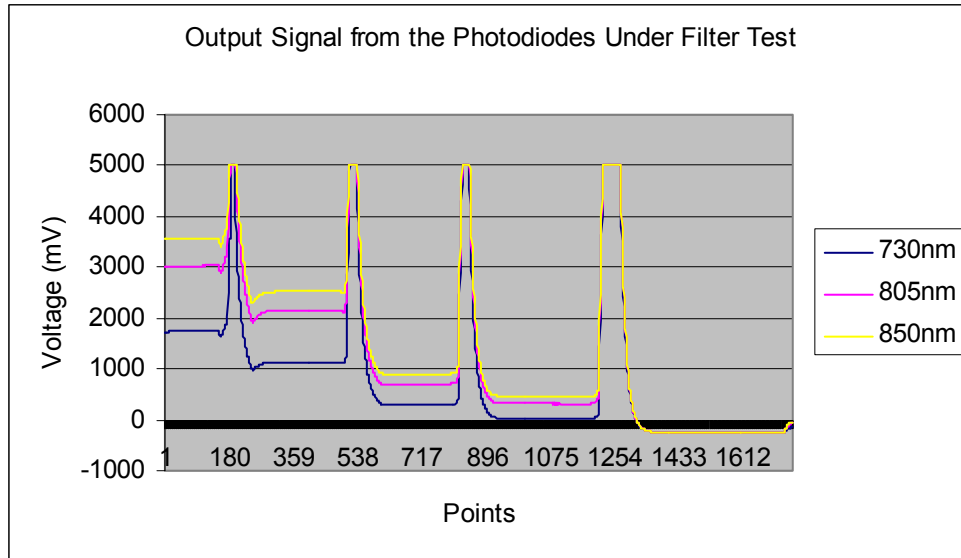


Figure 9 – Plot from the filter test for photodiodes at wavelengths 730nm, 805nm, and 850nm. This graph shows that the detectors were sensitive to different absorbance.

Experiment two specifically examined the output of the force sensors. Its result is shown in Figure 10, which displays a linear plot of the mass added to the probe against the voltage output from the two force sensors.

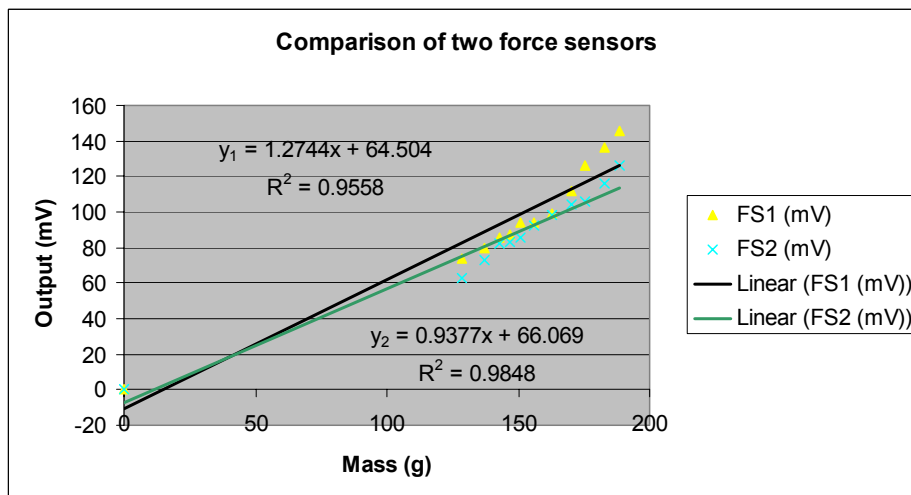


Figure 10 – Graph of output signals from the force sensors versus grams of mass added.

Figure 11 and figure 12 are both graphed from the abdominal test. Figure 11 combines the voltage output from both the force sensors and the photodiode together by extracting the points at each increase of 100 grams. By comparison, figure 12 is an enlarged view of the signals from the photodiode alone to closely analyze the voltage output from the diode. Note that each arrow indicates an increase of 100g mass.

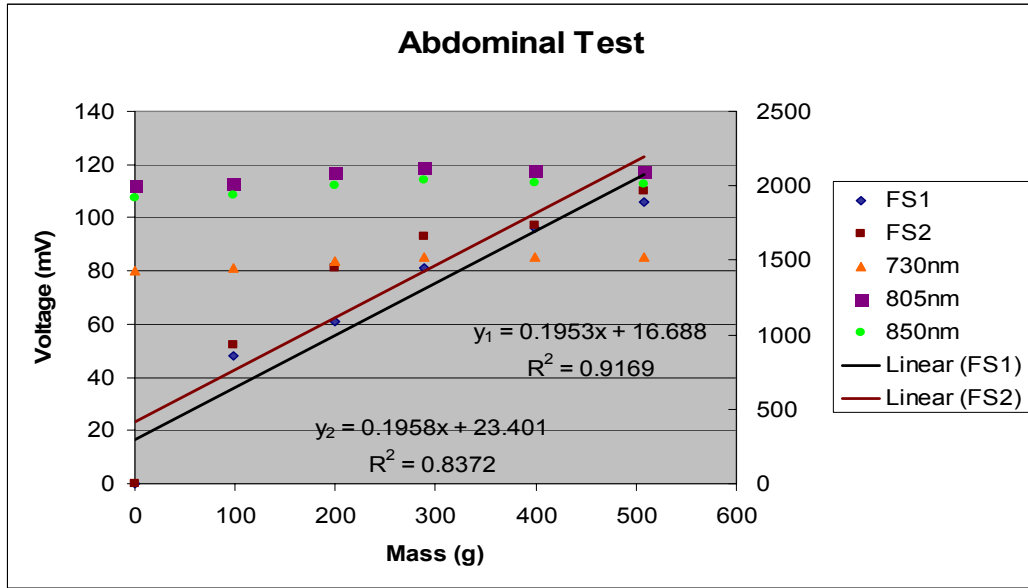


Figure 11 – Experimental results from the abdominal test, which examines the function of the probe on human skin.

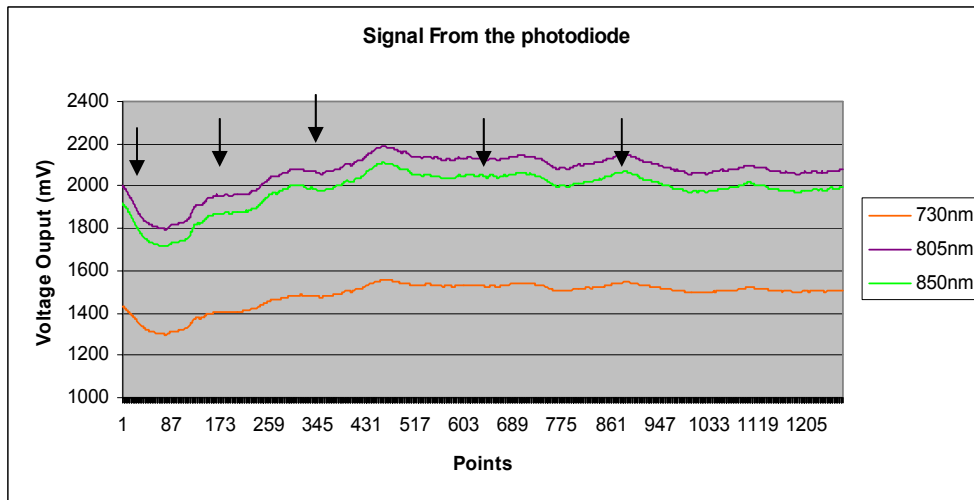


Figure 12 – An enlarged view of the signal output from the photodiodes under abdominal test.

## 7. DISCUSSION

The result from the filter test demonstrates that the photodiode has a higher output when the light absorbance is small. There are four spikes on the graph; when switching the filter paper, the diodes detect dim room lights in the media. Under normal condition

without any light filtration, the signal output is the highest. As the filter papers with increasing absorbance are used, the output gets smaller and smaller. Such a result is reasonable because high absorbance lessens the light transmission, leaving a smaller voltage output signal.

The results from the force sensors suggest that the two sensors have output readings close to each other. Both show a linear relationship between grams of mass and the voltage output. It seems as if the gain is bigger at higher forces for both force sensors. This may be because the force sensors might behave a little differently from each other. The output amplification may also augment this difference. In the abdominal experiment, the two force sensors have the same slope with a small offset. The reasons for their unexpected behaviors may be random, such as the nonzero voltage output under no force and the different slopes displayed by the two force sensors. First of all, the high sensitivity of the force sensors alters the results when the orientation of the wires is different. Second, the internal impedances of the transducers itself may differ from one another. After a number of trials, it has been ascertained that when the operator accidentally moves the cable wires, the reading on the digital voltmeters differs immediately without changing the force added to the probe. It is reasonable to believe that the torque produced by twitching the wires puts additional force on the force sensors and the photodiodes may not anticipate this unexpected force, resulting in experimental errors. In addition, there are frictional forces between the foam and the walls of the probe, which can also be a contributing factor to the slight output difference of the two force sensors.

The results from the photodiodes in the abdominal test seem reasonable. Output is minimal at no force. When 100g sand bags were added to the probe one after another, the signal increased linearly until the fourth one. After that, the output seems to level off. One possibility is that the blood vessels keep narrowing as they accept the first 300 grams of weight, and the output signals increases linearly as a result. The fat in the abdomen cushions the blood vessels after 300 grams, protecting them from narrowing further due to the force increase. So from that point on, the output signal fluctuates randomly. These three experiments give sufficient evidence that the probe works as expected although some experimental errors contaminated the force sensor outputs. Overall, the renovated prototype has operational improvements over the previous one.

## **8. RECOMMENDATIONS AND CONCLUSIONS**

There are several things that can be done to improve on this prototype. The most important and challenging one is to minimize the friction between the walls of the probe and the foam to get a more accurate result from the force sensors. The difficulty encountered in doing so is as follows: friction is necessary to tightly encase the foam in the probe, however it might cause random force change. Reshaping the foam such that only four corners of the rectangular foam push against the walls to keep the pieces of each unit in place can greatly reduce the friction force while remaining the required tension to ensure that the foam does not fall out of the probe.

A second improvement to this prototype is to use an improved amplifier specifically designed for differential circuits. There is no null offset to the force sensor circuitry right now, making it hard to compare the outputs of the two force sensors. Starting all the force sensors at the same reference voltage, preferably 0 mV, will make it easier for the operator to compare the voltage outputs. A bigger improvement would be to display the voltage readings on a computer screen, graphing the results in lines, instead of point readings, and placing it adjacent to the photodiode output. This would eliminate the digital voltmeter on a circuit board and also enable automation.

At present, the weight of cable wires is believed to be an error factor for the force sensor output. An optimal output may be attainable by switching to thinner and lighter wires, thereby imposing less weight and less torque on the force sensors. Packaging of the probe also needs to be improved so that no wires can be seen by the patients. The appearance of the probe directly affects its potential to be involved in clinical trials for further validation. One possible solution to the complex wiring is to use telemetry. As an alternative to cable connections, Bluetooth should be considered for wireless communication. In the future, we hope to commercialize this device at an affordable price. The ultimate goal of this project is to be able to provide patients who suffer from breast cancer with better imaging and diagnostic techniques.

## **9. ACKNOWLEDGMENTS**

I want to thank everyone in Chance's lab, especially Juan Du and Kiran Gangavarapu, for their kindness and encouragement in making my SUNFEST experience a memorable one. I would like to extend my gratitude to Dr. Britton Chance for his advice, patience, and dedication to this project. I also appreciate Michael, who works at the machine shop for his technical support. Thanks to the National Science Foundation for their support through an NSF-REU grant and Microsoft Corporation for their financial support. Without any of them, SUNFEST would never be possible.

## **10. REFERENCES**

1. American Cancer Society, Available from [http://www.cancer.org/docroot/CRI/CRI\\_2\\_1x.asp?dt=5](http://www.cancer.org/docroot/CRI/CRI_2_1x.asp?dt=5), accessed 31 July 2004.
2. C.C. Boring, T.S. Squires, T. Tong, Cancer Statistics, *CA Cancer J. Clin.*, 44 (1994) 7-26.
3. G. Simonetti, E. Cossu, M. Montanaro, C. Caschili, V. Giuliani, What's new in mammography, *Eur J Radiol*, 27(1998)S234-S41.
4. J. Elmore, M. Barton, V. Mocerri, S. Polk, P.J. Arena, S.W. Fletcher, Ten-year risk of false positive screening mammography and clinical breast examinations, *New Engl J Med*, 338(1998)1089-96.
5. R.P. Burns, Image guided breast biopsy, *Am J Surg*, 73(1997)9-11.

6. Silicone Rubber, Available from <http://www.azom.com/details.asp?ArticleID=920>, accessed 31 July, 2004.
7. S.L. Edell, M.D. Eisen, Current imaging modalities for the diagnosis of breast examinations. *Del Med J*, 71(1999)377-82.
8. Y. Zou, Z. Guo, A review of electrical impedance techniques for breast cancer detection, *Medical Engineering & Physics*, 25(2003)79-90.

*University of Pennsylvania*  
Center for Sensor Technologies

SUNFEST

NSF REU Program  
Summer 2004

**INTERVERTEBRAL DISC IMAGING AND ANALYSIS  
PROTOCOL ENHANCEMENT**

NSF Summer Undergraduate Fellowship in Sensor Technologies  
David Jamison, IV (Engineering Mechanics) – The Johns Hopkins University  
Advisors: Dawn M. Elliott, PhD and Chandra S. Yerramalli, PhD

**ABSTRACT**

Scientists in human tissue research often use animal tissue as alternative for human samples. Animal tissue samples are desired for their low cost and greater availability compared to human tissue. In human spine research, mouse, rat, and sheep intervertebral discs are often used as mechanical models for the human disc. They have proven effective models because they often possess mechanical properties similar to human discs. However, no one has explored whether those animal models are good geometric models of human discs. If they are, it may establish an even stronger argument for the use of these animal tissues as alternatives to human tissue. An intervertebral disc imaging and analysis protocol was devised at this lab, enabling the assessment of the geometric properties of this disc. However, additional measurements were needed so that more geometric properties could be examined. I set out to improve and expand the original protocol so that it may be used for this purpose.

## Table of Contents

<b>Introduction</b>	<b>3</b>
<b>Background</b>	<b>3</b>
<b>The Planning Stage</b>	<b>4</b>
<b>Basic Understanding of the Original Protocol</b>	<b>5</b>
<b>Devising Methods for Improvement and Expansion</b>	<b>5</b>
<b>New Protocol Execution</b>	<b>9</b>
<b>Discussion and Conclusion</b>	<b>10</b>
<b>Recommendations</b>	<b>11</b>
<b>Acknowledgements</b>	<b>11</b>
<b>References</b>	<b>11</b>
<b>Appendices</b>	<b>12</b>

## **1. INTRODUCTION**

In human tissue research, models are often used in place of an actual human tissue sample. Models are important for this type of research because they offer the scientist a way to effectively study the properties of human tissue without having the actual tissue, which in many cases is hard to come by in quantities sufficient for extensive research. Animal tissues, mathematical equations, and computer simulations can all serve as excellent human models in different ways. In the field of biomechanics, animal tissue models are often the most desired since actual mechanical tests (such as compression, tension, torsion, etc.) can be applied to the tissue to obtain its mechanical properties.

For an animal tissue to be considered a good mechanical model, the mechanical properties that are being analyzed must be similar to that of human tissue. The composition and structure of the tissue should be similar to, if not the same as, its human counterpart. In addition, an ideal model is relatively inexpensive, easy to obtain in large quantities, and has been used in other studies (justifying its use as a model).

For studies of the intervertebral disc (IVD), the most frequently used models are mouse, rat, and, to a lesser extent, sheep. Numerous studies have shown that these animals have discs with similar structure, composition, and mechanical properties to that of the human disc [1,2]

However, no literature really attempts to show if these disc models have geometric properties similar to humans. To this end, Dr. Yerramalli and Patrick Antowick at the University of Pennsylvania devised a protocol which would enable them to use a digital image of a mouse or rat disc and, using a code written in MatLab, measure the area of the sample disc. This protocol was useful; however, more was needed.

The current protocol, after my modifications, serves two purposes. The first addresses the issue of analyzing mouse, rat, and sheep discs to see if they are useful geometric models for the human spine. This will essentially strengthen the argument for the use of those animals as models for the human intervertebral disc. The second use of this protocol is comparing and contrasting the geometric properties of the lumbar and tail sections in a mouse or rat and, using these similarities and differences, try to explain the similarities and differences in the mechanical properties of those two disc sections.

This paper explains my role in the development of the protocol. It shows how I came to understand the original protocol with the help of Dr. Yerramalli, the ideas I came up with to improve the protocol, and the steps that led to the final product.

## **2. BACKGROUND**

In spring 2004, Patrick worked on his senior design project here at this lab. The underlying goal of his project was to find a way to compare the geometric measurements of the lumbar and tail sections of the mouse intervertebral disc. These measurements would then be used to compare and explain the differences in mechanical properties of

the two sections of the mouse spine. His procedure is outlined as follows [also see fig. 1]:

1. Dissect lumbar and tail sections of the mouse spine.
2. Remove individual discs from those sections, recording the disc removed (for example, L1L2). One cut is made transecting the disc while one transects the adjacent vertebrae, thus freeing the disc from the rest of the spine.
3. Stain the disc so that, when viewed under a microscope, the nucleus pulposus can be distinguished from the annulus.
4. Use a microtome to shave off micrometer-thick sections of the disc so as to obtain a flat surface, ideal for imaging
5. Prepare a slide of the individual disc.
6. Take pictures of the disc using the SONY digital camera attached to an overhead light microscope in the lab.
7. Run the MatLab program code that takes the saved digital image of the stained disc and then calculates nucleus area, annulus area, and gross disc area.
8. Record measurements. [3]

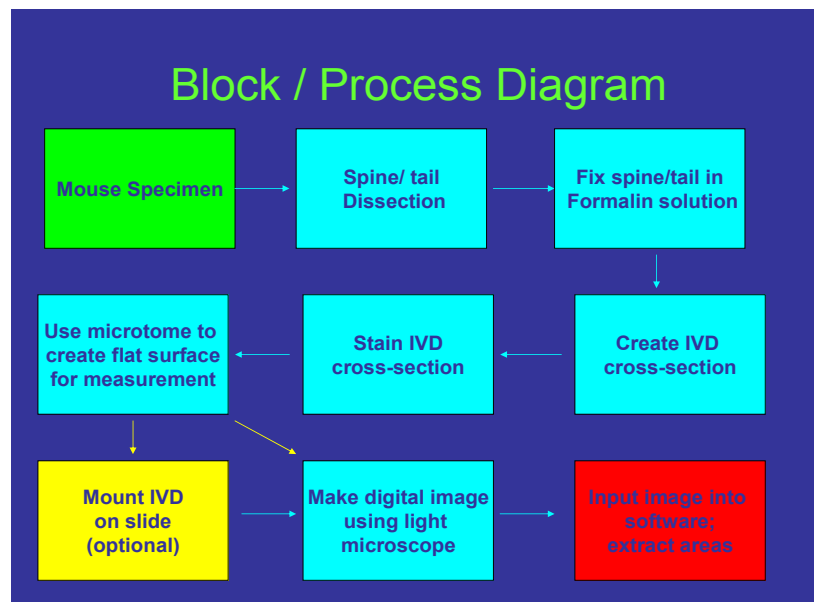


Figure 1: A block diagram of the original protocol process [3].

### 3. THE PLANNING STAGE

The project I carried out involved the continuation and expansion of the original IVD protocol. In particular, there were problems with the staining and imaging of the discs – many of the images are of poor quality, resulting in the inability to visually distinguish the annulus from the nucleus. Also, additions had to be made to the MatLab program so that it could make more measurements. I broke down my project into three phases: understand the original protocol, find methods of improvement and expansion, and execute the new protocol.

#### **4. BASIC UNDERSTANDING OF THE ORIGINAL PROTOCOL**

In this first phase of my project, I spoke to Dr. Yerramalli (who was the advisor for the previous project) and received his suggestions for improvement. I also reviewed the report for the original protocol to understand how it was devised and its goals, as well as see the Patrick's suggestions for improvement. His final report noted that the staining was not done very well, since the nucleus could not be distinguished from the rest of the disc.

After this I viewed the images myself and tested the MatLab program, trying to understand how it worked and what each part of the code meant. This was especially difficult because I had no prior programming experience.

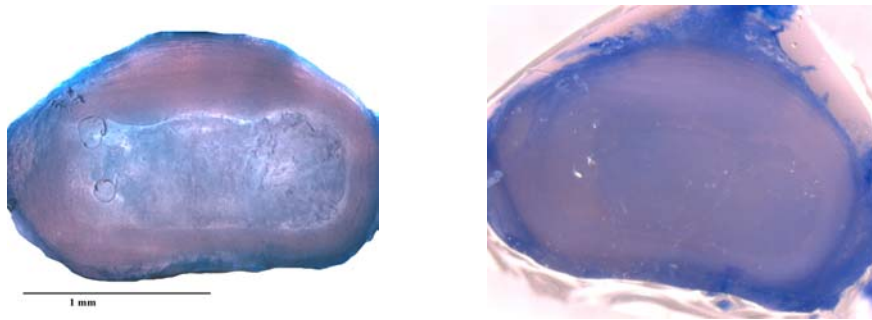
#### **5. DEVISING METHODS FOR IMPROVEMENT AND EXPANSION**

##### **5.1 Improving the Staining and Imaging Process**

The images created by the original protocol were not very useful because the nucleus could not be distinguished from the annulus in most cases. The entire disc was stained one color, making differentiation between sections nearly impossible. The original protocol called for the use of two dyes, Red Eosin and Brilliant Blue Dye. The Red Eosin dye was placed on the disc via a dropper; after five seconds the dye was washed off. The Brilliant Blue dye was then placed on the disc in the same fashion for 45 seconds before being washed off.

Given the poor staining results seen in images obtained using the original protocol, Dr. Yerramalli and I thought that we should use a more elaborate staining process, so we decided to implement the hemotoxylin and eosin staining procedure often used for immunohistochemistry. This 17-step process was employed for two reasons. First and most importantly, hemotoxylin and eosin are good at staining proteoglycans, a major component of the IVD. These stains ensure that the annulus and nucleus are distinguishable, since they contain different amounts of proteoglycans and thus will be stained slightly differently from each other. Secondly, this staining procedure calls for the stains to be left on the disc sample for 10 minutes – much longer than the amount of time that the dyes were applied in the original protocol. This new staining procedure yielded much better results than the former procedure used in the original protocol [see fig. 2].

a.)



b.)

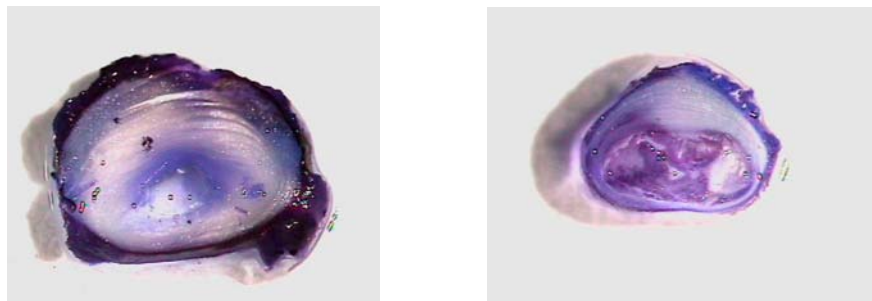


**Figure 2: The two images of the discs in (a) were obtained from the original protocol. Notice the inconsistency in the pictures. In (b), the nucleus can be easily differentiated from the annulus. Also, individual lamellae can be seen in the annulus. All discs are from the lumbar region of a mouse or rat.**

## **5.2 Improving the imaging process**

The main problem with the images obtained by the original process was the lack of quality of the discs that were being imaged. I already improved the staining process to yield better visual differentiation between the nucleus and the annulus of the disc. However, another problem remained. The discs, even if stained relatively well, were not entirely in the picture. As you can see in figure 2, the disc on the left in part (a) is not fully in the picture. There are many such images taken, and would obviously be unacceptable for use. Using the SONY digital camera in the lab I was able, with good stained discs, to capture a photo that kept the entire disc in the image.

Also, I had to manipulate the focus and the lighting to obtain the best digital image from the camera attached to the overhead light microscope. I found that blocking the light coming from one of the two lamps and dimming the remaining lamp gave the best viewing results.

### 5.3 Modifying the MatLab code

The original disc measurement program uses a user-defined function called DiscArea. The user would type “discarea” in the MatLab the command window, along with an image for the function to be applied to and a number for the scale (how the scale was determined was never made clear in Patrick’s project report). Then the user would use the mouse to select points on the perimeter of the disc, effectively making an outline of the disc. Then this process would be applied again to the nucleus. After pressing the ENTER key, the program would calculate the area of the whole disc, the nucleus, and the annulus, give the percent of the disc occupied by the nucleus, and display a binary image [see fig. 3].

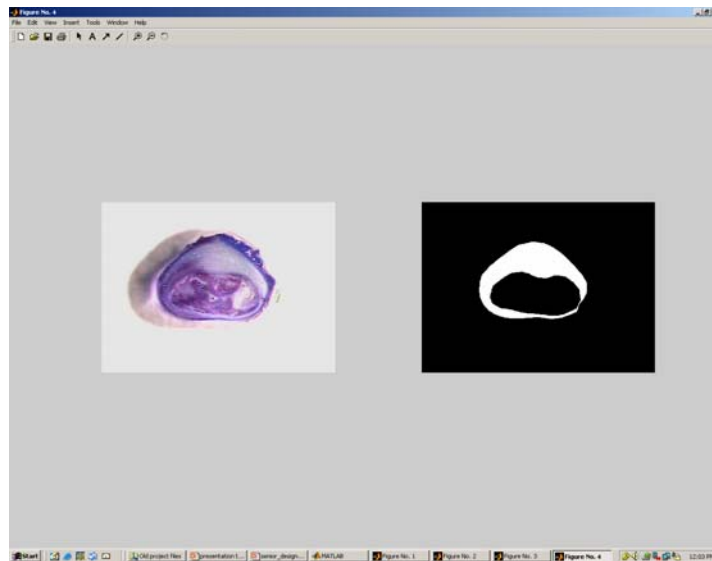


**Figure 3: The original disc image on the left and the binary image on the right (showing what the user outlined and what the program uses to calculate the area measurements) come up as one figure when the DiscArea function is applied.**

While the function was useful, we wanted the program to compute more measurements. In addition to the three area measurements, the percent nucleus calculation, and the binary image, I incorporated into the DiscArea function:

- A plot of the gross disc centroid and nucleus centroid superimposed on the disc image
- A plot of the gross disc and nucleus major and minor axes, also superimposed on the image
- Calculation of the distance between the two centroids
- Calculation of the lengths of all major and minor axes
- Calculation of the aspect ratio for both the gross disc and nucleus (major axis length divided by the minor axis length).

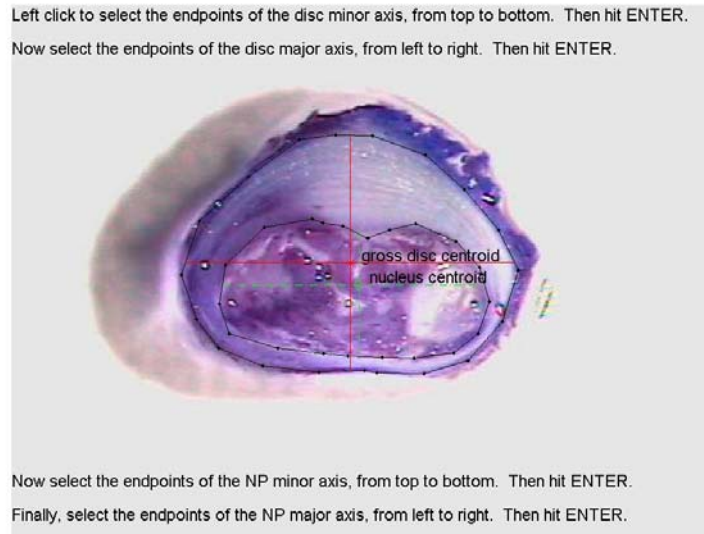


**Figure 4: Output from the new DiscArea function, showing the original disc with the two centroids and two sets of major and minor axes superimposed on the disc itself. The user-selected outlines of the disc and nucleus are also in the image.**

To calculate the centroid, the program takes the x and y coordinates of all the points clicked (for the outline of the nucleus and of the entire disc), computes the averages of the x and y coordinates separately, and then plots those points on the image (thus superimposing it on the disc). I included a function to make a line connecting the points that were selected by the user as the outline of the disc and nucleus. This outline was important for obtaining the major and minor axes. The user then chooses the endpoints of the major and minor axes (which are easy to spot due to the line which outlines the disc and nucleus), making sure that the axes intersect at their respective centroid. Once the endpoints were chosen, another line function connects those points, thus superimposing the axes onto the disc image [see fig. 4]. Calculations of the lengths of those axes as well as the aspect ratio were made in pixels and then expressed in the desired unit of measurement (usually millimeters).

To make the conversion from pixels to the desired unit, I created a new scale calculation. Previously, the scale was assumed to be fixed; however, if this program was to be used on many different images of disc samples from various animals, and if different cameras were used to produce the images, the scale could not be assumed to be the same for all images and thus, it would have to be specified each time. For a new scale calculation to be possible, a ruler would be required on every disc image so it could be referenced later. A line function that I wrote into the DiscArea program allows the user to manually select the length of the unit of measurement from the ruler in the image. The program then stores the length of that unit (in pixels) to be used as the pixel-to-unit conversion factor.

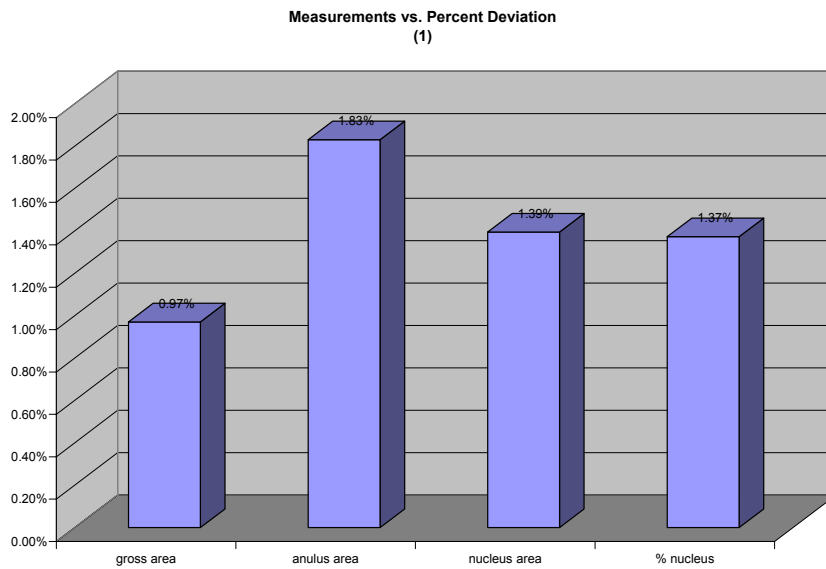
In addition to the extra calculations and measurements, I wanted to make the DiscArea function more user friendly. Originally, the directions were rather unclear and flashed on the command window before being covered by the disc image, making them unreadable. To combat this problem, I inserted an indefinite pause function into the code to halt the

running of the DiscArea code until the user presses any key, which should not happen until he finishes reading the directions; only then would the image appear on the screen. Once the figure containing the image appears, more directions are shown on the figure itself, giving the user step-by-step instructions. Figure 4 illustrates some of the on-screen directions.

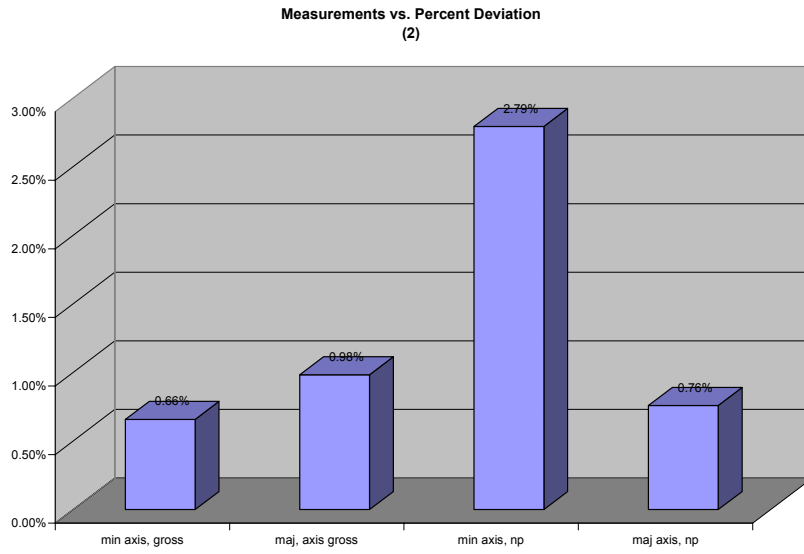
## 6. NEW PROTOCOL EXECUTION

Once I made all the improvements to the original protocol, I carried out the entire protocol from start to finish. The process turned out to be much more effective and useful than the original. When applying the DiscArea function to the same image multiple times, it yielded low percent deviations and showed that the calculations are accurate and repeatable [see figure 5].

a.)



b.)



c.)

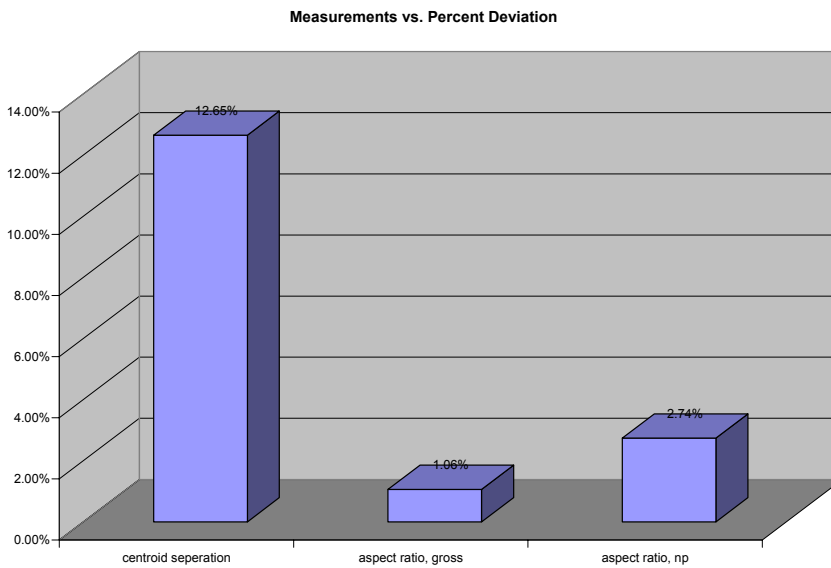


**Figure 5:** Here are graphs of the percent deviation for (a) gross disc area, nucleus area, annulus area and percent nucleus, (b) major and minor axes for both gross disc and nucleus, and (c) the centroid separation, and aspect ratio for nucleus and gross disc. The DiscArea function was applied 15 times to the same disc image. As you can see, only the centroid separation value has a percent deviation above three percent, and it is still on the order of  $10^{-6}$  meters.

## 7. DISCUSSION AND CONCLUSIONS

By improving the disc staining and imaging, and by making additions to the DiscArea function in MatLab, the new protocol is much improved from its predecessor. Now this protocol can be applied to the many samples of rat and mouse discs that we have in the lab to see if the different geometric properties of the lumbar and tail sections of the spine correlate to differences in mechanical properties. Also, the MatLab program can be

applied to prepared samples of sheep and human lumbar disc samples as well as the mouse and rat. This will, in the end, enable us to see whether or not the animal models we use are good geometric approximations of the human intervertebral disc.

## **8. RECOMMENDATIONS**

I suggest finding another way to calculate the position of the centroid. The position of the centroid plot depends on the spacing of the points chosen to outline the disc or nucleus (the plot is just the average of the perimeter values). For example, if the user selects many more points to the right of the perimeter, the centroid will be shifted to the right. This obviously poses problems for measurements and calculations that are based on the centroid position, such as major and minor axes positions and lengths and centroid separation.

## **9. ACKNOWLEDGMENTS**

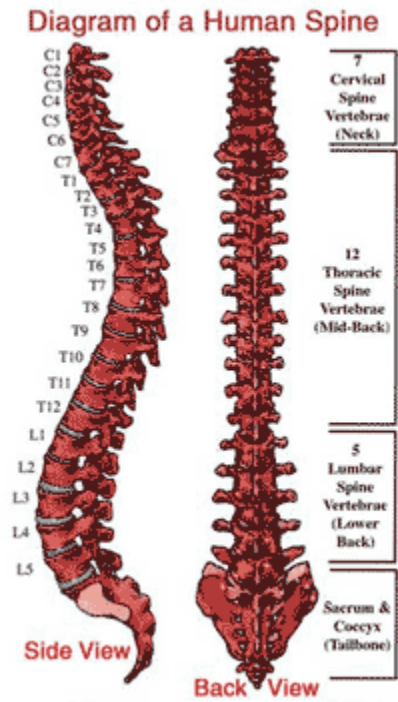
I would like to thank Dr. Louis Soslowsky, the director of McKay labs, and Dr. Dawn Elliot, my advisor, for granting me the opportunity to work in their lab this summer. Thank you to my advisors Wade Johannessen and Chandra Yerramalli for their guidance and help. Thanks to Dr. Jan Van der Spiegel, the director of the SUNFEST program. Also, I want to thank the National Science Foundation for their support through an NSF-REU grant and the Microsoft Corporation for their financial support as well.

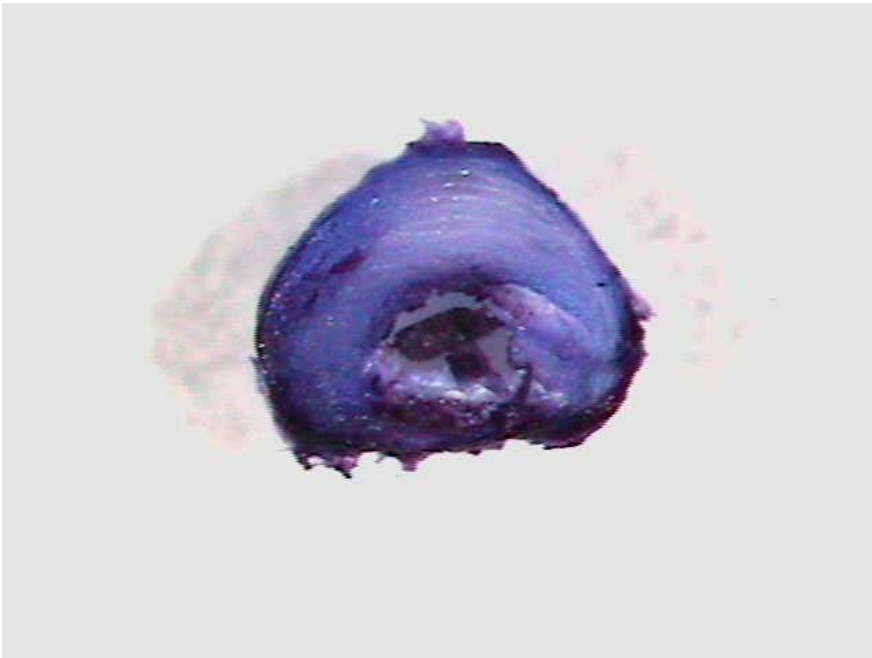
## **10. REFERENCES**

1. D.M. Elliot and J.J. Sarver, Young Investigator Award Winner: Validation of the Mouse and Rat as Mechanical Models of the Human Lumbar Disc, *Spine*, 29, (2004), 713-722
2. H. Wilke, A. Kettler, L.E. Claes, Are Sheep Spines A Valid Biomechanical Model for Human Spines?, *Spine*, 22, (1997), 2365-2374
3. P. Antowick, "Senior Design Project Final Report", April 2004

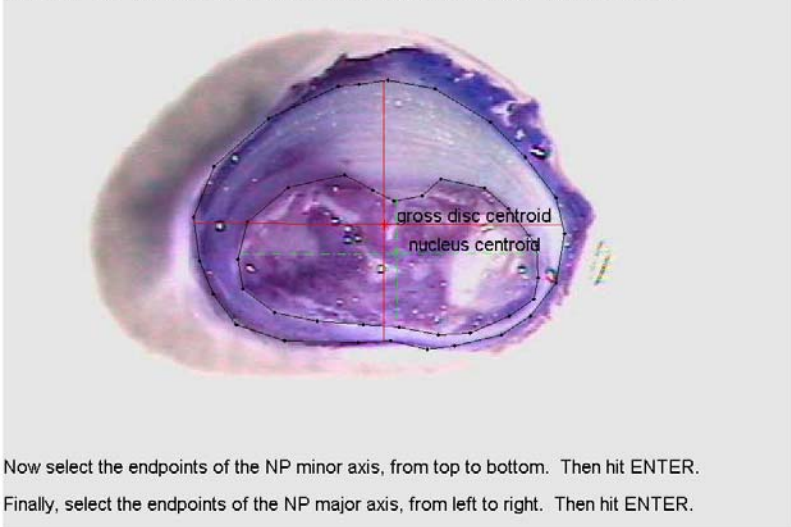
# Appendix A

## Human Spine diagram and other disc images





Left click to select the endpoints of the disc minor axis, from top to bottom. Then hit ENTER.  
Now select the endpoints of the disc major axis, from left to right. Then hit ENTER.



Now select the endpoints of the NP minor axis, from top to bottom. Then hit ENTER.  
Finally, select the endpoints of the NP major axis, from left to right. Then hit ENTER.

## Appendix B

### DiscArea MatLab code

```
function [areas, regions]=discarea(image, scale)
% Provides area measurements of a mouse disc
% given the image and scale input by user.
% The user selects the regions for the area calculations manually by
% approximating the disc as a polygon.

% This program was modified summer 2004 by David Jamison.

warning off
if nargin==2
% Reads and displays the image; allows calculation the unit-pixel
scale.
    %disp('To begin, you will measure the pixel-per-unit scale')
    %disp('Select the length of the unit (inch, mm, etc.) at least 5
times.')
```

```
    %disp('Press ENTER to continue.')
```

```
    %pause
    disc=imread(image);
    %imshow(disc);
    % [x,y]=ginput;
    %scale=sqrt((mean2(x)^2)+(mean2(y)^2))
    %close

% Reads and displays the image; "roipoly" command outlines the disc and
% NP. Also gives instructions for the user.
    disp('First, you will be outlining both the entire disc and the
NP.')
```

```
    disp('Press ENTER to begin')
```

```
    pause
    imshow(disc);
    axis on;
    text(1,1,'Use the crosshairs and click points to select the entire
disc.');
```

```
    text(1,40,'Right click the mouse when you have finished selecting
the region.');
```

```
    [BW,xi,yi]=roipoly;           % saves gross region as disc_gross in
binary
```

```
    text(1,70,'Now, do the same, this time outlining the nucleus.');
```

```
    [BW2,xi2,yi2]=roipoly;       % saves nucleus region as
'disc_nucleus' in binary
```

```
    X_avg_gross=mean2(xi);
    Y_avg_gross=mean2(yi);
    X_avg_np=mean2(xi2);
    Y_avg_np=mean2(yi2);
    close all;

% Displays more user instructions. Plots both the gross disc and NP
% centroids as well as the disc and NP outlines previously drawn by
the user on the image.
    disp('Now you are going to select the endpoints of the major')
    disp('and minor axes of the gross disc and NP.')
```

```
    disp('Press ENTER to continue')
```

```
    pause
```

```

figure
imshow(disc)
hold on
plot(xi,yi,'k.-')
plot(xi2,yi2,'k.-')
plot((X_avg_gross),Y_avg_gross,'r*')
plot((X_avg_np),Y_avg_np,'gd')
text(X_avg_gross + 10,Y_avg_gross - 7,'gross disc centroid')
text(X_avg_np +10,Y_avg_np - 7,'nucleus centroid')

% User selects the endpoint of the gross disc and NP major and minor
% axes.
text(1,10,'Left click to select the endpoints of the disc minor
axis, from top to bottom. Then hit ENTER.')
[x,y]=ginput;
text(1,40,'Now select the endpoints of the disc major axis, from
left to right. Then hit ENTER.')
[x2,y2]=ginput;
text(1,430,'Now select the endpoints of the NP minor axis, from top
to bottom. Then hit ENTER.')
[x3,y3]=ginput;
text(1,460,'Finally, select the endpoints of the NP major axis,
from left to right. Then hit ENTER.')
[x4,y4]=ginput;
% Superimposes the plots for gross disc and NP axes onto the image.
plot(x,y,'r-')
plot(x2,y2,'r-')
plot(x3,y3,'g-.')
plot(x4,y4,'g-.')

%Print the image
%print
pause(2)

%the following is Chandra's method of calculating major and minor axes
% More figures appear
figure;
[gross_radius,
gross_theta]=gross_axis(xi,yi,X_avg_gross,Y_avg_gross);
plot(gross_theta*180/pi,gross_radius,'*');
%ig1 = find((gross_theta*180/pi<91) & (gross_theta*180/pi > 0) )
[np_radius, np_theta]=gross_axis(xi2,yi2,X_avg_np,Y_avg_np);
pause(1)
figure
plot(np_theta*180/pi,np_radius,'+')
pause(1)
figure
subplot(1,2,1);
imshow(disc); % shows original image
subplot(1,2,2);
regions=visualize(BW, BW2); % shows binary composite image

% The following calculates and displays all measurements given the
inputs obtained above
total=find(BW); % finds nonzero elements (selected
region) of total disc

```

```

nucleus=find(BW2);           % selected region of nucleus
gross_area=size(total)/scale^2
nucleus_area=size(nucleus)/scale^2
annulus_area=gross_area-nucleus_area
percent_nucleus=nucleus_area/gross_area      %finds percent of disc
that is occupied by nucleus
Min_axis_gross=((y(2,1)-y(1,1))/scale)
Maj_axis_gross=((x2(2,1)-x2(1,1))/scale)
Min_axis_np=((y3(2,1)-y3(1,1))/scale)
Maj_axis_np=((x4(2,1)-x4(1,1))/scale)
X_Offset=abs(X_avg_gross-X_avg_np)/scale
Y_Offset=abs(Y_avg_gross-Y_avg_np)/scale
%Centroid seperation=(sqrt((X_avg_gross-X_avg_np)^2+(Y_avg_gross-
Y_avg_np)^2)/scale)
Aspect_ratio_gross=(Maj_axis_gross/Min_axis_gross)
Aspect_ratio_np=(Maj_axis_np/Min_axis_np)

% Writes the data calculated above to a .dat file.
B=[gross_area(1,1), nucleus_area(1,1), annulus_area(1,1),
percent_nucleus, Min_axis_gross, Maj_axis_gross, Min_axis_np,
Maj_axis_np, X_Offset, Y_Offset, Aspect_ratio_gross, Aspect_ratio_np];
fid = fopen('Disc_measurements.dat','a');
%fprintf(fid,'Total Disc Area, NP Area, AF Area, Percent NP,
Gross Min. Axis, Gross Major Axis, NP Min. Axis, NP Major Axis,
Centroid Offset X, Centroid Offset Y, Gross Aspect Ratio, NP Aspect
Ratio\n');
fprintf(fid,'\n');
fprintf(fid,'%6.5g, ',B);
fclose(fid);
end

function selected= visualize(gross, nucleus)
% allows user to visualize the selected regions
nucleus= +nucleus;
gross= +gross;
total=nucleus+gross;
S=size(gross);
for row=1:S(1)
    for col=1:S(2)
        if total(row,col)==2
            total(row,col)=0;
        end
    end
end
imshow(total);
selected=total;

function [r_g,theta_g]=gross_axis(xi,yi,xg,yg)
clk_no=size(xi);
for k=1:clk_no
    r_g(k)=sqrt((xi(k)-xg)^2 + (yi(k)-yg)^2);
    theta_g(k)=asin((xi(k)-xg)/r_g(k));%atan((xi(k)-xg)/(yi(k)-yg));
end

```

*University of Pennsylvania*  
Center for Sensor Technologies  
Philadelphia, PA 19104

SUNFEST REU Program 2004

## **DEVELOPMENT OF A NOVEL THERAPY FOR OCULAR NEOVASCULARIZATION**

NSF Summer Undergraduate Fellowship in Sensor Technologies  
Dominique Low (Mathematical and Computational Biology) – University of  
Pennsylvania

Advisors: Elaine Wu and Dr. Tolentino

### **ABSTRACT**

Age-related macular degeneration (AMD), the leading cause of blindness in the developed Western World, affects over 10 million Americans. Intravitreal injection of triamcinolone acetonide (TA) has been successfully used in the clinic to treat age-related macular degeneration and other similar neovascular diseases, but its mechanism of action is still unclear. However, this experiment sheds light on the subject and leads to a better understanding of the investigational therapy for human disease. It is hypothesized that TA inhibits development of neovascularization (NV) by reducing Vascular Endothelial Growth Factor (VEGF). The goal of this project is to determine if TA decreases VEGF, a protein associated with the development of NV in AMD and other retinopathies.

**Table of Contents**

**DEVELOPMENT OF A NOVEL THERAPY FOR OCULAR  
NEOVASCULARIZATION**

Dominique Low (Mathematical and Computational Biology) – University of  
Pennsylvania

Advisors: Elaine Wu and Dr. Tolentino

1 INTRODUCTION .....	3
2 MATERIALS AND METHODS .....	3
2.1 Testing the effectiveness of Triamcinolone .....	3
2.1.1 Cell Culture .....	3
2.1.2 ELISA .....	4
2.1.3 Real Time RT-PCR .....	5
2.2 Preliminary Cytotoxicity Test .....	6
2.2.1 Cell Culture .....	6
2.2.2 Alamar Blue Cytotoxicity Test .....	7
3 RESULTS AND DISCUSSION .....	7
3.1 Testing the Effectiveness of Triamcinolone .....	7
3.2 Preliminary Cytotoxicity Test .....	12
4 CONCLUSIONS .....	15
5 FUTURE WORK .....	15
6 ACKNOWLEDGEMENTS .....	16
7 REFERENECES .....	16
8 APPENDICES .....	17

## **1. INTRODUCTION**

Drawing from earlier research findings, it has already been demonstrated that vascular endothelial growth factor (VEGF) plays a pivotal role in the development of age-related macular degeneration, one of the most common causes of blindness in developed Western world. A number of investigators have demonstrated that VEGF is sufficient and necessary to produce ocular changes seen in both non-proliferative and proliferative diabetic retinopathy. In particular, VEGF induces neovascularization, the blinding complication of diabetic retinopathy. Several companies have developed anti-VEGF compounds that are in clinical trials for the treatment of neovascular retinal diseases.

One novel strategy for targeting VEGF is through intravitreal injection of triamcinolone acetonide. Triamcinolone acetonide inhibits choroidal neovascularization in a rat model that mimics neovascular retinal disease. The mechanism of this is unclear. One hypothesis is that it downregulates VEGF. We intend to test this hypothesis in vitro.

Also, since intravitreal injections of triamcinolone have been used clinically to treat age-related macular degeneration and other neovascular retinopathies, we would like to test the toxicity of triamcinolone acetonide on human cells. We will implement an Alamar Blue Cytotoxicity Test. Alamar Blue is a dark blue dye added to the cells' media. Healthy cells will oxidize the dye to violet or pink tint. Unhealthy or deceased cells would be unable to oxidize the dye and their surrounding solution would remain dark blue. This test would therefore serve as an appropriate gauge of TA toxicity.

The purpose of this project is to develop a treatment for age-related macular eye degeneration and other neovascular retinopathies, using intravitreal injection of triamcinolone acetonide directed against vascular endothelial growth factor to the retina.

## **2. MATERIALS AND METHODS**

### **2.1 Testing the Effectiveness of Triamcinolone**

#### **2.1.1 Cell Culture**

To determine if triamcinolone is indeed inhibiting VEGF production, human ARPE-19 cells were exposed to varying doses of triamcinolone in addition to various controls. The cell cultures were then challenged with 130 uM deferoxamine, a hypoxic stimulus. The cells were incubated in a plate as follows:

-	+ CtrlT	+ 1 TA	+ 6 TA	+ Ctrl5	+ C5
-	+ CtrlT	+ 1 TA	+ 6 TA	+ Ctrl5	+ C5
-	+ CtrlT	+ 1 TA	+ 6 TA	+ Ctrl5	+ C5
<b>Just Cell</b>	<b>Just Cell</b>	<b>Just Cell</b>			

Each group of cells was tested in triplicates to obviate well-to-well deviations.

The “-“ groups of cells were not treated with deferoxamine. Therefore, they would experience no hypoxia, be healthy, and express healthy levels of VEGF. They acted as negative controls for the “+ ctrl TA” and “+ ctrl C5” cells.

The “+ ctrl TA” group of cells represented cells treated with deferoxamine to induce hypoxia so as to generate abnormally high levels of VEGF. However, the cells were bathed in media without TA, and thus acted as negative controls for the “1 mg/mL TA” and “6 mg/mL TA” cells.

The “1 mg/mL TA” cells were treated with deferoxamine to induce hypoxia and with 1 mg/mL TA suspension at a dosage similar to the lower range of dosages used clinically for human. This constituted the first of two TA dosages tested.

The “6 mg/mL TA” cells were treated with deferoxamine to induce hypoxia and with 6 mg/mL TA, at a dosage similar to the higher range of dosages used clinically in humans. This constituted the second of the two TA dosages tested.

The “+ ctrl C5” cells were treated with deferoxamine to induce hypoxia and with siRNA Candidate 5’s solvent, aqueous OptiMEM. This acted as a negative control for “+ C5”.

The “+ C5” cells were treated with deferoxamine to induce hypoxia and with siRNA Candidate 5. The agent siRNA Candidate 5 had already been demonstrated in previous studies to be capable of suppressing the VEGF gene. It therefore serves as a positive control for the “1 mg/mL TA” and “6 mg/mL TA” cells.

The “Just cells” group of cells was incubated along with the other groups for the purpose of establishing a standard curve to measure the RNA levels.

### 2.1.2 ELISA

To determine if TA decreases cellular concentrations of VEGF protein, a VEGF Enzyme-linked Immunosorbent Assay (ELISA, R&D Systems) was used. Briefly, ELISA is a colorimetric method of detecting VEGF that has been bound by a VEGF-specific

antibody. By comparing results to a standard curve, the concentration of VEGF in unknown samples can be determined.

-	-	-
+	+	+
<b>CtrlT</b>	<b>CtrlT</b>	<b>CtrlT</b>
+	+	+
<b>1 TA</b>	<b>1 TA</b>	<b>1 TA</b>
+	+	+
<b>6 TA</b>	<b>6 TA</b>	<b>6 TA</b>
+	+	+
<b>ctrl C5</b>	<b>ctrl C5</b>	<b>ctrl C5</b>
+	+	+
<b>C5</b>	<b>C5</b>	<b>C5</b>
<b>2000</b>	<b>1000</b>	<b>250</b>
<b>pg/mL</b>	<b>pg/mL</b>	<b>pg/mL</b>
<b>125</b>	<b>62.5</b>	<b>31.25</b>
<b>pg/mL</b>	<b>pg/mL</b>	<b>pg/mL</b>

Supernatant was obtained from each treatment and control group of cell culture that had been spun down in a centrifuge at 13,000 rpm for 2 minutes. In order to reduce TA's interference with the ELISA measurement of VEGF, the supernatant of the "1 mg/mL TA" and "6 mg/mL TA" cell cultures had to be centrifuged to spin down the TA particles suspended in the supernatant. This was done by first transferring the supernatants of all control and treated cell cultures to the low retention 1.5 mL tubes for centrifuge. After centrifuge, 200 uL of each tube was transferred to the ELISA plate. All tests were performed in triplicates to counter potential slight deviation of results between wells.

A standard curve was constructed from a stock solution of human VEGF protein, with concentrations varying from 31.25 to 2000 pg/mL. Readings from different concentrations of VEGF protein were later used to create a standard curve to assay the concentration of VEGF protein in each of the treatment and control samples.

### 2.1.3 Quantitative Real Time RT-PCR

A real time Reverse Transcription Polymerase Chain Reaction (RT-PCR) was used to determine if TA decreased VEGF mRNA. Because real time RT-PCR was performed in real time, an additional set of controls was needed. As the amounts of loaded RNA may differ, it is vital to normalize all VEGF results relative to a housekeeping gene, 18s srRNA. Thus, the real time RT-PCR was performed on a 96-well plate as follows:

VEGF						18s srRNA					
100	25	6.25	- hyp	+ C5	+1 TA	100	25	6.25	- Hyp	+ C5	+1 TA
100	25	6.25	- hyp	+ C5	+1 TA	100	25	6.25	- Hyp	+ C5	+1 TA
100	25	6.25	- hyp	+ C5	+1 TA	100	25	6.25	- Hyp	+ C5	+1 TA
50	12.5		+ctl C5	+ctl TA	+6 TA	50	12.5		+ctl C5	+ctl TA	+6 TA
50	12.5		+ctl C5	+ctl TA	+6 TA	50	12.5		+ctl C5	+ctl TA	+6 TA
50	12.5	NTC	+ctl C5	+ctl TA	+6 TA	50	12.5	NTC	+ctl C5	+ctl TA	+6 TA

After the supernatant was removed for ELISA, total RNA was isolated from cells using RNeasy (Qiagen) and treated with DNase (Ambion) to remove contaminating DNA. Total RNA was then reversed transcribed into cDNAs using reverse transcriptase (ABI). VEGF and 18s srRNA cDNAs were amplified using gene-specific Taqman probes on a real time cyler. Non-template control (NTC) wells were included. They received no RNA and therefore served as negative control. Standard curves for VEGF and 18s srRNA were generated with serial dilutions of RNA (100, 50, 25, 12.5, and 6.25 ng/uL). Results were samples were extrapolated to the corresponding standard curve.

## 2.2 Preliminary Cytotoxicity Test

One of the theories to account for the unexpected results in 2.1 prompted a cytotoxicity test for triamcinolone.

### 2.2.1 Cell Culture

Human ARPE-19 cells were plated in the following manner.

-	+ CtrlT	+ 1 TA	+ 6 TA	+ Ctrl5	+ C5
-	+ CtrlT	+ 1 TA	+ 6 TA	+ Ctrl5	+ C5
-	+ CtrlT	+ 1 TA	+ 6 TA	+ Ctrl5	+ C5
Media Only	Media Only	Media Only	Just Cell	Just Cell	Just Cell

<b>1 TA only</b>	<b>6 TA only</b>	<b>Media +AB</b>			
<b>1 TA only</b>	<b>6 TA only</b>	<b>Media +AB</b>			
<b>1 TA only</b>	<b>6 TA only</b>	<b>Media +AB</b>			
<b>Media Only</b>	<b>Media Only</b>	<b>Media Only</b>			

Since triamcinolone acetonide has a solubility of 21 mg/L, we were concerned that some triamcinolone might remain in solution and thereby interfered with the oxidation process. Hence, we included “1 mg/mL TA only” and “6 mg/mL TA only” controls, which were free of cells and contained only triamcinolone and growth media.

On Day 0, we plated the human ARPE-19 cells. On Day 1, we added the TA and transfected the cells with siRNA Candidate 5. On Day 2, we added the deferoxamine to induce hypoxia. On Day 3, the cells were harvested to be tested.

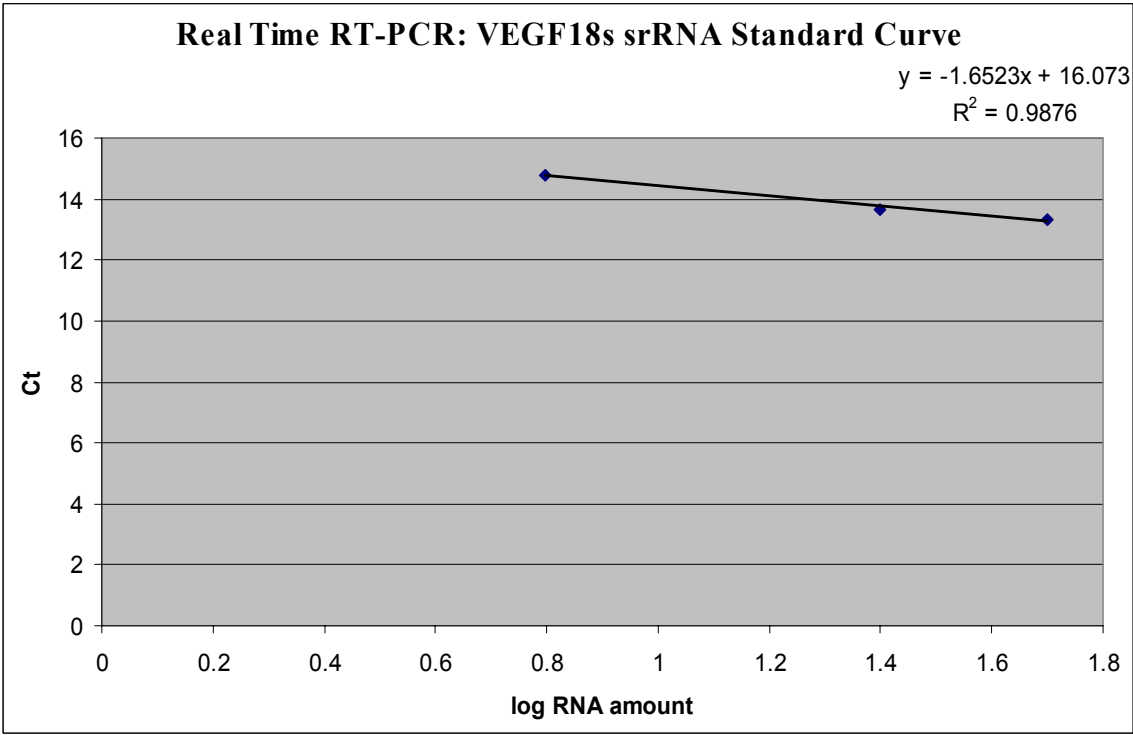
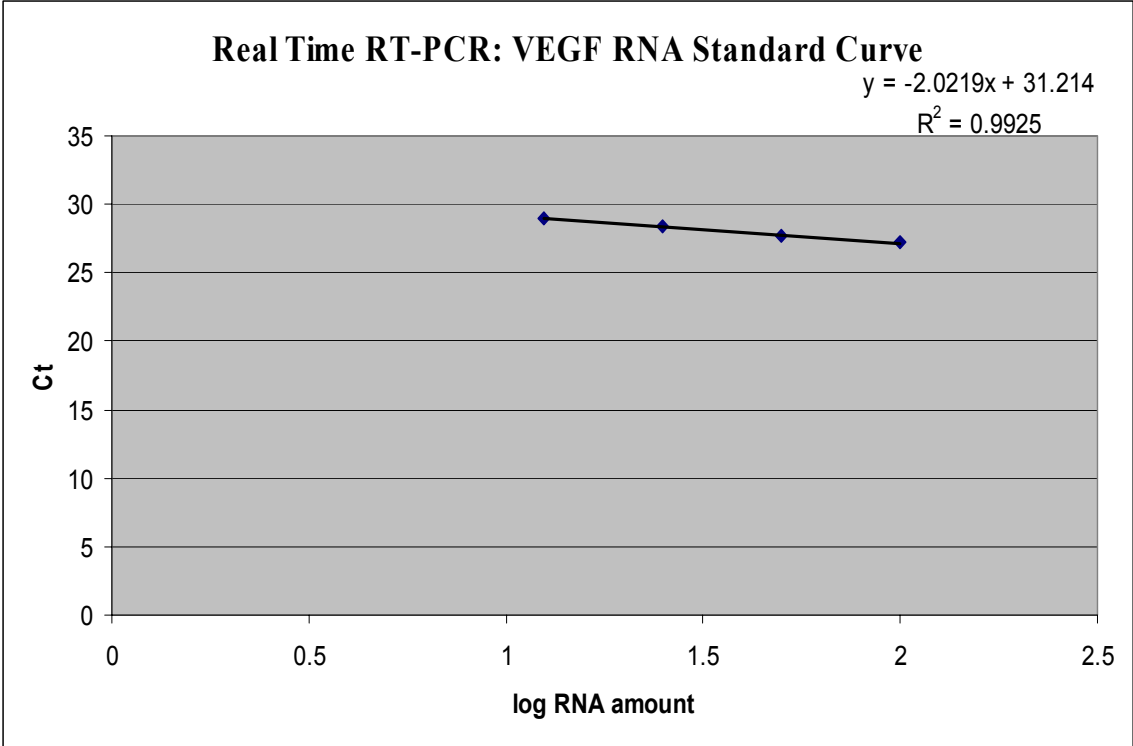
### **2.2.2 Alamar Blue Cytotoxicity Test**

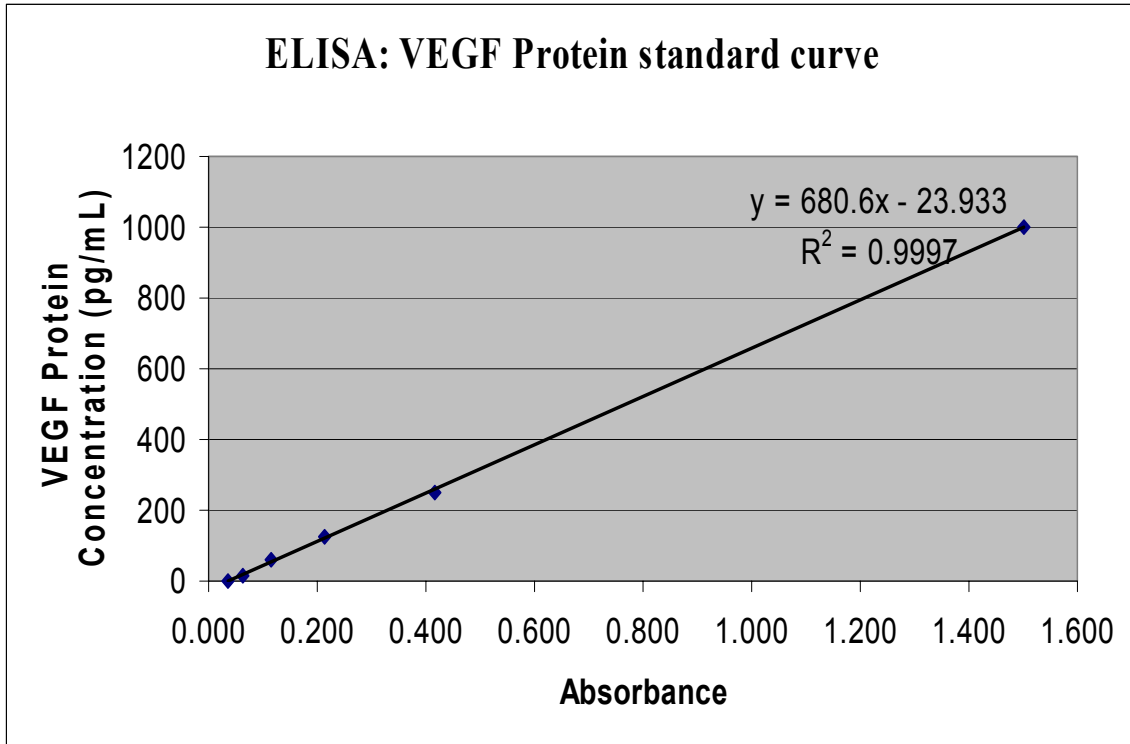
On Day 3, 12 mL of 10% Alamar Blue (Biosource) growth media was prepared by mixing 1.2 mL of alamar Blue with 10.8 mL of regular growth media. Then the growth media was removed from all groups except “media only” cells, and replaced with 300 uL Alamar Blue media in each well. Afterwards, the cells were allowed to incubate for 4 hours at 37 degrees C. At the end of the incubation, the supernatant was centrifuged to remove the suspended triamcinolone particles. The supernatant from each well was then placed into individual square vials and tested by a DU-640 spectrophotometer set at wavelengths 570 and 600 nm.

## **3. RESULTS AND DISCUSSION**

### **3.1 Testing the Effectiveness of Triamcinolone**

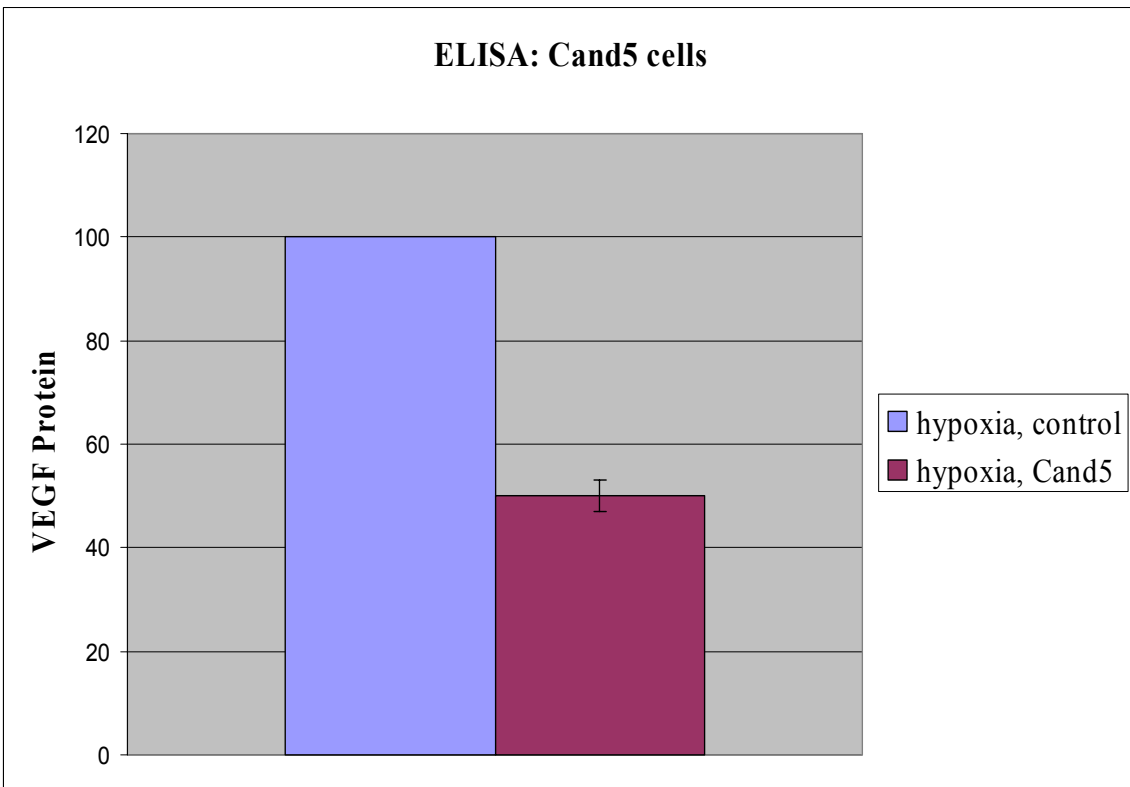
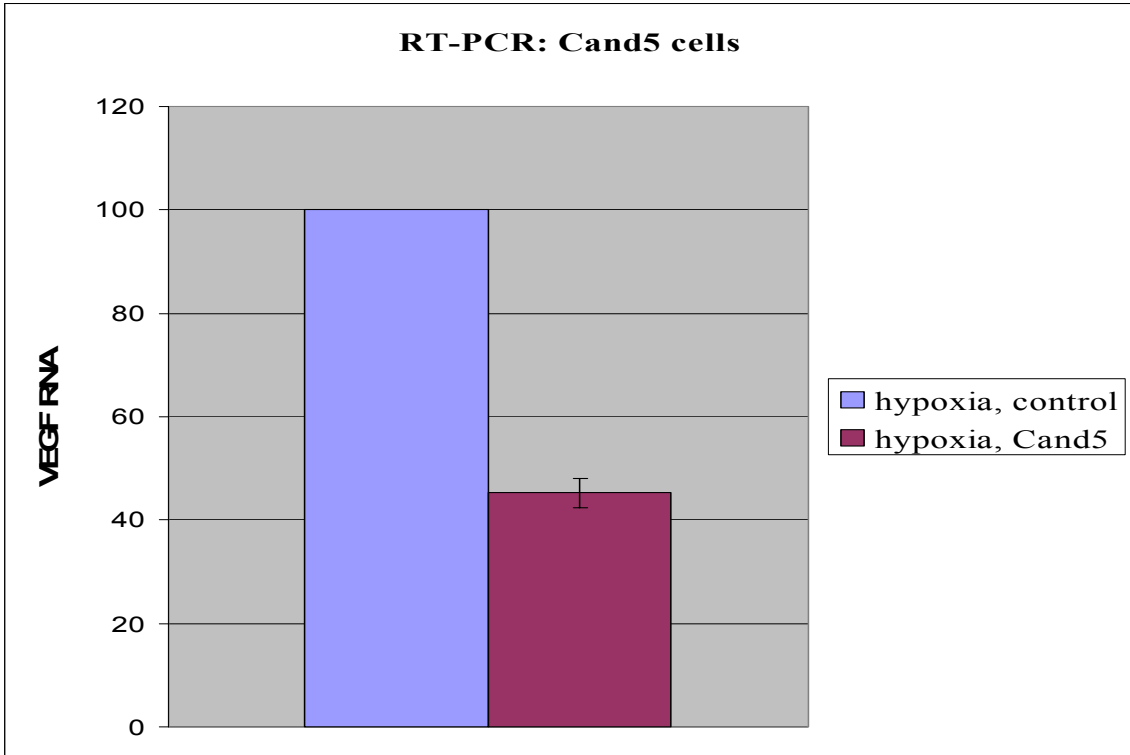
In order to accurately measure the VEGF RNA and protein levels expressed by the cells, the following standard curves were constructed.



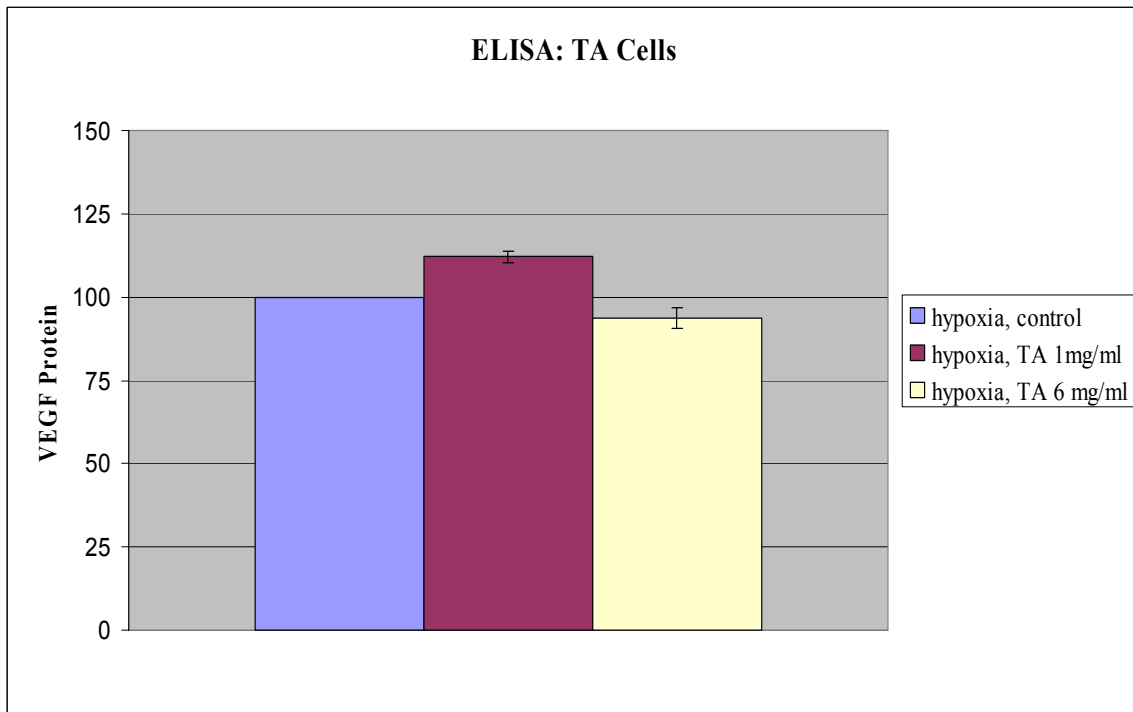
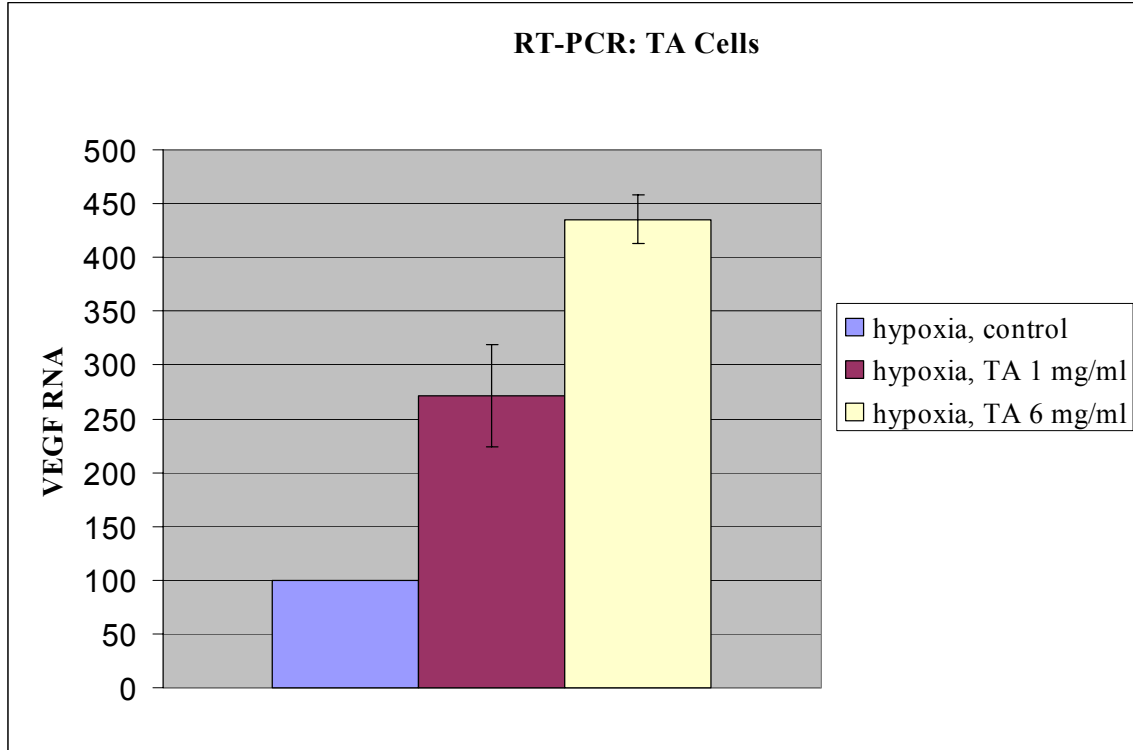


Determination of the concentrations of VEGF RNA and protein from the standard curves above allowed subsequent comparisons of the data obtained from the treatment and control groups.

The positive control, siRNA Candidate 5, decreased both VEGF RNA and protein levels. Both measurements had p-values less than 0.05 and were therefore statistically significant.



Initially, the TA treatments were expected to mimic Candidate 5's ability to lower VEGF protein and RNA levels. However, the cells treated with TA did not behave as expected. The TA increased VEGF RNA significantly, but had minimal effect on VEGF protein.



It was observed that TA did not reduce and might actually increase VEGF RNA 24 hours after treatment. Also, among the TA treated cells, the ELISA result did not mimic that of RT-PCR.

There are several possible explanations for this unexpected result. First, TA may be interfering with ELISA reading. As it has a solubility of 21 mg/L, a small amount of TA would still remain in solution after removal of suspended TA particles by centrifugation. Second, the triamcinolone may need more than 24 hours to affect the cellular RNA and protein expressions. Third, TA particles might settle toward the bottom of the wells, thus increasing the TA concentration that the cells are exposed to and consequently enhanced its cellular effects. Lastly, TA's cytotoxicity and its reaction to heat may affect the experimental results.

### 3.2 Preliminary Cytotoxicity Test

Suspecting that triamcinolone might be cytotoxic<sup>11</sup> and that this property might be responsible for the unexpected results noted in 3.1, a preliminary cytotoxicity test was performed on TA. Calculations were made using the formulas described by BioSource, the manufacturer of the Alamar Blue used.

The calculation of % Reduced is as follows when the samples are read at

$$\lambda_1 = 570 \text{ nm}$$

$$\lambda_2 = 600 \text{ nm}$$

$$\% \text{ Reduced} = \frac{(\epsilon_{\text{ox}} \lambda_2) (A \lambda_1) - (\epsilon_{\text{ox}} \lambda_1) (A \lambda_2)}{(\epsilon_{\text{red}} \lambda_1) (A' \lambda_2) - (\epsilon_{\text{red}} \lambda_2) (A' \lambda_1)} \times 100$$

Where:

$(\epsilon_{\text{red}} \lambda_1)$  = 155,677 (Molar extinction coefficient of reduced alamarBlue<sup>TM</sup> at 570 nm)

$(\epsilon_{\text{red}} \lambda_2)$  = 14,652 (Molar extinction coefficient of reduced alamarBlue<sup>TM</sup> at 600 nm)

$(\epsilon_{\text{ox}} \lambda_1)$  = 80,586 (Molar extinction coefficient of oxidized alamarBlue<sup>TM</sup> at 570 nm)

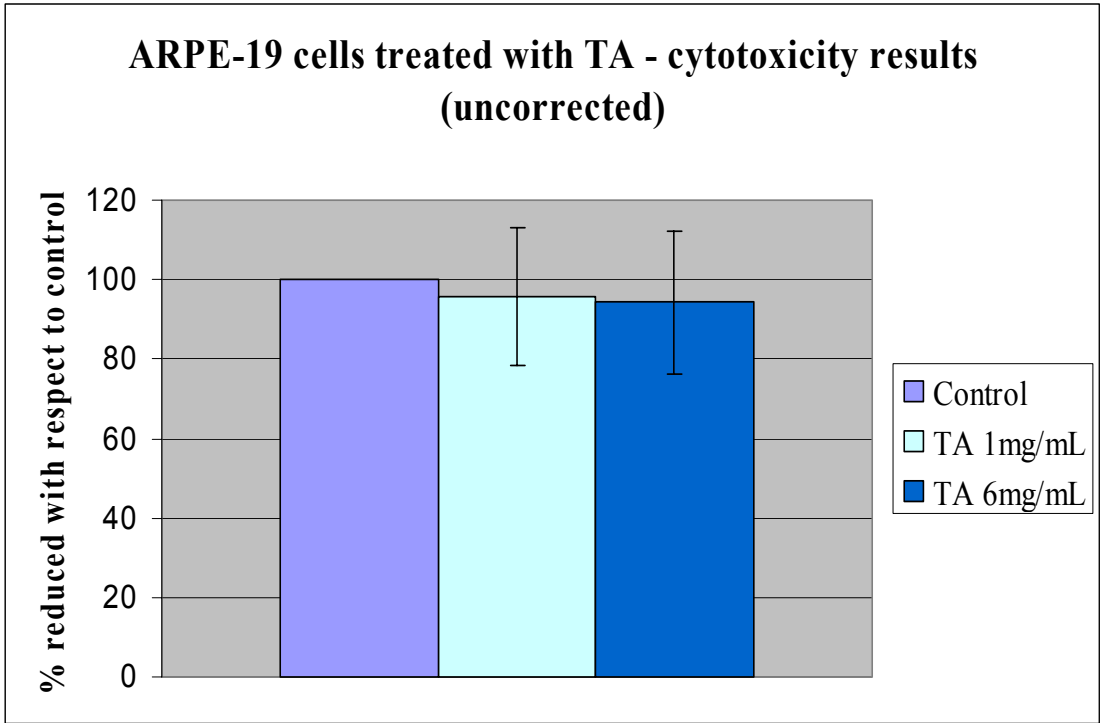
$(\epsilon_{\text{ox}} \lambda_2)$  = 117,216 (Molar extinction coefficient of oxidized alamarBlue<sup>TM</sup> at 600 nm)

$(A \lambda_1)$  = Absorbance of test wells at 570 nm

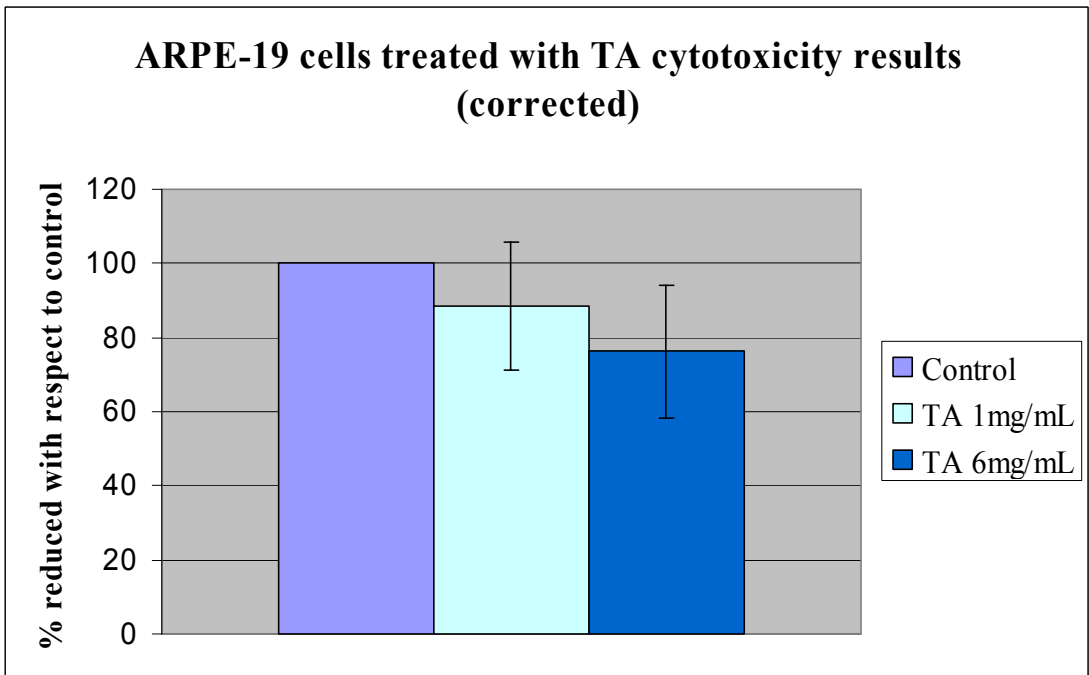
$(A \lambda_2)$  = Absorbance of test wells at 600 nm

$(A' \lambda_1)$  = Absorbance of negative control wells which contain medium plus alamarBlue<sup>TM</sup> but to which no cells have been added at 570 nm.

$(A' \lambda_2)$  = Absorbance of negative control wells which contain medium plus alamarBlue<sup>TM</sup> but to which no cells have been added at 600 nm.

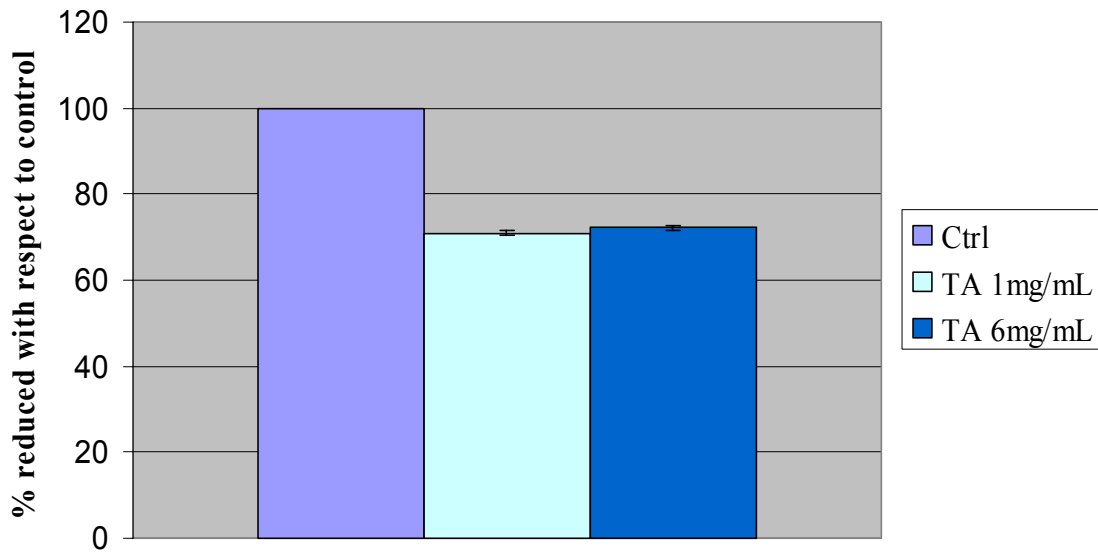


The TA cytotoxicity readings were then corrected using the cytotoxicity readings for the “TA and media only”.

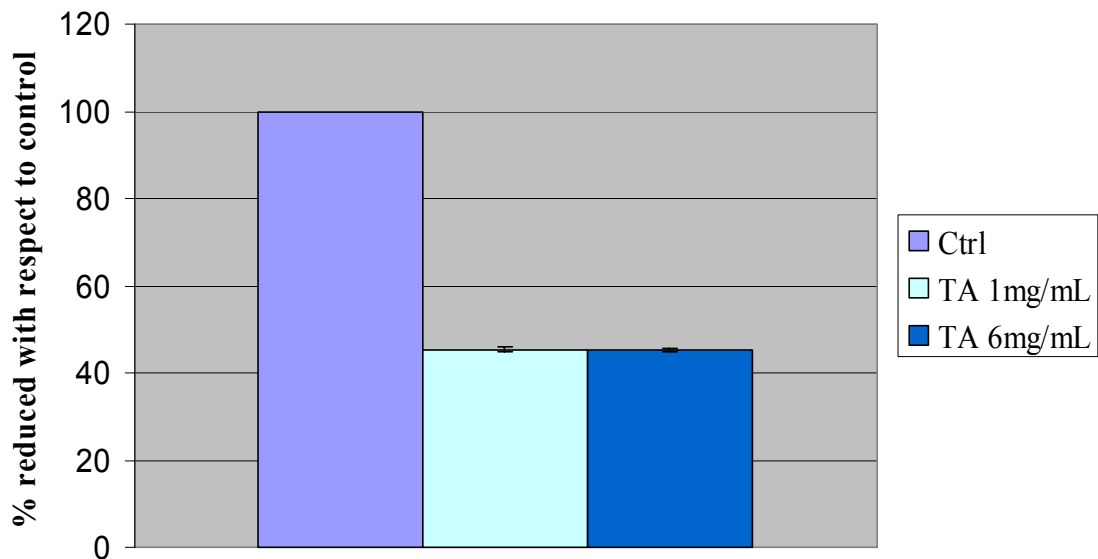


Due to the high variance in the data, the experiment was repeated to confirm the results.

### ARPE-19 cells treated with TA - cytotoxicity (uncorrected)



### ARPE-19 cells treated with TA - cytotoxicity (corrected)



The percent of Alamar Blue reduced by the TA treated cells was significantly smaller than the percent reduced by the control cells. Thus, TA was determined to be significantly cytotoxic.

#### **4. CONCLUSIONS**

The hypothesis that TA, at its clinical dose of 1 mg/mL, inhibits choroidal neovascularization by downregulating VEGF was refuted in this experiment. At 1 mg/mL, triamcinolone acetonide significantly increases VEGF RNA and protein levels.

Further investigation addressed the cytotoxicity of TA. Overall, at 1 mg/mL and 6 mg/mL doses, TA appears to be toxic. Additionally, such doses also correlate with a significant increase in VEGF level. This increase is likely a stress response to TA's cytotoxicity.

It was observed that TA at concentration of 6 mg/mL did not appear to kill more cells or increase VEGF more than TA at concentration of 1 mg/mL. This may be because all the intracellular receptors for TA are completely saturated at a TA concentration of 1 mg/mL. Therefore, higher concentrations of TA suspension could not further increase TA binding to its intracellular receptors, and thus, there were no further increase in VEGF expression nor enhancement of its cytotoxicity at concentrations higher than 1 mg/ml.

Intravitreal injection of triamcinolone acetonide has been successfully used clinically in the treatment of age-related macular degeneration, but its mechanism of action still remains unclear. However, these experiments have refuted the theory of attributing triamcinolone's clinical efficacy to possible reduction of VEGF expression.

#### **5. FUTURE WORK**

Further investigation is recommended to address the effects of TA over a wider range of doses, ranging from .01 to 6 mg/mL. Also, it would be helpful to determine if there is any correlation of VEGF levels to TA's dose-toxicity curve. Additionally, it would be constructive to determine whether or not there is still a significant increase in VEGF level after normalizing it to total protein level, cell count, and total RNA level.

This project is part of a larger, long-term initiative to test various treatments for age-related macular degeneration and other similar neovascular retinopathies. Other alternatives have been proposed, such as the transfection of short hairpin RNA. Each option will be compared and the one which proves itself the most effective will be chosen for clinical testing. One of the approaches is to apply sensor technology to non-invasively measure the clinical effects of various treatment modalities, thus facilitating the search for the optimal therapy and the monitoring of the patients' clinical response to treatment. Examples of such potential sensor technology include surface measurement of electrical activities in the visual cortex during the treatment and convalescent phases.

## 6. ACKNOWLEDGEMENTS

I would like to take this opportunity to thank my advisors, Elaine Wu and Professor Michael Tolentino, for their guidance, encouragement, support, and supervision. I extend a special note of thanks to Elaine for introducing me to sensor technologies critical in this project, including the ABI Prism 7000 Sequence Detection System, Wallac Victor 1420 Multilabel Counter, and PTC-400 Thermocycler. I would also like to thank the National Science Foundation for their support through the Research Experience for Undergraduates Grant that made the Summer Undergraduate Fellowship in Sensor Technologies program possible.

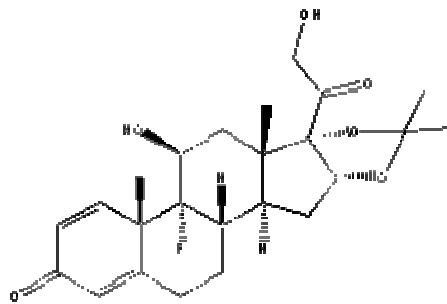
## 7. REFERENCENCES

1. Al-Haddad CE, Jurdi FA, Bashshur ZF. Intravitreal triamcinolone acetonide for the management of diabetic papillopathy. *Am J Ophthalmol.* 2004 Jun;137(6):1151-3.
2. Canakis C, Livir-Rallatos C, Zafirakis P, Livir-Rallatos G. Acute endophthalmitis following intravitreal triamcinolone acetonide injection. *Am J Ophthalmol.* 2004 Jun;137(6):1158-9.
3. Chen SD, Mohammed Q, Bowling B, Patel CK. Vitreous wick syndrome--a potential cause of endophthalmitis after intravitreal injection of triamcinolone through the pars plana. *Am J Ophthalmol.* 2004 Jun;137(6):1159-60.
4. Degenring RF, Jonas JB. Serum levels of triamcinolone acetonide after intravitreal injection. *Am J Ophthalmol.* 2004 Jun;137(6):1142-3.
5. Jonas JB, Degenring RF, Kreissig I, Friedemann T, Akkoyun I. Exudative age-related macular degeneration treated by intravitreal triamcinolone acetonide. A prospective comparative nonrandomized study. *Eye.* 2004 Jun 25.
6. Klais CM, Spaide RF. Intravitreal triamcinolone acetonide injection in ocular ischemic syndrome. *Retina.* 2004 Jun;24(3):459-61.
7. Peyman GA, Moshfeghi DM. Intravitreal triamcinolone acetonide. *Retina.* 2004 Jun;24(3):488-90.
8. Sallum JM, Farah ME, Saraiva VS. Treatment of cystoid macular edema related to retinitis pigmentosa with intravitreal triamcinolone acetonide: case report. *Adv Exp Med Biol.* 2003;533:79-81.

9. Yuen HK, Chan CK, Lam D. Acute endophthalmitis following intravitreal triamcinolone acetonide injection. *Am J Ophthalmol*. 2004 Jun;137(6):1166.
10. Yeung CK, Chan KP, Chan CK, Pang CP, Lam DS. Cytotoxicity of triamcinolone on cultured human retinal pigment epithelial cells: comparison with dexamethasone and hydrocortisone. *Jpn J Ophthalmol*. 2004 May-Jun;48(3):236-42.
11. Yeung CK, Chan KP, Chiang SW, Pang CP, Lam DS. The toxic and stress responses of cultured human retinal pigment epithelium (ARPE19) and human glial cells (SVG) in the presence of triamcinolone. *Invest Ophthalmol Vis Sci*. 2003 Dec;44(12):5293-300.

## 8. APPENDICES

### APPENDIX 1: Triamcinolone Acetonide



### APPENDIX 2: Sensors

1. ABI Prism 7000 Sequence Detection System
2. Wallac Victor 1420 Multilabel Counter
3. PTC-400 Thermocycler

*University of Pennsylvania*  
Center for Sensor Technologies

SUNFEST

NSF REU Program  
Summer 2004

**INTEGRATED ELECTROCHEMICAL GATING OF  
CARBON NANOTUBE FETs FOR BIOSENSING  
APPLICATIONS**

NSF Summer Undergraduate Fellowship in Sensor Technologies  
Emmanuel U. Onyegam, Electrical Engineering  
University of Texas at Dallas

Advisor: Dr. A.T. Charlie Johnson, Dept. of Physics and Astronomy  
University of Pennsylvania

**ABSTRACT**

Carbon nanotubes have emerged as the leading candidate of electronic materials used for future nanoscale chemical and molecular sensors. Recently, nanotube field effect transistors (CNFETs) have been exploited as biodetectors of the thyroid hormone, triiodothyronine (T3). Although significant progress has been towards the development of actual nanotube based sensor devices, the next challenge is to integrate the devices into a single chip. Numerous gate configurations to CNFETs have been proposed, but few have been shown to be effective, and even fewer can be integrated to a chip. An electrolytic “tip” gate design has been shown to be more effective than the conventional backgate geometry. The drawback to the “tip” gate geometry lies in the fact that an external electrode is required to gate the devices. In this paper, a novel integrated gate design is proposed. Lithographically patterned electrodes on the chip surface are fabricated to effectively gate CNFET devices.

## **TABLE OF CONTENTS**

<b>1. Introduction.....</b>	<b>3</b>
<b>2. Nanotube FETs.....</b>	<b>4</b>
<b>3. Nanotube Sensors.....</b>	<b>5</b>
<b>4. Gating Techniques.....</b>	<b>6</b>
<b>5. Device Fabrication.....</b>	<b>8</b>
<b>6. Results and Discussions.....</b>	<b>9</b>
<b>7. Conclusions and Recommendations.....</b>	<b>10</b>
<b>8. Acknowledgements.....</b>	<b>11</b>
<b>9. References.....</b>	<b>11</b>

## 1. INTRODUCTION

Carbon nanotubes (CNTs) are one-dimensional nanoscale structures with unique electrical, chemical, and mechanical properties. There are two kinds of CNTs: single-walled nanotubes (SWNTs) and multi-walled nanotubes (MWNTs). Although MWNTs were discovered first (in 1991), SWNTs have been studied more because of their simpler and more stable physical structure. The structure of a SWNT is equivalent to a sheet of graphene rolled up to form a cylinder<sup>1</sup>. Depending on their chirality, SWNTs can exhibit either semiconducting or metallic characteristics; this is perhaps the most important reason scientists and engineers are interested in them. Field-effect transistors (FETs) based on semiconducting SWNT for example, have been found to have carrier mobilities and transconductances that far exceed that of silicon<sup>2</sup>, the best known semiconducting material and the active element in modern electronic devices. On the other hand, metallic nanotubes have been shown to have conductivities that rival some of the finest metals such as copper.

With the semiconductor industry facing increasing challenges in scaling silicon devices to smaller dimensions, carbon nanotubes are certainly one of the most promising candidates for future nanoelectronics. The remarkable properties of nanotubes have led to their being exploited as channels in FETs, field emission display sources, scanning probes, and memory devices. Furthermore, because of their extreme sensitivity to chemicals on their surface, nanotube based chemical and molecular sensors have also been reported<sup>1-3, 5-8</sup>. While significant progress has been made towards the realization of nanotube based sensors, one of the challenges faced lies in the integration of the sensing components into single devices. Here, we present a novel integrated electrolyte gating of CNFETs.

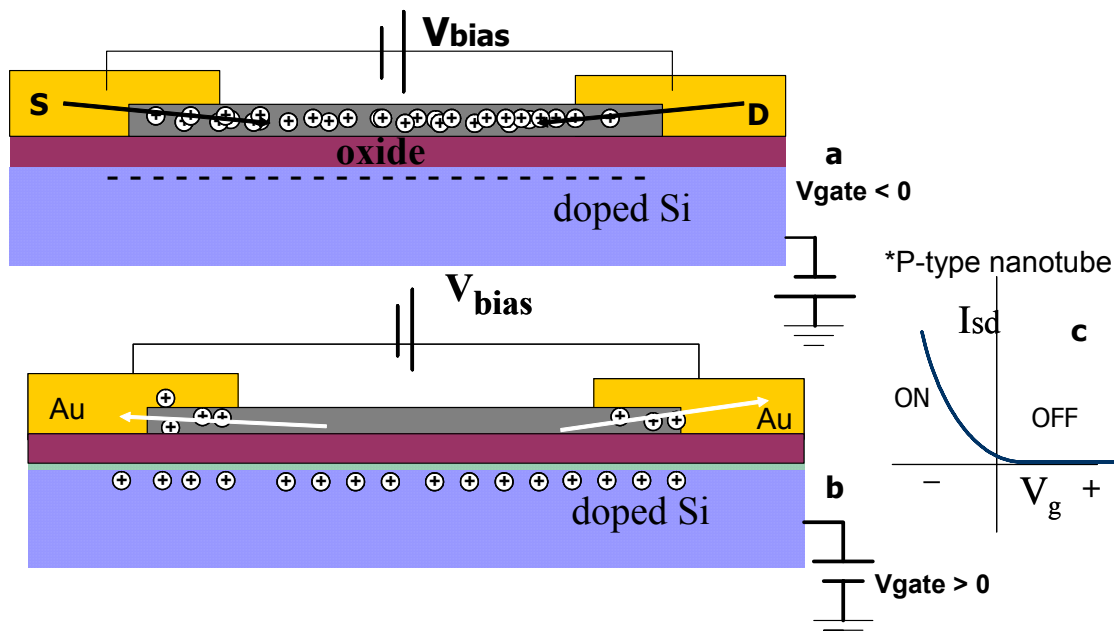


**Figure 1.** Schematic and I-V characteristics of a nanotube transistor. (a) For negative gate voltages the device turns ON due the accumulation of excess positive charge carriers. (b) Positive gate voltage result in the depletion of charge carriers into the metal contacts, thus turning OFF the device. (c) I-V curve showing the response of the device to positive and negative gate voltages

## 2. NANOTUBE FETS

Single walled nanotube transistors are electronic devices based on a semiconducting nanoscale molecule. Figure 1 shows the structure of a carbon nanotube transistor along with its I-V characteristics. Nanotube transistors consist of a semiconducting carbon nanotube typically 1 to 2 nm in diameter bridging a gap of about 1  $\mu\text{m}$ , formed by two closely separated metal electrodes which are fabricated on a Si substrate. The source-drain electrodes are usually patterned via electron-beam (e-beam) lithography. Gold electrodes commonly serve as the source-drain leads. Applying a voltage to the silicon substrate turns on and off the flow of current across the nanotube-channel by controlling the movement of charge carriers onto it. A bias voltage applied to the source-drain electrodes is used to establish the direction of current flow along the tube.

At zero at gate voltage, there is little current flow across the nanotube. The source of the charge carriers is not clear; the carriers may be intrinsic to the nanotube (due to doping) or could come the source-drain electrodes due to work function differences. Application of negative gate voltage results in the accumulation of positive charged holes (from the electrodes) across the nanotube, which are then free to conduct current (figure 1a). The characteristic of a CNFET is very similar to that of a Si-channeled MOSFET. As shown in the device I-V characteristics of figure 1c, the current across the nanotube increases strongly with a more negative gate voltage, and decreases for positive voltages.

This is a typical behavior of a p-type semiconducting SWNT, one with holes as majority carriers. Typically, nanotubes are grown to be p-type; research suggests that this results from oxygen doping<sup>3</sup> during growth. There have been reports of n-type characteristics achieved via alkali metal n-dopants such as potassium or by polymer doping<sup>3</sup>. Furthermore, some devices exhibit both p-type and n-type behavior, referred to as ambipolar. Ambipolar characteristics are generally due to the Schottky barriers at the metal-nanotube interface.

The interest in nanotube-FETs lies in their potential to perform better than conventional silicon based FETs. Parameters such as *mobility* and *transconductance* dictate the performance of a FET. Mobility is a measure of the ease with which electrons and holes can flow through a material<sup>4</sup>. Hole mobilities in the range of 2,000 to 4000 cm<sup>2</sup>/V-s for CNFETs have been reported<sup>5</sup> compared with 500 cm<sup>2</sup>/V-s for Si MOSFETs. Furthermore, CNFETs have also been shown to have significantly higher transconductance, the measure of current carrying capability of FETs. High transconductance implies that the transistors can operate faster. Along with their small size and versatility as chemical and molecular sensors, nanotubes certainly have several advantages over silicon for future nanoelectronics.

### 3. NANOTUBE SENSORS

The electrical resistances of semiconducting SWNTs change dramatically when exposed to chemicals. This property makes them useful for chemical and molecular sensing. Sensing is achieved by exposing nanotube-FET devices to chemicals and monitoring the change in conductance. Nanotube based detection of various gases and chemicals has been reported by several groups. J. Kong et al reported<sup>6</sup> the detection of gases such as NH<sub>3</sub> and NO<sub>2</sub>, while the detection of protein-receptor interactions such as streptavidin-biotin binding<sup>7</sup> was reported by A. Star et al.

The possible electrical interaction between DNA and the thyroid hormone, triiodothyronine (T3), is of interest to chemists and biologists. T3 is formed by two

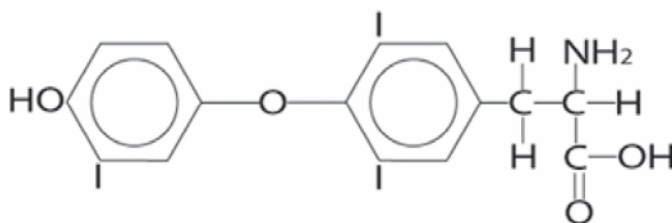


**Figure 2.** Structure of the T3 molecule

benzene rings decorated with three iodine atoms, as shown in figure 2. The role of the iodine atoms is not well understood. One theory is that iodine is essential to the *electrostatic* interaction between T3 and DNA<sup>1</sup>. Because the electronic properties of DNA are not well understood, carbon nanotubes provide a possible model for DNA as 1-dimensional conductors<sup>1</sup>, assisting in understanding the electronic properties of T3.

Figure 3 shows the  $I-V_g$  characteristics of a CNFET device before and after exposure to T3. Before exposure to T3 (black curve), the device was characterized by placing a drop of a NaOH solvent on the device and taking  $\pm 0.8V$  electrolyte gate sweeps (refer to Section 4, “Gating Techniques”). Afterwards, the devices were exposed to a 0.1mM T3 solution dissolved with 0.1 mM NaOH in water; further gate sweeps were taken at a constant bias voltage of 10mV. As shown in figure 3, the device exhibits a shift in conductance towards negative gate voltages in response to the presence of T3. The device characteristics suggest that nanotube is p-type. Electron donation from T3 effectively shifts the valence band of the nanotube away from the Fermi level, which results in hole depletion, thus the left shift in conductance. Experimentation suggests that the amount of shift strongly depends on the concentration of T3, with stronger shifts at higher concentrations due to greater T3-nanotube charge transfer. Biodetection of T3 is achieved even at concentrations as little as 1uM.

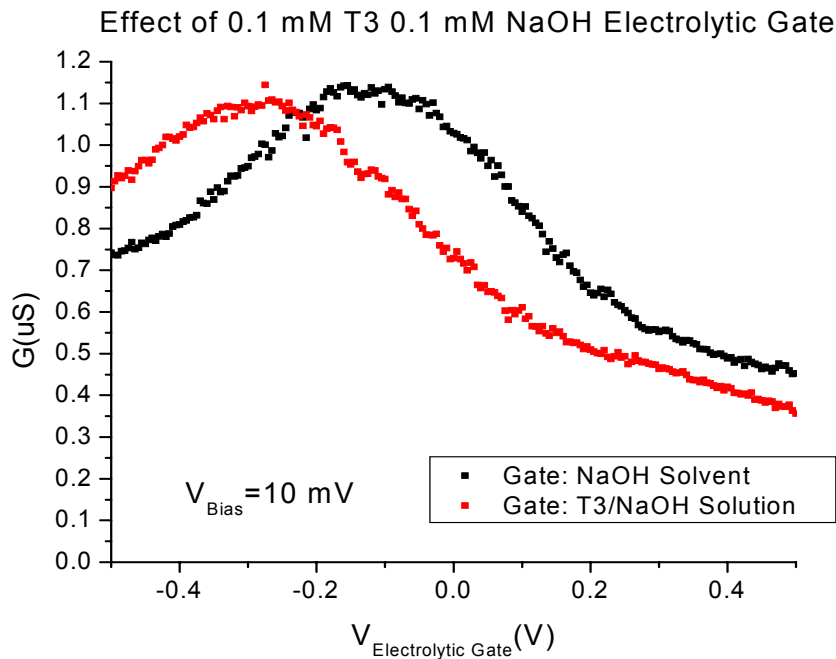


**Figure 3.** Shift in conductance vs. gate voltage after exposure to T3. The black curve represents the initial device characteristics prior to T3 exposure. The device characteristics after exposure to T3 is shown in red.

#### 4. GATING TECHNIQUES

The mechanism of gating nanotube FETs for biosensing is of interest for optimal device performance. The most widely used gating techniques are the *backgate* (or *bottom-gate*) and *tip-electrolytic gate*. The *backgate* is the most common and oldest method of gating FET devices. In this configuration, devices are gated by applying voltage to the supporting silicon (Si) substrate (Figure 4a). An oxide material usually more than 100 nm thick serves as the gate dielectric. One disadvantage of the backgate geometry is that it requires all devices on the substrate to share one gate, so the devices

cannot be addressed individually. Additionally, due to the thickness of the gate dielectric, the voltage required to turn on the devices is very high.

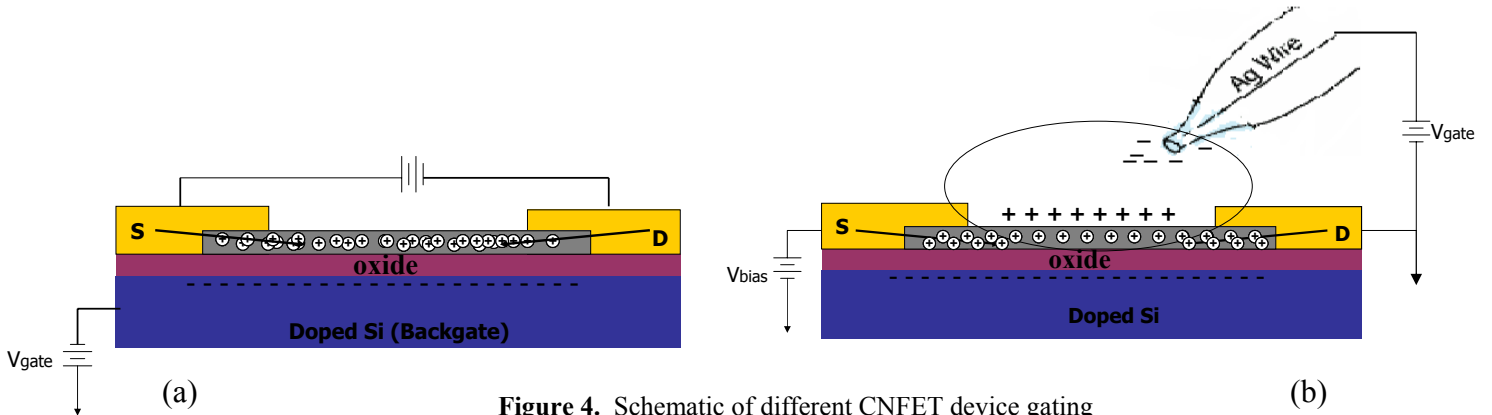


**Figure 4.** Schematic of different CNFET device gating geometries. (a) Backgate geometry. (b) Electrolyte “tip” gate geometry.

The tip-electrolyte gating technique (figure 4b) addresses these weaknesses. The idea is that by placing the gate as close as possible to the nanotube, ultimately into intimate contact, the device transconductance is dramatically increased<sup>8</sup>. The setup is similar to that described by Rosenblatt et al. A micropipette is used to place a micron-sized electrolyte droplet over the nanotube device. A voltage applied to a silver wire in the pipette is used to establish an electrochemical potential in the electrolyte relative to the device. The electrolyte functions as a well-insulated liquid gate and exhibits a strong capacitive coupling between the gate and the tube. As shown in Figure 5, the end result is a much lower operating voltage and steeper switching behavior. The drawback to the tip-gating regime however lies in the fact that an external electrode is used to gate the devices, making it difficult to integrate into chips.

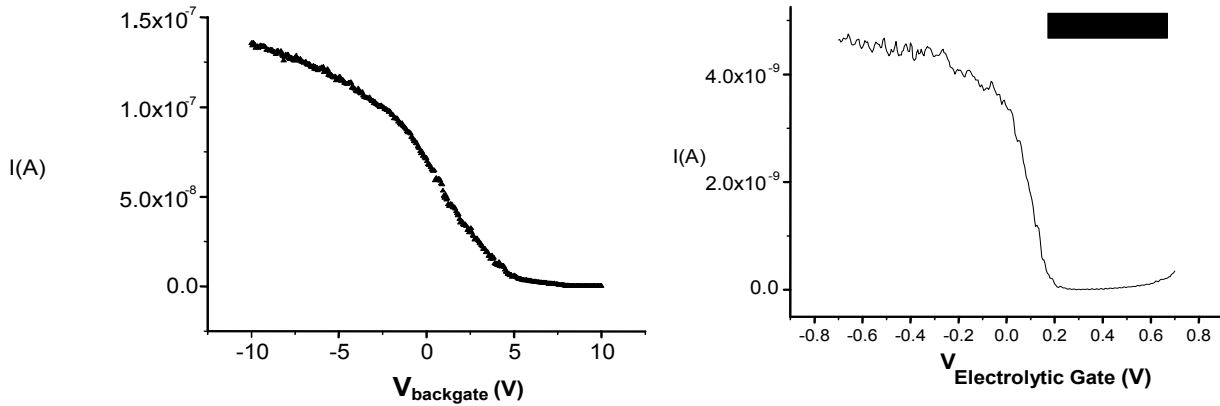


**Figure 5.** Response of a semiconducting SWNT to: (Left) Backgate configuration. (Right) Electrolyte “tip” gate configuration.  $V_{bias} = 10\text{mV}$ .

In this report, we present a novel integrated gate geometry. We exploit the strong gate coupling effect of the tip-electrolyte configuration and fabricate electrodes on the chip surface to gate the CNFET devices. According to our results, the new design effectively gates the CNFETs and its efficiency is comparable to the results achieved with the externally applied tip-gate setup. Figure 6 shows the structure of the proposed integrated gate CNFET.

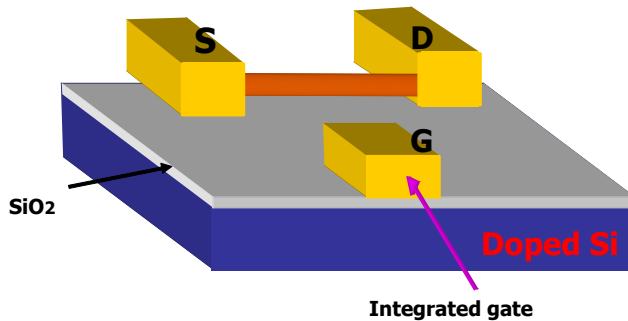


**Figure 6.** Schematic of an integrated gate CNFET

## 5. DEVICE FABRICATION

Our nanotubes were synthesized via chemical vapor deposition (CVD) following an approach similar to that described by Rojas et al. Fifteen drops of a 100 mg/L iron nitrate,  $\text{Fe}(\text{NO}_3)_3 \cdot 9(\text{H}_2\text{O})$ , in isopropanol were spun onto a degenerately doped Si substrate layered with 400 nm of  $\text{SiO}_2$ . The substrates were then heated to  $900^\circ\text{C}$  in an Ar atmosphere and growth was carried out for 15 minutes under 3500 sccm  $\text{CH}_4$  and 450 sccm  $\text{H}_2$ . Subsequently, several hundred source, drain, and gate leads were randomly

patterned on the substrate using electron beam (e-beam) lithography. The source-drain separation is approximately  $1\ \mu\text{m}$ , while the gate is positioned  $10\ \mu\text{m}$  from the center of the source-drain leads. Finally,  $10\ \text{nm}$  of Cr and  $30\ \text{nm}$  of Au were thermally evaporated onto the patterns. Chromium serves as an adhesive of gold to the  $\text{SiO}_2$  substrate.

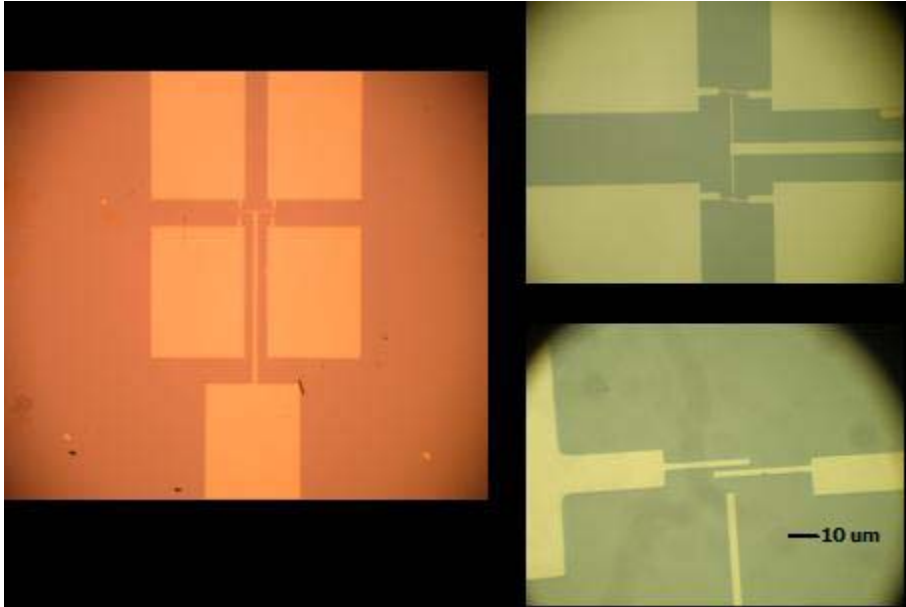


**Figure 7.** Optical images of an integrated gate configuration. Source-drain gap =  $1\ \mu\text{m}$ , gate distance =  $10\ \mu\text{m}$  from source-drain leads.

## 6. RESULTS AND DISCUSSION

Figure 7 shows photographs of the completed device structure. The devices were fabricated such that two pairs of samples shared a single gate to minimize the circuitry involved. Typically, we were able to attain 10-15 circuits with one s-SWNT for every 150 pairs of source-drain electrodes. Approximately 30 leads are bridged by metallic SWNTs while few leads are contacted by multiple or bundled SWNTs. Figure 8 shows the  $I-V_g$  curves for the two electrochemical gating methods, the previous external “tip” gate technique and the novel integrated gate geometry. A NaOH in DI-water solution was the electrolyte of choice. The new integrated electrode effectively gates our CNFETs, with the two methods exhibiting similar switching characteristics. The devices proved to be ambipolar, with strong conductance in either direction. Although a comparable gate response to the initial external gate configuration was achieved with the new integrated gate CNFET, there is a noticeable difference in the current drives. This is possibly due to the much thicker diameter Ag wire used for the external gate.

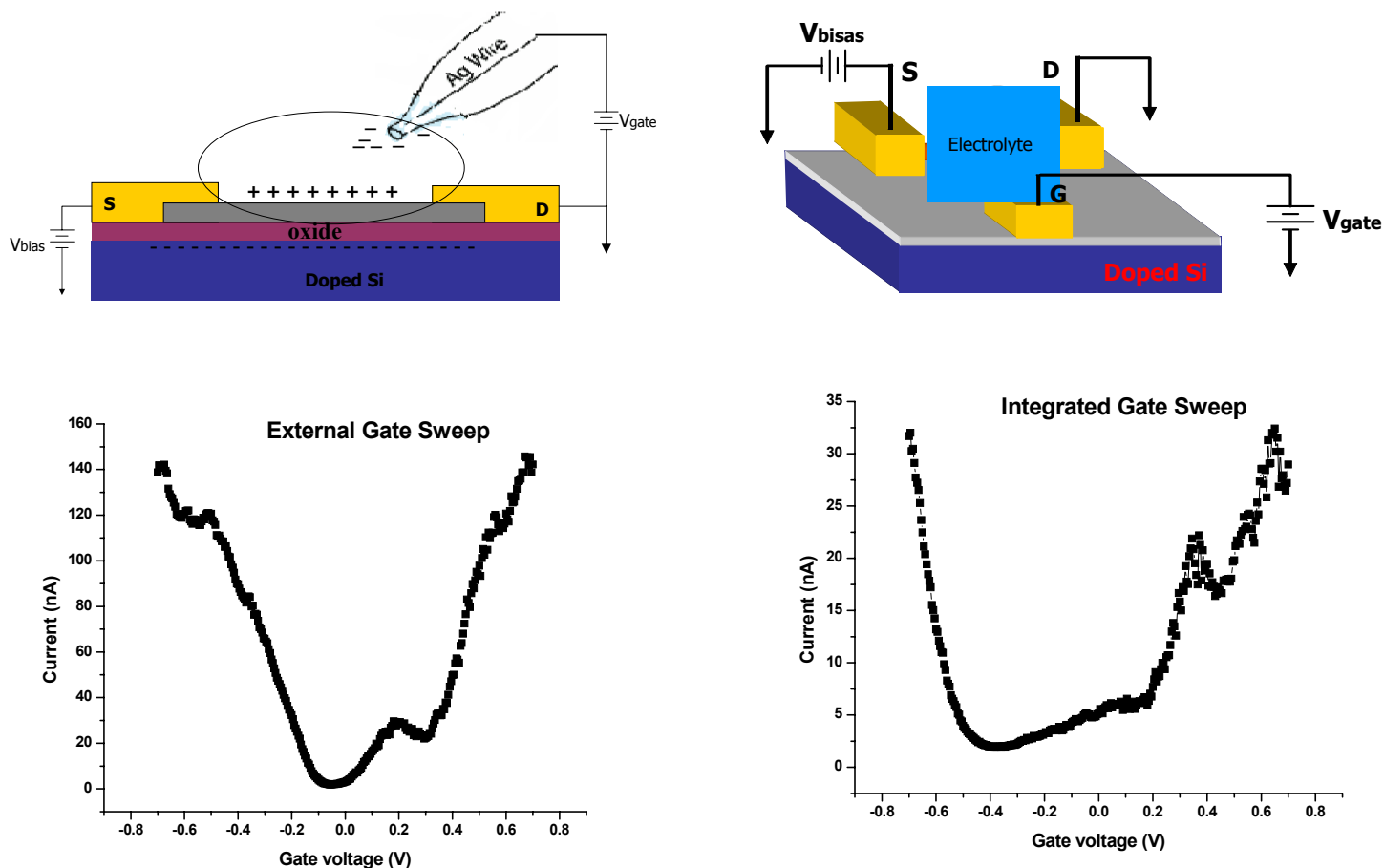


**Figure 8.** Response of a semiconducting SWNT to (Left) Backgate configuration (Right) Electrolyte “tip” gate configuration.  $V_{\text{bias}} = 10\text{mV}$ .

## 7. CONCLUSIONS AND RECOMMENDATIONS

The results presented show that the biodetection of the thyroid hormone, T3, is possible via electrochemical gated CNFETs. Electrochemical gating of CNFETs has been shown to have stronger gating effects than the conventional backgate geometry. However, the challenge of integrating device components into single chips has led to our fabrication of a novel device gating structure. Lithographically patterned on-chip gate electrodes are fabricated.

Our results show that the new integrated gate structure act as effective gates to CNFET devices. Comparison of the gate response of the new structure to the previous externally gated configuration proves that similar switching behaviors at low device operating voltages can be attained. Though it is not much of a concern, the current drive attained with the integrated gate is less than that for the external gate. One solution to this might be to increase the thickness of the integrated Au gate electrodes. Nevertheless,

our new integrated gate structure offers advantages such as, individual addressability of devices, strong gate capacitive coupling and low device operating voltage.

Besides the advantage of integration offered by our new gate structure, a project proposal (not yet underway) is the design of a microfluidic array of channels whereby fluidic paths are fabricated to direct an automatic flow of electrolyte solution to various samples such that several devices can be tested simultaneously. This task would be almost impossible with the previous gating technique since multiple external gates would be required. The microfluidic arrangement will prove especially valuable to our current T3 experiments; instead of having to apply drops individually to the samples, a single drop will be applied which then can be directed to different samples. Hence, multiple devices can be tested at a fraction of the normal time.

## 8. ACKNOWLEDGEMENTS

I would like to thank my advisor, Dr. A.T. Charlie Johnson from the Department of Physics and Astronomy, for his assistance, expertise, and kindness. I also would like to thank Mike Stern, Deirdre Smith, and everyone from Professor Johnson's Group for their contributions to this project. I am very grateful of this wonderful opportunity given to me by the SUNFEST program. Thanks to Dr. Van der Spiegel, the SUNFEST staff, and my fellow SUNFEST students for all the great memories. Thanks to my generous sister, "Chika" Onyegam for supplying me with food (a difficult task) and her patience. Finally, thanks to my professor, Dr. Lawrence Overzet from the University of Texas at Dallas for his inspirations. This research was funded by NSF through the SUNFEST REU program.

## 9. REFERENCES

- 
- <sup>1</sup> E. Rojas, Carbon nanotube-based biodetection of triiodothyranine, *SUNFEST Report 2003*.
  - <sup>2</sup> P.L. McEuen, J.Y. Park, Electron Transport in Single-Walled Carbon Nanotubes, *MRS Bulletin*, **April 2004**.
  - <sup>3</sup> H. Dai, Carbon Nanotubes: Synthesis, Integration, and Properties, *Accounts of Chemical Research*, **2002**, Vol. 35, NO. 12.
  - <sup>4</sup> B.G. Streetman, S. Banerjee, *Solid State Devices*, Upper Saddle River, NJ: Prentice Hall 2000
  - <sup>5</sup> S. Rosenblatt, Y. Yaish, J. Park, J. Gore, V. Sazonova, P.L. McEuen, High Performance Electrolyte Gated Carbon Nanotube Transistors, *Nano Letters*, **2002**, Vol. 2, No.8, 869-872.
  - <sup>6</sup> J. Kong, N.R. Franklin, C. Zhou, M.G. Chapline, S. Peng, K. Cho, H. Dai, Nanotube Molecular Wires as Chemical Sensors, *Science*, **Jan. 28, 2000**, Vol. 287.
  - <sup>7</sup> A. Star, J.P. Gabriel, K. Bradley, G. Gruner, Electronic detection of specific protein binding using nanotube FET devices, *Nano Lett.*, *2003*, Vol. 3, No. 4.
  - <sup>8</sup> M. Kruger, M.R. Buitelaar, T. Nussbaumer, C. Schonenberger, Electrochemical carbon nanotube field-effect transistor, *Appl. Phys. Lett.*, **2001**, Vol. 78, No.9.

*University of Pennsylvania*  
Center for Sensor Technologies

SUNFEST

NSF REU Program  
Summer 2004

**The Hand-Held Breast Cancer Detector: A 2-D Phased Array System**

NSF Summer Undergraduate Fellowship in Sensor Technologies  
J. Miguel Ortigosa (Electrical Engineering) – Florida Atlantic University  
Advisor: Dr. Britton Chance

**ABSTRACT**

Presently, there are well known non-invasive methods in the detection of breast cancers. The most important include Magnetic resonance, X-ray, and Ultra-sound mammograms. However, due to their high cost, inconvenience, and time considerations, alternative methods are emerging. The Hand-Held Breast Cancer Detector (HHBCD) is designed to be an inexpensive and convenient way to replace other mammograms for some circumstances. It can detect small size tumors (1mm) up to 1 cm into the skin. The goal of this project is to expand the detection range to 3 cm. The device is based on the interference of two paired anti-phase near-infrared light (NIR) sources, a Photomultiplier tube detector (PMT) that detects a portion of this light, and a 2-D phased array method that discerns inequalities in the breast tissue. Most of the efforts put into the device were dedicated to improved signal interpretation, a more effective light source driver, and a shut-off protection system. The discussed individual parts were built but time did not permit them to be integrated. Successful completion of the device could prove useful for quick tumor detection and as a localization tool.

## TABLE OF CONTENTS

1. Introduction.....	3
2. The Hand-Held Breast Cancer Detector (HHBCD).....	4
2.1 Device Description.....	4
2.1.1 Navigation Probe and 2-D Phased Array.....	4
2.1.2 Computer Read-out.....	7
2.2 Device Goals.....	8
2.2.1 Objective.....	8
2.2.2 Future Implications.....	8
3. Device Assessment and Results.....	9
3.1 Full System Test and Results.....	9
3.2 LED Driver Test and Results.....	11
3.3 Signal Interpretation Test and Results.....	12
4. Determinations for Improvement.....	13
5. Redesigning LED Driver Circuit.....	14
6. Completed Upgrade: Voltage Shut-off Protection System.....	15
7. Future Work.....	17
8. Acknowledgments.....	18
9. References.....	19

## INTRODUCTION

Breast cancer is the most commonly diagnosed cancer among women in the United States and worldwide. In 2002, approximately 40,000 women died from the disease in the U.S. alone [1]. Many of these deaths can be attributed to the late detection of cancerous breast tumors; advanced stage tumors much harder to treat. Early detection through mammography and clinical breast exams is essential for effective breast cancer screening. For women between the ages of 50-69, regular mammograms can reduce the chance of death from breast cancer by approximately 30% [1]. Early detection of breast cancer greatly improves treatment options, the chances for successful treatment, and survival [2]. As a result, finely tuned detection devices have been developed to effectively expose very small tumors.

Breast cancer detection devices are powerful weapons in combating breast cancer casualties. Of the many non-invasive devices on the market today, the most important and commonly used are X-rays, magnetic resonance imaging (MRI), and ultrasound (US) mammograms. These devices can uncover tumors that may be too small to feel. While they have been generally reliable, their pitfalls are too great to ignore. Their shortcomings include inconvenience, high cost, and long inspection time. In the case of X-rays, inconvenience comes in the form of painful examination techniques and radiation exposure. For MRI and US, their high cost makes them inaccessible to the masses. Consequently, many women who see no palpable change in their breasts may opt not to get a check up. A new method of detection that can eliminate the drawbacks in current mammograms would bring the benefits of early breast cancer detection to everyone.

The Hand-Held Breast Cancer Detector (HHBCD) is a device that uses Near Infrared (NIR) Light to reveal and localize cancerous tumors in the breast. It is being developed by Dr. Britton Chance at the University of Pennsylvania. This device seeks to eliminate the problems of other non-invasive detection techniques. Due to the use of light as the main tool for detection, the HHBCD is an inexpensive and convenient apparatus for early detection. When perfected, this device will be able to replace existing mammograms for cases where the tumor is located up to 3 cm into the skin.

The objective for the project during SUNFEST 2004 is to assess the effectiveness of the current device and determine changes and improvements to be made.

The purpose, implications, and description of the HHBCD are explained in more detail in **Section 2**. Its principles for tumor detection are presented in **Section 3**. An assessment in performance of the HHBCD is seen in **Section 4**. **Section 5** discusses the recommendations made to fix and enhance the device. **Section 6** explains the changes made. **Section 7** discusses unfinished and future work. Finally, **Section 8** acknowledges the organizations and people who made my contributions to the project possible.

## 2. THE HAND-HELD BREAST CANCER DETECTOR (HHBCD)

The HHBCD is composed of a small navigation probe, a 12V DC power supply, a

circuit interpretation box, a data acquisition (DAQ) card, and a computer. **Section 2.1** describes components and function of the probe. Then, it illustrates the signal read-out on the computer screen. **Section 2.2** clarifies the purpose and future implications of the HHBCD.

## 2.1 Device Description

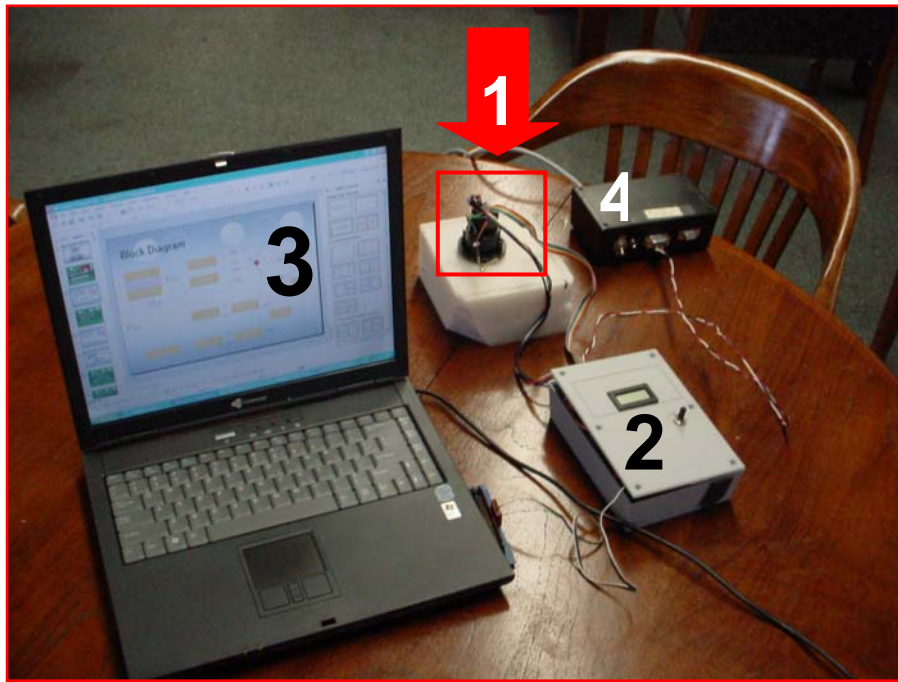


**Figure 1:** The HHBCD in its complete form. Its elements include 1) a navigation probe, 2) a signal interpretation box, 3) a computer display, and 4) a power supply.

### 2.1.1 Navigation Probe

The Navigation probe consists of a Photomultiplier Tube (PMT) and four light sources called light emitting diodes (LED's). The PMT is a very sensitive light detector that can be designed to read specific wavelengths. In our case, we have used PMT that operates in the near infrared region (NIR). The LED's are then chosen to produce light (photons) in the NIR region. The intricacies of the PMT and photon diffusion in highly scattering media (breast tissue) merit a report in themselves – references 4, 5, and 6 provide more information for the curious reader.

The PMT produces a measurable electrical signal proportional to the light to which it was exposed [3]. The trajectory of the light is predicted to propagate in the tissue outward from the light source as a spherical wave [4]. This basic understanding in PMT and photon diffusion theory is enough to comprehend the HHBCD's detection method ahead.

The device's probe is home to the PMT and LED's acting as a navigation tool to

scan around the surface of the breast. It is circular at the point of contact and is about the size of a toddler's fist. At its center, the probe holds the PMT which is surrounded by two paired LED's placed around it perpendicular to each other as in a cross. These LED's are placed at a distance of 2 cm from the PMT. The fashion in which the LED's are placed permits detection in two dimensions (2-D). **Figure 2** shows the configuration of the PMT in respect to the LED's.

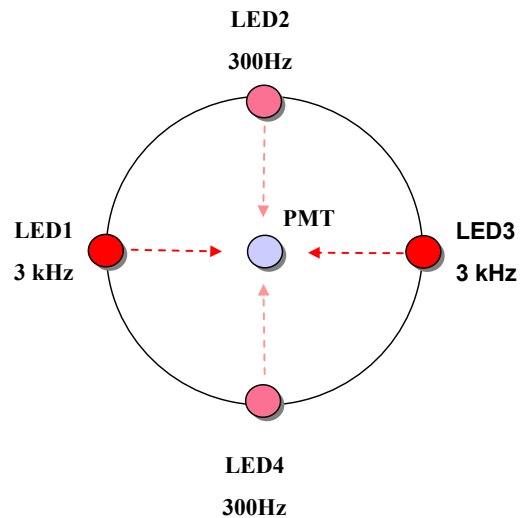
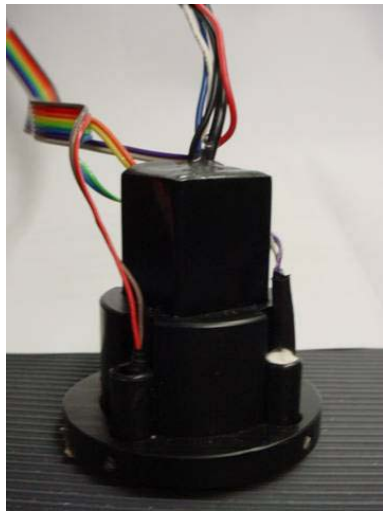


**Figure 2:** From left to right: picture of navigation probe and a drawing of its face. The components configuration on the face of the probe (phased-array geometry) is easily seen on the drawing. The face is what will come in contact with the breast tissue during inspection.

This arrangement is known as phased array geometry [5]. From this, a 2-D Phased Array system of detection can be implemented when dual out-of-phase sources are used [6]. To detect a small object embedded inside the turbid media, the dual-interfering-source configuration (phased array) is used because it is basically a cancellation technology. To put it more clearly, a phased array system can sensitively detect and locate small objects in turbid media (breast tissue) [5].

With the aid of **Figure 2** it is shown how the interaction of these two components result in the formulation of a signal that can be used for the detection of a cancerous tumors.

Since we have two paired LED's, the circuit contains two frequencies corresponding to each pair: 300 Hz and 3 kHz. This permits the user of the Hand-Held Cancer Detector to know which of the two planes the tumor is located when scanning over the breast.

One must understand two fundamental requirements for effective light localization and detection by the PMT. These include light variation and light intensity.

Light variation, in plain terms, refers to making the LED's light very dim and very bright (by being out-of-phase they change at opposing intervals). This is accomplished by driving the LED by a sinusoidal current. Without proper swing (very dim to very bright), localization cannot be effectively accomplished as the waves are not able to differentiate each other sufficiently for our circuitry to make a clear distinction. We can go back to the color analogy to simplify: without proper swing, the PMT cannot distinguish between green, red, or yellow. As a consequence, localization is lost.

In addition, without a suitably high current in the driver the LED's light intensity might also become insufficient to be read by the PMT. Lack of intensity would then result in losing all capabilities of the HHBCD. Not only would localization be lost but also plain detection of a cancerous tumor.

For simplification purposes, **Figure 3** (in the next page) illustrates only the 1-D case, that is, one plane. The 2-D case would include the plane bisecting the PMT perpendicular to this page. This would allow for two planes of detection simultaneously.

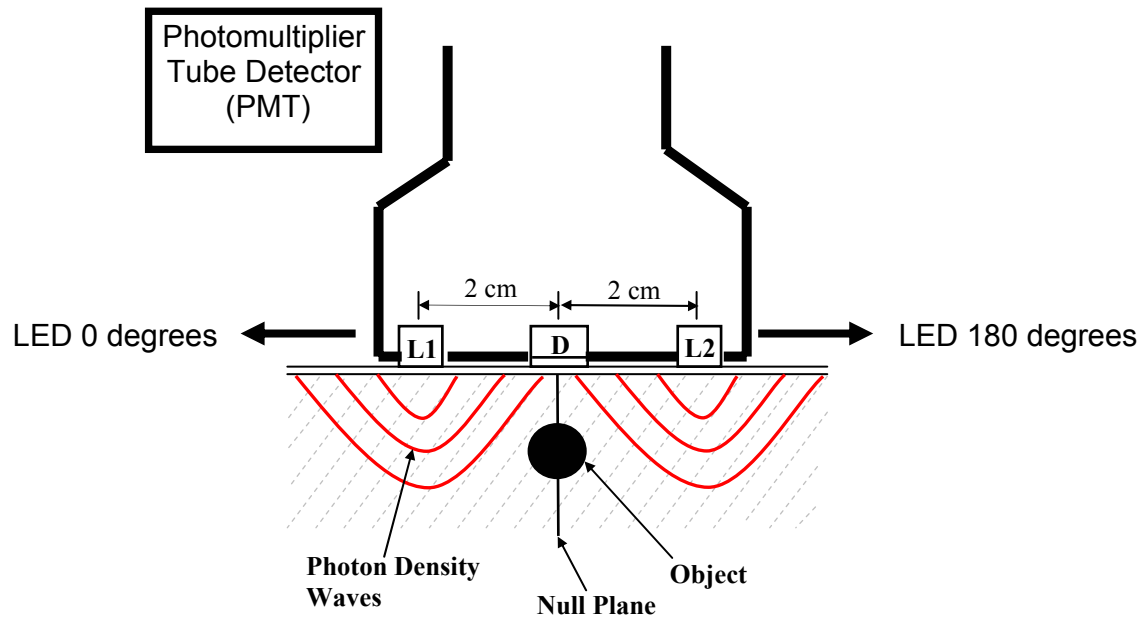


**Figure 3:** The figure shows a 1-D breast cancer detection. The navigation probe is facing down on a breast surface. As it scans around it will detect a heterogeneous object.

The basic phased array unit consists of a pair of in-phase and out-of-phase amplitude modulated sources (L1 and L2). Thus, a  $0^\circ$  and  $180^\circ$  phase transition is generated in the plane bisecting these two sources in a homogeneous medium, and this pattern can be sensitively perturbed by the presence of an absorbing object to form the signal for detection [5].

Breast tissue is a highly scattering medium. Due to the physical properties of NIR light in highly scattering media, a cancerous tumor will be a strong absorber of light. As a result, the PMT will read a smaller intensity coming back to it than in a completely

homogenous solution. For instance, if an object is found to be in front of L1 the PMT will read a higher light intensity for L2 than for L1.

An interesting behavior occurs when the cancerous object is right in front of the PMT: the light intensity of L1 and L2 is the same since the object is affecting both sources equally. This has great significance as this property is used for localization which is explained in the next paragraph.

To explain the way we can localize tumors I use colors in this paper only as a tool to explain the HHBCD's read-out. No colors actually are used in the device, only a graph with various offsets. The real read-out is explained in **Section 2.1.2**.

We can think of HHBCD's read-out to be red, yellow, and green. Each signals different positions of the probe with respect to a tumor. Different read-outs can then be created when the tumor is in front of L1, L2, and the PMT.

For example, when an object is in front of L1 we can think of the read-out as the color red. As the probe keeps moving in the direction where it first yielded red, the object will be in front of the PMT; the HHBCD's read-out will then be yellow. If the probe continues to move in the same direction the object will end up in front of L2; the read-out will then be green. In such a way one can trace the exact location of a tumor by moving around the breast. In other words, a tumor can be detected regardless of having three different read-outs (in this example, colors). However, the advantage of having three different read-outs is useful to determine where the tumor lies in respect to the probe's components. With the localization feature one is able to know a tumor lies directly underneath the middle of the probe (where the PMT is located) when the read-out is yellow.

### **2.1.2 Computer Read-out**

Since the probe itself cannot output a color, a computer screen is integrated into the system to display information. Rather than using colors, the read-out on the computer screen give three different responses in the form of voltage offsets on a graph. These offsets are negative, positive, and neutral (zero). This is depicted in **Figure 4**. As in Figure 3, only one plane of detection is shown for simplification purposes. In actual testing, two graphs appear on the screen, each corresponding to its respective plane.

To make clear the connection between offset and colors we only need to relate the previously used colors with their respective offsets. During the real operation of the HHBCD the graph displays a positive offset when the PMT output was red in the previous color example; a neutral (zero) offset is displayed when the PMT output was yellow; and a negative offset appears when it was green. Experimental data on human

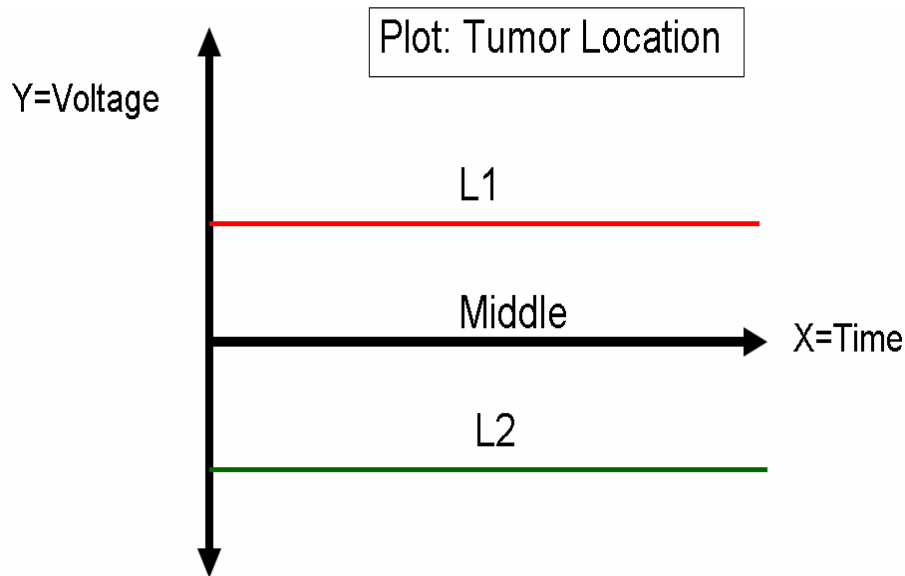


**Figure 4:** Computer Read-out for the HHBCD. There are three responses: 1) a positive offset occurs when a tumor is in front of source L1, 2) a negative offset when the tumor is in front of source L2, and 3) a neutral or zero offset when the tumor is in front of PMT.

breast phantoms (an object that simulates breast tissue) demonstrates that localization accuracy within several millimeters has been accomplished through this method [6].

In this way, the HHBCD can provide a graphic display that can be interpreted by almost anyone. There is no need for an expensive trained specialist to study the results. If the read-out works as expected for the 3 cm case, creation of a home device would not be out of question.

## 2.2 Device Goals

### 2.2.1 Objective

The HHBCD will not replace other non-invasive methods in their entirety. It is currently useful in cases where tumors are as small as **1 mm** and are located up to **1 cm** from the breast surface. If deep enough, the size is small enough that a human hand would most likely not be able to differentiate a change in the breast. Unfortunately, a range of 1cm is insufficient to significantly improve over breast clinical examinations (hand scanning around breast). The final goal is to extend the range to **3 cm** where a tumor is much less likely to be found by touch alone.

### 2.2.2 Future Implications

The HHBCD offers solutions to a number of problems encountered with existing devices:

1) X-rays: radiation exposure; cold at point of contact, and painful squeezing of the breast.

- 2) MRI: patient must lie down inside very tight chamber; very long inspection time, very loud rambling noise, and expensive.
- 3) US: gel must be put on the breast; expensive.

With the HHBCD, the probe is slowly and softly navigated around the breast. Due to the unobtrusive and friendly design of the HHBCD's navigation probe patients will not experience pain or be subject to foreign environments. In addition, the inspection time is fast compared to the methods described previously.

Financial limitations are an important source of lower survival rates among women as those who are financially strapped do not often get mammograms. According to the American Cancer Society, a lack of health insurance is associated with lower survival among breast cancer patients [2]. Breast cancer patients with lower incomes are more likely to be diagnosed with advanced stage of disease and to have lower 5-year relative survival rates than higher-income patients. For example, low-income African American women experience lower survival than higher-income African American women. The presence of additional illnesses, lower socioeconomic status, unequal access to medical care and disparities in treatment are found to contribute to the observed differences in survival between lower- and higher- income breast cancer patients [2].

The HHBCD is inexpensive to build, maintain, and operate. This combination provides for low inspection costs. This could prove invaluable to racial and ethnic minorities and other populations who have not benefited equally from advances in the past. Not only that, it would also contribute to developing countries in much the same way as low-income individuals in the U.S.A. These countries may not otherwise be able to benefit from mammogram technology.

In addition, the HHBCD can also serve as a guide for surgeons to localize tumors for extraction. This is especially important when surgical biopsies are needed. In such cases, a quick and easy-to-interpret signal read-out to localize the tumor is important to verify exactly the tumor's location and minimize the incision made in the breast.

### **3. DEVICE ASSESSMENT AND RESULTS**

This section discusses the assessment performed on HHBCD. We start with full system analysis in **Section 3.1**. After that, we break the analysis into two portions: the LED driver circuit in **Section 3.2** and the signal interpretation circuitry in **Section 3.3**. The results found were then used to determine areas for improvement, discussed in **Section 4**.

#### **3.1 Full System Test and Results**

The first step towards improving the HHBCD was to test the device as a whole and find possible problems. The HHBCD block diagram is shown in **Figure 5**.



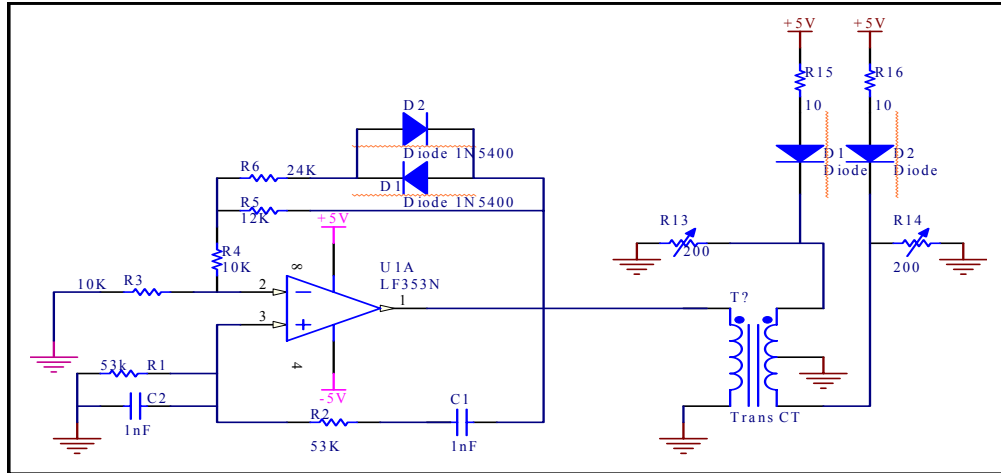


**Figure 5:** Old LED driver circuit; a load-down effect was caused by the transformer causing a low current intensity on the LED's.

Two problems were found:

- 1) The low resistance seen by the transformer's output created a load-down voltage effect.
- 2) The voltage swing generated by the oscillator was low,

A load-down effect is nothing more than an improperly low transfer of voltage to the circuit. In other words, the transformer's output resistance was higher than the resistance it saw. Thereby, by voltage division principles, not all of the voltage was fed to the LED's. The low voltage swing was occurring due to voltage limitations that resulted from a low voltage supplied (5 V) to the op-amps in the oscillator circuit.

After the problems were found in the LED driver, it was obvious there would not be good light swing or light intensity. The low voltage caused by the load-down effect resulted in low power to the LED's. To make matters worse, even with enough power to create good light intensity the low swing would result in a loss of localization capabilities at a distance of more than 1 cm. Solutions to these problems are briefly discussed in **Section 4**.

### 3.3 Signal Interpretation Test and Results

Once it was discovered the LED driver was not functioning properly it was important to test each component in the signal interpretation circuitry (Section 2, Fig. 4). Testing of this circuitry did not take place until after the LED driver was fixed.

The signal interpretation circuitry consists of the following items (in the order encountered by the PMT output signal):

- 1) Current-to-voltage converter
- 2) Band-pass filter

- 3) Non-inverting amplifier
- 4) Transformer (splitter)
- 5) Analog Switch

We tested each component individually by running it with the corrected LED driver. Each element's voltage was sampled using an oscilloscope. The approach was to systematically track any unusual change of signal block by block. Our intention was to discover possible sources of noise that might contribute to the unstable read-out mentioned in **Section 3.1**.

By testing each individual component we discovered the following problems:

- 1) The band-pass filter was not filtering out undesired frequencies.
- 2) The Transformer (splitter) was deficient.

The band-pass filter being used was of first order. A first order filter does not attenuate other frequencies as effectively as higher-order filters [7]. As a result, some of the 300 Hz frequency was not completely cancelled at the 3 kHz filter and vice versa. This resulted in an unwanted signal – or noise. The deficient transformer was affecting the signal by distortion. It seems the transformer had been tampered with which resulted in its malfunction.

#### **4. SUGGESTED IMPROVEMENTS**

Based on the findings in **Section 3**, a number of improvements were made. The old LED driver was changed and tested on a breadboard but not rebuilt on a circuit board. The resistance seen by the transformer was increased to eliminate the load-down effect and somehow provide sufficient light swing and intensity. These details are explained with the discussion of the redesigned LED driver circuit in **Section 5**. A higher-order filter was recommended to replace the old band-pass filter in order to better attenuate unwanted frequencies. Finally, the faulty transformer will simply be replaced when the new system is constructed.

There are many effective high-order band-pass filters. One would simply need to choose a known design and construct it onto the circuit. For example, a simple way of accomplishing this would be by cascading (connecting in series) various first order band-pass filters. This would increase its order each time one new band-pass filter is connected. Since choosing a band-pass filters is not a concern, they are not covered further from this point on in the report.

After identifying problems in the HHBCD and recommending solutions, it was necessary to choose between two courses of action:

- 1) Reconstruct the device and test it.
- 2) Postpone reconstruction and design new improvements.

I chose the second option as due to time constraints. Working on new components would add scope to the Hand-Held Breast Cancer Detector. For this reason, reconstruction of the HHBCD was delayed in hopes of coming up with new components that would be included in the reconstruction of a new device.

The suggested improvements address protection and noise elimination. The PMT is sensitive to light and physically fragile. If exposed to too much light, the PMT will get permanently damaged. Also, due to its fragility, if not handled with care its parts can be broken. Finally, interference was created by having the LED's on at 300 Hz and 3 KHz. Solutions to these problems are explained in **Section 5, 6, and 7**.

## 5. REDESIGNING LED DRIVER CIRCUIT

To explain the redesigned LED driver circuit let us go back to the initial problem. The old LED driver was loading-down the voltage provide to the LED's resulting in low intensity. Also, there was not enough swing in the sinusoidal current driving the LED's crippling the capabilities of the HHBCD for localization.

The problems encountered were solved by the redesigned circuit in **Figure 6**.

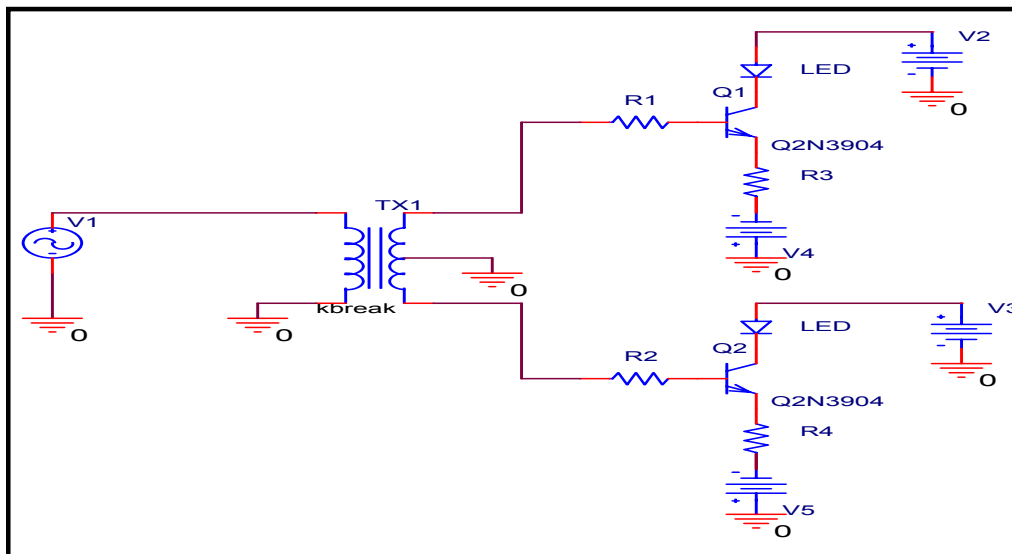


**Figure 6:** Redesigned LED driver. It consists on the addition of a transistor with a high base resistance and the placing of the LED's on the transistor's collector side.

The circuit's improvement was due to the implementation of Bipolar Junction Transistors (BJT). Their contributions were important in the following two ways:

- 1) A high resistance was placed at the base of the transistor thereby significantly decreasing the load-down effect. This is due to the voltage division principle: the voltage will travel to the highest resistance. Since the resistance seen by the transformer was much higher than its own output resistance, almost all the voltage moved on to the transistor base.

- 2) BJT transistors could provide more current and swing as they can increase small currents by a factor of approximately a hundred. This provided for more swing in the LED's as well as greater intensity (due to higher power). This is a result of being able to keep a constant voltage across the LED terminals (V3 in Figure 6) and the ability to increase a small current in the base to a large current at the collector side of the transistor. Since an LED intensity is regulated by current (LED's maintain a constant voltage as they act like diodes), its light intensity increased. Also, due to the small current changes required at the base to create large currents at the collector, a good swing (variation of high to low intensity) could be achieved.

To summarize, the addition of the transistor to the design was enough to correct the problems encountered during testing while not having to completely redesign the LED driver.

## 6. COMPLETED UPGRADE: VOLTAGE SHUT-OFF PROTECTION SYSTEM

The incredible sensitivity of the PMT makes it very vulnerable to damage when exposed to too much light. When using the HHBCD, one must operate in a dark room. If the HHBCD were to be operated in an environment other than a dark room, other light would interfere with the signal to be read from the NIR light sources. Such precautions can be arranged without much difficulty. Lamentably, a safeguard to an unexpected strong source of light did not exist in the HHBCD. Unanticipated situations can include turning on the room switch, or lifting up the window curtains where inspection is being performed. A protection device that could save the PMT from strong light was constructed. A picture of the circuit that corrected this problem is shown in **Figure 7**.

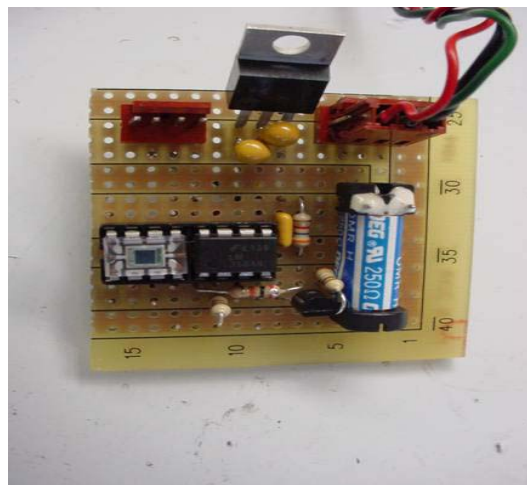


**Figure 7:** A picture of the voltage shut-off protection system. It was designed to protect the PMT from light overexposure by turning its supply voltage off when exposed to room light.

Ahead, the shut-off protection circuit schematic is shown in **Figure 8** with its explication to follow.

# Shut-off Schematic

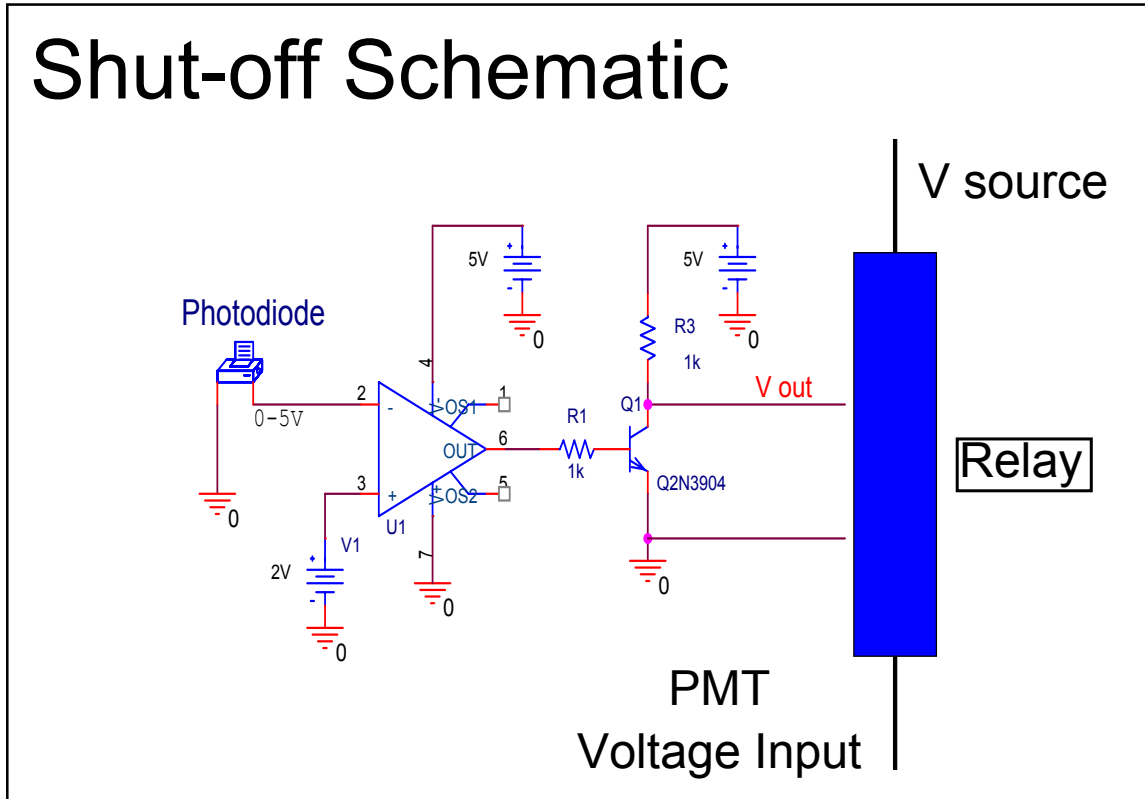


**Figure 8:** Schematic for the voltage shut-off protection system. Four components are used: 1) an OPT101 (photodiode), 2) a LF353N op-amp, 3) a 3904 transistor, and a 4) mechanical relay.

The circuit in **Figure 8** is effectively impedes voltage supply to the PMT in approximately less than one second. It is comprised of a photodiode (OPT101), an op-amp (LF353N), a BJT transistor (3904), and a mechanical relay.

The photodiode outputs 5 volts (V) when exposed to a strong light – room light qualifies. The output is connected to the inverted input of an LF353N op-amp. The positive input of the comparator is held at 2 V. By having a static voltage at one terminal and varying at the other a comparator is formed [7]. A comparator outputs a voltage equal to its power supply. Which power supply it uses depends on what input terminal is higher in voltage. In our circuit, the negative power supply of the comparator ( $V_{ee}$ ) is connected to 5 V and the positive power supply ( $V_{cc}$ ) is 0 V. In such a configuration, the comparator output is 5 V when the photodiode is exposed to strong light and 0 V when very dim light is present.

When the base of the transistor is 0 V (no light), the transistor is forced into cut-off mode [8]. In this state, the NPN junction acts as an open circuit forcing the voltage supply of the transistor to appear across the input of the mechanical relay. This allows flow of the power supply to the input voltage pin of the PMT. Thus, the device would be in operation mode.

Where the base of the transistor is 5 V (strong light), the transistor is forced into saturation mode [8]. This is a consequence of the low resistance placed in the collector of the transistor. The low resistance permits high current to flow through it which creates a high drop in the resistance. The input of the relay then becomes approximately 0.3 V which shuts-off the relay and quickly stops current from flowing through it. If the PMT is connected to the relay, its voltage supply is abruptly ended by the shut-off protection system.

The shut-off protection system effectively discontinues power to the PMT. Unfortunately, to completely save the PMT under room light conditions our system would have to turn off the power supply in less than 10 nanoseconds [3]. Our device can only do it in less than a second which is too slow. However, with the use of optical band-pass filters at the face of the PMT, much of the light could be prevented from reaching our highly sensitive detector. Since the photodiode will still see the light and shut the power to the PMT, this design would still be capable of significantly protecting the PMT from light overexposure.

## 7. FUTURE WORK

The following work has been accomplished:

- 1) Full System Test and Results
- 2) LED Driver Test and Results
- 3) Signal Interpretation Test and Results

This work resulted in 1) a new LED driver, 2) a higher order band-pass filter, 3) the replacement of a transformer, 4) and a voltage shut-off protection system. These items were completed and are ready for reconstruction. However, a time-shared system to reduce noise and a new probe casing design remain under construction. They are briefly described in **Figure 9** and **10**.

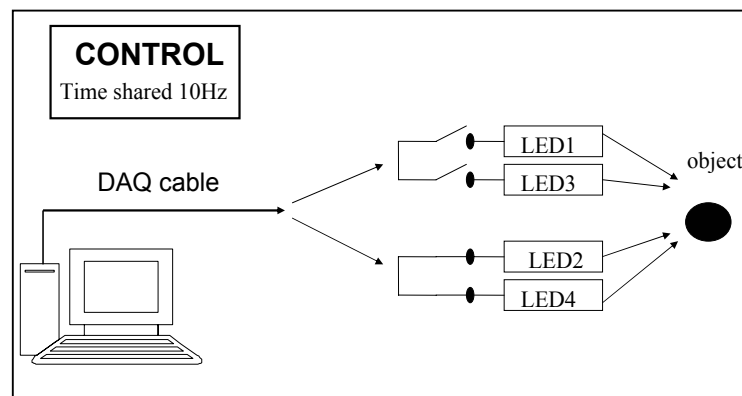


**Figure 9:** A computer controlled time-shared system. An LED pair is turned on while the other pair is off at a rate of 10 Hz. If successful, the filters in the signal interpretation will work independently. Thus, the LED's will not interfere with each other, stabilizing the read-out on the computer screen. A program that can do this is under development.

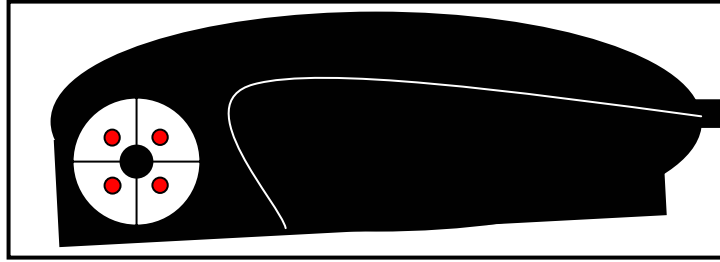


**Figure 10:** A rough drawing of a new probe casing idea. Its main purpose is to place the PMT at a location other than the probe. The plan is to use fiber optics from the PMT area of detection to the Black dot seen in above Figure. The attenuation inside the cable is believed to be negligible due to the short distance from the box to the probe. Also, the probe is made in the shape of a computer mouse (familiar feel) to facilitate its handling.

If these two devices are completed successfully, the project can then move to the integration and construction of the new HHBCD. Once the circuitry has been reconstructed, testing on a breast phantom must be done. That would be followed by testing on human subjects.

## **8. ACKNOWLEDGEMENTS**

This is my time to thank everyone, from the bottom of my heart, for making SUNFEST 2004 a truly motivating and enriching experience. I would first like to thank UPENN for hosting the program. The National Science Foundation for funding the program and trusting that young students like me will one day give fruits to their investment. Thank you Dr. Van der Spiegel for selecting me to participate in this prestigious program. I feel very fortunate and thankful that you trusted in me. To Dr. Britton Chance, for being kind enough to offer a project for undergraduates out of pure joy for teaching. To the grad students in the lab of room 203 in the Anatomy/chemistry building, especially Sammy, Simon, Kiran, and Lan Lan. Thank you Sammy for being so patient and helpful to me.

I want to thank Dr. Pappas, Dr. Kassam, Dr. Lee, Dr. Santiago, and Salvador for helping me in the search to better accomplish my goals.

I want to thank Delores, Shelley, and Denise for being so nice and informative every time I needed any kind of help. Delores, thank you for your football insight.

Finally, I want to thank God, my family, and my princess. Without your love, none of my work would mean anything.

**Thank you.**

## 9. REFERENCES

1. American Cancer Society: Cancer Facts and Figures – 2002, *American Cancer Society* (2002).
2. American Cancer Society: Breast Cancer Facts and Figures – 2003-2004, *American Cancer Society* (2004).
3. Hamamatsu: Photomultiplier Tube Detector Technical Manual – 2003, *Hamamatsu* (2003).
4. J. B. Fishkin and E. Gratton, Propagation of photon-density waves in strongly scattering media containing an absorbing semi-infinite plane bounded by a straight edge, *J. Opt. Soc. Am. A*, 20 (1993) 127-140.
5. Y. Chen, *Contrast Enhancement for Diffuse Optical Spectroscopy and Imaging: Phase cancellation and targeted fluorescence in cancer detection.*, Dissertation in Bioengineering, University of Pennsylvania (2003).
6. Y. Chen, C. Mu, X. Intes, and B. Chance, Adaptive calibration for object localization in turbid media with interfering diffuse photon density waves, *Applied Optics*, 41 (2002) 7325-7333.
7. S. Franco, *Design with operational amplifiers and analog integrated circuits*, McGraw-Hill, New York, 3<sup>rd</sup> ed., 2002.
8. S. Schwarz, *Electrical engineering: an introduction*, Oxford University Press, New York, 2<sup>nd</sup> ed., 1993.

*University of Pennsylvania*  
Center for Sensor Technologies

SUNFEST

NSF REU Program  
Summer 2004

**MINIMIZATION OF DISTORTION AND INCREASING  
RESOLUTION IN WIDE-ANGLE VIEWING BY MEANS  
OF ACTUATED MICRO-MIRRORS**

NSF Summer Undergraduate Fellowship in Sensor Technologies  
William Rivera (Electrical Engineering) – University of Puerto Rico, Mayagüez  
Advisor: Dr. Suresh G. K. Ananthasuresh and Dr. Andrew Hicks

**ABSTRACT**

Mirrors of numerous shapes, including spherical and paraboloidal mirrors, have been employed for many different commercial and industrial uses, despite their tendency to distort and warp images. When the object in consideration is planar and oriented normal to the optical axis of the mirror, the amount of distortion introduced by a paraboloidal mirror is less than the distortion introduced by a spherical mirror. Previous research has found an optimal mirror shape that minimizes distortion of images of planar objects normal to their optical axes.

The goal of this project was to design and construct a single-axis micro-mirror, to form the basis for future work. The micro-mirror construction used a (110) silicon wafer. The design consists of a square mirror supported by two torsional beams. Several design variations were considered to see how these variations affected the fabrication. Due to time limitations, the construction was not completed. It was achieved through the photoresist stripping of the bottom pattern step. Although, the construction was not completed, microfabrication techniques were learned such as mask drawings design, resist processing, photolithography, and the proper use of the Microfab Lab facility equipment. A mechanical modeling of the movement of the single axis micro-mirror was developed. Piezoelectric actuation was explored but due to malfunction of the piezoelectric materials available, it was not possible. Characterization of the voltage differences across the piezoelectric materials was performed to determine why actuation was not possible.

## Table of Contents

<b>1. INTRODUCTION .....</b>	<b>161</b>
<b>2. BACKGROUND.....</b>	<b>162</b>
<b>2.1 WIDE-ANGLE VIEWING (WAV) DISTORTION .....</b>	<b>162</b>
<b>2.2 IMAGE RESOLUTION .....</b>	<b>164</b>
<b>2.3 FABRICATION USING (110) SILICON WAFERS .....</b>	<b>165</b>
<b>3. FABRICATION OF THE DESIGN.....</b>	<b>166</b>
<b>3.1 PROCESS FLOW .....</b>	<b>166</b>
<b>3.2 AUTOCAD DESIGN .....</b>	<b>171</b>
<b>4. RESULTS.....</b>	<b>173</b>
<b>4.1 FABRICATION RESULTS .....</b>	<b>173</b>
<b>4.2 MECHANICAL MODELING .....</b>	<b>174</b>
<b>4.3 PROTOTYPE ACTUATION.....</b>	<b>176</b>
<b>5. DISCUSSION AND CONCLUSIONS .....</b>	<b>177</b>
<b>6. RECOMMENDATIONS .....</b>	<b>179</b>
<b>7. ACKNOWLEDGMENTS.....</b>	<b>179</b>
<b>8. REFERENCES .....</b>	<b>179</b>

## 1. INTRODUCTION

Extensive research into wide-angle viewing (WAV) in recent years has resulted in the use of WAV in military, visual sensors, and automotive applications. The development of vision systems technologies using WAV has made its fusion with other fields such as electronics and micromachining attractive to many researchers. As a result, devices called micro-mirrors (MM) have been developed. MM are microelectromechanical systems (MEMS) that are capable of rotating in order to redirect reflected light. MM has found applications in optical switching, digital light processing (DLP), and optical scanning [1].

Mathematical algorithms and fabrication processes exist for the design of different mirrors shapes to achieve WAV. These algorithms lead to mirrors with paraboloidal and spherical shapes. Unfortunately as long as the mirrors are deformed, distortion is introduced to the images they reflect. Minimization of this image distortion has been achieved by finding an optimal shape between paraboloidal and spherical mirrors [2]. One problem with this kind of mirror is that they are designed for a specific optical axis perpendicular to the tip of the mirror, as shown in Figure 1.

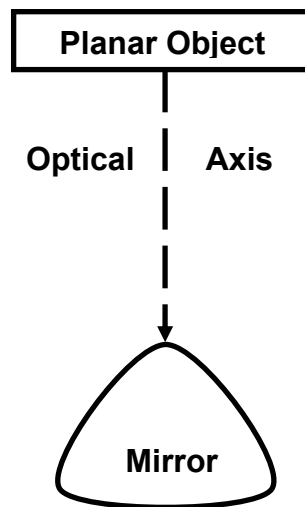


Figure 1: Optical axis of a mirror designed to minimize the distortion in the reflected images.

A long-term objective of this research is to simulate this optimal mirror shape with actuated MM to avoid having to design for just one optical axis. At the same time, the MM increases the resolution of the images since the number of mirrors used to reflect the images is increased.

Presently, this research has three main goals: 1) minimize the distortion in wide angle viewing, 2) study the ways in which the increasing the number of actuated MM can increase the resolution of images, and 3) design and fabricate a device that uses actuated MM to achieve the first two research goals. The tasks assigned for the summer project

were: masks design, microfabrication of the MM, study a mechanical modeling for a single-axis MM and, if time permitted, investigate ways of actuating a macro scale prototype of the MM. The result of the work done through the SUNFEST project made a contribution that forms the basis for future work on the third goal of this research.

## 2. BACKGROUND

### 2.1 Wide-angle Viewing (WAV) Distortion

A mirror is a surface capable of reflecting the light that hits it and forms an image on it. Although most commonly used mirrors are planar, some are fabricated in a variety of shapes and sizes such as spherical and paraboloidal. Cameras use mirrors to redirect the images reflected into a set of lenses. Because the field of view of conventional cameras is limited, omnidirectional or WAV cameras have gained popularity for panoramic viewing. The applications for WAV cameras include space optics, robotics, and surveillance. WAV images are achieved by using mounting shown in Figure 2(a).

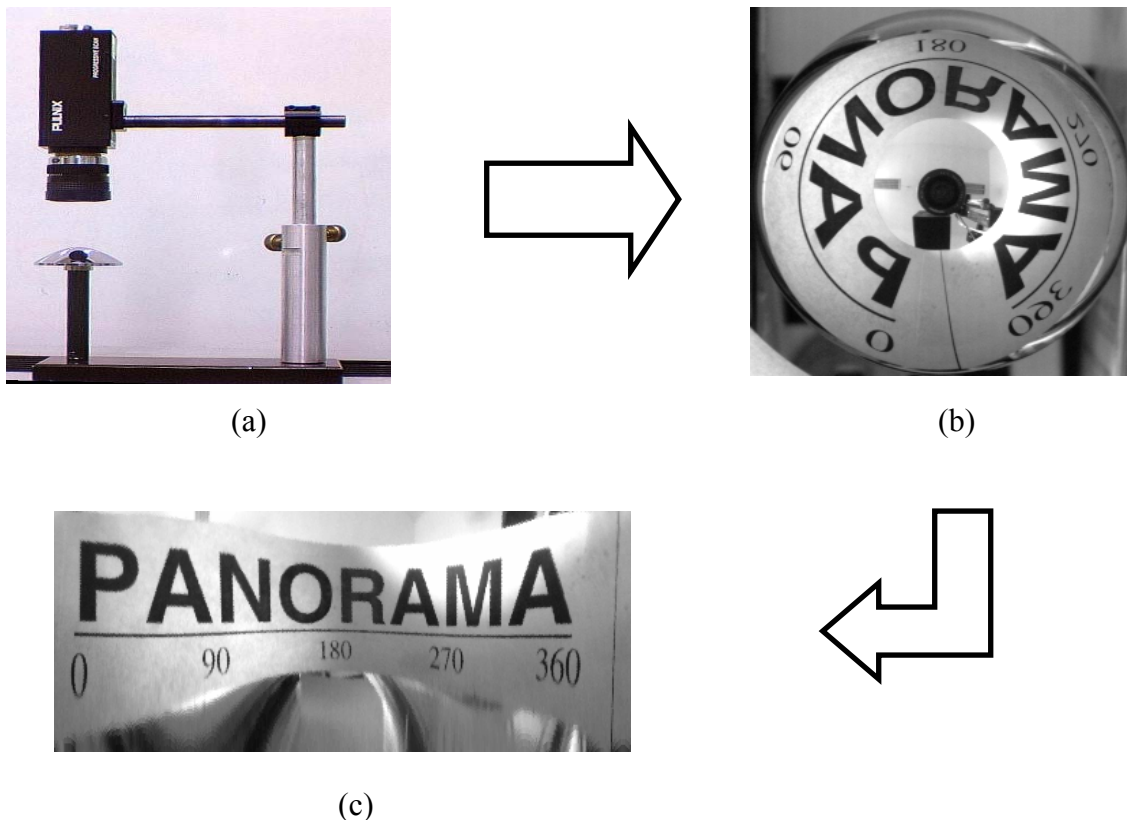


Figure 2: (a) WAV setup mounting, (b) warped image, (c) fixed image using computer techniques.

The image obtained from these mirrors is similar to that shown in Figure 2(b). With the help of computer algorithms, this image can be rearranged to better represent reality, as

shown in Figure 2(c). However, even with the use of such special mirrors, the edges of the resulting image are distorted. The amount of distortion depends on the camera's position. The best results are obtained by focusing the mirror through just one optical axis perpendicular to its tip. In this position, image distortion is minimized.

Mathematical algorithms have been developed to find a mirror design that minimizes image distortion in WAV [2]. Although this is a remarkable achievement, to have a WAV image from another point of view, the mirror has to be repositioned. Otherwise, the resulting image will have more distortion.

The use of MM to solve this problem has been suggested. Mathematically, the problem can be represented by a differential equation. If non-planar objects and inclined optical axes are considered, the resulting differential equations cease to have continuous surfaces as solutions. As a future work, the objective of this research is to design and fabricate a versatile device capable of simulating numerous mirror shapes that can emulate the discontinuous solutions. In this manner, if the optical axis is changed, the MM could change their orientation and shape to achieve a position normal to the new optical axis. A description of the proposed method that uses MM is shown in Figure 3.

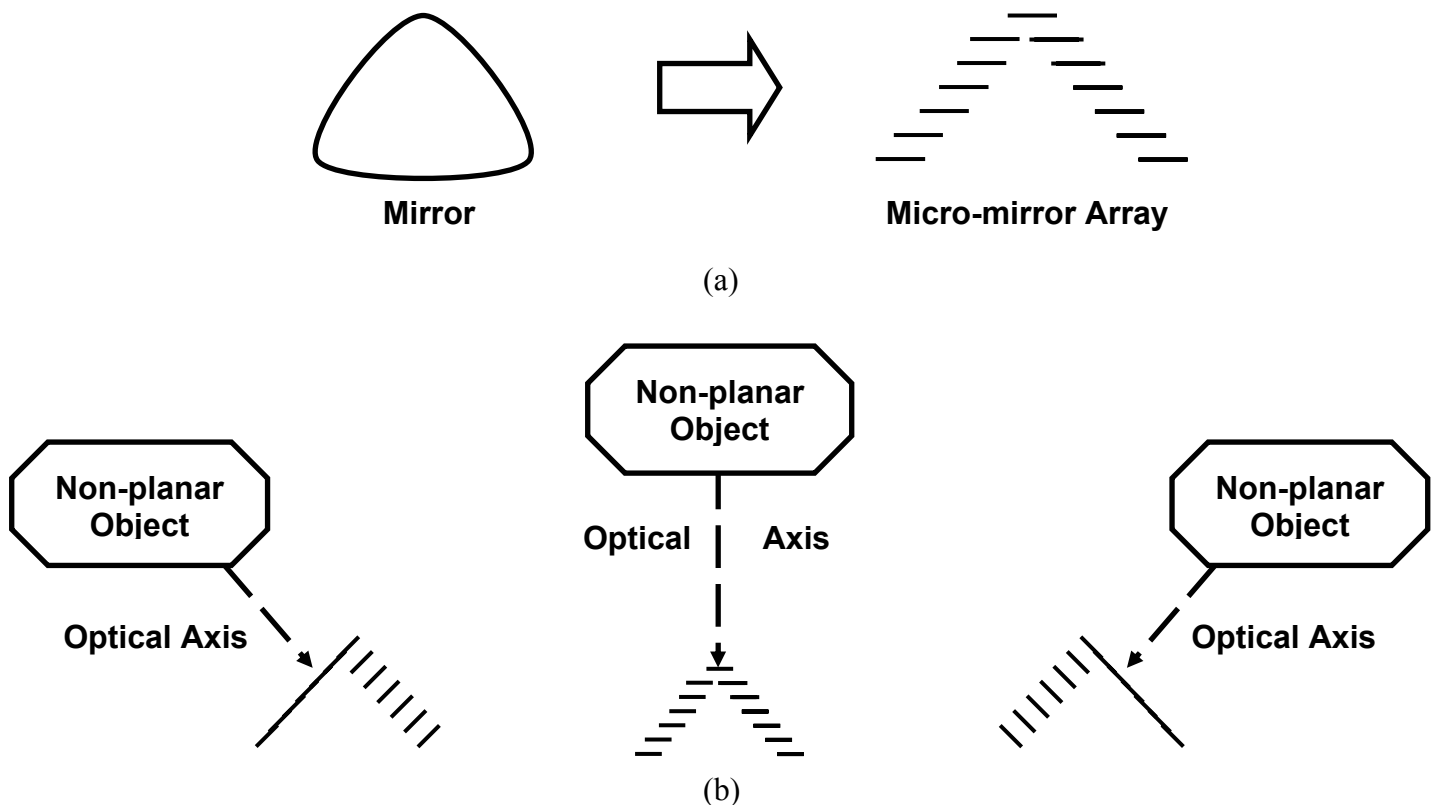


Figure 3: WAV proposed method. (a) Mirror surface simulation through a MM array, (b) MM array orientation change with different optical axis.

## 2.2 Image Resolution

Pixels are the basic component of computer graphics images. The word comes from the phrase “picture element”. They are the tool by which image colors are programmable in a language that computer understands. The number of pixels per inch (ppi) defines the resolution of an image. Resolution contributes to important characteristics of images such as sharpness, quality, and size. Increasing the resolution of images has effects in applications including space observation, image printing, monitor visualization, remote sensing, and medical studies.

The method by which this research intends to increase images resolution can be understood by following example. Suppose that two pictures are taken from an object at different angles so that they share some part of the picture. Computer techniques can take these two pictures and overlap them only in the shared area. In this way the number of pixels in the shared area increases to the sum of the pixels in that area in the individual pictures. This case is demonstrated by Figure 4.

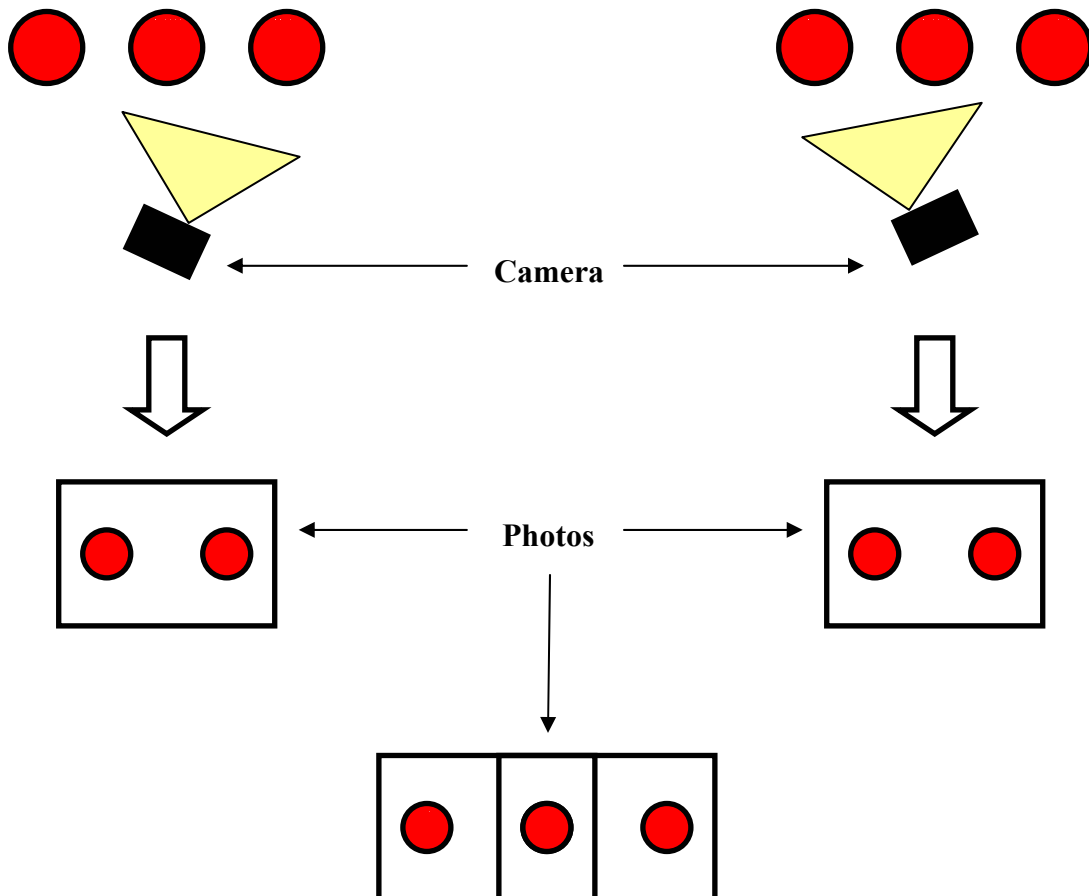


Figure 4: Increase in resolution in overlapped section of pictures taken at different angles. The color is darker in the shared area, indicating that the resolution of that area increased.

Now, instead of having a camera taking single pictures, if a video camera is used, the number of pictures taken could be increased from one picture at a time to 30 pictures per second. If these pictures are overlapped on their shared areas, resolution can be increased. We can go even further if instead of having one single main mirror to receive that light in traditional video cameras, an array of MM is placed. WAV video cameras can use MM not only to reduce the distortion of the fixed images, but to increase the resolution of every single picture captured.

### 2.3 Fabrication using (110) Silicon Wafers

Silicon single crystal provides uniform, reproducible device characteristics and thus the ability to integrate millions of identical components side by side on a chip. Also, silicon provides a controllable, stable, and reproducible surface layer ( $\text{SiO}_2$ ) which has enabled modern integrated circuit (IC) technology [3]. Crystalline materials such as silicon wafers have a uniform, periodic molecular arrangement through the whole material. Therefore, crystalline materials have specific orientations, which mean that the atoms are arranged in a specific order to form the bonds of the molecules. This orientation defines the properties of the material such as the electrical and the etch rate properties. Also, some applications such as micro heat exchangers choose a specific crystalline orientation of silicon [4]. Figure 5 shows the three basic unit cells or lattices for crystalline materials.

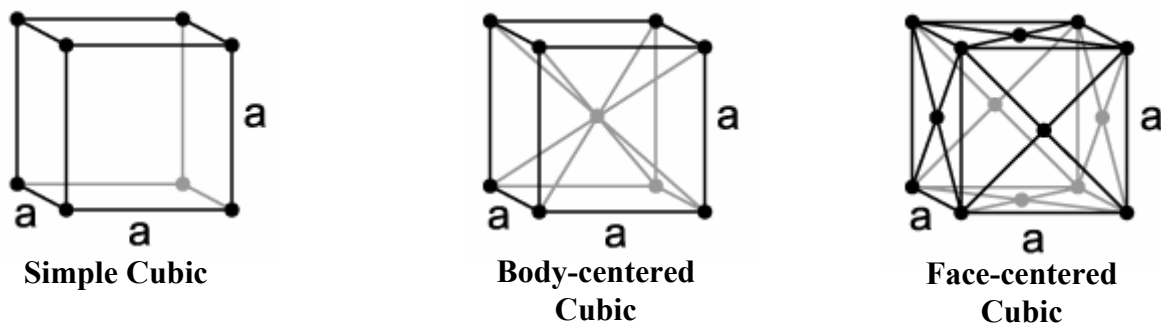


Figure 5: Basic unit cells for crystalline structure materials.

The directions between the atoms in a crystalline material are described by vectors using Cartesian coordinates in this manner:  $[xyz]$ . In the same way, planes within the crystals are described by what are called Miller indices, which are reciprocals of the planes' interceptions with the Cartesian coordinates' axes. The Miller indices of the planes are written between parentheses. To help visualize these concepts, it is important to note that in cubic lattices the direction of the atoms is perpendicular to the planes that describe them. Figure 6 shows three examples of planes' orientations for crystalline structures.

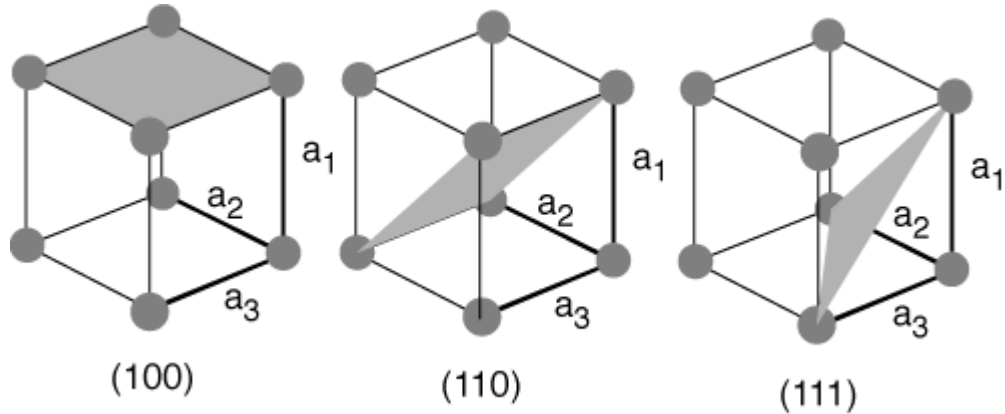


Figure 6: Plane orientation for crystalline materials.

In integrated circuits there are two main silicon crystal orientations: (111) and (100) [5]. For the fabrication of the MM, silicon wafers that have (110) plane orientations were chosen. This orientation permits fabrication of structures with narrow trenches with vertical side walls. Characteristic desired for the mirrors' fabrication since it requires etching the wafer as straight as possible to have a high aspect ratio. Also, the fabrication requires fine structures as straight beams and serpentine spring beams.

### 3. FABRICATION OF THE DESIGN

#### 3.1 Process Flow

In order to fabricate the MM, a process flow, of the steps to construct it was designed. It is shown in Figure 7. The process flow offered a method to study and understand all the processes involved in the MM fabrication. The process flow starts with the selection of the orientation of the silicon wafer. Then, the wafer is put into an oxidation furnace until a  $\text{SiO}_2$  layer of desired thickness is grown. This layer, after patterning, serves as a mask for KOH etching. Next, a layer of positive photoresist is spun onto its surfaces, and it is soft-baked to harden the photoresist. The wafer is then placed on the photolithography machine and is aligned with the top mask in order to expose the wafer to ultra violet (UV) light for 14 seconds. The UV light changes the chemical composition of the exposed portion of the photoresist be exposed, making it more soluble. In this manner, the pattern of the bottom mask is transferred to the bottom wafer surface. After that, the wafer is introduced into a solvent to remove the exposed photoresist. Other solvents are used to take out the uncovered  $\text{SiO}_2$  and the unexposed photoresist. These steps serve as a preparation for KOH etching which removes the pure silicon where there is no  $\text{SiO}_2$ . KOH etching is performed on the bottom surface first because the top surface, which is the reflective part of the MM, will form a thin plate. The etch-rate varies for the different crystal orientation structures. For that reason, when KOH etching, one has to be aware of the time that the wafer is been etched. Also, it is possible to estimate the desired amount of etching by visual inspection.

After the wafer is etched on the bottom surface a layer of photoresist is spun on both sides to prepare the wafer to be exposed to UV light on the top surface. Then, the wafer and the bottom masks are aligned in the photolithography machine, and the pattern of the top masks is transferred to the top surface of the silicon wafer. Then the stripping processes are repeated. At the end only a pure silicon structure is left.

Figure 7: Process Flow of the MM fabrication

Step 1: Selection of the silicon wafer



Step 2: Silicon layer oxide growth



Step 3: Photoresist Layer Spinning

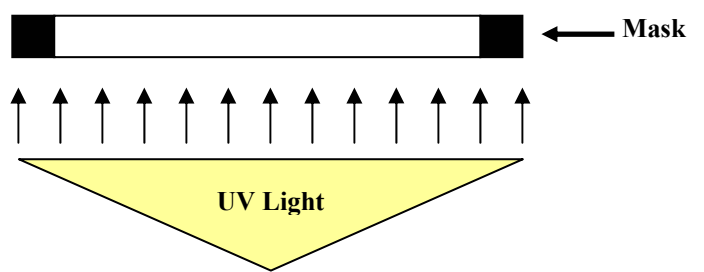
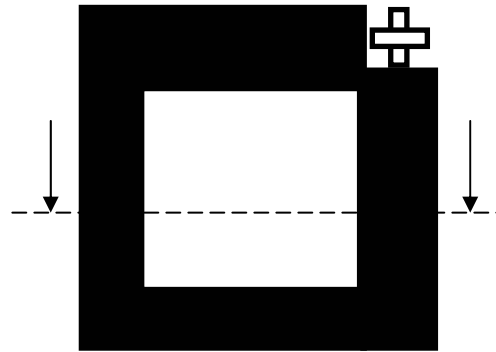


Step 4: Soft Baking



Step 5: UV Exposure of the single axis MM on the bottom mask

Cross-sectional View Plane of the MM Bottom Mask



 Silicon wafer with (110) orientation

 Thin layer of silicon oxide

 Resist Layer

 Exposed Resist Layer

Q = Heat

Step 6: Development of the photoresist



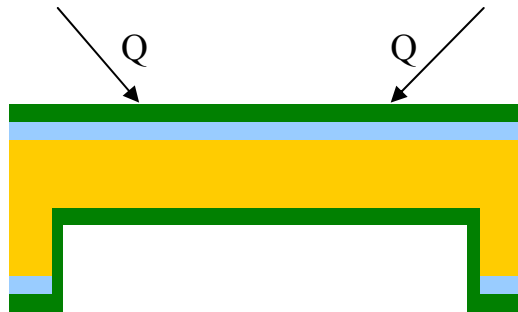
Step 10: Photoresist Layer Spinning



Step 7: Oxide Etching



Step 11: Soft Baking



Step 8: Photoresist Stripping



 Silicon wafer with (110) orientation

 Thin layer of silicon oxide

 Resist Layer

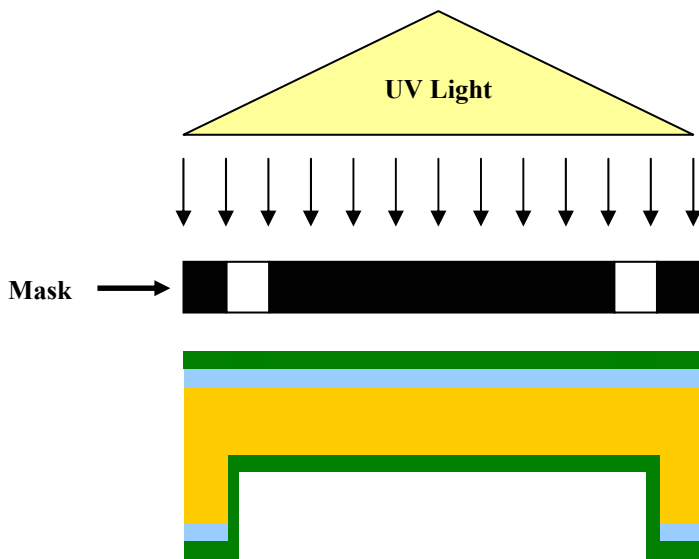
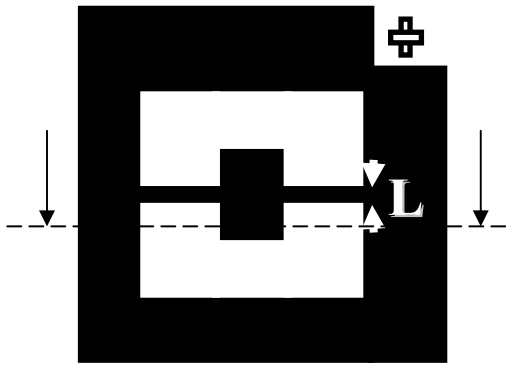
Q = Heat

Step 9: Bottom KOH etching



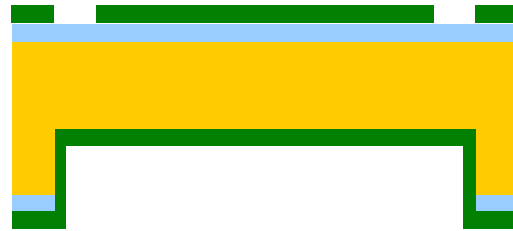
Step 12: UV Exposure of the single axis MM on the top mask

Cross-sectional View Plane of the MM Top Mask



-  Silicon wafer with (110) orientation
-  Thin layer of silicon oxide
-  Resist Layer
-  Exposed Resist Layer

Step 13: Development of the photoresist



Step 14: Oxide Stripping



Step 15: Photoresist Stripping



Step 16: Top KOH Etching



Step 17: Oxide Stripping



### **3.2 AutoCAD Design**

The MM designs were done using AutoCAD. The designs contain the shapes for two different masks: the top and the bottom masks. The top mask was used to expose the silicon wafer on the polished side and the bottom mask on the opaque side. The drawings include the designs for two kinds of MM. The first is a single-axis MM, consisting of a square plate supported by two torsional beams as shown in Figure 8(a). The beams thickness was varied to investigate how thin they could be made. They had thickness of 25 $\mu\text{m}$ , and 50 $\mu\text{m}$ , and 75 $\mu\text{m}$ . The second kind of MM has serpentine spring beams; it is shown in Figure 8(b). This variation in the design was to explore other fabrication possibilities.

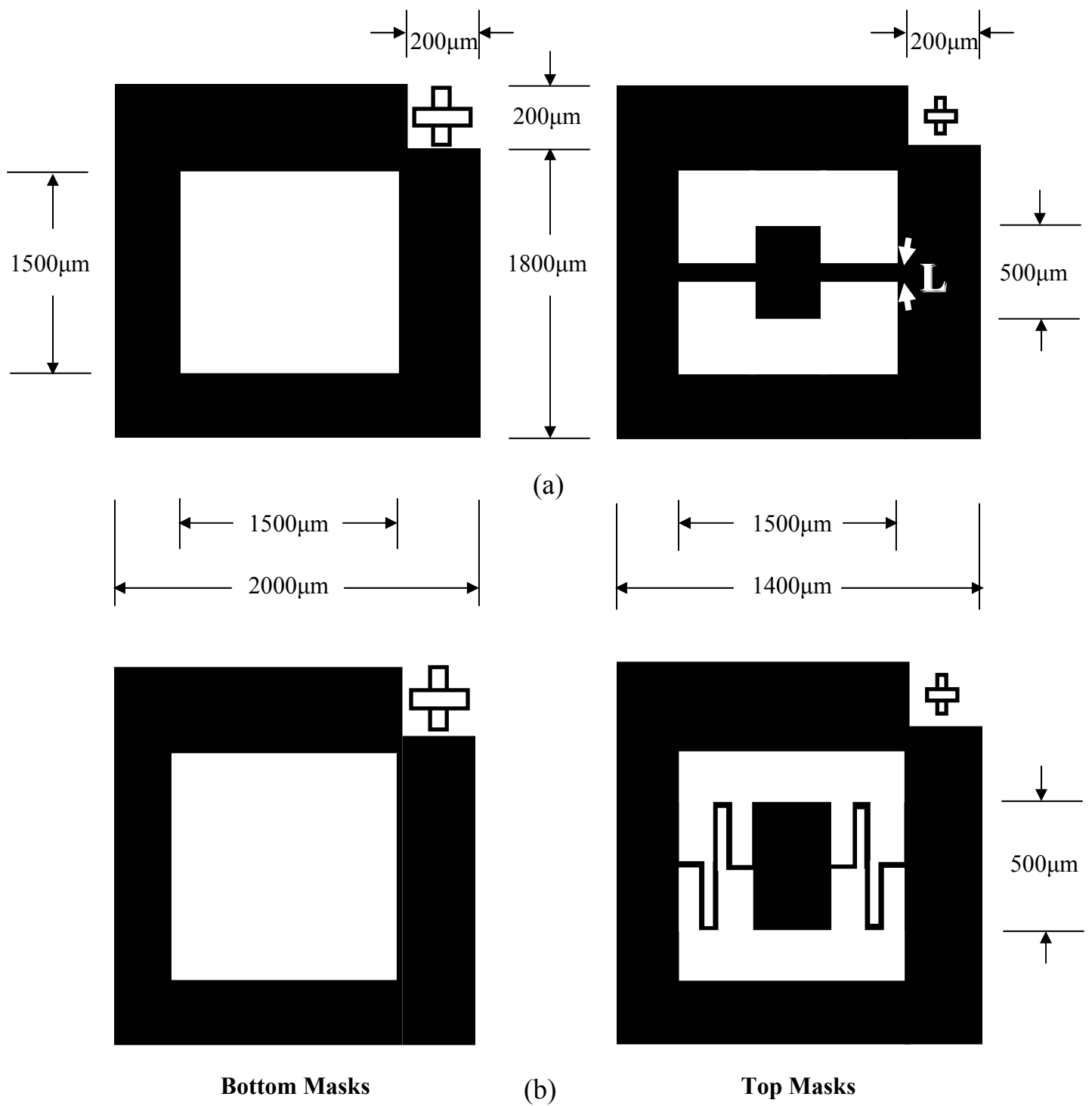


Figure 8: Drawings of the MM designs. (a) Single-axis MM, (b) Serpentine spring MM

## 4. RESULTS

### 4.1 Fabrication Results

The masks design was completed using AutoCAD and fabricated in the Microfab Lab facility. The mask is shown in Figure 9.

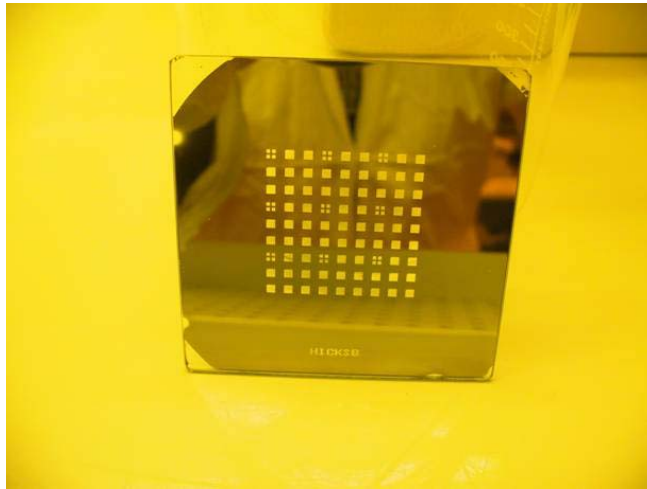


Figure 9: Bottom mask with corrected polarity.

The other fabrication result was the construction of the MM. Due to time limitations, the construction of MM was stopped after Step 8 in the process flow was finished. The unfinished silicon wafer is shown in Figure 10.

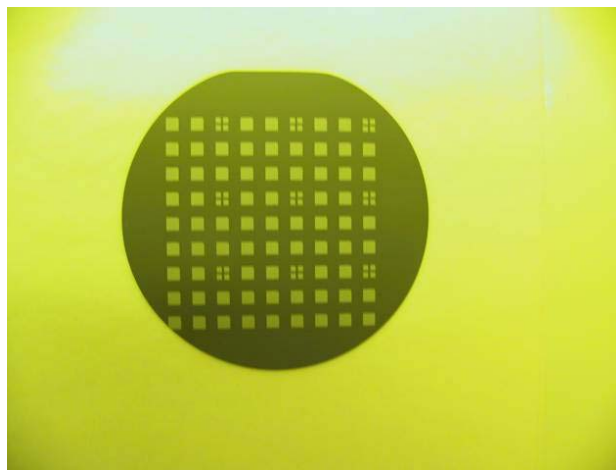


Figure 10: Silicon wafer used for the MM fabrication. This is how it looks after the Step 8 of the process flow was finished.

## 4.2 Mechanical Modeling

The mechanical modeling task was accomplished through the use of a macro scale prototype of a single-axis mirror. The material used for the prototype was polycarbonate and the Excimer Laser machine was used to cut it. The model considers the dependence of the force and torque on the prototype dimensions. Also, torsional properties of the material were considered with a maximum rotational movement of  $10^\circ$ . For polycarbonate two values of Young's modulus  $E$  and Poisson's ratio  $\nu$  were considered. Figure 11 shows a drawing of the prototype along with the forces/moments and dimensions.

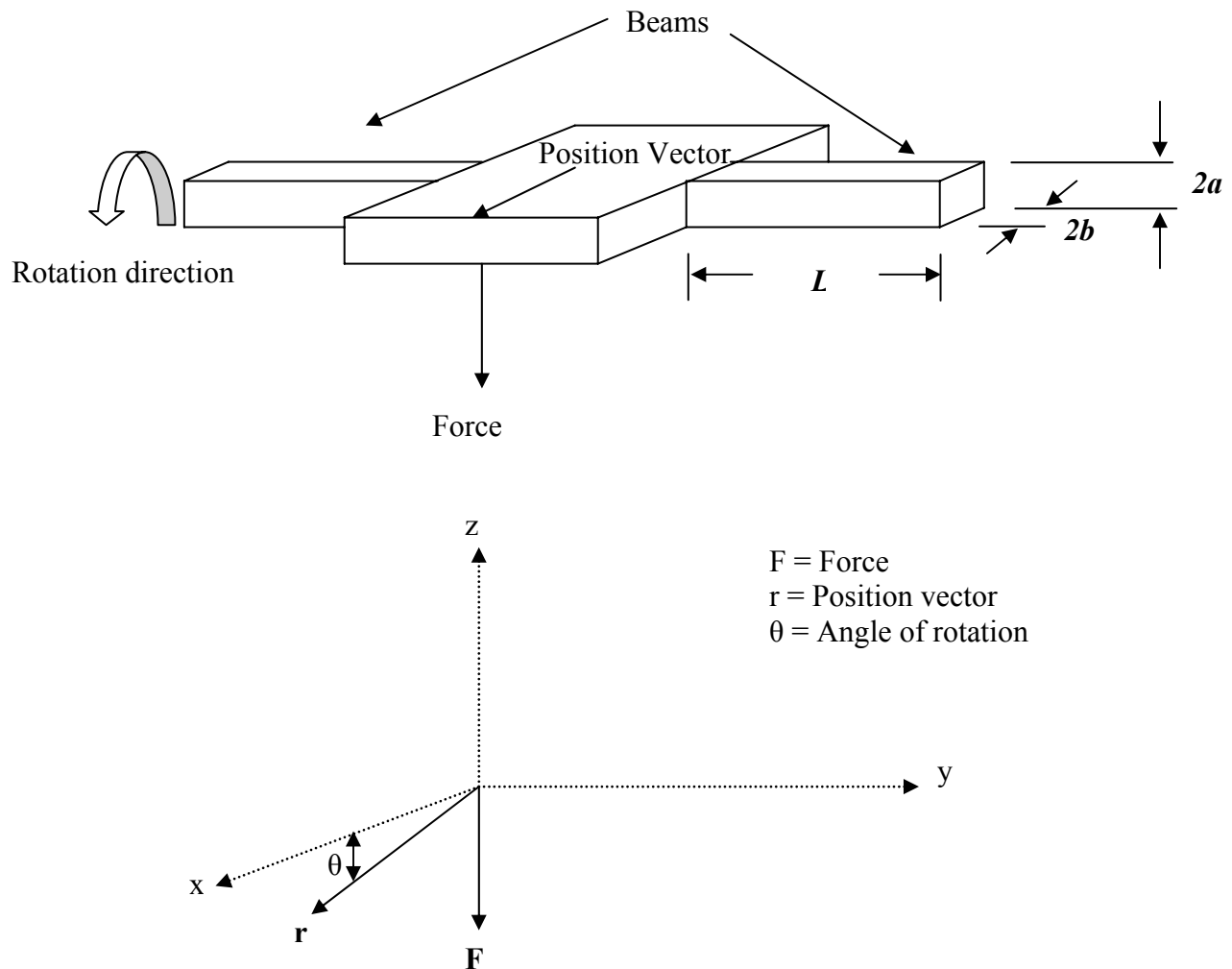


Figure 11: MM prototype drawing and its force diagram representation.

Geometrical properties of the solid rectangle beams:

$$Width = 2a \rightarrow a = \frac{Width}{2} = 0.01 \text{ in}$$

$$Thickness = 2b \rightarrow b = \frac{Thickness}{2} = 0.0625 \text{ in}$$

$$L = 0.369 \text{ in}$$

Modulus of rigidity:

$$G = \frac{E}{2(1+\nu)} \Rightarrow \nu \approx 0.4 - 0.5 \text{ and } E = 2.9, 6.9 \text{ GPa for polycarbonate}$$

Function of cross-sectional geometry:

$$K = ab^3 \left[ \frac{16}{3} - 3.36 \frac{b}{a} \left( 1 - \frac{b^4}{12a^4} \right) \right] = 0.003288 \text{ mm}^4$$

Toque calculation:

$$\mathbf{T} = \mathbf{r} \times \mathbf{F} = \begin{vmatrix} a_x & a_y & a_z \\ r_x & 0 & -r_z \\ 0 & 0 & -F \end{vmatrix}$$

$$\mathbf{T} = r_x F \mathbf{a}_y = Fr \cos(\theta) =$$

$$T = \text{Torque} = \frac{\theta GK}{l}$$

$$F = \frac{T}{r \cos(\theta)}$$

Solving for the torque and force for a maximum angle  $\theta = 10^\circ$  gives:

At  $E = 2.4 \text{ GPa}$  and  $\nu = 0.4$

$$T = 0.1627 \text{ N}\cdot\text{m}, F = 32.5173 \text{ N}$$

At  $E = 6.9$  GPa and  $\nu = 0.4$   
 $T = 0.4677$  N·m,  $F = 93.4871$  N

At  $E = 2.4$  GPa and  $\nu = 0.5$   
 $T = 0.1518$  N·m,  $F = 30.3494$  N

At  $E = 6.9$  GPa and  $\nu = 0.5$   
 $T = 0.4365$  N·m,  $F = 87.2547$  N

### 4.3 Prototype Actuation

The actuation of the macro scale polycarbonate prototype was attempted. The intention was to implement a method that could be reproduced in the micro scale. The proposed method was to make a piezoelectric material to move the MM replica of polycarbonate. The piezoelectric material plate shown in Figure 12 has length = 1.25", width = 0.125" and thickness = 0.015". (The dime is included to show the scale of the object.)

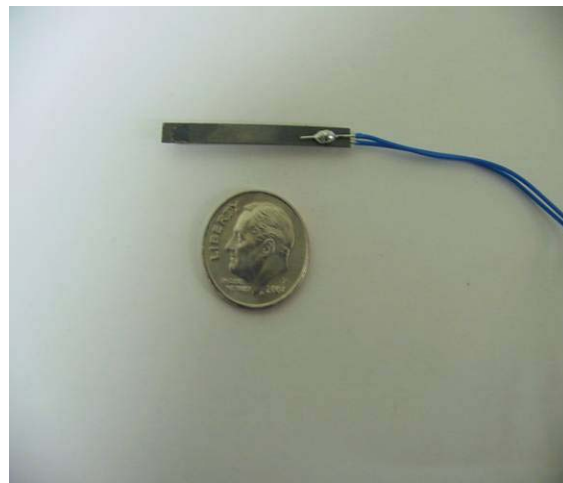


Figure 12: Piezoelectric material used for the actuation try.

To see appreciable movement, it was necessary to apply 120V across the thickness of the piezoelectric material. The movement was measured and compared to the results of the mechanical model. The voltage across the thickness of the piezoelectric material was measured along the length of each piece. The measurements are shown in Figure 13.

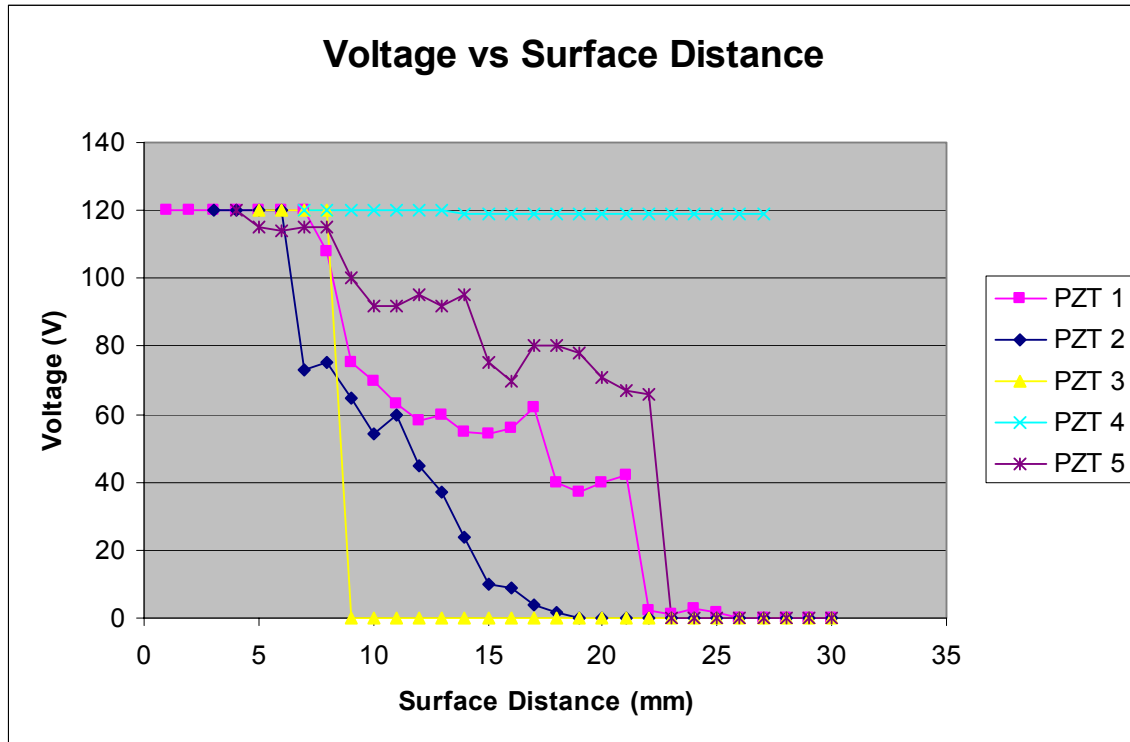


Figure 13: Voltage distribution along the length of the piezoelectric materials.

## 5. DISCUSSION AND CONCLUSIONS

During the summer, some complications slowed down the completion of the assigned tasks. First, the translator of Microfab Lab was not able to read the AutoCAD file that contained the mask drawings. Much time and effort was spent correcting the file to make it readable. Another factor was that the first fabricated masks had the wrong polarity, so what was supposed to be a dark section that wouldn't allow UV light to pass was clear. In the same way, what was supposed to be the clear section was dark. The masks with the wrong polarity are shown in Figure 14.

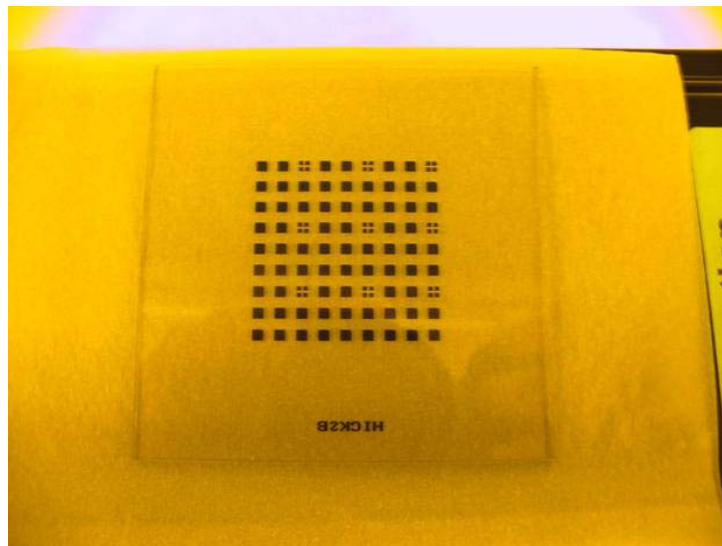
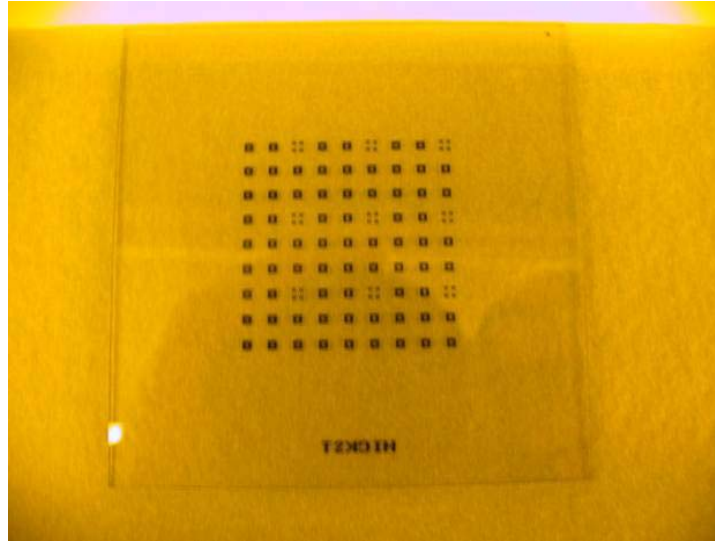


Figure 14: Fabricated masks with wrong polarity.

Although the completion of the fabrication of the MM was not possible, the wafer processing could be continued along the lines indicated in this report.

Of the five pieces of piezoelectric materials that were available, only two showed movement. However, of these two, only one moved well. In Figure 13 the results for the two piezoelectric materials that moved are denoted as PZ1 and PZ5. The measurements from the plate that move very well (PZ1) show that the voltage across the material is almost constant, which means that the charge distribution across its length is almost constant, too. In the case of plate PZ5, it does not have a uniform charge distribution

across it. This suggests that there should be a minimum voltage and distance to make this kind of material move.

## 6. RECOMMENDATIONS

To continue this work in the future, finish the fabrication of the single-axis MM, and explore two-axis MM fabrication. I recommend finishing the fabrication and trying to design and implement the actuation at the macro and micro levels. Since the wafers are thinner than the ones currently used in the Microfab Lab, it is important when KOH etching to check how deeply the wafer is etched at frequent intervals. Also, for the actuation, it will be important to make the proper selection of the piezoelectric materials used. Another alternative for the actuation is to use a compliant mechanism to amplify the movement of the piezoelectric materials.

## 7. ACKNOWLEDGMENTS

I would like to thank the National Science Foundation for the support for undergraduate students and give the opportunity to experience research. Also, I would like to express my gratitude to the SUNFEST program for giving me the opportunity to be a participant. The more special thanks are for my advisors Dr. Ananthasuresh and Dr. Hicks for their tremendous advising and availability, and for giving me the opportunity to work with them. Finally, I would like to thank Prof. Van der Spiegel, Prof. Santiago, Prof. Lee, Prof. Bloomfield, Prof. Zemel, Salvador, and Dr. Scott Slavin for their support and help during this research.

## 8. REFERENCES

- 1) <http://www.i-o.com/content/includes/MEMSmirror.pdf>  
H. Goldberg, D. Yu, B. Reichert, K. Speller, *A MEMS Mirror for Optical Scanning*, Applied MEMS, Inc.
- 2) R. A. Hicks, R. Bajcsy, *Catadioptric Sensors that Approximate Wide-angle Perspective Projection*, CVPR 2000. pp. 545-551.
- 3) J. D. Plummer, M. D. Deal, P. B. Griffin, *Silicon VLSI Technology: Fundamentals, Practice and Modeling*, Prentice Hall, New Jersey, 2000, pp 7-8, 94-96, 201-281
- 4) S. Kang, Y. Chen, G. Chang, *The Manufacture and Test of (110) Orientated Silicon Based Micro Heat Exchanger*, Tamkang Journal of Science and Engineering, Vol. 5, 2002, pp. 129-136

- 5) M. Madou, *Fundamentals of Microfabrication*, CRC Press, New York, 1997, pp. 1-86.
- 6) K. J. Gabriel, *Engineering Microscopic Machines*, Scientific American, September 1995, pp. 150-153
- 7) D. J. Bishop, C. R. Giles, S. R. Das, *The rise of Optical Switching*, American, January 2001, pp. 88-94
- 8) G. T. A. Kovacs, *Micromachined Transducers Sourcebook*, McGraw-Hill, New York, 1998, Ch. 5
- 9) [http://www.ee.byu.edu/cleanroom/./EW\\_orientation.phtml](http://www.ee.byu.edu/cleanroom/./EW_orientation.phtml)
- 10) [http://whatis.techtarget.com/definition/0,,sid9\\_gci212793,00.html](http://whatis.techtarget.com/definition/0,,sid9_gci212793,00.html)
- 11) [http://www.opticsforkids.org/resources/Intro\\_to\\_Mirrors\\_and\\_Lenses.pdf](http://www.opticsforkids.org/resources/Intro_to_Mirrors_and_Lenses.pdf)
- 12) <http://www.bmva.ac.uk/bmvc/1998/pdf/p021.pdf>

*University of Pennsylvania*  
Center for Sensor Technologies

**SUNFEST**

NSF REU Program  
Summer 2004

**PORPHYRIN THIN FILM DIELECTRICS**

NSF Summer Undergraduate Fellowship in Sensor Technologies  
Matthew Saucedo (Electrical Engineering) Texas A&M University- Kingsville  
Advisor: Dr. Jorge Santiago

**ABSTRACT**

New advances in technology are creating numerous power electronic applications. These applications require a substantial amount of energy that can be produced using capacitor technologies. Novel molecular dielectrics are now being incorporated in capacitors to achieve high energies, and high polarizability.

In this project, different methods of characterizing the molecular chromophore porphyrin were evaluated. The first approach was to spin cast polypropylene doped with Zinc tetraphenylporphyrin (ZnTPP) or zinc diphenylporphyrin (ZnDPP) onto gold sputtered wafers which were to be characterized using a newly constructed capacitance testing device. Analysis of the data produced by this device suggested other potential characterization methods, including the fabrication of Indium Tin Oxide (ITO) Sandwich Cells and the use of microfabrication techniques. Multi-layering porphyrin thin film layers was also under experimentation. These methods have set a firm foundation such as providing experimental methods, as well as troubleshooting that will eventually lead to the proper characterization of thin film porphyrin dielectrics.

## Table of Contents

1. INTRODUCTION.....	3
2. BACKGROUND.....	4
2.1. Dielectrics.....	4
2.2. Capacitor Fundamentals.....	5
2.2.1 Theory.....	5
2.2.2 Capacitors Today.....	5
2.3. Porphyrin.....	6
3. EXPERIMENTAL METHODS.....	7
3.1. Capacitance Device.....	7
3.1.1 Substrate.....	8
3.1.2 Spin Coating.....	8
3.1.3 Testing and Results.....	9
3.2. (ITO) Sandwich Cell Capacitor.....	10
3.2.1 Testing and Results.....	10
3.3. Photolithography.....	11
3.3.1 Testing and Results.....	13
4. DISCUSSION AND CONCLUSIONS.....	14
5. RECOMMENDATIONS.....	14
6. ACKNOWLEDGEMENTS.....	14
7. REFERENCES.....	15
APPENDIX A: Device. Blueprints.....	16
APPENDIX B: Theoretical Calculations.....	17
APPENDIX C: Cole-Cole plot.....	18

## 1. INTRODUCTION

New advances in technology are generating numerous power electronic applications that require considerable amounts of energy. This unprecedented growth can be attributed to the confluence of several technologies, such as computers, wireless telecommunications, electrical vehicles, and power transmission [1, p.16]. These applications have paved the way for a revolution in capacitor technologies.

There are a wide variety of capacitors in use including ceramic and polymer film capacitors. Ceramic capacitors are largely used because of their high dielectric constants,  $K > 5000$ . However, they suffer from low breakdown strengths. Polymeric film capacitors exhibit an enormous dielectric strength, ranging up to 10,000 V, but typically exhibit a very low dielectric constant [1, p.20]. The major advantages of polymeric films are low cost, and ease of production.

Over the last couple of decades, capacitor technologies have evolved due to breakthroughs in molecular chemistry, better understanding of molecular polarizability, and the introduction of new synthesis techniques. Different dielectric media are being established and subjected to a variety of tests. The dielectric media under observation include molecular chromophores.

Several labs at the University of Pennsylvania, directed by Dr. Santiago and Dr. Therein, are evaluating methods for characterizing molecular dielectrics. The overall goal is to develop dielectric composites using ferroelectric nanoparticles and molecular chromophores for the fabrication of high energy capacitors. These various composites may eventually give rise to novel dielectrics exhibiting both high dielectric breakdown, and high dielectric strength.

The objective for the SUNFEST 2004 project is to successfully create porphyrin thin films and composites, and derive various methods for measuring the dielectric response, and other properties exhibited by the dielectric media. Zinc tetraphenylporphyrin (ZnTPP) and Zinc diphenylporphyrin (ZnDPP) are two different types of porphyrin that were explored.

## 2. BACKGROUND

### 2.1 Dielectrics

Dielectrics are electrical insulating materials that have the ability to absorb charge. They contain charges that are tightly bound to individual nuclei. These charges can move only a fraction of an atomic distance away from their equilibrium positions [2, p.132]. When dielectrics are subjected to an external electric field (polarizing field), electron clouds distort (or polarize) forming electric dipoles (as in Figure 1). This in turn generates an opposing electric field that changes the macroscopic field inside and outside the dielectric.

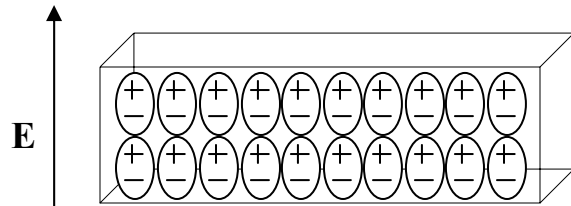


**Figure 1.** A uniformly polarized dielectric

Dielectrics can be classified into two categories, linear and non-linear. A dielectric is said to be linear when the relative permittivity is constant and independent of applied voltage. The relationship between the polarization vector and the Electric Field of the dielectric media is expressed mathematically through the equation:

$$\mathbf{P} = \chi_e \epsilon_0 \mathbf{E} \quad [3]$$

where  $\mathbf{P}$  = polarization vector,  $\chi_e$  = electric susceptibility,  $\epsilon_0$  = permittivity of free space.

This equation merely demonstrates that the polarization vector is proportional to the electric field since the electric susceptibility is a unitless constant, which is the measure of ease with which dipoles can be formed into the dielectric [2, p.134].

In dielectric composites and non-homogeneous materials, the electric susceptibility,  $\chi_e$ , varies with position, thus allowing different magnitudes of polarization. In nonlinear media,  $\chi_e$  is a function of the magnitude of the Electric Field,  $\mathbf{E}$  [2, p.134]. Since this project involves a homogeneous layer, and composites of the dielectric porphyrin, different magnitudes of the polarization vector were expected. An external electric field (polarization field) is achieved by sandwiching the dielectric between two conducting plates, forming a capacitor.

## 2.2 Capacitor Fundamentals

### 2.2.1 Theory

A capacitor is essentially an electronic device that can store electrical charge. The amount of charge a capacitor can store is equivalent to the expression:  $Q=CV$ . To calculate the capacitance of an element that consists of two or more distinct conductors, this equation can be rewritten in terms of the Electric Field generated by charges on the conductors:

$$C = \frac{\oint_{S^+} \epsilon \mathbf{E} \cdot d\mathbf{s}}{\int_{S^+} \mathbf{E} \cdot d\mathbf{l}} \quad [\text{F}] \quad [2, \text{p.180}]$$

When using a parallel plate configuration, the capacitance is defined as:

$$Q/V = (\rho_s S)/V = (\epsilon VS)/(dV) = \epsilon S/d \quad [\text{F}] \quad [2, \text{p.181}]$$
$$\epsilon = \epsilon_0 \epsilon_r$$
$$\epsilon_0 \sim 8.85 \times 10^{-12} \quad [\text{F/m}]$$

where  $S$ ,  $V$ ,  $d$ ,  $\epsilon_r$  represent the area, Voltage, and relative permittivity respectively.

It is easily seen through this equation that the relative permittivity (dielectric constant) affects the total capacitance.

### 2.2.2 Capacitors Today

Existing capacitor technologies include the minimization of capacitor devices and the incorporation of thin film polymer dielectrics. Although these dielectrics tend to exhibit a low dielectric constant, they exhibit very large dielectric strengths, enduring up to 10,000 volts [1, p.20]. Another advantage displayed by these thin films is that they can be used in metallized film capacitors. Metallized film capacitors are advantageous because they exhibit a “self healing” phenomena. Two electrodes short-circuit through a defect in the dielectric, resulting in the current vaporizing the metallization near the short. This effectively disconnects the shorted portion from the rest of the capacitor [1, p.22].

Although these capacitors constitute a mature technology, dramatic improvements in their performance can be realized through established electronic materials chemistry. Novel approaches in molecular chemistry are now creating and exposing potential dielectric substitutes and composites. One such molecular chromophore is porphyrin.

## 2.3 Porphyrin

Porphyrins, from the greek word *porphura* (purple), are based on 16-atom rings containing four nitrogen atoms [4]. Porphyrins occur widely in nature and play vital roles in various biological processes. One example is Heme, which contain iron porphyrins that are largely responsible for oxygen transport and storage in living tissues [5]. One unique quality of porphyrin is the ability to insert metals into their molecular structure. Metals such as iron, cobalt, copper, nickel, and zinc have been used in establishing different porphyrins.

The porphyrins in this research project contain zinc as their central metal ion. Various literature searches indicate that Zinc porphyrins are one of the easiest to prepare from free base porphyrins, as well as being the most stable. This project uses Zinc tetraphenylporphyrin (ZnTPP), and Zinc diphenylporphyrin (ZnDPP). These porphyrins have a slightly different molecular structure from one another; ZnDPP exhibits open meso positions, while ZnTPP does not, (Figure 2).

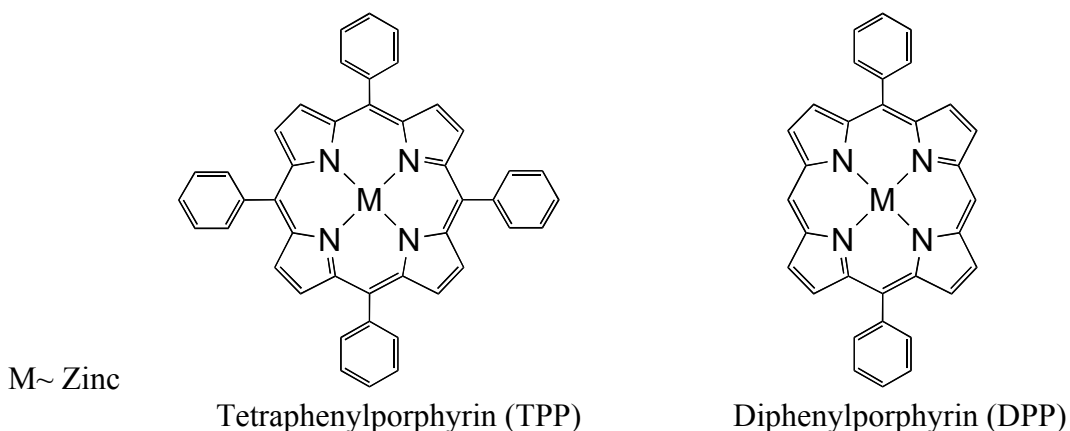


**Figure 2.**  
Molecular structure of porphyrins used in the research experiment.

### Polarization

Porphyrins are polarizable because their ground state electronic structure has almost all pi electrons delocalized throughout the linear molecule. When external fields are introduced, the electrons/ electron density shift so that there is an overall negative charge at the positive electrode and an overall positive charge at the negative electrode. Since the electrons are delocalized and constantly moving through the pi orbitals of all the atoms, the polarized state is rather stable.

## **Potential Disadvantage**

One potential disadvantage that porphyrins tend to display is the phenomena of photobleaching. Photobleaching, also commonly referred to as “fading,” occurs when a fluorophore permanently loses the ability to fluoresce due to photon-induced chemical damage and covalent modification [6]. This changes the chemicals electrical properties, possibly making it more conductive. Since we are experimenting with porphyrin as a dielectric, this would lead to unwanted results.

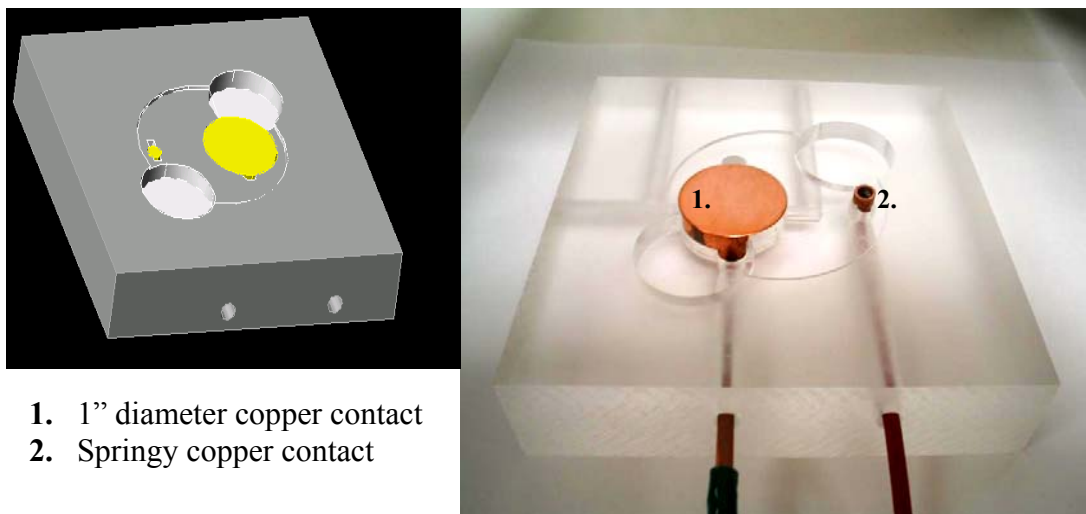
To limit the “fading” of our samples, a desiccator was used with aluminum foil sides to prevent the penetration of light. Samples were also stored in small containers in the microfabrication laboratory. Although these precautions were taken, the samples were eventually exposed to light during e-beam evaporation and spin coating. This could have caused unwanted light activation as well as a greater potential to interact with oxygen, but since exposure was kept to a minimum, the porphyrin thin films were suggested to be testable up to a week.

## **3. EXPERIMENTAL METHODS**

This section reports on efforts to create experimental setups for characterizing composites and homogeneous layers of the porphyrins Zinc tetraphenylporphyrin (ZnTPP), and Zinc diphenylporphyrin (ZnDPP).

### **3.1 Capacitance Device**

The first method employed was the construction of a capacitance device, enabling relatively quick, precise measurements of capacitance with dielectric coated substrates. Initial designs for the device were created using AutoCAD 2000i software. The device was fabricated in the Mechanical Engineering machine shop located at Towne building (see Appendix A). Two copper contacts were also constructed using a lathe machine. After the fabrication, silver epoxy was used to attach braided copper wire to the copper contacts. The fully assembled device is displayed in Figure 3.



1. 1" diameter copper contact
2. Springy copper contact

**Figure 3.** (left) Autocad design of Capacitance Device, (right) constructed Capacitance Device

### 3.1.1 Substrate

The substrate in use is a silicon wafer. After the wafer was chemically cleaned and dried, a thin layer of silicon dioxide was applied to the surface of the substrate. The wafer was then placed inside an e-beam evaporator machine to deposit gold contacts. In an e-beam evaporator machine, a small amount of gold is placed inside a crucible. The crucible is bombarded by a beam of electrons evaporating gold onto the surface of the substrate. The wafers were now ready for spin coating.

### 3.1.2 Spin Coating

Spin coating allows the simple production of relatively thin films. The action of centrifugal forces due to the rotating substrate spreads the drop of solution as the solvent evaporates leaving a thin film on its surface [7, p.104]. Five gold coated wafers were used to spin coat different porphyrin composites. The first step was to tape an outside edge of the wafer, thus allowing a conducting edge after spinning. A solution was produced using a half a gram of polypropylene and 25ml of the solvent decalin. Two to three drops of this solution was then applied to the surface of the wafer, which was spun at 4000 rpms for approximately 60 seconds. The wafer was then placed onto a 240°C hotplate for approximately two minutes. After annealing, 5mg of ZnTPP was dissolved in a 20 M polypropylene solution, and spun onto the wafer under similar spinning conditions. This process was repeated on a total of three gold wafers, (see Figure 4). The porphyrin ZnDPP was used on the other two wafers, following the same process.

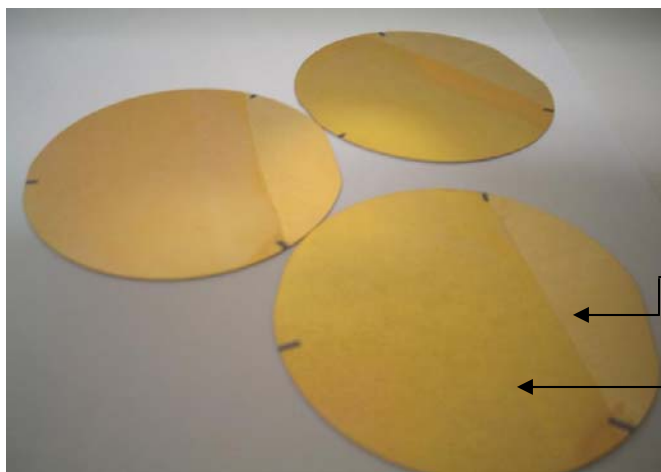


**Figure 4.**  
Spin Coated Wafers  
-Conducting Edge  
-Thin film dielectric

### 3.1.3 Testing and Results

The dielectric coated wafers were tested using the capacitance device and an HP 4276A LCZ meter. In order to make capacitance measurements the wafer is placed dielectric face down onto the 2” dish in the capacitance device, with the conducting edge over the springy contact. A foam cushion is placed on the back of the wafer, with a 200 gram weight on top to establish pressure. The other 1” diameter copper contact completes the capacitor. The two copper wires were then connected to the LCZ meter to make appropriate measurements of capacitance versus frequency (Figure 5).

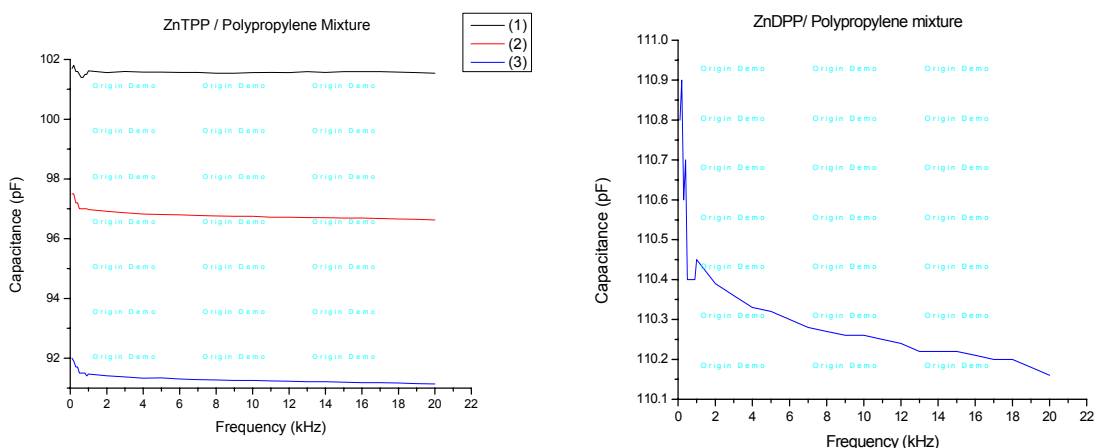


**Figure 5.** *capacitance vs. frequency*  
(Left) ZnTPP / Polypropylene Mixture, (Right) ZnDPP / Polypropylene mixture.

Unfortunately, this method encountered a significant number of problems. Due to the malfunctioning stylus profilometer the thickness of the thin film could not be measured. Ellipsometry could not be used either because the film was not very transparent. It was assumed that the thickness was less than one micron, and using this assumption the derived result was a dielectric constant less than one. The capacitance values obtained were also

questionable, due to the oxidizing copper contacts. After the copper contacts were chemically cleaned, the device still produced similar results. Further investigation determined that the device contained internal parasitic capacitance from the copper contacts, diminishing the actual capacitance.

### 3.2 (ITO) Sandwich Cell Capacitor

A new method was devised allowing precise contacts to be established by creating sandwich cell capacitors. Indium Tin Oxide (ITO) was sputtered onto glass plates to create a conducting substrate. These conducting substrates were used since the supply of gold and silicon wafers were exhausted. A solution was created using 20mg of Zinc tetraphenylporphyrin (ZnTPP) with 2 ml of the solvent tetrahydrofuran (THF). Three to four drops of this solution was placed onto the substrate, and spun at 4000 rpms for approximately 60 seconds. This process was done on a total of four ITO substrates. Since ITO is transparent, a silica substrate is spun with the same solution so film thickness could be measured using the ellipsometry device.

An Infrared Laser machine (Universal Laser Systems X660) was used to create a 3mm square pattern onto clear plastic Mylar; the pattern served as a shadow mask during e-beam evaporation. Gold was evaporated through the mask and onto the dielectric, creating a gold square contact. Thin copper wire was then connected to the ITO substrate and gold square contact with silver epoxy. The final results were four sandwich cell capacitors ready for testing, Figure 6.

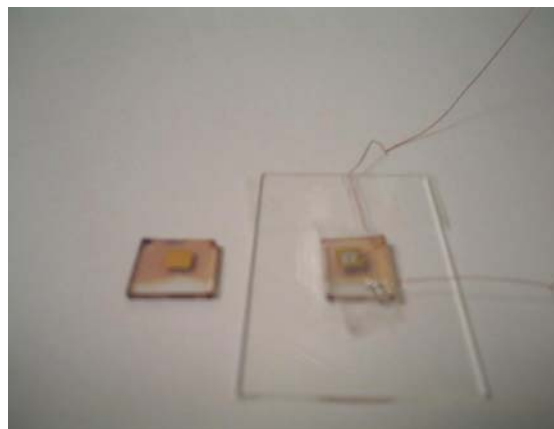
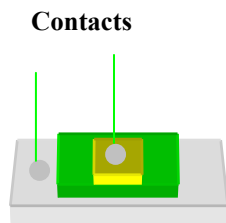


**Figure 6.** Indium Tin Oxide Sandwich Cell Capacitors

#### 3.2.1 Testing and Results

Upon testing, it was discovered that the porphyrin thin films contained minor pinholes, creating shorts. One possible solution was to experiment with the “self healing” characteristics of porphyrin. As noted in Section 2.22, metallized capacitors exhibit a certain phenomenon that when connected to high levels of voltage, the small shorted contacts are destroyed preventing conduction. Ten volts was applied to each ITO capacitor for approximately thirty minutes. Upon inspection, it was observed that the ITO capacitors still suffered from minor shorts. Two possible explanations for this predicament are that the

dielectric thin film was burned, allowing conduction to continue, or several small pinholes remained causing shorts. The same spinning process was performed a second time, but the film still exhibited the same behavior.

Multi-layering porphyrin thin films was also tried, but did not produce the desired results. Most samples spun and hard baked displayed non-uniformity. Also, the porphyrin solutions always aggravated and disturbed the previous thin film layer.

Another method employed involved using different porphyrin samples. A trimer porphyrin (DDD) and Zinc diphenylporphyrin were exposed to similar spinning conditions. It was observed under microscope analysis that these porphyrin films suffered from the same pinhole phenomena, although the size of the pinholes varied widely, as shown in Figure 7.

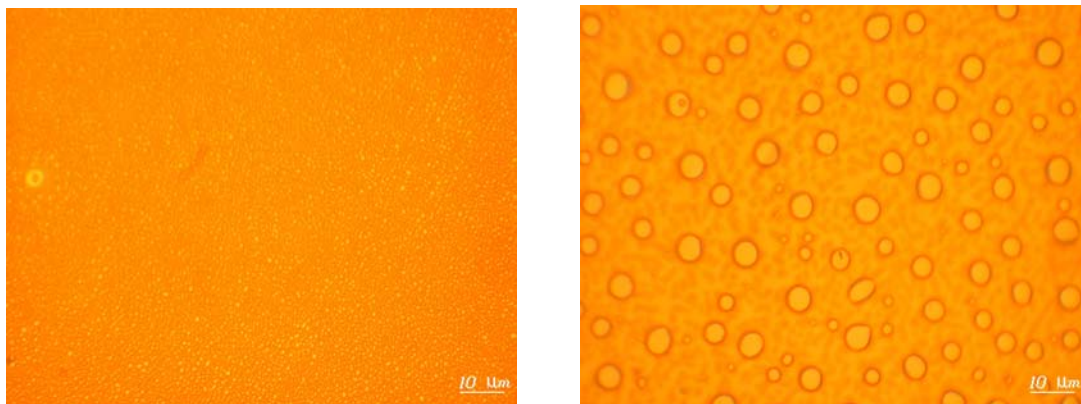


**Figure 7.** Zinc-diphenyl-porphyrin (ZnDPP) (DDD) Trimer porphyrin

Due to the time consuming process of e-beam evaporation and thin film layering this method was eventually abandoned.

### 3.3 Photolithography

A final method was then introduced involving the micro-fabrication of fixed electrodes for measuring the dielectric response of the porphyrin (ZnTPP). The electrodes were produced using a micro-fabrication technique known as photolithography.

Photolithography is an optical means for transferring patterns onto a substrate [8]. It can generally be performed using positive or negative photoresist. These two photoresists have different chemical reactions when exposed to ultra violet light. Positive photoresist becomes soluble in developer solution, while negative photoresist hardens and becomes practically insoluble. For our experiment a positive photoresist was used.

First, glass substrates were chemically cleaned to remove impurities and organic residue. The glass substrates were then placed inside the e-beam machine, evaporating a maximum gold thickness of 250 nm. A second cleaning was performed by rinsing the gold plates with acetone, isopropanol, and de-ionized water. They were then spun dry and prepared for the process of photolithography.

Positive photoresist was applied to the surface of the gold substrate, and spun at 4000 rpms for approximately 30 seconds. The gold plate was then soft baked, allowing solvent to evaporate and photoresist to harden.

After the soft bake was completed a mask was aligned with the gold substrate. Ultraviolet light was projected through the mask and onto the photoresist. As a result, the exposed

photoresist was chemically changed, becoming soluble in resist developer. After 15 seconds of UV exposure, the slide was developed in positive photoresist developer for approximately 35 seconds. The gold substrate was then submerged in deionized water for one minute, and spun dry. Hard baking was performed to harden photoresist and enhance adhesion, which was followed by gold etching with potassium iodide and iodine. The final product was a substrate of gold patterned electrodes spaced 20um apart, shown in Figure 8. Positive photoresist was then removed and the substrate was prepared for spin coating.

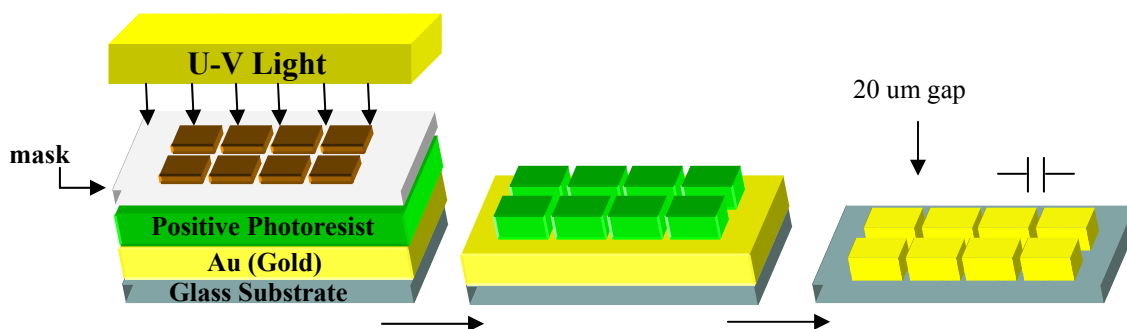


**Figure 8.** The photolithography process, shown in order from left to right

A 10 M solution of Zinc tetraphenylporphyrin (ZnTPP) was created with the solvent tetrahydrofuran (THF), and placed onto the gold patterned substrate. The sample was then spun at 4000 rpms for 60 seconds. Under microscope investigation it was observed that the dielectric had a slightly darker appearance within the 20um gaps, suggesting it was successfully within the gap. The electrodes were then chemically cleaned with tetrahydrofuran (THF) solvent, and connected with thin copper wire using silver paint (see Figure 8).

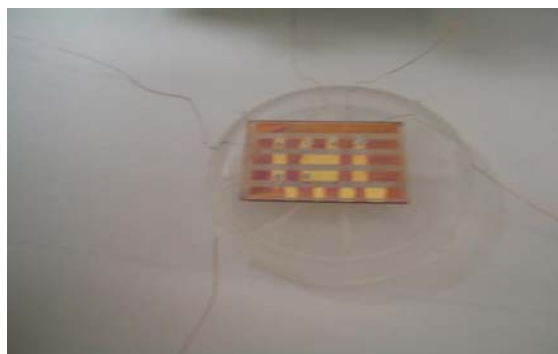


**Figure 8.** Final Product: Dielectric covered substrate

### 3.3.1 Testing and Results

The substrate was tested with an Agilent impedance analyzer 4249a. This particular equipment was used to see if the substrate behaved like a capacitor. Since the dielectric had a thickness greater than 250 nm it was expected to display fringing capacitance. A very small capacitance was also expected due to the small area of the electrodes (see Appendix B). The impedance was measured with varying frequency and a cole-cole plot (Figure 9) was produced. (Since some dielectrics tend to exhibit a small amount of leakage current, dielectric capacitors are usually modeled as a parallel combination of a resistor and capacitor. A cole-cole plot of this equivalent circuit is illustrated in the Appendix C). The measured results did not show this relationship. Certain measurements seemed to be out of range of the equipment. It was suggested that this was due to the thickness of the dielectric, causing fringing capacitance. The true capacitance could not be calculated due to the erratic pattern of the cole-cole plot. However, under ideal conditions the capacitance was calculated to be approximately 4pF. A possible explanation for this large capacitance resides in the instrument itself; it was speculated that the internal capacitance of the instrument was measured, rather than the small capacitance produced by the substrate.

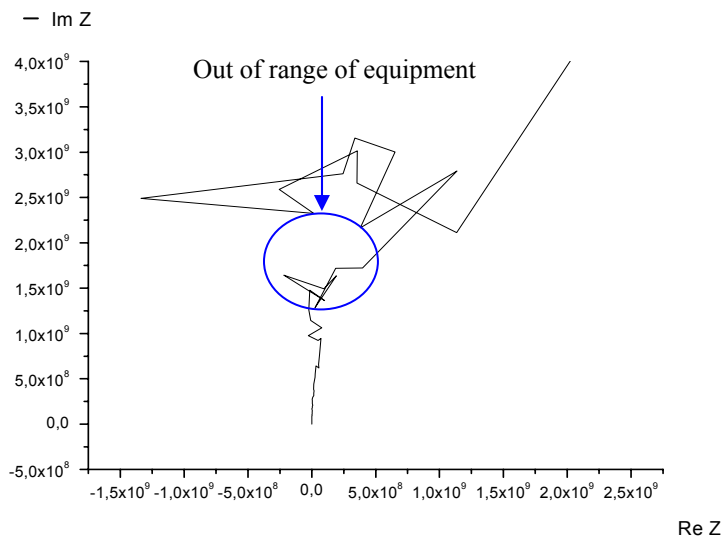
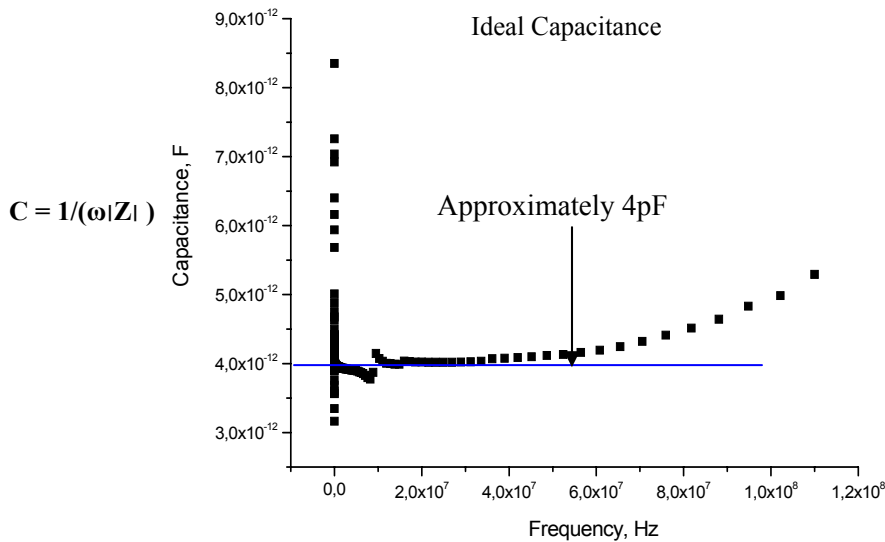


**Figure 9.**  
**Top**  
 Cole-cole plot  
**Bottom**  
 Calculated Ideal  
 Capacitance



#### **4. DISCUSSION AND CONCLUSIONS**

Although these methods did not produce the desired results, they provided a vital stepping stone toward future implementations. Various methods were investigated and compared to one another, establishing a concrete chain of steps to follow for future work. In the future, different molarities of porphyrin should be explored in establishing uniform thin films. Although this was a desired investigation in this experiment, limited amounts of porphyrins were available limiting the concentration of the solutions. For better spinning results, the spinning process should continue in the microfabrication laboratory clean room. The microfabrication clean room has different filtering systems than the chemistry laboratory, which would provide better spinning conditions, thus providing better results.

#### **5. RECOMMENDATIONS**

Spin coating is just one of the methods of film deposition. Another experimental method that could be used is vapour phase film deposition. Under high vacuum, the vapours of the solution are deposited as films which can be successfully measured by a stylus method [7, p.39]. This could provide a uniform, homogeneous thin film, enabling the proper characterization of the dielectric. Journal searches also suggest the use of a scanning probe microscopy apparatus in making successful calculations of capacitance.

Various composites, such as porphyrin mixtures with PZT can be created and studied in future work. These specific types of composites may eventually lead to novel dielectrics that have a very large dielectric breakdown, and dielectric constant.

#### **6. ACKNOWLEDGMENTS**

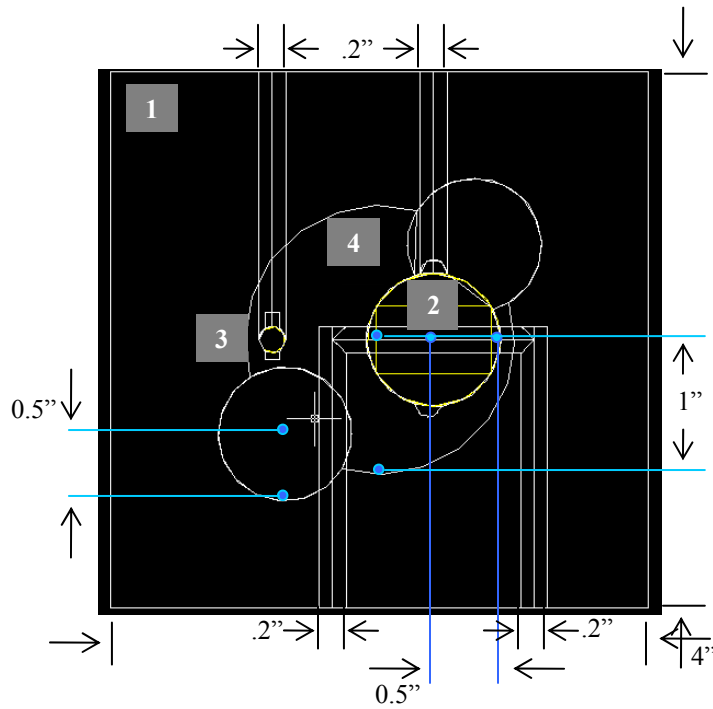
I would first like to extend my appreciation to Dr. Santiago for his help and guidance throughout the summer project. I would also like to take this opportunity to express my gratitude to Paul Frail, who provided me with porphyrin samples as well as valuable knowledge regarding porphyrin chemistry. I am also grateful to Dr. Scott Slavin for his guidance in the microfabrication laboratory, and other staff for all of their support throughout the duration of the project. Last, but not least, I would like to thank the National Science Foundation for supporting such a beneficial program (SUNFEST) that has greatly influenced my intention of pursuing graduate studies.

## 7. REFERENCES

- [1] R. Anklekar, M. Lanagan, *Trends and Developments in Capacitor Technologies for Power Electronics Applications*, Passivecomponent Industry, July/August 2001
- [2] K. Demarest, *Engineering Electromagnetics*, Prentice Hall, New Jersey, 1998
- [3] C. Kittel, *Introduction to Solid State Physics 7<sup>th</sup> edition*, John Wiley & Sons Inc., New York, 1996, pg. 385.
- [4] “Porphyrin and Metalloporphyrin chemistry” Available from:  
<http://www.scs.uiuc.edu/suslick/execsummporph.html>, Accessed from: 5 Aug 2004.
- [5] “The Porphyrin Page” Available from:  
[http://www.washburn.edu/cas/chemistry/sleung/porphyrin/introduction\\_frame.html](http://www.washburn.edu/cas/chemistry/sleung/porphyrin/introduction_frame.html),  
Accessed from: 5 Aug 2004.
- [6] “Photobleaching” Available from:  
<http://micro.magnet.fsu.edu/primer/java/fluorescence/photobleaching/>, Accessed from: 5 Aug 2004
- [7] K. Kadish, K. Smith, R. Guilard, *The Porphyrin Handbook Volume 17 Phthalocyanines: Properties and Materials*, Academic Press, San Diego, CA, 2003
- [8] “Photolithography” Available from:  
<http://www.eng.utah.edu/~gale/mems/photolithred.pdf>, Accessed from: 5 Aug 2004

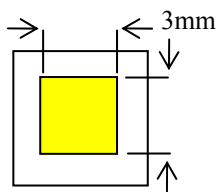
**APPENDIX A:**

**Autocad drawing - Capacitance Device**

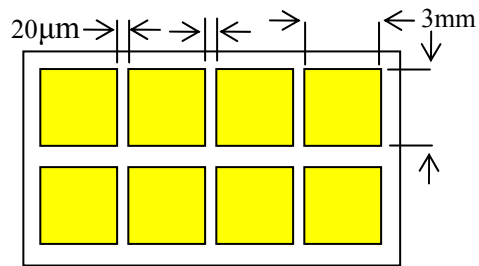


	(1) platform	(2) Large contact	(3) Small contact	(4) Circular dish
diameter	-----	1"	.2"	2"
height	.8"	.5"	.5"	-----
depth	-----	-----	-----	1mm

**ITO capacitor  
(Top view)**



**Gold patterned substrate  
(Top view)**



Height of gold contact: 250nm

## APPENDIX B:

### Theoretical calculations

#### (First method) Capacitance device

$$\begin{aligned}\text{Capacitance} &= (\epsilon_r \cdot \epsilon_0 \cdot \pi \cdot r^2)/d & \epsilon_r &= \epsilon_{\text{mixture}} \\ &= ((\epsilon_r \cdot 8.85\text{EE-12})(\pi \cdot (0.0127)^2))/d \\ &= (\epsilon_r \cdot 4.48\text{EE-15})/d \quad [\text{F}]\end{aligned}$$

$$(d < 1\mu\text{m}) \text{ -----} > (\text{Capacitance} > \epsilon_r \cdot 14.088\text{EE-9} [\text{F}])$$

#### (Second method) ITO sandwich cell capacitor

$$\begin{aligned}\text{Capacitance} &= (\epsilon_r \cdot \epsilon_0 \cdot A)/d \\ &= ((\epsilon_r \cdot 8.85\text{EE-12})(9\text{EE-6}))/d \\ &= (\epsilon_r \cdot 79.65\text{EE-18})/d \quad [\text{F}]\end{aligned}$$

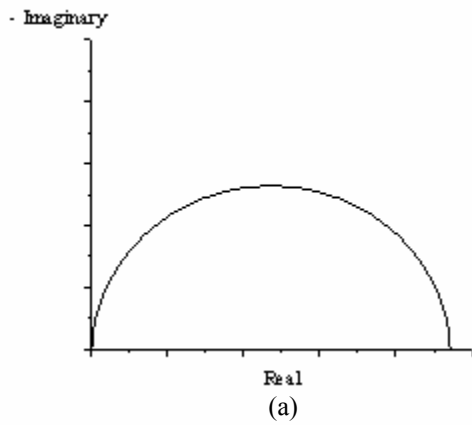
$$(d < 1\mu\text{m}) \text{ -----} > (\text{Capacitance} > \epsilon_r \cdot 79.65\text{EE-12} [\text{F}])$$

#### (Third method) Photolithography produced substrate

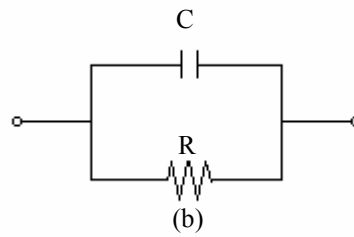
$$\begin{aligned}\text{Capacitance} &= (\epsilon_r \cdot \epsilon_0 \cdot A)/d & A &= 250\text{EE-9} \cdot 3\text{EE-3} \\ &= ((\epsilon_r \cdot 8.85\text{EE-12})(750\text{EE-12}))/d \\ &= (\epsilon_r \cdot 6.638\text{EE-21})/(20\mu\text{m}) \quad [\text{F}] \\ &= (\epsilon_r \cdot 331.875\text{EE-18}) \quad [\text{F}]\end{aligned}$$

## APPENDIX C:

### Cole-Cole plot



(a) Cole-Cole plot for a lossy capacitor



(b) Equivalent circuit

Equations:

$$|Z| \cos(\theta) \rightarrow \text{Real}$$

$$|Z| \sin(\theta) \rightarrow \text{Imaginary}$$

*University of Pennsylvania*  
Center for Sensor Technologies

**SUNFEST**

NSF REU Program  
Summer 2004

**DYNAMOMETER –  
THE NEW ACTIVITY MONITOR**

NSF Summer Undergraduate Fellowship in Sensor Technologies  
Olivia Tsai (Elec. & Comp. Engineering/Psychology) – Carnegie Mellon University  
Advisor: Jay N. Zemel

**ABSTRACT**

Activity monitors are convenient tools for extracting empirical information about a person's physical activity patterns, which may be the source of various health issues. The purpose of the "dynamometer" under development in this research effort is to monitor physical activity that impacts on the emerging issue of childhood obesity, and which also can be related to the development of bone deficiencies such as osteoporosis. The dynamometer consists of a piezoelectric sensor that is embedded into a shoe insole and is connected to a microcontroller for data acquisition and analysis. The analysis of the signal results in information about the magnitude, frequency, and duration of a child's actions such as running and jumping. An amplifier circuit amplifies the signal produced by the sensor. The full implementation of signal processing by the microcontroller was not completed due to time constraints.

A sensor calibrator was designed and fabricated to provide a standard stimulus to test the sensors. The results of testing indicated that although noise was present in the amplified signal, the output was reproducible and clean enough to provide accurate results regarding the sensor response to various forces.

## Table of Contents

1. INTRODUCTION.....	3
2. BACKGROUND.....	4
2.1. Overall.....	4
2.2. Piezoelectric Sensor.....	4
2.2.1. Output.....	5
2.3. Amplifier.....	6
2.3.1. Buffer Circuit.....	6
2.3.2. Gain Circuit.....	7
2.4. Microcontroller.....	8
2.4.1. ADC.....	9
2.4.2. Functions.....	10
3. SENSOR CALIBRATOR DESIGN.....	10
3.1. History of Ideas.....	10
3.2. Parts.....	11
4. RESULTS.....	12
5. RECOMMENDATIONS.....	14
5.1. Issues.....	14
5.2. Microcontroller.....	15
5.3. Wireless.....	15
5.4. Prototype.....	15
5.5. Testing on Children.....	15
5. CONCLUSIONS.....	16
6. ACKNOWLEDGEMENTS.....	16
7. REFERENCES.....	17
APPENDIX A: Sensor Calibrator Blueprints/Photos.....	18
APPENDIX B: Microcontroller C Code.....	22
APPENDIX C: Pin diagram for PicMicro 16F876.....	23
APPENDIX D: Device Prototype.....	24

## 1. INTRODUCTION

The lack of physical activity has become an increasingly serious concern in today's society, especially among children. From this deficiency stem a variety of health issues and the question of how to either prevent or eliminate these concerns. These issues range from obesity to osteoporosis. According to the American Obesity Association, the proportion of obese American children over the past 25 years has risen from 4.3% males and 3.6% females to 16% and 14.5% respectively [1]. It is reasonable to assume that there is a relationship between a person's physical activity patterns and his or her overall health; hence a means of quantifying activity would be a step toward understanding these interactions. While the subject of obesity has been explored to a limited extent, the related issue of how physical activity impacts the strength and density of bones has not yet been extensively addressed. Much as physical exercise is beneficial for one's health with respect to obesity and overall cardiovascular condition, physical activity is also important for children to gain bone mass. Specifically, it would be valuable to know whether it is the maximum force or the accumulation of all forces that affects the quality of a person's bone structure. These findings may be relevant in diagnosing the causes or influences behind the onset of osteoporosis.

Activity monitors would be an integral part of any effort to learn more about these health issues. Empirical information about physical activity would be best obtained through the use of an unobtrusive, but precise activity monitor. These devices should also be sufficiently versatile and adaptable so that they can be easily modified or expanded to address a variety of physical activity by extracting the desired physical measurements.

The current project addresses this issue by developing a device to measure the energy output (specifically, the magnitude, frequency, and duration of physical activity) of children between the ages of 4 and 8. This age group is targeted since it is hypothesized that the roots of many adult health problems originate during childhood. The proposed device, referred to as a dynamometer, is based on a piezoelectric PVDF sensor that responds to the forces arising on the soles of the feet of children as they go about their normal daily activity. The electrical output of the pedometer is fed into a signal processing circuit consisting of a preamplifier, a microcontroller and data storage unit. The microcontroller can be programmed in either C or Assembly language to extract the desired information, such as the overall or the maximum force generated by the child during normal activity. Other software can then process the signals to extract the energy expended.

It is essential that the device be thin and comfortable enough to fit within a child's sock. Another issue is processing the continuous stream of data to extract a timeline of the child's activity patterns. The computational capabilities of the electronics and related software determine how much data analysis can be carried out locally. Lastly, wireless communication is needed between the measuring circuitry and a central data storage site in order for a child to be able to function freely while wearing the device. Although the device is being designed for a very specific goal, it can be easily adapted to address a number of similar problems. Combining sensors with microcontrollers has significant

technological implications, particularly those in the health-related research, since much physical data can be collected using such devices at a low cost.

## 2. BACKGROUND

### 2.1 Overall

The basic design of the pedometer is shown in Figure 1. It consists of a sensor feeding into an amplifier circuit that outputs a signal to the analog-to-digital converter in the microcontroller. Once the data is converted by the microcontroller, they can be processed and locally stored in the memory of the microcontroller or output to a remote location using a wireless transmission.

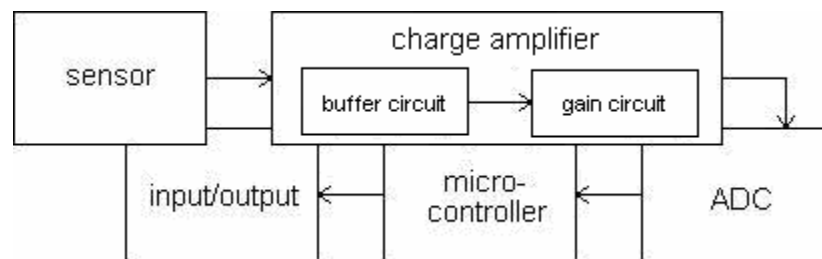


**Figure 1. Dynamometer Flowchart**

### 2.2 Piezoelectric Sensor

Sensors can be categorized as active sensors or passive sensors, and then further divided into more specific categories depending on their characteristics and functions [2, p.2]. These functions include, for example, sensing temperature changes, detecting movement using infrared beams and measuring liquid flow.

The sensor material used for the dynamometer is polyvinylidene fluoride, or PVDF in the form of a thin sheet that has electrically conductive nickel copper alloy electrodes deposited on each side.

An electrical current is generated when forces are applied to the piezoelectric material. Consequently no external source is needed to power the sensor [2, p.1]. The piezoelectric response is due to the strains arising in the piezoelectric material when a force is applied to it. The result is a displacement of atomic (or molecular) charges that the observed external currents. The electrical signal is amplified, processed, and converted to digital format for further analysis.

There are various advantages to using piezoelectric sensors instead of other types of sensors. Because this type of transducer possesses a wide measuring range of over  $10^8$  Newtons, it is able to handle a correspondingly wide range of force inputs. The outputs are stable and reproducible. Piezoelectric sensors are also generally insensitive to the

effects of electromagnetic fields and radiation [2, p.2]. On the other hand, it is unable to measure static forces. Time varying force data must be collected and analyzed immediately [1, p.3]. Because piezoelectrics are excellent dielectrics, they retain their charge after the application of a constant force, depending on the capacitance and leakage resistance of the element.

The sensor samples used for this research were provided by Dr. Mitch Thompson, Director, Development Engineering, Piezo Sensors Division, MSI Sensors, Inc., Wayne, PA 19087. Some preliminary testing suggested that the laminated LDT1-028K model would be the most appropriate sensor to use for the project since it was small enough to be less sensitive to bending than a longer sensor, yet large enough to be able to cover a suitable surface area under the foot. The overall dimensions of the sensor are 16mm x 41mm x 205 $\mu$ m.

It is necessary to calibrate the sensors to insure reliable data [4].

### 2.2.1 Measurement

The output current generated is a result of applying a force (stress) to the material. This force-current relationship arises from the thermodynamic free energy relation between the factors of strain, stress, electric field, and displacement. These relationships can be used to show that the current, when integrated over time leads to the total force exerted over the time period of interest. The current going into the amplifier is:

$$I = V/R + C \, dV/dt,$$

while the magnitude of the charge is:

$$Q = CV \\ Q = 10^{-8} \text{ F} * 12 \text{ V} = 1.2 * 10^{-7} \text{ Coulombs.}$$

The main question is whether the maximum force or the accumulation of the forces impacting the skeletal tissue determines how the bone adapts to these pressures. The maximum forces, the duration of the forces, and the frequency of the forces are all valuable pieces of information that need to be extracted from the signal.

The oscilloscope probe has an internal resistance of 1 M $\Omega$ , which shunts the small piezoelectric sensor current; hence, a much higher input resistance is needed.

Some noise problems arose in obtaining the signal. Part of this was due to problems with the ground reference point for the electronic components such as the power supply, oscilloscope, and amplifiers. This resulted in a large noise signal. In addition, 60-Hz pick-up was an issue because of the lack of proper shielding.

## 2.3 Amplifier

In order to successfully extract and analyze the signal output by the sensor, a simple high input impedance amplifier was designed and constructed to interface between the piezoelectric film and the other electronics (in this case, the microcontroller).

A LT1112CN8 op-amp was used in the actual amplifier circuit, while a LT1012ACN8 was used in the simulation. All simulations were done using MultiSim software to observe the effects of changing certain components in the amplifier design without potentially burning out the chips. The op-amps were powered by  $\pm 12$  volts from a dual power supply.

Specifically, there are two parts of the amplifier circuit (see Figure 4). The first stage uses a buffer circuit, and the second stage consists of a gain circuit.

### 2.3.1 Buffer circuit

The buffer circuit (shown in Figure 2) acts as a unity gain impedance transformer, meaning that the gain of the output does not change. Although the input and output voltages remain the same, the circuit converts a very high input impedance into a very low output impedance, on the order of tens of ohms. As shown in Figure 2, the input impedance of the buffer is 1 M $\Omega$ , although in practice a 100 M $\Omega$  resistance would be used. The low impedance output from this first stage insures that the second stage can track the buffered signal without additional delays.

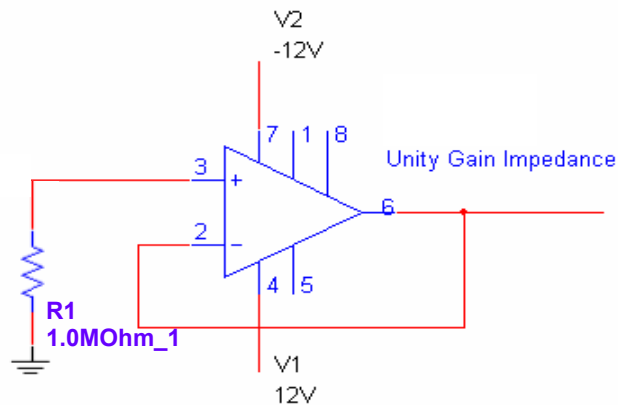


**Figure 2. Buffer Circuitry (Stage 1 of the Amplifier Circuit)**

### 2.3.2 Gain circuit

The purpose of the gain circuit (see Figure 3) is to amplify the buffered signal. The significance of this circuitry is that high gain can be achieved without decreasing the bandwidth of the signal. The gain can be calculated using the following formula:

$$\text{Gain} = R_g + R_{out} / R_{out}$$

This effect is demonstrated in Figure 5. So if more gain is desired, the feedback resistor can be increased.

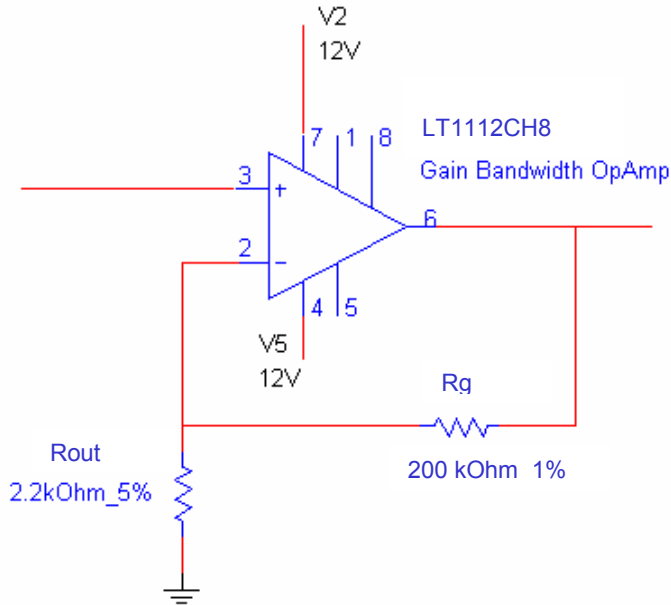


**Figure 3. Gain Circuitry (Stage 2 of the Amplifier Circuit)**

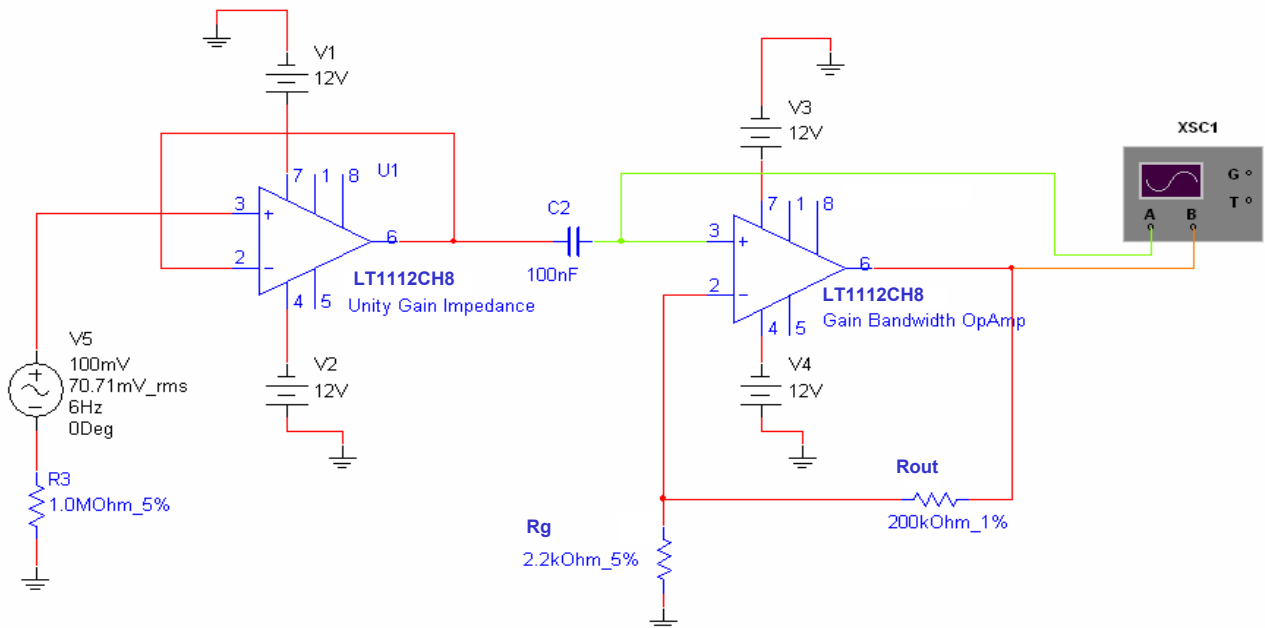


**Figure 4. Amplifier Circuit. R3 represents the high impedance necessary to shunt the input, V5 represents the piezoelectric sensor input, the first op-amp represents stage 1 of the circuit, and the second op-amp represents stage 2 of the amplifier.**

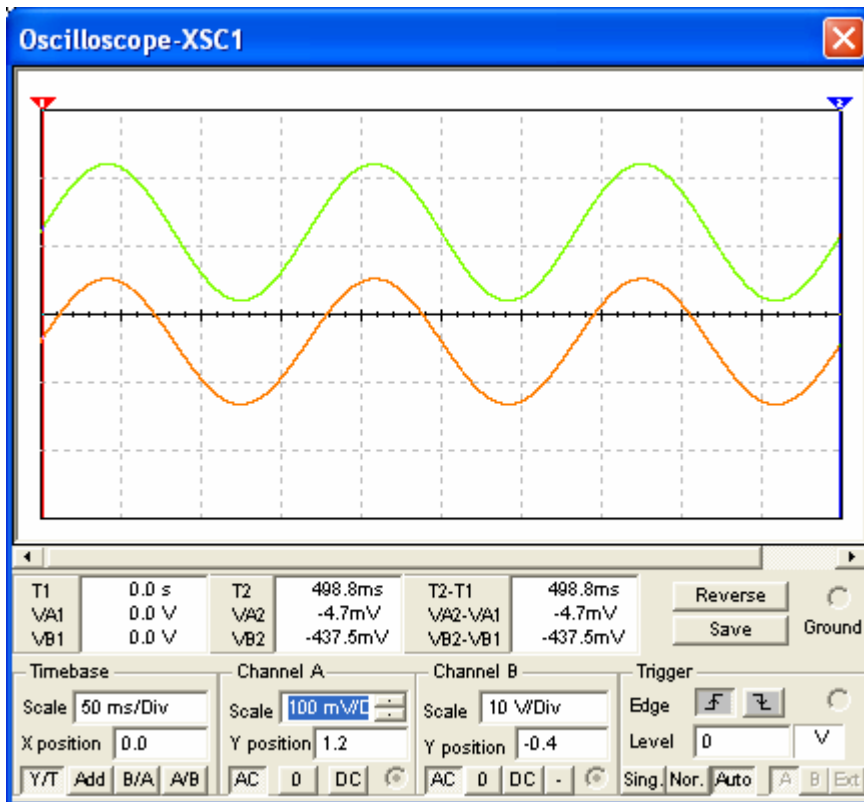


**Figure 5. Input into stage 2 (green) and Output (orange) of overall Amplifier Circuit**

## 2.4 Microcontroller

The PicMicro 16F876 microcontroller was chosen for this project since it was a compromise to achieve both an affordable price and simple functionality. The 14-bit core peripheral interface controller (PIC) was programmed and compiled using the CC5X B. Knudsen C compiler as an extension of the MPLab 6.5 software.

Some smaller programs were written to test the relationship of the microcontroller with both digital and analog inputs. The digital signal was generated by a function generator, while an analog signal was obtained by connecting the output of the sensor into the microcontroller. The bi-functionality of the IO ports allowed us to specify whether the pins acted as inputs or outputs by setting the TRIS function to the appropriate bits. As a test, a simple 5-volt sine wave, offset by 2.5 volts, was sent into one of the input ports. The microcontroller was then programmed to output the same value it received. By using the PORTC registers as outputs with each pin representing one of 8 bits of the output value, we were able to use the oscilloscope to determine that the lowest bit was represented on Pin 11. Pins 12, 13, 14, 28, 27, 26, and 25 represented increasingly higher bits since high bits are represented by waves of lower frequency, while the low bits are represented by waves of higher frequency. Basically, the registers store the value of the wave ranging from 0 to 5 as a hexadecimal value from 2 to 255 (see Appendix C for pin diagram).

### **2.4.1 ADC (Analog to Digital Converter)**

The ADC is located on pins 2 and 3 of the PicMicro 16F876. The purpose of this feature is to convert the analog signals (the varying forces exerted) into signals that can be read and processed digitally by the microcontroller. The resolution of the ADC determines how many units a reading can be broken down into; in the case of the PIC, the ADC is 10-bits wide. This means that an analog input signal can be digitized and read in as a value between 0 and 1023, since  $2^{10} = 1024$ . Working with 10-bit values can get complicated since 10-bit values need to be processed as 16-bit words, so it is common to use 8-bit values represented as 8-bit words. Dividing the input into a smaller number of units also reduces the size of the program required to handle the numbers involved and the amount of processing required. On the other hand, choosing to use 8-bits over 16 bits is throwing away a factor of 4 in resolution, i.e. 256 instead of 1024. That is 0.4% resolution instead of 0.1%, which could be a problem if the data required is of high resolution.

### **2.4.2 Functions**

The desired functions of the microcontroller are to be able to find the maximum signal and to integrate the area under the signal to extract the overall force exerted by the child. Some secondary outputs are the duration of activity, which can be obtained by isolating a block of activity and subtracting the start time from the end time, and the frequency of activity.

## **3. SENSOR CALIBRATOR DESIGN**

In order to be able to test the electronics and the output of the sensors, a standard stimulus was designed; it was fabricated in the Physical Sciences Machine Shop located in David Rittenhouse Laboratory (see Appendix A). The design of the sensor calibrator cyclicly stressed the sensor with a period of approximately 3 seconds. As a result, a prescribed periodic force could be applied to the different sensors, thereby providing calibrated and detailed measurements of the signals. Hence, when the sensors are attached to an insert of a shoe, it would be possible to calculate the force that generated the observed charge.

### **3.1 History of ideas**

The initial inspiration for stamping a cyclical pattern onto the sensor stemmed from the repetitive nature of many toy movements. For example, using a mechanical wind-up toy or a battery-powered car on a racetrack seemed like an inexpensive and quick means of obtaining a calibrator. However, a more efficient calibration technique would feature a stationary device.

One option was to use the switching power of an electromagnetic relay to simulate the up and down movement necessary to vary the force of a mass on top of the sensor. The problem was that the electromagnetic forces induced would not be sufficiently strong to

lift a large mass comparable to a child's weight since relays are usually very small and a huge current would need to be drawn to create an electromagnetic field of the appropriate strength.

For simplicity, the next idea involved simply attaching the sensor to a foot-like structure and pushing it off a fixed height to calibrate the sensors. Although the height would be calibrated, the exact force exerted on the sensor would vary depending on how the "foot" hit the floor. Also, it would not be possible to attain a cyclical motion from this type of design.

Linear motors were researched since the unidirectional movement of such a device would be ideal for inducing a repetitive response onto the sensor. The main problem with this idea was the high cost of such devices.

The final approved idea was to use an oscillator in conjunction with a spring to vary the weight of a fixed mass on top of the sensor to be tested. Specifically, a spring with spring constant  $K$  was attached to an oscillatory driver on one side and fixed on the other to a mass  $M$  that was large enough so that the maximum lifting force exerted on it when the spring is displaced by  $+A$  cm is less than  $Mg$ , the weight of the mass. The spring displacement is given by  $A(t) = A \sin(2\pi f_0 t)$ . Hence the force will vary by  $\pm KA$  and because  $KA < Mg$ , the weight remains stationary but the force is not (see Figure 7).

The forces are affected by the following parameters, where  $M$  is the mass of the weight,  $A$  is the displacement of the spring, and  $k$  is the spring constant:

$$F_{\text{total}} = Mg - kA(t)$$

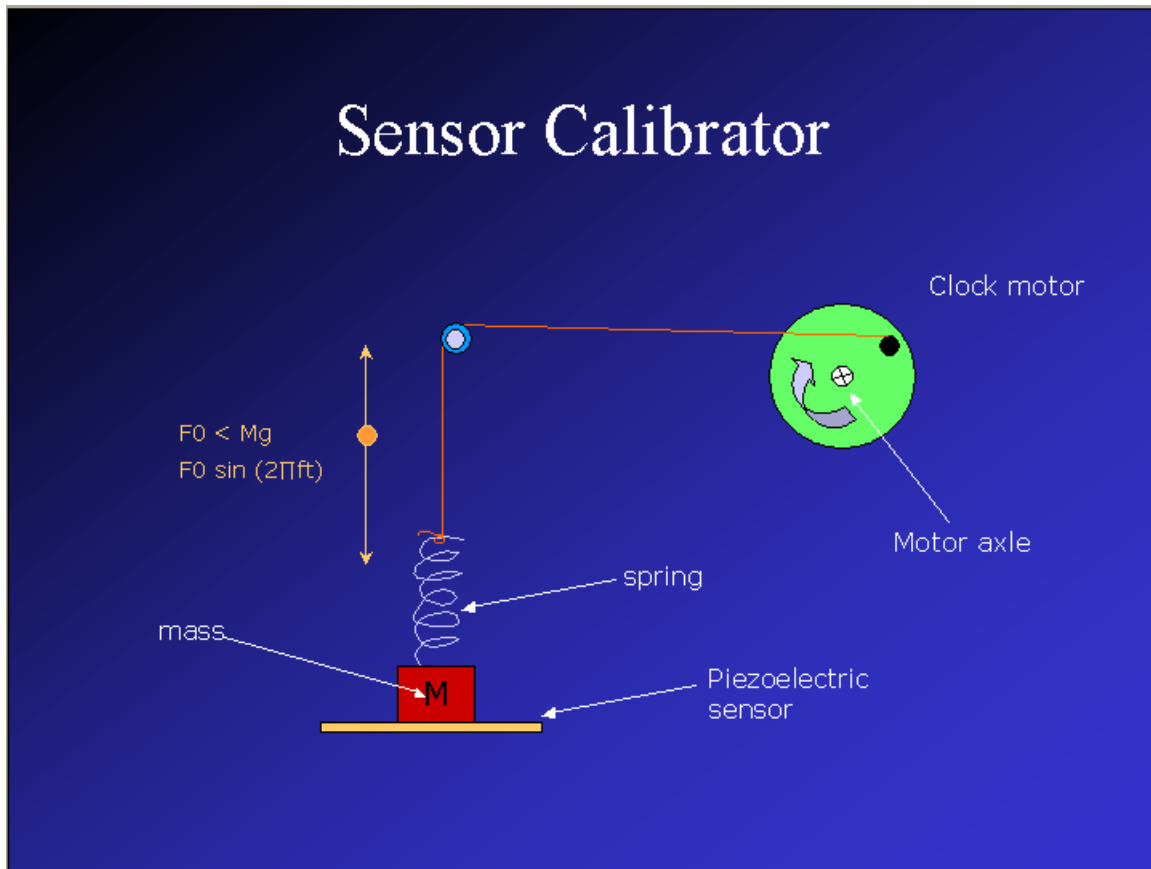


**Figure 7. Diagram indicating varying forces of the spring-mass system**

The design process required that the spring displacement be calculated in order to decide the necessary size and radial position of the drive wheel. It is important that the drive wheel have enough clearance to be able to turn without any obstructions while also rotating enough for the desired spring displacement. The greater the spring displacement, the greater the range of force values exerted onto the sensor. PowerPoint, Canvas 9, and AutoCAD were used to share the ideas and receive critiques, as well as to draw out the final blueprints for the machine shop to fabricate. (Canvas 9 is a technical drawing software program primarily used to create blueprints.)

### 3.2 Parts

Aluminum was used for the calibrator since this material is strong and relatively cheap. A clock motor with a low speed of 16-RPM CCW was chosen since the 25-lb in torque specifications would be sufficient to lift a mass the weight of a small child. A tubular instrument scale was selected for its reasonable force constant and its ability to handle up to 25 kg (approximately 55 lbs). Additionally, a pulley with bearings was ordered to change the direction of the wire holding up the mass from left-to-right to up-and-down. The mass used was about 21.5 pounds.

#### 4. RESULTS

Before testing the effectiveness of the sensor calibrator, steps were taken to solve the problems with the raw information produced by the sensor (see Figure 8). After grounding the motor, the oscilloscope, and the sensor to the same reference point used by the circuitry, the signal showed fewer signs of interference from external factors (see Figure 9) than when the circuitry was not connected to ground.

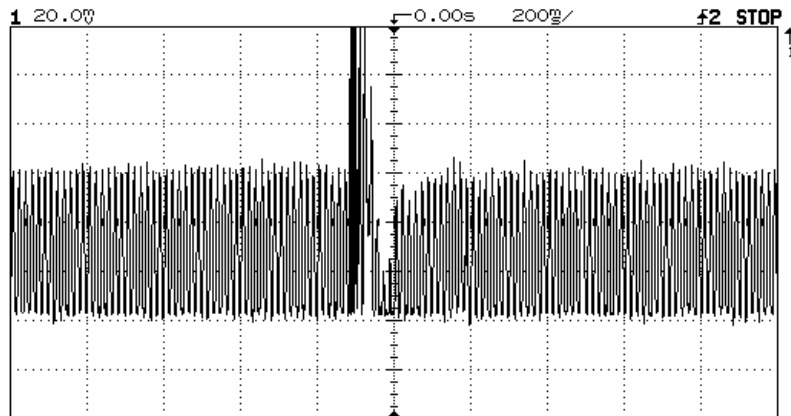


**Figure 8. Signal before grounding the electronics. The amount of noise (pick-up) present in the signal is evident.**

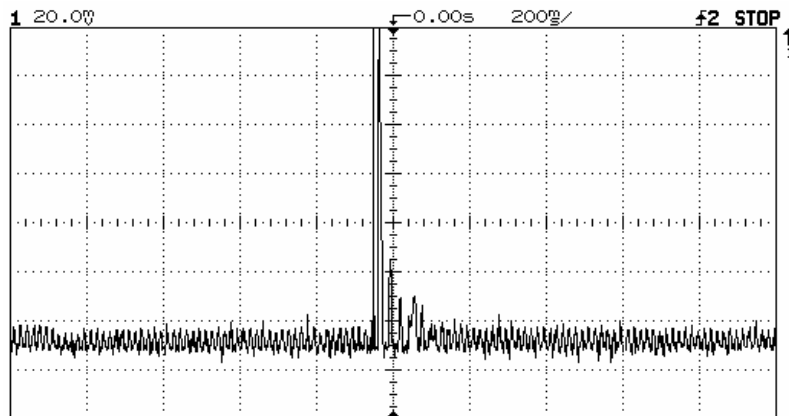


**Figure 9. Signal after grounding the electronics (some noise eliminated)**

Next, the sensor calibrator was used to check for the response of the sensors. A 9.75 kg (21.5 lb) weight was attached to the spring to allow the oscillatory motion of the calibrator to vary the forces of the weight on the sensor. The outputs of the sensors (see Figures 10 and 11) confirmed the reproducibility of the force-sensor relationship, since the measurements taken at different times resulted in similar output behaviors.

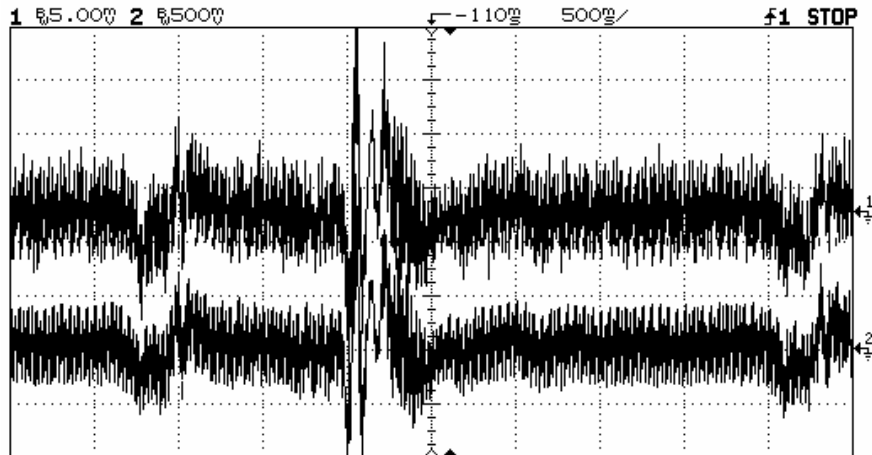


**Figure 10. Output of Sensor using Sensor Calibrator (Scale 5.00mV/500mV)**

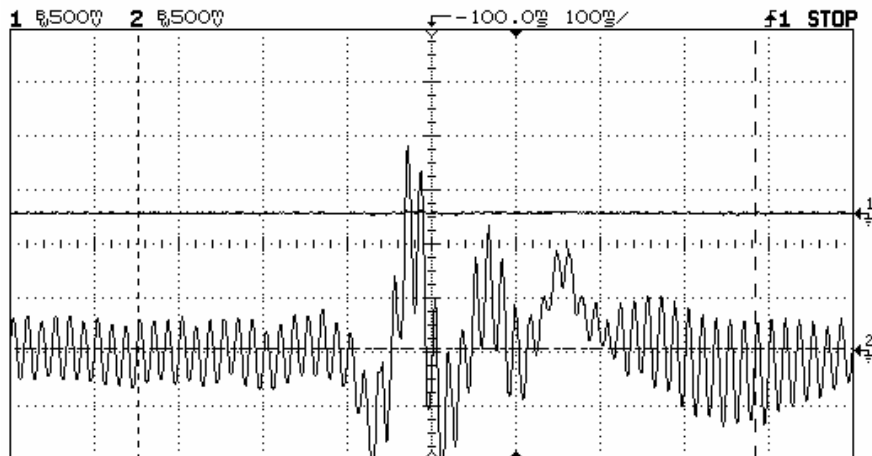


**Figure 11. Output of Sensor using Sensor Calibrator (Scale 500mV/500mV)**

The microcontroller aspect of the project was started; however, the microcontrollers failed before the functions written could be tested and debugged. The framework of various functions was outlined (see Appendix B). These functions included the calculation of the maximum value of the signal, the initialization of the analog-to-digital property of the microcontroller, as well as the conversion of a digital signal to an analog value.

The sensor calibrator appears to work well giving reproducible signals. Despite the presence of 60-cycle noise, it is clear that the peaks from both figure 7 and figure 8 correspond to the same maximum force applied. This suggests that the signals produced could be directly related to a person's activity. It is also evident that the amplifier is behaving correctly since the output of the sensor (represented by channel 2) has a gain of approximately 100 over the original signal (represented by channel 1). The actual gain is 92.

## **5. RECOMMENDATIONS**

### **5.1 Issues**

The sensitivity of the sensors to bending affects their ability to exclusively measure forces. Since larger sensors are more sensitive to this property, it is recommended that smaller sensors be used for the dynamometer, while still maintaining a large enough surface area to be able to collect the force data. The issue of noise can be dealt with by shielding the system in order to reduce the presence of unwanted frequencies.

### **5.2 Microcontroller**

The Texas Instrument family of microcontrollers provides much superior, smaller chips that could be used in place of the PicMicro 16F876 chip. Its main advantage is that it is smaller than the PicMicro, which would make it easier to design a desirable, unobtrusive dynamometer device. Some of the device's key features include high-performance analog (ideal for precise measurement), in-system programmable Flash, which permits flexible code changes, and pricing as low as \$0.49 per unit. One of the intended applications of this microcontroller is for intelligent sensing, which encompasses the goals of the dynamometer. [5]

### **5.3 Wireless**

Wireless technology should eventually be incorporated into the design of the dynamometer in order to be able to continually transmit data from the microcontroller to a remote location using the serial ports of the microcontroller. The Bluetooth SiPs (Systems-in-a-Package) are ideal modules to introduce wireless functionality to the activity monitor. These Bluetooth SiPs take up an area as small as  $49 \text{ mm}^2$ , coexist with 802.11 WLAN, and require only an external clock source and antenna for operation [6].

On the other hand, the microcontroller could store up to 5 kilobytes locally, so if wireless was possible, the microcontroller could transmit data every time it was in close proximity to a wireless hub. An EEPROM chip can also be connected serially to the microcontroller for additional memory storage, since this memory is not directly mapped in the register file space. This function is categorized under the role of the special function registers [7].

## **5.4 Prototype**

The goal was to have a working prototype that a child can wear comfortably while collecting data. Clearly, a child's activity patterns will not represent normal activity if the device worn is obtrusive with wires hanging out. In fact, if the child is unwilling to wear the device, data cannot even be collected. Most likely, all the circuitry other than the actual sensor will be encased in a small box that can be strapped onto the child's ankle. The design of the box is not a trivial matter. A child's interests must be considered when choosing the size and shape of the box containing the electronics (see Appendix D).

## **5.5 Testing on Children**

Drs. Babette Zemel and Dr. Anne Buisson, a post-doctoral Fellow, have agreed to handle the human testing aspect of the device. Once they confirm the type of data they want to collect, the microcontroller can be modified to extract this type of information. Ideally, the data collected about a child's activity will be useful in determining what types of activity promotes the level of bone growth and strength. This data can then be used to reduce the number of cases of osteoporosis occurring in adults by targeting childhood prevention.

## **6. CONCLUSIONS**

The idea of a pedometer is relatively simple, but the implications are huge. If obesity or other health issues can be monitored, significant health benefits may be achieved for a very low cost. Specifically, it would be possible to learn more about bone development and the relationship between activity and bone strength, which has significant implications for osteoporosis diagnosis and prevention.

The sensor-microcontroller design is extremely versatile. For one, it can be used in an unlimited number of places since the sensor is thin and wearable. This surpasses the functionality of a force plate, which is too large to be moved around with a person during their daily routine. The design is also easily adaptable to serve other functions as long as the signals produced by the sensors can be captured. The microcontrollers used can be modified to collect different data, depending on the type of data desired and the type of sensor used. For example, if the desired data is the speed of a runner, an accelerometer sensor could be used and attached to the athlete's wrist or leg.

## 7. ACKNOWLEDGMENTS

I would like to thank my advisor, Dr. Jay N. Zemel, for his all his guidance and advice regarding not only my research project, but on planning for my future career. I would also like to thank all the faculty, administration, and researchers involved with the SUNFEST program for making this summer an unforgettable experience—especially Dr. Van der Spiegel for devoting so much time in planning the program, Dr. Tamar Granor for critically editing my final paper, Sid for always playing the devil’s advocate to my ideas, and the lovely ladies of Moore 203 for sharing their microwave. A special thanks to Rob Callan for his invaluable assistance in helping me tackle the microcontroller aspect of the pedometer and Alex Chang for keeping me sane by introducing me to the idea of taking breaks. Finally, I would like to thank the National Science Foundation and Microsoft Corporation for their financial support of this REU Program.

## 8. REFERENCES

- [1] “American Obesity Association – AOA Fact Sheets” Available from: [http://www.obesity.org/subs/fastfacts/obesity\\_youth.shtml](http://www.obesity.org/subs/fastfacts/obesity_youth.shtml), Accessed from: 4 Aug 2004.
- [2] G. Gautschi, *Piezoelectric Sensorics*, Springer, New York, 2002.
- [3] “Piezoelectric Film” Available from: <http://www.imagesco.com/articles/piezo/piezo03.html>, Accessed from: 4 Aug 2004.
- [4] “ME 117/220 Lecture #6” Available from: [http://design.stanford.edu/Courses/me220/lectures/lect06/lecture\\_6](http://design.stanford.edu/Courses/me220/lectures/lect06/lecture_6), Accessed from: 4 Aug 2004.
- [5] “Microcontrollers – MSP430 MCUs” Available from: [http://focus.ti.com/mcu/docs/overview.tsp?familyId=342&templateId=5246&navigationId=11466&path=templatedata/cm/mcuovw/data/msp430\\_ovw](http://focus.ti.com/mcu/docs/overview.tsp?familyId=342&templateId=5246&navigationId=11466&path=templatedata/cm/mcuovw/data/msp430_ovw), Accessed from: 4 Aug 2004
- [6]”Phillips Semiconductors - Bluetooth” Available from: <http://www.semiconductors.philips.com/technologies/bluetooth/systems>, Accessed from: 4 Aug 2004.
- [7] “PicMicro Device Documentation” Available from: <http://ww1.microchip.com/downloads/en/DeviceDoc/31007a.pdf>, Accessed from: 4 Aug 2004

**APPENDIX A:  
Blueprints for Sensor Calibrator**

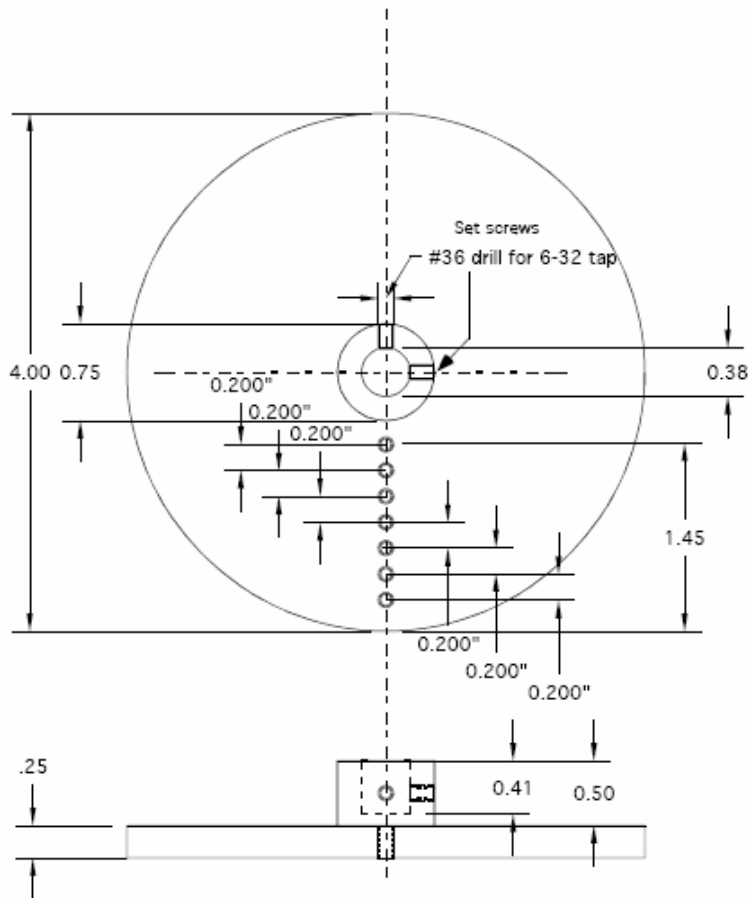
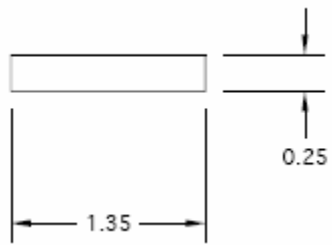


Figure 5  
mild steel Stock  
±0.010  
A 7 holes 6-32 tapped

Drive Wheel of Calibrator



Pin for pulley. Round ground stock

Press fit to the 0.250" in hole in the Motor Mount  
on one side and to the pulley on the other. To be aligned  
with the cord.





Calibrated Spring and Clock Motor



Drive Wheel and Pulley



Calibrated Spring and Mass with  
Dynamometer prototype

## APPENDIX B: Microcontroller C Code

```
/* function written by Rob Callan: setup for ADC */
uns8 get8BitADC() {
    ADCON0.0= 1; //      0=TURN ON Analog
    ADCON0.2= 1; //      2=MAKE CONVERSION
    while(ADCON0.2==1); // while incoming signal
    return ADRESH;
}

uns8 getIntegration(uns8 y, uns8 samplerate) {
    uns8 sum, area;
    sum = 0;
    while ( // more samples to be read in, or reach cutoff) {
        area = y * samplerate; // y * deltax (small)
        sum += area;
    }
    return sum;
}

uns8 getMax (uns8 y) {
    uns8 max;
    max = 0;
    if ( y > max)
        max = y;
    return max;
}

/*      function written by Rob Callan: set-up for DAC      */
void setupPWM() {
    CCP1CON&= 0xf0;
    CCP1CON|= 0x0c;
    CCP2CON&= 0xf0;
    CCP2CON|= 0x0c;
    PR2= 0xff;
    T2CON&= 0xf8;
    T2CON|= 0x00;
    T2CON.2= 1;
}

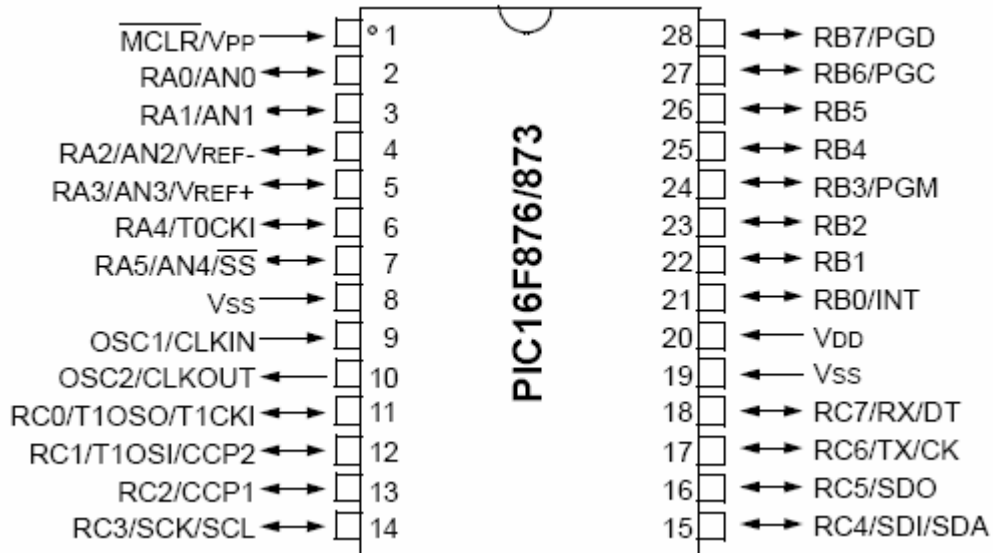
/*      function written by rcallan: output for DAC      */
void setOutputOfPWM(uns8 toOutput, uns8 outputReg) {
    if(outputReg==1) CCPR1L= toOutput;
    else              CCPR2L= toOutput;
}

void main( void) {
    uns8 temp, temp2;
    PORTC = 0b.1111.1111; /* out = 1 */
    TRISC = 0b.0000.0000; /* xxxx 0001 */
    setupPWM();

    /*while(1) {
        PORTC = 0xff; // set all ports to high
        temp = get8BitADC(); // get input from fxn gen
    }*/

    setOutputOfPWM(51,1); // 51 -> 1 V //128 approx 2.5 V
    while(1);
}
```

**APPENDIX C:**  
**Pin diagram for PicMicro 16F876**



**APPENDIX D:  
Device Prototype**

